ACCURACY ASSESSMENT OF THE DEM AND ORTHOIMAGE GENERATED FROM ASTER

A THESIS SUBMITTED TO
THE GRADUATE SCHOOL OF NATURAL AND APPLIED SCIENCES
OF
MIDDLE EAST TECHNICAL UNIVERSITY

BY

ALİ ÖZGÜN OK

IN PARTIAL FULFILLMENT OF THE REQUIREMENTS
FOR
THE DEGREE OF MASTER OF SCIENCE
IN
GEODETIC AND GEOGRAPHIC INFORMATION TECHNOLOGIES

SEPTEMBER 2005

Approval of the Graduate School of Natural and Applied Sciences

Prof. Dr. Canan ÖZGEN
Director

I certify that this thesis satisfies all the requirements as a thesis for the degree of Master of Science.

Assist. Prof. Dr. Zuhal AKYÜREK
Head of Department

This is to certify that we have read this thesis and that in our opinion it is fully adequate, in scope and quality, as a thesis for the degree of Master of Science.

Assoc. Prof. Dr. Mustafa TÜRKER
Supervisor

Examining Committee Members

Prof. Dr. Vedat TOPRAK	(METU, GEOE)	
Assoc. Prof. Dr. Mustafa TÜRKER	(HU, JDZ)	
Prof. Dr. Volkan ATALAY	(METU, CENG)	
Assist Prof. Dr. M. Onur KARSLIOĞLU	(METU, GGIT)	
Dr. Uğur Murat LELOĞLU	(TUBITAK)	

I hereby declare that all information in this document has been obtained and presented in accordance with academic rules and ethical conduct. I also declare that, as required by these rules and conduct, I have fully cited and referenced all material and results that are not original to this work.

Name, Last name: Ali Özgün OK

Signature :

ABSTRACT

ACCURACY ASSESSMENT OF THE DEM AND ORTHOIMAGE
GENERATED FROM ASTER

OK, Ali Özgün
M.Sci., Department of Geodetic and Geographic Information Technologies
Supervisor: Assoc. Prof. Dr. Mustafa TÜRKER

September 2005, 236 pages

In this study, DEMs and orthoimages were generated from ASTER imagery and their accuracies were assessed. The study site covers an area of approximately 60 x 60 km and encloses the city of Ankara.

First, DEMs were generated from stereo ASTER images. In order to find the best GCP combination, different number of GCPs (8, 16, 24, and 32) was used. The accuracies of the generated DEMs were then assessed based on the check points (CP), slopes and land cover types. It was found that 16 GCPs were good compromise to produce the most accurate DEM. The post processing and blunder removal increased the overall accuracy up to 38%. It was also found that there is a strong linear relationship between the accuracies of DEMs and the slopes of the terrain. The accuracies computed for water, urban, forest, mountainous, and other areas were found to be 5.01 m, 8.03 m, 12.69 m, 17.14 m, and 10.21 m, respectively. The overall accuracy was computed as 10.92 m.

The orthorectification of the ASTER image was carried out using 12 different mathematical models. Based on the results, the models First Order 2D Polynomial, Direct Linear Transformation and First Order Polynomial with Relief have produced the worst results. On the other hand, the model Second Order Rational Function appears to be the best model to orthorectify the ASTER images. However, the developed model Second Order Polynomial with Relief provides simplicity, consistency and requires less number of GCPs when compared to the model Second Order Rational Function.

Keywords: ASTER, Digital Elevation Model (DEM), Orthorectification, Accuracy, Mathematical Models.

ÖZ

ASTER'DEN ÜRETİLEN SYM VE ORTOGÖRÜNTÜLERİN DOĞRULUK ANALİZLERİ

OK, Ali Özgün
Yüksek Lisans, Jeodezi ve Cografi Bilgi Teknolojileri E.A.B.D.
Tez Yöneticisi: Doç. Dr. Mustafa TÜRKER

Eylül 2005, 236 sayfa

Bu çalışmada, ASTER görüntüsünden SYM'ler ve ortogörüntüler üretilmiş ve doğrulukları test edilmiştir. Çalışma alanı, Ankara'yı da içine alan 60 x 60 km'lik bir alanı kapsamaktadır.

İlk olarak, bindirmeli ASTER görüntülerinden SYM'ler üretilmiştir. En iyi YKN dağılımını bulabilmek için farklı sayıda YKN'ler (8, 16, 24, and 32) kullanılmıştır. Daha sonra, doğruluklar bağımsız denetim noktalarında (BDN), belirli eğim aralıklarına ve arazi örtüsü türlerine göre değerlendirilmiştir. Doğruluğu en yüksek SYM'nin 16 YKN kullanılarak oluşturulduğu bulunmuştur. Hataları düzeltme ve kaba hataları temizleme işlemleri genel doğruluğu %38'lere varan düzeylerde artırdığı hesaplanmıştır. Ayrıca, SYM doğrulukları ve arazi eğimi arasında kesin doğrusal bir ilişki olduğu da bulunmuştur. Su yüzeyleri, şehirsel, ormanlık, dağlık, ve diğer alanlar için doğruluklar sırasıyla 5.01 m, 8.03 m, 12.69 m, 17.14 m ve 10.21 m olarak hesaplanmıştır. Genel doğruluk ise 10.92 m olarak bulunmuştur.

ASTER görüntüsünün ortorektifikasyonu 12 farklı matematiksel model kullanılarak yapılmıştır. Elde edilen sonuçlara göre, en kötü ortorektifikasyon doğrulukları Birinci Dereceden 2 Boyutlu Polinom, Direkt Lineer Dönüşüm ve Rölyef Düzeltmeli Birinci Dereceden Polinom Modellerinde hesaplanmıştır. Diğer taraftan, ASTER görüntülerinin ortorektifikasyonunda en iyi sonuç İkinci Dereceden Rasyonel Fonksiyon'da elde edilmiştir. Ancak, geliştirilen Rölyef Düzeltmeli İkinci Dereceden Polinom Modeli, İkinci Dereceden Rasyonel Fonksiyona göre basitlik ve tutarlılık sağlamakta ve daha az YKN gerektirmektedir.

Anahtar Kelimeler: ASTER, Sayısal Yükseklik Modeli (SYM), Ortorektifikasyon, Doğruluk, Matematiksel Modeller.

To My Parents

ACKNOWLEDGMENTS

I would like to gratefully thank to my supervisor Assoc. Prof. Dr. Mustafa TÜRKER for his great guidance, continuous support and motivation during both the development of this thesis and my master program. This research would have been impossible without his valuable technical assistance.

I would also like to thank Assist. Prof. Dr. Mahmut Onur KARSLIOĞLU for sharing his valuable knowledge throughout the preparation of this thesis.

I would like to thank Prof. Dr. Vedat TOPRAK, Prof. Dr. Volkan ATALAY and Dr. Uğur Murat LELOĞLU for reading and reviewing my thesis. Their evaluation and comments improved this thesis considerably.

I wish to express my deepest gratitude to Prof. Dr. Ülkü YETİŞ, Prof. Dr. Ayhan İNAL and Prof. Dr. Filiz B. AKIN for their endless support and motivation. I will never forget your assistance and positive approach.

I would like to thank Hacettepe University, Faculty of Engineering, Department of Geodesy and Photogrammetry for supplying the precious reference data. I also thank Birol GÜÇLÜER who supplied the differential GPS receivers without any cost for a long period of time.

I would like to thank my dear friends Evren AKYÜZ, Oya DİNLER, Murat ATALAY, Mert AYDIN, Eren ÖZMEN, Murat KUŞ and Metin KUŞ for their invaluable friendship during this thesis. Extraordinary driving and helps of Evren AKYÜZ, Murat ATALAY and Mert AYDIN during the fieldworks will always be remembered.

I would like to express thanks to Özgün BALKANAY and Nilhan ÇİFTÇİ for their endless support and thoughtful friendship during my study in METU. It was my chance to get a view of such love and relationship between you two. Once more, it will be my honor to be at your wedding.

I am thankful to my dear friends Dilek KOÇ and Aslı ÖZDARICI for their supportive approach and kind friendship all the way to conclude my master program. I want you to know that without your positive approach, this thesis would not have been concluded.

I would like to express thanks to “Lord” Kıvanç ERTUĞAY and “Pasha” Serkan KEMEÇ for their tolerance and understanding during the preparation of this thesis. The games played with two of you have always been a relaxive effect and reduced the stress on me. Thank you for everything.

I would like to thank Gülcan SARP, Reşat GEÇEN, Arzu ERENER, Pınar ASLANTAŞ and Ayten KOÇ for their supportive attitude towards me. Special thanks go to Gülcan SARP for helping my writing process which was reduced my task significantly.

I wish to thank my colleagues M. Alper TEMEL, Sema Nur GÜLAL TEMEL, Birol YILMAZ, Bumin Kağan ÖZTÜRK, Özkan ÖZER and Ali Vehbi BUTUK for their understanding during the development of this thesis. Special thanks go to M. Alper TEMEL for trying to find a vital data which is essential in this thesis.

I would like to thank Emre SÜMER and Emre ERDOĞAN for their motivation and kind friendship during this study. Their suggestions and supportive approach was crucial to recover my morale in my desperate times.

I would like to express my deepest gratitude to Sadi YETİŞ and İhsan YETİŞ, my maternal uncles, for purposely loosing the backgammon games which we played during this thesis. Their support and positive attitude forms one of the key points of my success in my education.

Special thanks go to Tuğçe, Serra, Begüm and Mediha YETİŞ for supporting me all the time even when I lost the backgammon games. They do really mean a lot to me and thanks for everything.

I cordially would like to dedicate this thesis to my dear parents Nuri OK and Semra OK. Their continuous affection, encouragement, patience and belief made me who I am. I am really glad to have a father and mother like you. Thank you for everything.

TABLE OF CONTENTS

LIST OF TABLES

TABLES

LIST OF FIGURES

FIGURES

CHAPTER 1

INTRODUCTION

1.1 Scope and Purpose

Digital elevation models (DEM) are important resource used for geo-spatial analysis. When the first commercial satellite was launched, the importance and the application areas of the satellite images were apparent. Until that time, the improvements in remote sensing and computing technologies have evolved many research areas including the photogrammetry and mapping and gave new opportunities to researchers. One important innovation in these areas is the modeling and visualization of the Earth’s surface in digital representation.

Nowadays, the demand for DEMs is getting increased with their utilization in GIS for many leading applications. The incorporation of DEM in a GIS has a broad range of applications linked to land management and terrain modeling, rail and road infrastructure studies, telecommunication planning, oil and gas exploration, military mapping, flight and airport landing simulations, 3D city modeling and the like. Elevation data, integrated with satellite imagery is also used for many purposes such as generating orthoimages and perspective views, route planning for transportation and tourism. The orthorectification of the satellite images enables users to utilize images in conjunction with a DEM and other spatial information in a GIS. For this reason, the generation of DEMs and orthoimages is quite important for many applications in the field of remote sensing. Despite a broad range of applications, DEMs and orthoimages are still not available for many areas of the Earth surface.

The SPOT satellite series are the first satellites which enable contiguous stereoscopic coverage. Therefore, stereo SPOT images have been extensively used for DEM generation. Today, a series of Earth observation satellites are monitoring our planet and acquiring a large number of stereo images. SPOT 4 and 5, TERRA (ASTER), IRS 1 C/D, IKONOS-2, EROS A1, QUICKBIRD-2, and ORBVIEW-3 are the most popular satellites that acquire stereo images. Of these satellites, the TERRA (ASTER) is considered to be an important satellite because it provides the largest coverage with minimum cost. It is therefore believed that, TERRA (ASTER) can provide DEMs and orthoimages that can be used for many applications. However, sufficient accuracy of DEMs and orthoimages are required for such studies.

The objective of this study is to assess the accuracies of DEMs and orthoimages generated from ASTER imagery. To do that, DEMs were generated using four different sets of GCPs to assess the accuracies based on the number of GCPs. In addition, the accuracies of the DEMs were assessed based on the slopes and land cover types. The orthorectification of the ASTER imagery was performed using twelve different mathematical models. With the implementation of the twelve models not only the accuracies of the orthoimages generated were assessed but also the best mathematical model for orthorectifying the ASTER imagery was determined.

1.2 The Software Used

During this study, the PCI Geomatica image analysis software was used to generate the DEMs from ASTER images. The mathematical model provided by the software is one of the models used for the orthorectification process. This software was also used for generating the reference DEM and slope map, data transferring etc. Microstation SE digital photogrammetric workstation software was used to merge and transfer the vector data to the PCI Geomatica software. The SPSS statistical analysis software was used for the implementation of Pearson's correlation test and several graphical presentations. The Microsoft Excel was used for preparing the tables and most of the figures in the thesis. Finally, the implementation and processing of the eleven mathematical models for performing the orthorectification were carried out using MATLAB 6.5, which is a high-performance language for technical computing. Using MATLAB, the orthorectified images were obtained for each of the eleven mathematical models both textual and graphical presentations.

1.3 Organization of the Thesis

This thesis is composed of seven chapters. The next chapter (chapter 2) provides the literature review about DEM generation and orthorectification from ASTER imagery.

In chapter 3, the theoretical bases of DEM generation from satellite stereo images are described. This chapter starts with the explanations of stereoscopy and stereoscopic acquisition techniques. Then, the stereoscopic processing stages are explained. Finally, the orthorectification of the satellite imagery using the forward and backward algorithm are provided.

The study area and data sets used in the study are provided in chapter 4. After describing the study area, the image data, reference vector and orthophoto data are explained. Next, the method for generating the reference DEMs from vector data is explained. Finally, the GCPs and their collection methods are described.

The following chapter (chapter 5) presents the DEM generation steps from ASTER stereo imagery. First, the Terra satellite, which carries the ASTER sensor, is explained. Second, the DEM generation process from stereo ASTER images is described. Finally, the results of the assessment of the generated DEMs are provided. The results comprise of two sections, (i) the results of the least squares bundle adjustment and (ii) the results of DEM accuracy evaluation.

Chapter 6 involves the orthorectification of ASTER imagery. First, the processing steps of the orthorectification procedure performed during this study with the use of MATLAB software are provided. Then, the results of orthorectification of the nadir ASTER image using different twelve models are given.

In the final chapter, the conclusions derived from this study and the recommendations that can be useful for further studies are provided.

CHAPTER 2

PAST STUDIES RELATED TO ASTER DEM GENERATION

The DEM accuracy analysis for ASTER images has started before the launch of the Terra satellite. One of the first studies on ASTER DEM accuracy was performed by Welch et. al. (1998) with a simulated data. The 10 m SPOT stereo panchromatic images were resampled to 15 m to obtain the ASTER image resolution. The stereo images were taken for two different ASTER validation sites. The stereo model was registered to the UTM coordinate system with a RMSE of ±14.5 m using six GCPs. DEMs were then generated by *R-WEL* DMS software with a 30 m grid spacing using 13 x 13 correlation window size. The vertical accuracy was assessed using 16 points and a comparison between the computed elevation coordinates against the known elevation coordinates produced an accuracy of ±17.4 m. In this respect, it was stated that the ASTER stereo images would provide accuracies between ±15 and ±25 m.

Toutin (2001) evaluated the automated DEM accuracy using a stereo pair of ASTER data. The selected study area was semi-arid with few cultural features and vegetation. Sixty percent of the area was relatively flat and the rest was steep and rugged. The elevation range was between 1300 and 2600 m above sea level. For the entire DEM generation process and the accuracy assessment the Orthoengine module of PCI Geomatica image analysis software was used. Eight GCPs and six check points were collected during the study. The GCPs were collected using DGPS with an accuracy of ±1 m and located from within the borders of the images and at the high and low elevation points. The generated DEM was compared with a USGS 7.5-minute DEM. The accuracy of the reference DEM was around 7.5 meters. To compute the statistics of the difference between the ASTER DEM and the USGS DEM, 150,000 elevation points were used. The accuracy was found to be 11.8 m with a level of confidence of 85 percent. It was stated that 30-meter contour lines can be derived from the generated ASTER DEMs.

Toutin (2002) investigated the accuracy of DEMs generated from ASTER stereo data. The study area was characterized by rugged topography where the elevation ranged from 342 m to 2137 m with a mean slope of 10º and slopes approaching 87º. The land cover composed of coniferous and deciduous trees with patches of agricultural land and clear-cut areas. Topographic data having the planimetric accuracy of 25-30 m and the vertical accuracy of 10 m was used for GCP collection and the assessment. The main processing stages for DEM generation included (i) image preprocessing, (ii) stereo-model setup, (iii) data extraction or capture by image matching, (iv) 3-D stereo intersection and (v) DEM editing. Different GCP/ICP configurations were evaluated to find the optimum number of GCPs. After seven combinations of GCP/ICP configurations, fifteen GCPs and twenty ICPs were selected in order to keep redundancy in the least square adjustment and to insure the pixel accuracy. DEM accuracy was evaluated as a function of different parameters like preprocessing, post-processing and slope analyses. First, the analysis was carried out based on the radiometric preprocessing of the ASTER images. It was stated that this preprocessing increased the overall accuracy a little less than 10%. Similarly, the post-processing of the lakes improved the accuracy of the final DEM by 10%. The final results of 28 m and 51 m were obtained for the 68% and 90% confidence levels with the correction of lake elevations, but without taking into account the mismatched areas. It was also found that the generated DEM was almost inversely correlated with the terrain slopes, and 20 m accuracy could be obtained on a medium topography using ASTER stereo images.

An accuracy comparison between DEMs generated from ASTER and SPOT 4 stereo images was conducted by Toutin and Cheng (2002). The DEMs were generated over an area of hilly mountains which was mainly semi-arid and consisted of few cultural features and little vegetation. In the area, the difference between the lowest and highest point was around 1300 m. The ASTER level 1A data (61.5 by 63 km) were chosen due to their better reflectance of the imaging geometry. The SPOT 4 stereo pair (60 by 60 km) was acquired with 30 days apart with the angles of +12.4 and -15.2. Eight stereo GCPs and six independent check points were used in this study. The GCPs used in the study were obtained by Differential GPS (DGPS) with an accuracy of sub-meter. For generating the DEMs for both ASTER and SPOT 4 stereo images Toutin's satellite geometric model which was implemented in PCI Geomatics' Orthoengine software was used. The resulting DEMs for ASTER and SPOT 4 were compared with a USGS DEM which had an accuracy of 7.5 m. A total of 140.000 elevation points were used for the comparison. The resulting DEM accuracy achieved for ASTER and SPOT 4 images were 11.6 and 4.6 m, respectively. It was stated that the SPOT 4 extracted DEM results were closer to the USGS DEM than the ASTER DEM results.

A detailed study for generating DEMs from ASTER stereo image data was performed by Hirano et. al. (2003). The study examined ASTER stereo DEM results using four different test sites. The study sites were selected in different parts of the world, which contains various terrain and land use types such as rice fields, lava flow areas, densely populated regions, forest and agricultural lands. The highest and the lowest total relieves in the test sites were 2200 m and 300 m, respectively. DEMs were generated by using the *R-WEL* DMS software. The GCPs were collected from topographic maps and/or from DGPS surveys with varying numbers for each test site. Stereo correlation was undertaken using 13 x 13 and 19 x 19 correlation windows. It was indicated that the success of the correlation was ranged from 97% to 99%. For each test site, the generated DEMs were compared with different reference data. The evaluations of the vertical accuracy resulting from stereo correlation indicated that ±7 to ±15 m accuracy could be expected from ASTER stereo images.

In a similar study, Cuartero et. al. (2004) investigated the accuracy of ASTER stereoscopic images by automated stereo-matching techniques using two different commercial softwares, OrthoBase PRO and Orthoengine. The imaged topography included steep slopes and flat surfaces and the elevation ranged between 300- 2800 m with an average height of 1060 m. They have generated 55 DEMs in order to analyze the influence of some aspects, such as number and spatial distribution of GCPs, the data structure and the sample interval. A set of 315 randomly distributed check points whose coordinates were determined by DGPS techniques were used. According to the results, the Orthoengine obtained the best ASTER DEM with 30 m cell size, using 15 GCPs. On the other hand, the Orthobase PRO generated the most accurate DEM using 12 GCPs, 13 x 13 correlation window and an acceptance threshold value of 0.6.

Another recent study on the accuracy analysis of ASTER images was performed by Goncalves and Oliveira (2004). The region (160 km^2) for the comparison they used had heights ranging from 30 to 600 meters. 11 GCPs were collected from 1:25000 scaled topographic maps. A DEM produced by the army mapping service, which had an accuracy of 2 m, was used to assess the ASTER stereo DEM. The evaluations showed that the accuracy of the ASTER stereo DEM was around 8.7 meters. One interesting part of this study was the radiometric correction of the ASTER images. The authors performed 7 units of grayscale value shifting to the even lines in the ASTER images rather than using the coefficients provided in the HDF format. On the contrary to the Toutin (2002), they also stated that this radiometric improvement did not effect the matching process and the overall DEM accuracy.

Finally, Eckert et. al. (2005) investigated the ASTER stereo DEM accuracy in three different mountain sites. The accuracy was tested using three different reference DEMs which have different resolutions. They found that with the accurate and well distributed GCPs, the accuracies between 15 m and 20 m in hilly terrain and about 30 m in mountainous terrain can be achieved. They also stated that flat regions and smooth slopes produce accuracies around ±10 m. It is also affirmed that the generated DEMs contain extreme errors of a few hundred meters.

CHAPTER 3

DEM GENERATION AND ORTHORECTIFICATION FROM SATELLITE IMAGERY

Remotely sensed data provides crucial information for many researches in various fields. Two important parts in these fields are the digital elevation model generation and the orthorectification of satellite imagery. In this chapter, first the theoretical bases of the DEM generation from satellite stereo images are described. Then, the orthorectification of the satellite imagery using the forward and backward algorithm are provided.

3.1 DEM Generation

A DEM is defined as a file or a database containing elevation points over a contiguous area (Manual of Photogrammetry, 2004). In this part, the theoretical bases and the processing steps of the DEM generation from satellite stereo images are described.

3.1.1 Stereoscopy

Stereoscopy is the science and art that deals with the use of images to produce a three dimensional visual model with characteristics analogous to those of actual features viewed using true binocular vision (Manual of Photogrammetry, 1980). There are two main factors that influence the perception of the space in binocular vision: (i) Binocular disparity (also called binocular parallax) and (ii) Convergence angle. The binocular disparity is the difference between the images of an object projected onto each retina (Toutin, 2001). Besides, convergence angle determines the degree of disparity between two projected images. In order to produce DEMs, the principles of binocular vision are implemented using the stereo images. The success of the stereoscopic processing is closely related to the parallax inherit in the stereo images. In this respect, stereoscopic acquisition geometry is of great importance because it directly determines the degree of parallax.

3.1.2 Stereoscopic Acquisition Geometry

In order to obtain stereoscopy with images, three solutions are possible (Toutin, 1999):

- The adjacent-track stereoscopy using two different orbits
- The across-track stereoscopy using two different orbits
- The along-track stereoscopy using the same orbit using fore and aft images.

3.1.2.1 Adjacent-track Stereoscopy

The first attempts of the elevation information extraction from satellites started with only nadir view capable sensors. Due to the lack of a steering mechanism, these sensors could be able to acquire stereo images only in successive orbits. This successive orbit stereo acquisition technique is called “adjacent-track stereo” and used frequently for LANDSAT (MSS or TM). Because the stereo images are acquired from two adjacent quasi-polar orbits the overlapping area coverage grows from around 10% at the Equator to about 85% at 80° latitude. From 50° north and south the coverage overlap (45%) enables quasi-operational experiments for elevation extraction (Toutin, 2001). The nature of the acquisition geometry of adjacent-track stereoscopy only allows poor B/H ratios that are between 0.1 and 0.2.

The stereoscopic capabilities and applicabilities of adjacent-track stereoscopic satellite data still remain limited because (Toutin, 2001):

- it can be used for large area only in latitude higher than 45° to 50° north and south,

- it generates a small B/H ratio leading to elevation errors of more than 50 m, and

- only medium to high relief areas are suitable for generating enough vertical parallaxes.

3.1.2.2 Across-track Stereoscopy

In order to achieve large intersection angles to generate better stereo geometry, across-track stereoscopy can be used. Like the previous method, different orbits are used but this time rather than using the consecutive orbits non-successive orbits are used. This is achieved by using the advantage of not only the steerable sensors but also the rollable satellites and gives perfect B/H ratios that are suitable for terrain elevation determination.

B/H ratios of 0.6 to 1.2 are the typical values to meet the requirements of topographic mapping (Light, 1980). The SPOT and IKONOS systems can generate such B/H ratios by using across-track steering capabilities and IRS system can generate such B/H ratios by rolling the satellite (Figure 3.1).

By using the across-track stereo data more symmetrically viewed images can be obtained. On the other hand, the main drawback of using an across-track stereopair data is the use of multi-date stereo data with radiometric variations due to the different dates and seasons or environmental conditions (Toutin, 2002). The time difference between the two stereo images can produce difficulties for automated matching process which can be highly affected from the clouds, sun illumination conditions, vegetation growth, cultivated areas, water bodies etc.

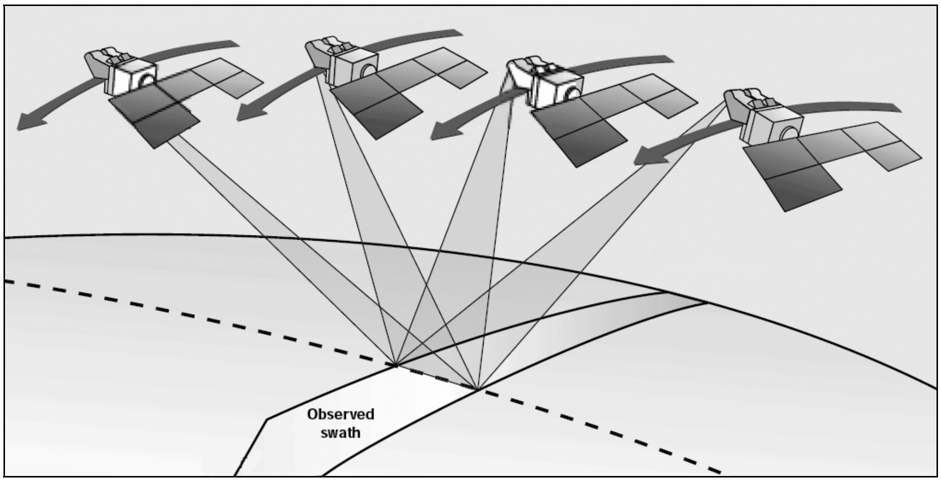

Figure 3.1 Across-track stereo image acquisition.

3.1.2.3 Along-track Stereoscopy

On the contrary to previous two methods, stereo image acquisition can also be taken on the same orbit by steering the sensor or by changing the pitch of the platform to the forward and backward directions. This technique is called along-track stereoscopy and used in several satellites such as ASTER and IKONOS (Figure 3.2). Again B/H ratios that are convenient for topographic mapping can be easily obtained from along-track stereoscopy.

The simultaneous along-track stereo data acquisition gives a strong advantage in terms of radiometric variations versus the multi-date stereo data acquisition with across-track stereo (Toutin, 2001). Because the stereo images are acquired in terms of seconds or minutes the consistency and quality of the stereo images are much better than those that are acquired by other methods. Therefore, the resulting stereo pairs are well prepared for the automated matching process. Besides, this type of acquisition technique compensates for the weaker geometry compared to the across-track technique resulting one image is taken from the nadir or forward and the other is taken from backward viewing direction.

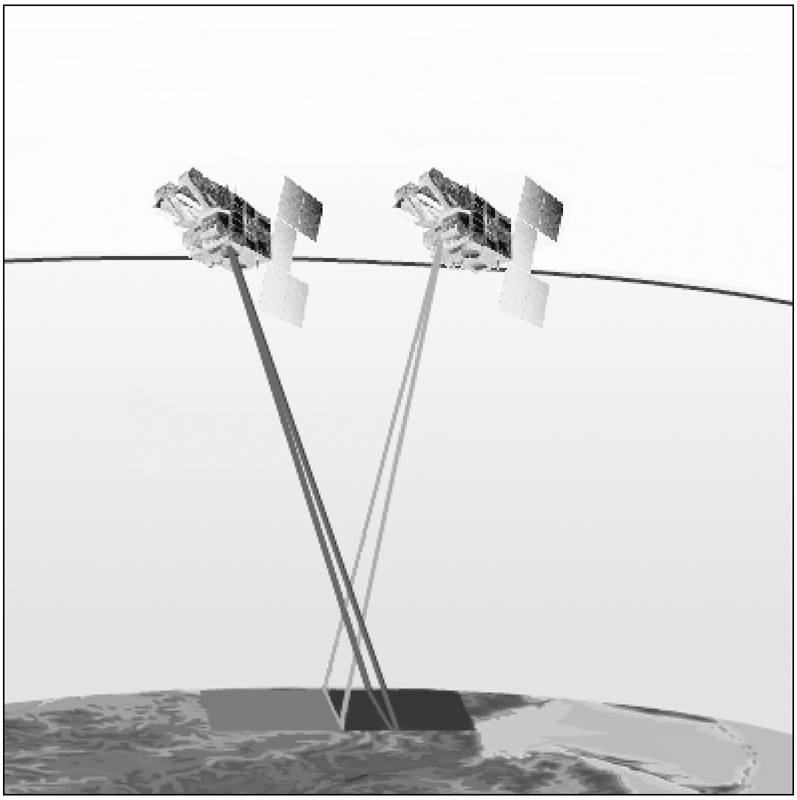

Figure 3.2 Along-track stereo image acquisition.

3.1.3 Stereoscopic Processing

The different processing steps to produce DEMs using stereo images can be described in broad terms as follows (Toutin, 2001):

- To acquire the stereo image data with supplementary information such as ephemeris and attitude data if available

- To collect GCPs to compute or refine the stereo model geometry

- To extract elevation parallax

- To compute the 3D cartographic coordinates using 3D stereo-intersection

- To create and post-process the DEM (filtering, 3D editing and smoothing)

- Converting the DEM to a desired Map Projection.

3.1.3.1 Stereo Image Data Acquisition System and the Stereo Model

Raw images that are taken from different acquisition systems generally contain several distortions. These geometric distortions vary considerably with different factors. However, it is possible to group them into two main categories (Toutin, 2004):

- The “observer” or the acquisition system distortions

- The “observed” system distortions

The observer system distortions may include distortions due to platform variations, sensor, instrument and viewing angle errors. Atmospheric effects, Earth based distortions and map projection errors are grouped into the observed system distortions. Table 3.1 summarizes these errors (Toutin, 2004):

Table 3.1 Description of error sources.

Category	**Sub-category**	**Description of error sources**
The Observer system	Platform	Variation of the movement Variation in platform attitude
	Sensor	Variation in sensor mechanics Viewing/look angles Panoramic effect
	Measuring Instruments	Time variations or drift Clock synchronicity
The Observed system	Atmosphere	Refraction and turbulence
	Earth	Curvature, rotation, topographic effect
	Map	Geoid to ellipsoid Ellipsoid to map

All these distortions must be modeled and corrected by using a specific mathematical model. Several mathematical models can be used for this purpose but the availability of the ephemeris and attitude data directly influences the model type. If the position and the attitude data of the sensor are known during the image acquisition, then a rigorous (physical) model can be used. Otherwise, a simple geometric model must be used in order to cope with the distortions.

3.1.3.1.1 Rigorous Geometric Models

A rigorous model is a complex model which uses the physical reality of the sensor by integrating the knowledge of the ephemeris and attitude data. Several models and considerable research have been carried out but the milestone of all the models to derive a rigorous model is the very well known photogrammetric collinearity equations (Figure 3.3):

$$x_a = x_0 - f\left[\frac{m_{11}(X_A - X_L) + m_{12}(Y_A - Y_L) + m_{13}(Z_A - Z_L)}{m_{31}(X_A - X_L) + m_{32}(Y_A - Y_L) + m_{33}(Z_A - Z_L)}\right]$$

$$y_a = y_0 - f\left[\frac{m_{21}(X_A - X_L) + m_{22}(Y_A - Y_L) + m_{23}(Z_A - Z_L)}{m_{31}(X_A - X_L) + m_{32}(Y_A - Y_L) + m_{33}(Z_A - Z_L)}\right]$$

where (x_a, y_a) are the image coordinates of the point *a*, (X_A, Y_A, Z_A) are the object space coordinates of the point *A*, (X_L, Y_L, Z_L) are the object space coordinates of the exposure station, *f* is the focal length of the sensor, x_0 and y_0 are the coordinates of the principal point usually known from camera calibration and m_{ij} are the elements of the rotation matrix (Wolf, 2000). The derivation of the collinearity equations can be found in Appendix A.

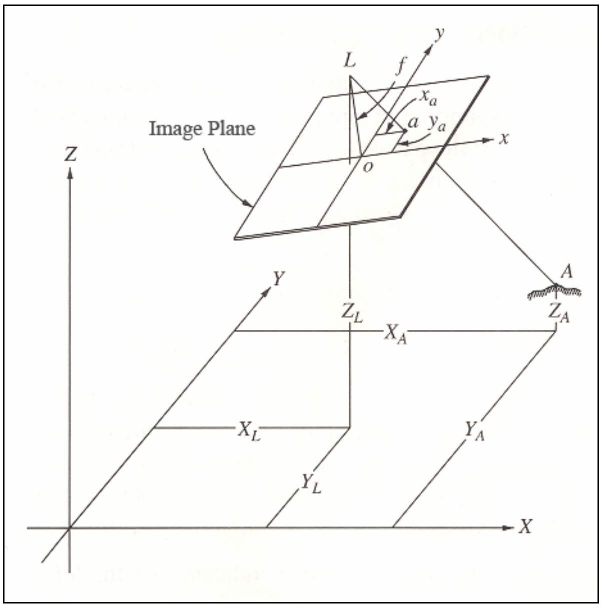

Figure 3.3 The collinearity condition (Wolf, 2000).

The three dimensional character of the photogrammetric formulation allows to consider all physical aspects of satellite orbiting and of the Earth imaging, together with geometric conditions of the time-dependent intersection of corresponding imaging rays in the model space (Kratky, 1989). As a result, high modeling accuracy can be obtained which is usually less than one pixel in many conditions. The types of the optical sensors are based on different techniques such as frame, whiskbroom and pushbroom. Realizing the imaging geometry of all these different sensors require different sensor models. In addition, the platforms (airborne or spaceborne) where the images acquired are also an important factor in the sensor modeling.

A frame camera uses the collinearity equations to relate the image space and the object space. However, because the pushbroom image acquisition technique use line perspective geometry when acquiring the images, the collinearity conditions cannot be implemented in the same way. The mathematical model of the collinearity equations must be modified to line perspective (Novak, 1992):

$$x_a^i = x_0 - f\left[\frac{m_{11}^i(X_A - X_L^i) + m_{12}^i(Y_A - Y_L^i) + m_{13}^i(Z_A - Z_L^i)}{m_{31}^i(X_A - X_L^i) + m_{32}^i(Y_A - Y_L^i) + m_{33}^i(Z_A - Z_L^i)}\right]$$

$$0 = y_0 - f\left[\frac{m_{21}^i(X_A - X_L^i) + m_{22}^i(Y_A - Y_L^i) + m_{23}^i(Z_A - Z_L^i)}{m_{31}^i(X_A - X_L^i) + m_{32}^i(Y_A - Y_L^i) + m_{33}^i(Z_A - Z_L^i)}\right]$$

where x_a^i is the coordinate in scan line, orthogonal to the direction of travel. Because the images are acquired in lines, y_i dimension can be neglected and defined as zero. Another difference between the frame and pushbroom sensors is the exterior orientation parameters of the acquired images. Because a frame sensor acquires the whole image in an instantaneous of time the exterior orientation parameters of a frame camera images are fixed. On the other hand, because the pushbroom sensors acquire the images in a period of time they have different exterior orientation parameters for each scan line which makes the computations much more complicated than the frame sensor. Until now, the change of the exterior orientation parameters has been approximated by different polynomial orders of time. The first order polynomial approach was used in Salamonowicz (1986), Gugan (1987), Gugan and Dowman[1] (1988), Westin (1990), and Novak (1992) who assumed the change based on a linear variation in exterior orientation parameters. The linear polynomial formulation of the change in exterior orientation was expressed as follows:

$$X_L^i = X_L + a_1 \times t_i \qquad \omega^i = \omega_L + a_4 \times t_i$$

$$Y_L^i = Y_L + a_2 \times t_i \qquad \varphi^i = \varphi_L + a_5 \times t_i$$

$$Z_L^i = Z_L + a_3 \times t_i \qquad \kappa^i = \kappa_L + a_6 \times t_i$$

where X_L^i, Y_L^i, Z_L^i are the exterior orientation parameters of line *i*, X_L, Y_L, Z_L are the positional exterior orientation parameters of the center-line of the scene, $\omega_L, \varphi_L, \kappa_L$ are the rotational exterior orientation parameters of the center-line of the scene, a_1, a_2, a_3, a_4, a_5 and a_6 are the linear coefficients of the exterior orientation parameters and t_i is the time of line *i*. In this case, there are additional 6 unknown parameters (a_1, a_2, a_3, a_4, a_5 and a_6) to the regular 6 unknown parameters ($X_L, Y_L, Z_L, \omega_L, \varphi_L, \kappa_L$) when compared to the frame sensors.

Gugan and Dowman (1988), Kratky (1989), Chen and Lee (1993), Zoej and Petrie (1998), Fritsch and Stallmann (2000) used the second order polynomial to model the change for the exterior orientation parameters. In this case, the unknowns of the parameters increased to a total of 18. The quadratic polynomial formulation of the change in exterior orientation was defined as:

$$
\begin{aligned}
X_L^i &= X_L + a_1 \times t_i + b_1 \times t_i^2 & \omega^i &= \omega_L + a_4 \times t_i + b_4 \times t_i^2 \\
Y_L^i &= Y_L + a_2 \times t_i + b_2 \times t_i^2 & \varphi^i &= \varphi_L + a_5 \times t_i + b_5 \times t_i^2 \\
Z_L^i &= Z_L + a_3 \times t_i + b_3 \times t_i^2 & \kappa^i &= \kappa_L + a_6 \times t_i + b_6 \times t_i^2
\end{aligned}
$$

Later, Radhadevi et al. (1998), Li et. al. (2002), used the third order polynomial approximations to the exterior orientations parameters. The cubic form of the estimation brings much more computation burden relative to the first and second order estimations and formed as:

$$
\begin{aligned}
X_L^i &= X_L + a_1 \times t_i + b_1 \times t_i^2 + c_1 \times t_i^3 & \omega^i &= \omega_L + a_4 \times t_i + b_4 \times t_i^2 + c_4 \times t_i^3 \\
Y_L^i &= Y_L + a_2 \times t_i + b_2 \times t_i^2 + c_2 \times t_i^3 & \varphi^i &= \varphi_L + a_5 \times t_i + b_5 \times t_i^2 + c_5 \times t_i^3 \\
Z_L^i &= Z_L + a_3 \times t_i + b_3 \times t_i^2 + c_3 \times t_i^3 & \kappa^i &= \kappa_L + a_6 \times t_i + b_6 \times t_i^2 + c_6 \times t_i^3
\end{aligned}
$$

The mathematical formulations to the exterior orientation parameters look so non-problematic. However, there is a problem which causes from the nature of the pushbroom sensor. For instance, in the case of a second order polynomial approximation to the exterior orientation parameters, 18 unknowns cannot be solved in a single estimation procedure due to the correlations between the parameters. Unlike the frame sensor, the results of the least squares estimation are unstable due to the one dimensional nature of the sensor. This problem was explained and solved by Orun and Natarajan (1994). Figure 3.4 shows the differences between the frame sensor and pushbroom sensor after performing small changes in the exterior orientation parameters.

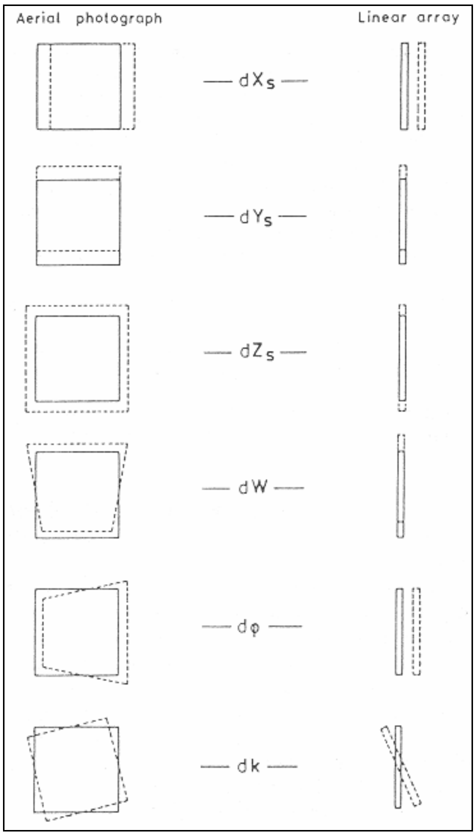

Figure 3.4 The comparison of the effect of small changes in parameters for frame and pusbroom sensors (Orun and Natarajan,1994).

It is shown that for pushbroom sensors a small change (dω) in ω is indistinguishable from a small change (dY) in Y. Similarly, a small change (dφ) in φ cannot be differentiated from a small change (dX) in X. Therefore, it is necessary to eliminate either ω or Y and either φ and X from the set of parameters to remove the instability (Orun and Natarajan, 1994). The proposed resulting model for the exterior orientation was:

$$
\begin{aligned}
X_L^i &= X_L + a_1 \times t_i + b_1 \times t_i^2 & \omega^i &= \omega_L + a_4 \times t_i + b_4 \times t_i^2 \\
Y_L^i &= Y_L + a_2 \times t_i + b_2 \times t_i^2 & \varphi^i &= \varphi_L \\
Z_L^i &= Z_L + a_3 \times t_i + b_3 \times t_i^2 & \kappa^i &= \kappa_L
\end{aligned}
$$

The resulting model changes the pitch and roll orientations to time independent values, while other parameters remain unchanged. As a result, 16 unknowns in the general model reduce to 12 unknown parameters in the Orun and Natarajan model.

The different forms of the extensions of the general exterior orientation model were also performed. Rodriguez et al. (1988) assume the whole orientation parameters as constants while Priebbenow and Clerici (1988) assume a linear variation for yaw and roll orientations and a quadratic variation for pitch orientation. All these models try to estimate the exterior orientation parameters more accurately by trying to model the movement of the sensor.

3.1.3.1.2 Simple Geometric Models

A simple geometric model usually involves mathematical functions, which are easier to understand and do not require the knowledge of image sensor physics (Toutin, 2002). These systems neither use nor require information related to the sensor, platform and Earth and do not reflect the geometry of described distortions. In this respect, simple geometric models require mathematical functions to relate the image space and object space. The general form of the 2D and 3D functions can be written as:

$$x = f_1(X, Y) \quad y = f_2(X, Y)$$
$$x = f_3(X, Y, Z) \quad y = f_4(X, Y, Z)$$

where x and y are the image coordinates, X, Y and Z are the object coordinates and f_1, f_2, f_3 and f_4 are the mathematical functions which perform the relation between the image and object space. It is also possible to write the inverse form as:

$$X = f_5(x, y) \quad Y = f_6(x, y)$$
$$X = f_7(x, y, Z) \quad Y = f_8(x, y, Z)$$

The mathematical function parameters are solved with the help of the GCPs collected throughout the image by using the least squares adjustment process. Once the mathematical function parameters are determined, the correct positions of each pixel in the image can be estimated by these functions.

These functions are based on different mathematical models:

- 2D Polynomial Functions
- 3D Polynomial Functions
- 3D Rational Functions
- Projective Transformation
- Direct Linear Transformation

3.1.3.1.2.1 2D Polynomial Functions

In this method, the relation between the image space and the object space is performed by using the planimetric coordinates of the GCPs only. The general mathematical formulation of a 2D polynomial function can be expressed as (Toutin, 2004):

$$P_{2D}(x, y) = \sum_{i=0}^{m} \sum_{j=0}^{n} a_{ij} X^i Y^j$$

where *X* and *Y* are the planimetric coordinates of the GCPs, *i* and *j* are the increament values, *m* and *n* determines the order of the polynomial model, generally between one and five, and a_{ij} are the polynomial coefficients to be determined by the least squares adjustment. The order of the model mainly depends on the number of available GCPs, and in general, the more the number of GCPs, the more the accuracy achieved (Novak, 1992).

Because 2D polynomial functions do not take into account the elevations of the GCPs these models can be efficiently used when the imaged area is relatively flat, namely where the image is not influenced by the topographic effects. Their usage is generally limited to images which have few or small distortions, such as nadir-viewing images (Bannari et. al., 1995). In order to achieve a good accuracy, GCPs have to be accurate, numerous and evenly distributed. The elementary transformations such as the rotation, shift and scale are accomplished by the first order polynomial model which is also called the 2D affine model. This polynomial has the form:

$$x = a_0 + a_1 X + a_2 Y$$

$$y = b_0 + b_1 X + b_2 Y$$

When the second order polynomial functions are used, in addition to the previous transformations, torsion and convexity are taken into account (Toutin, 2004). The second order polynomial functions have the form:

$$x = a_0 + a_1X + a_2Y + a_3X^2 + a_4Y^2 + a_5XY$$
$$y = b_0 + b_1X + b_2Y + b_3X^2 + b_4Y^2 + b_5XY$$

The higher order polynomial functions do not correspond to any physical reality of the image acquisition system and it should be remembered that, in general, a higher degree 2D polynomial will fit the GCPs better but it will produce undesired distortions far away from them (Pala and Pons, 1995).

3.1.3.1.2.2 3D Polynomial Functions

3D polynomial functions are generated by adding the elevation coordinates of the GCPs to the 2D polynomial functions using new parameters. However, because they are similar to the 2D order polynomial functions, the problems of the 2D order polynomial functions are also valid for these functions except for the topography. They still require accurate, numerous and evenly distributed GCPs. The general form of the 3D polynomial functions can be expressed as (Toutin, 2004):

$$P_{3D}(x, y) = \sum_{i=0}^{m}\sum_{j=0}^{n}\sum_{k=0}^{p} a_{ijk} X^i Y^j Z^k$$

where *X*,*Y and Z* are the coordinates of the GCPs, *i, j* and *k* are the increament values, *m, n* and *p* determines the order of the polynomial model, generally between one and three (Tao and Hu, 2001), and a_{ij} are the polynomial coefficients to be determined by the least square adjustment. Similar to the 2D polynomials, first order of the 3D polynomial function is called 3D affine model and can be written as:

$$x = a_0 + a_1X + a_2Y + a_3Z$$
$$y = b_0 + b_1X + b_2Y + b_3Z$$

Special forms of the 3D polynomial functions are also available. Pala and Pons (1995) have modified the first order 3D polynomial model by taking into account the relief displacement effect. They derived the 3D polynomial model for the images that are acquired from high altitude and they assumed a flat Earth model. The generated model has 4 additional unknowns for x, y when compared to the first order polynomial model and comprises a total of 12 unknown parameters:

$$x = a_1 + a_2X + a_3Y + a_4Z + a_5XZ + a_6YZ$$
$$y = b_1 + b_2X + b_3Y + b_4Z + b_5XZ + b_6YZ$$

They tested the model using Landsat, SPOT Pan and XS data with around 30 GCPs and found very good results approaching to the results of the rigorous model.

The author extended this model for the second order polynomial functions. Instead of using the first order polynomial model, the second order polynomial functions were used as the starting point. The resulting special form of the polynomial functions double the unknowns with respect to the first order special function and can be expressed as:

$$x = a_1 + a_2X + a_3Y + a_4X^2 + a_5Y^2 + a_6XY + a_7Z + a_8XZ + a_9YZ + a_{10}X^2Z + a_{11}Y^2Z + a_{12}XYZ$$
$$y = b_1 + b_2X + b_3Y + b_4X^2 + b_5Y^2 + b_6XY + b_7Z + b_8XZ + b_9YZ + b_{10}X^2Z + b_{11}Y^2Z + b_{12}XYZ$$

3.1.3.1.2.3 Rational Functions (RFs)

Rational Functions perform transformations between the image and the object spaces through a ratio of 3D polynomials. Rational Functions can be expressed as (OGC, 1999; Tao and Hu, 2001; Tao and Hu, 2002; Di et. al., 2003; Fraser and Hanley, 2003):

$$x_n = \frac{P_1(X_n, Y_n, Z_n)}{P_2(X_n, Y_n, Z_n)} \qquad y_n = \frac{P_3(X_n, Y_n, Z_n)}{P_4(X_n, Y_n, Z_n)}$$

where, polynomials P_i (i=1,2,3 and 4) have the general form of the 3D Polynomial Functions. One important difference is that both the image coordinates (x, y) and the object coordinates (X, Y, Z) are normalized to fit the range from -1 to +1 to minimize the errors during the computations and improve the numerical stability of the equations. The differences between the normalized and un-normalized computation results and the stability were demonstrated in Tao and Hu (2002). The normalization of the coordinates can be done using the following equations (Url 8):

$$x_n = \frac{x - x_0}{x_s} \qquad y_n = \frac{y - y_0}{y_s}$$

$$X_n = \frac{X - X_0}{X_s} \qquad Y_n = \frac{Y - Y_0}{Y_s} \qquad X_n = \frac{X - X_0}{X_s}$$

where, x_n and y_n are the normalized image space coordinates, X_n, Y_n and Z_n are the normalized object space coordinates, x_0 and y_0 are the offset values for the image coordinates, X_0, Y_0 and Z_0 are the offset values for the object coordinates, x_s and y_s are the scale values for the image coordinates and X_s, Y_s and Z_s are the scale values for the object coordinates. The general form of the rational functions can be written as (Toutin, 2004):

$$R_{3D}(x,y) = \frac{\sum_{i=0}^{m}\sum_{j=0}^{n}\sum_{k=0}^{p} a_{ijk} X^i Y^j Z^k}{\sum_{i=0}^{m}\sum_{j=0}^{n}\sum_{k=0}^{p} b_{ijk} X^i Y^j Z^k}$$

$$\begin{aligned}\sum_{i=0}^{m}\sum_{j=0}^{n}\sum_{k=0}^{p} a_{ijk} X^i Y^j Z^k = {} & a_0 + a_1 X + a_2 Y + a_3 Z + a_4 X^2 + a_5 Y^2 + a_6 Z^2 + a_7 XY + a_8 XZ + a_9 YZ + \\ & + a_{10} X^3 + a_{11} Y^3 + a_{12} Z^3 + a_{13} X^2 Y + a_{14} X^2 Z + a_{15} Y^2 X + a_{16} Y^2 Z + a_{17} Z^2 X + \\ & + a_{18} Z^2 Y + a_{19} XYZ\end{aligned}$$

where, a_{ijk} are the polynomial coefficients that are called Rational Function Coefficients (RFCs). The first order terms represent the distortions caused by the optical projection, the second order terms are for the Earth curvature, atmospheric refraction, lens distortion and the third order terms handle the unknown and accidental distortions (Tao and Hu, 2001).

Two general estimations of the RFCs are possible, that are:

- Terrain Independent Method, and
- Terrain Dependent Method

The popularity of the rational functions has increased when some of the image vendors and the government agencies did not want to deliver satellite information to the end users. Thus, these vendors looked for an alternative way to correct the image. As a result, they tried to approximate the 3D physical model results using the rational functions. They first corrected the image by using a 3D physical model of their own and then solved the RFCs by using the result of the existing 3D physical model.

Later, they appended the RFCs with the image for the end users to correct their image without using any of the satellite information. This method is commonly known as the “terrain independent” method and the methodological steps are explained in Tao and Hu (2001). On the other hand, this method includes some errors and biases which have to be removed with the help of the GCPs (Hu and Tao, 2002; Fraser and Hanley, 2003). Therefore, the usage of at least one GCP to remove these errors or biases occurred using this method turns the method terrain dependent (Toutin, 2004).

The second method totally uses the GCPs for the estimation of the RFCs. However, because they are the general form of the polynomial functions the general problems for the 2D and 3D polynomials are also valid for the rational function polynomials. For the third order rational functions, if the denominator constants of the functions are set to 1, a total of 78 parameters need to be solved using at least 39 GCPs. One important disadvantage is that the increase of the unknown RFCs also increases the possibility of the correlation between the RFCs and can make the least squares estimation instable.

3.1.3.1.2.4 Projective Transformation

The projective transformation describes the relationship between the two planes (Novak, 2002). It is the basic fractional model which can relate the image space and the object space. It integrates only the planimetric coordinates as the 2D polynomial model. The projective transformation is also called eight parameter transformation because the total of unknowns of the model are eight:

$$x = \frac{a_1 X + a_2 Y + a_3}{c_1 X + c_2 Y + 1} \qquad y = \frac{b_1 X + b_2 Y + b_3}{c_1 X + c_2 Y + 1}$$

where, a_1, a_2, a_3, b_1, b_2, b_3, c_1, c_2 and c_3 are the eight unknown parameters of the functions. Of course, projective transformation is written for the frame sensors. Based on the assumption that each scan-line has a different perspective and all are tied to a straight line approximating the orbit, the function has modified to the form (Novak, 1992):

$$x = \frac{a_1 X + a_2 Y + a_3}{c_1 X + c_2 Y + 1} \qquad y = b_1 X + b_2 Y + b_3$$

where, y is the flying direction whereas x represents the pixel in a scan line. Because the function performs the relation in two planes this method has little practical significance for satellites (Novak, 1992). On the other hand, Shi and Shaker (2003) implemented the projective transformation on IKONOS imagery and found that the accuracy achieved using the projective transformation is not significantly different from the accuracies achieved using the 2D polynomial models.

3.1.3.1.2.5 Direct Linear Transformation (DLT)

The DLT models the transformation between the image pixel coordinate system and the object space coordinate system as a linear function (Mikhail et. al., 2001). It has been widely used in close-range photogrammetry and can also be used for the satellite image geometric correction. Actually, the DLT model is often used to derive the approximate initial values of unknown parameters for the collinearity equations (Tao and Hu, 2001). The general collinearity equations are modified into the DLT functions so the collinearity equation unknowns are hidden in the 11 DLT unknown parameters. The collinearity equations are also modified for pushbroom sensors and the derivation steps are explained in El-Manadili and Novak (1996). The model can be expressed as:

$$x = \frac{L_1 X + L_2 Y + L_3 Z + L_4}{L_9 X + L_{10} Y + L_{11} Z + 1} \qquad y = \frac{L_5 X + L_6 Y + L_7 Z + L_8}{L_9 X + L_{10} Y + L_{11} Z + 1}$$

where, $L_1, L_2, ..., L_{10}, L_{11}$ are the linear orientation parameters between two dimensional image space and the three dimensional object space. Later, Okamoto et. al. (1999) extended the DLT model by adding two more parameters:

$$x = \frac{L_1 X + L_2 Y + L_3 Z + L_4}{L_9 X + L_{10} Y + L_{11} Z + 1} + a_{12} xy \qquad y = \frac{L_5 X + L_6 Y + L_7 Z + L_8}{L_9 X + L_{10} Y + L_{11} Z + 1} + a_{13} y^2$$

It was stated that this improvement to the model increases the performance when compared to the other rectification methods for the SPOT imagery.

In addition to the type of the function, the orders of the functions must also be considered. The order of the functions determines the number of the coefficients. The minimum number of GCPs varies with the order of the polynomials, namely the number of the unknown coefficients in the polynomial terms. Because each GCP yields two equations, the minimum number of GCPs is equal to the half of the number of unknowns. The model unknowns and the minimum number of GCPs required to solve the models are summarized in Table 3.2.

Since the simple geometric models are completely independent of the geometry of the sensor they are less accurate when compared to the rigorous models. On the other hand, they are easier to understand and have an advantage of simplicity. A simple geometric model is not recommended unless the image sensor information is not available at all (Toutin, 2002).

Table 3.2. The properties of simple geometric functions.

Function Type	Model Order	Model Coefficients	Model Unknowns	Minimum GCP number
2D polynomial Function	1	3	6	3
	2	6	12	6
	3	10	20	10
3D polynomial Function	1	4	8	4
	2	10	20	10
	3	20	40	20
Polynomial Function with Relief	1	6	12	6
	2	12	24	12
3D RFs	1	8	16	8
	2	20	40	20
	3	40	80	40
Projective Transformation	1	8	16	8
DLT	1	11	22	11

A comparison between the two methods is summarized by Toutin (1999) in Table 3.3:

Table 3.3 The comparison between simple and rigorous geometric models.

Simple Geometric Model	Rigorous Model
Does not respect the viewing geometry	Respects the viewing geometry
Not related to distortions	Reflects the distortions
Does not introduce attitude data	Uses ephemeris and attitude data
Corrects image locally at the GCPs	Corrects the image globally
Does not filter blunders	Filters blunders with the knowledge of the geometry
Individual adjustments of one image	Simultaneous adjustment of more than one image
Needs many (>20) GCPs	Need few (3-8) GCPs
Sensitive to GCP distribution	Not sensitive to GCP distribution

3.1.3.2 GCP collection and Refinement

Ground control points (GCP) refer to points whose ground positions are known with respect to a reference coordinate system and/or a reference datum. Whatever the geometric model used for the stereo model, a number of GCPs have to be acquired to refine the stereo model in order to obtain cartographic standard accuracy (Toutin, 2001). The required number of GCPs is mainly dependent on the geometric model types; whether rigorous or simple. Since the simple model does not reflect the real acquisition geometry, it requires many more GCPs than the minimum requirement. Any number of redundancies above the minimum requirement is taken care by the iterative least squares adjustment solution. The definitions and the derivation of the least squares adjustment process can be found in Appendix B. Other factors that affect the number and the accuracy of the GCPs include the method of collection, sensor type and resolution, image spacing, study site, physical environment, GCP definition and accuracy and the final expected accuracy (Toutin, 2004).

When the type of the GCPs is to be considered, three different types of GCPs can be defined (Toutin, 2001):

- Full control points with known XYZ coordinates
- Altimetric points with known Z coordinate
- Tie points with unknown cartographic coordinates.

The last two are used to reinforce the stereo model geometry and fill areas on the images where the full control points are missing.

When the method of collection property is to be considered, the GCP coordinates can be collected through using different methods and sources such as GPS surveys, paper or digital maps, orthorectified images or photos etc. All these sources have varying accuracy outcomes, for example differential GPS survey accuracies can go up to centimeter accuracy, whereas paper or digital map accuracies can deteriorate down to 50 meters. Thus, the collection method of the GCPs is a definitely crucial factor that affects the GCP accuracy and the final expected accuracy of a project.

One other important matter is the resolution of the image to be processed. For instance, if the GCPs are to be collected for Landsat imagery, there is no need to collect the GCPs using DGPS method with centimeter accuracy. Similarly, if the input image is IKONOS with 1 m resolution, 1:25000 or 1:50000 map GCPs would be incapable to be used for any kind of IKONOS processing.

The number of GCPs is also dependent to the study site to be investigated. If the terrain observed in the site is very steep and rugged and additionally if the image resolution is relatively coarse, the GCP collection will be challenging. For this kind of situation, it is not easy to find GCPs to cover all planimetric and elevation ranges in the study site. Thus, the resulting accuracy of any kind of output will be far away to accomplish the desired accuracy for both the rigorous and simple geometric models.

The last important factor is that the required final accuracy of an output. In terms of the simple models, when the accuracy of the GCPs is in the same magnitude as the resolution of the imagery, it is safer to collect more than twice the minimum required number of GCPs (Toutin, 2004). Since the rigorous models correct the image globally, the desired output accuracy can be easily reached by spreading the GCPs at the border of the images and by covering the full elevation range of the study site.

3.1.3.3 Elevation Parallax Extraction

Parallax is defined as the apparent displacement of the position of a body caused by a shift in the point of observation with respect to a reference point or a system. Similarly, stereoscopic parallax (also called image parallax) can be defined as the apparent displacement of the location of a particular object caused by the satellite motion and/or viewing angle differences with respect to the principle point of each stereo image. There are two types of possible stereoscopic parallaxes; (i) x parallax which occurs along the flight axis and (ii) y parallax which is perpendicular to the flight axis. The x parallax is a natural result of the movement of the spacecraft and forms the key point of the elevation generation from the observed objects. On the other hand, the y parallax generally occurs from improper orientation of the stereo images and can be removed with the knowledge of the image acquisition parameters.

Image matching forms the key part to retain the elevation parallaxes between the stereo images. Two methods principally can be used to extract the elevation parallax using image matching (Toutin, 2001):

- The computer-assisted (visual) methods
- Automatic methods.

These methods can also be combined to extract the elevation parallaxes more rigid and proper. The computer assisted method works on a stereo-plotter and uses the traditional photogrammetric method to extract the elevation parallaxes. It then requires full stereoscopic capabilities to generate the on-line 3D reconstruction of the stereo model and the capture in real time of 3D planimetric and elevation features (Toutin, 2001). However, this technique requires a long and expensive process and commonly used with paper-format images.

The recent research studies are directly affected from not only the tedious process of the computer assisted method but also the rapid increase of the production of the digital stereo images. In the last two decades most of these studies are changed their views towards on the second method which is the automatic methods. Obviously, the automatic methods use the advantage of the computer technology and its speed. The automatic methods developed to extract the elevation parallaxes from digital stereo images include (Wolf, 2000):

- Area based methods,
- Feature based methods, and
- Hybrid methods.

3.1.3.3.1 Area Based Methods

Area based methods perform the image matching based on the intensity values of the stereo images. Matching points between the left and the right images are determined by user-defined reference and search windows. The process is illustrated in Figure 3.5. First a small window array (reference array) is selected from the first image. In order to find the corresponding position of the reference array in the second image, a search area is defined in the second image. Then, small subarrays which are the same size of the reference array are selected inside the search area and each of them is statistically compared with the reference window. The degree of relationship can be determined by using several statistical techniques such as normalized cross-correlation coefficient, the sum of mean normalized absolute difference, the stochastic sign change or the outer minimal number estimator (Toutin, 2002). The maximum of the computed relationship values above the threshold in the search area is assumed to be the matching point for the reference window.

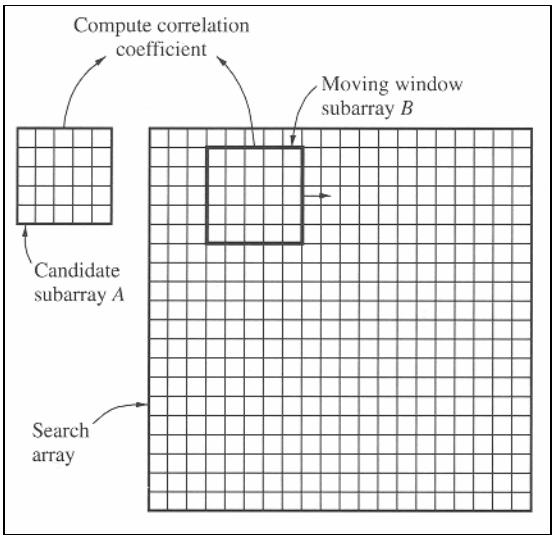

Figure 3.5 Area-based matching using reference and search arrays (Wolf, 2000).

Among the statistical techniques, the normalized cross-correlation coefficient is considered to be the most accurate one (Leberl et al. 1994). The correlation coefficient is computed by the following equation (Wolf, 2000):

$$c = \frac{\sum_{i=1}^{m}\sum_{j=1}^{n}\left[\left(A_{ij}-\overline{A}\right)\left(B_{ij}-\overline{B}\right)\right]}{\sqrt{\left[\sum_{i=1}^{m}\sum_{j=1}^{n}\left[\left(A_{ij}-\overline{A}\right)^2\right]\right]\left[\sum_{i=1}^{m}\sum_{j=1}^{n}\left[\left(B_{ij}-\overline{B}\right)^2\right]\right]}}$$

where, c is the correlation coefficient, m and n are the numbers of rows and columns, respectively, in the subarrays; A_{ij} is the digital number from subarray A at row i, column j; $\overline{A}$ is the average of all digital numbers in subarray A; B_{ij} is the digital number from subarray B at row i, column j; $\overline{B}$ is the average of all digital numbers in subarray B. The correlation coefficient can range from “-1” to “+1”. “-1” indicates a perfect negative correlation, “0” indicates no correlation and “+1” indicates a perfect positive correlation. Due to some reasons such as noise, the time interval between the two images and the acquisition geometry, a perfect positive correlation is extremely hard to obtain. A threshold value of 0.7 is selected in many cases and if the correlation coefficient exceeds this value, the subarrays, namely the center pixel of the subarrays are assumed to be matched (Wolf, 2000).

A second area-based matching method is the least squares matching technique which is able to obtain the corresponding location of the matching pixels in terms of a fraction of a pixel. The most common formulation of this method is:

$$A(x,y) = h_0 + h_1 B(x',y')$$
$$x' = a_0 + a_1 x + a_2 y$$
$$y' = b_0 + b_1 x + b_2 y$$

where, $A(x,y)$ is the digital number from the candidate subarray of the left image at location *x*, *y*; $B(x',y')$ is the digital number from a subarray in the search area of the right image at location x' , y' ; h_0 is the radiometric shift; and h_1 is the radiometric scale. Equations relate the left and the right images with the affine transformation (first order polynomial). Due to the nature of the least squares approach, this technique requires initial approximation values to the unknowns (h_0, h_1, a_0, a_1, a_2, b_0, b_1 and b_2). Each solution requires forming the linearized equations, obtaining the corrections and adding to the corrections to the initial approximations. The process continues until the results for the unknowns are satisfactory and the corrections are negligible.

One important factor that affects the accuracy of the area based methods is the subarray size. Generally, a subarray size of 20 x 20 to 30 x 30 gives satisfactory results (Wolf, 2000). If the subarray size is smaller, possible matching points may not be found. On the contrary, if the subarray size is larger, multiple matching points can be found. Both conditions would produce problematic conditions. One solution to the problems is producing the “epipolar images” from the raw stereo images prior to matching. The left and right stereo images are resampled in a way that the y parallaxes in the images are removed (Figure 3.6). Therefore, the search area is reduced from 2 dimensions to 1 dimension. This resampling preprocessing prevents the matching of false pixels and brings a substantial search time decrease when compared to the 2D searching.

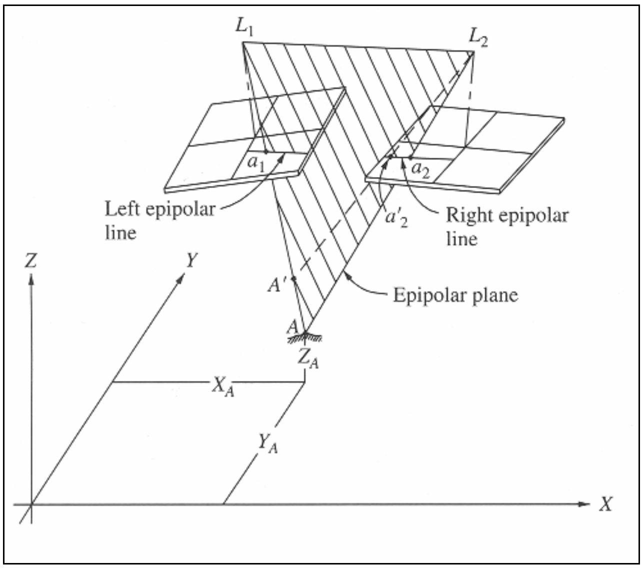

Figure 3.6 Epipolar geometry (Wolf, 2000).

3.1.3.3.2 Feature Based Methods

Feature based methods seek to extract and match the common features from the two images (Fonseca, 1996). In this respect, two sequential processes are required in order to find the matching locations; (i) feature extraction and (ii) feature matching. An image can be represented in two different domains when performing the feature extraction part. In the “spatial domain”, common features are edges, lines, intersections, regions etc. In general, region boundaries and edges are extracted during this procedure by using different feature extraction techniques such as Canny, Roberts, Prewitt, Sobel, Frei-Chen, region growing algorithms etc. On the other hand, in the “transform domain” where images are represented as a set of transform coefficients, the image is decomposed. The edge information in the image can be extracted by using classical transform domain functions such as Fourier, Wavelet etc.

The matching accuracy of the feature based methods is extremely dependent to the feature extraction method which is highly affected from the sensor geometry, the wavelength and noise. Because they do not directly use the pixel values which compose the images they often require sophisticated image processing algorithms. Despite their complex nature, they do not guarantee better results when compared to the area based methods.

3.1.3.3.3 Hybrid Methods

Aforementioned methods have their own particular advantages and disadvantages. For example, area based methods are straightforward and commonly used in many systems. However, feature based methods are more complicated and can manage better in certain circumstances. The combination of the two approaches is called hybrid method and it firstly involves extraction of edges by using the second method. Then, these points are used as seed points for the first method. Consequently, the integration of the two approaches gives users to combine the advantages of both. In addition, there are also other hybrid methods that can be used to find the matching pixels in both images.

3.1.3.4 3D Stereo Intersection

3D stereo intersection method is a geometrical issue that is used to convert the extracted parallax values to absolute elevation values. The method uses the idea that the corresponding rays to the same object point in the overlap area of the two images must intersect at that point (Figure 3.7).

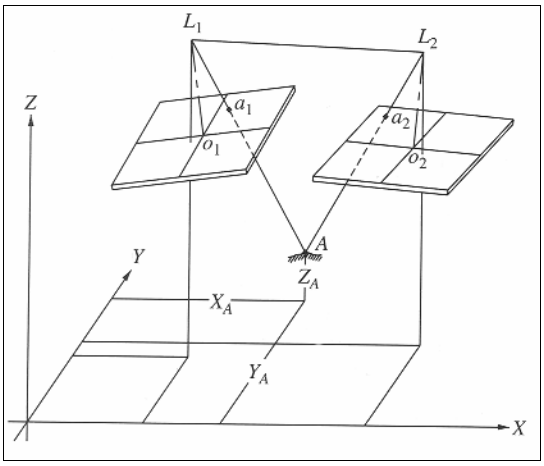

Figure 3.7 3D stereo intersection (Wolf, 2000).

In order to calculate the coordinates of a point, the collinearity equations must be written. Afterwards, these equations must be solved by using the least squares parameter estimation technique. However, to solve the linearized equations of the least squares for the unknown coordinates of the point (X_p, Y_p and Z_p), 6 exterior orientation parameters must be known initially either from image meta data or from space resection algorithm performed prior to the space intersection. As a result, two equations can be written for the point on the left image and two more for the point on the right image. Hence four equations are enough to solve three unknowns with a least squares estimation. Iterations to find the coordinates of the point are carried out up until the results for the unknowns are satisfactory and the corrections are negligible. Again, for these calculations the initial approximations for the unknowns must be determined.

3.1.3.5 Post-Processing and Projecting the Generated DEM

All matching points that are found from the parallax extraction step are converted to absolute elevation values by using the previous stage. The resulting DEM is neither in a common coordinate system (if it is not immediately geocoded after the DEM generation) nor free from errors. The errors may occur during the processings including the blunders, mismatched areas, failure of specific areas etc. Therefore, whatever the matching method is used, there is always a need for post-processing the extracted elevation data (Toutin, 2002).

Different methods can be used to correct these errors: (i) manual, (ii) automatic, or (iii) interactive (Toutin, 2002). Obviously, manual methods completely dependent to the human vision and perception during the editing process. The automatic methods use the advantage of the computer technology and its efficiency. Some algorithms to correct the blunders or noise inherent in the DEM are successfully adapted to be performed automatically. To correct the large mismatched areas (for example more than 200 pixels), an operator should seed stereo extracted points interactively. To reduce the largest errors, an operator can also extract some specific features prior to the correction.

In the following section, several automatic methods that are used for the noise identification and the noise removal are described.

3.1.3.5.1 Noise Identification

Noise refers to pixels that contain failure values. The algorithms used to detect the noise are based on the assumption that pixels that are adjacent to the failed pixels tend to contain incorrect values. Namely, the surrounding pixels of a pixel determine that the pixel is failed or not. Three methods can be used to define whether a pixel is failed or not (Orthoengine user guide, 2003):

- The first method calculates the average and variance of the eight elevation values immediately surrounding each pixel, excluding failed and background pixels. If the center pixel is more than two standard deviations away from the average, it is replaced with the failed value.

- The second method counts the number of failed values immediately surrounding each pixel. If five or more failed pixels border the center pixel, then the center pixel is also set to a failed value.

- Since pixels adjacent to failed pixels tend to contain incorrect values as well, the third method replaces the eight pixels around each failed pixel with the failed value.

3.1.3.5.2 Noise Removal

Noise removal functions use existing filters which are based on statistical computations (mean, standard deviation). In general, three filters are used for this process (Orthoengine user guide, 2003):

- The Median filter ranks the pixel values within a pixel frame according to brightness. The median is the middle value of those image pixel values, which is then assigned to the pixel in the center of the frame.

- The Smoothing filter is a filter that calculates the weighted sum of all the pixels in a three-by-three pixel frame and assigns the value to the center pixel in the frame. Failed and background pixel values are not replaced by the filter and are not used in the calculation.

- The Interpolate filter replaces failed values with an estimate weighted by distance calculated from the valid pixels surrounding the failed pixel(s).

After eliminating the blunders occurred in a DEM, the last stage is projecting the epipolar DEM into the desired map projection system. This is again performed using the collected GCPs and the computed stereo model. The map projection of the generated epipolar DEM prior to the post-processing step is not recommended because the failure areas can be examined by switching back and forth between the epipolar image channel and the epipolar DEM. Thus, the failure areas can be observed and identified straightforwardly.

3.2 Orthorectification

Unrectified satellite images contain various distortions which are explained in section 3.1.3.1. These distortions make the raw images impossible to be input to a Geographic Information System (GIS), or overlaying and editing with any kind of data already incorporated in a GIS (Lillesand et. al., 2004). In this respect, all these distortions have to be removed prior to the usage of the images. Therefore, the rectification of the remotely sensed images to a standard map projection enables users to utilize images in conjunction with the other spatial information in a GIS.

In general, two common processes are used for correcting such raw images; (i) rectification, and (i) orthorectification. The accuracy of the resulting final product is the main difference between the two methods. The rectified images are typically generated using simple mathematical models. Consequently, the resulting imagery is free from any kind of distortion except for the relief distortion. On the other hand, for an orthorectified image an elevation source that fully models the terrain surface is used so relief displacement errors are removed or minimized (Manual of Photogrammetry, 2004).

In a frame image, the perspective center is the single point where the rays of light pass before intersecting the image plane. This occurs because the perspective projection and points at the same horizontal location but at different elevations will therefore be imaged at different locations in the image (Figure 3.8). On the contrary, an orthoimage can be described as a digital image in which the pixels are corrected to an orthographic projection rather than the perspective projection (Manual of Photogrammetry, 2004). Because in an orthographic projection the projection of the rays is perpendicular to the horizontal plane the change in the elevation of a point does not differ from its position.

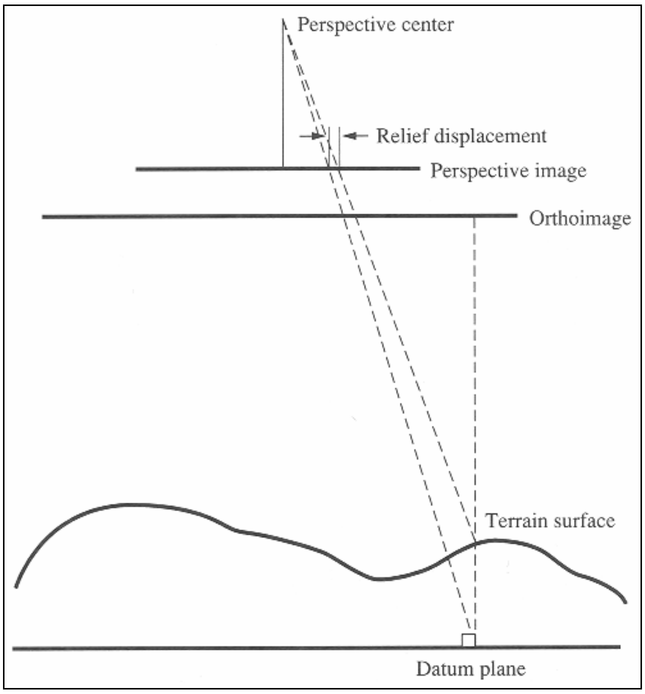

Figure 3.8 Relief displacement (Mikhail et. al., 2001).

The basic principals and methods of orthoimage generation were described by Konecny (1979), Novak (1992), Krupnik (2003), and Toutin (2004). There are two basic approaches to generate an orthoimage, (i) the forward projection and (i) backward projection (Novak, 1992). In the former one, the object space coordinates are first determined by projecting the raw image onto DEM. Then, the object space coordinates are projected into the orthoimage. Since the spaces between the points projected into the orthoimage vary due to terrain variation and perspective effects, the final orthoimage pixels must be determined by interpolating between the projected points. Figure 3.9.a illustrates the forward projection. In backward projection, the object space X, Y coordinates corresponding to each pixel of the final orthoimage are calculated. The elevation values for each pixel is determined from the DEM and the object space coordinates are projected into the raw image to obtain a gray level or a color value for the orthoimage pixel. Since the projected object space coordinates will not fall exactly at pixel centers in the raw image, resampling must be done in the raw image (Mikhail et. al., 2001). Figure 3.9.b illustrates the backward projection.

If the orthoimages are generated, they can be easily integrated for any kind of application such as map revision, forestry, geology, environmental studies etc. and offer users to use images like maps. However, a disadvantage of the rectified or orthorectified image product is that it has been resampled from the raw image and may have been prepared from a DEM which does not accurately model the surface. Thus, the product may loose some of its original resolution and the accuracy may be degraded because of the errors in the DEM (Manual of Photogrammetry, 2004). It is crucial to be aware of the input DEM characteristics such as elevation accuracy, positioning accuracy and grid spacing for the level of details. The last property gets more importance when the images get higher resolution because poor grid spacing when compared to the image spacing could generate problematic areas for linear features (roads, edges etc.) in the output orthoimage (Toutin, 2004).

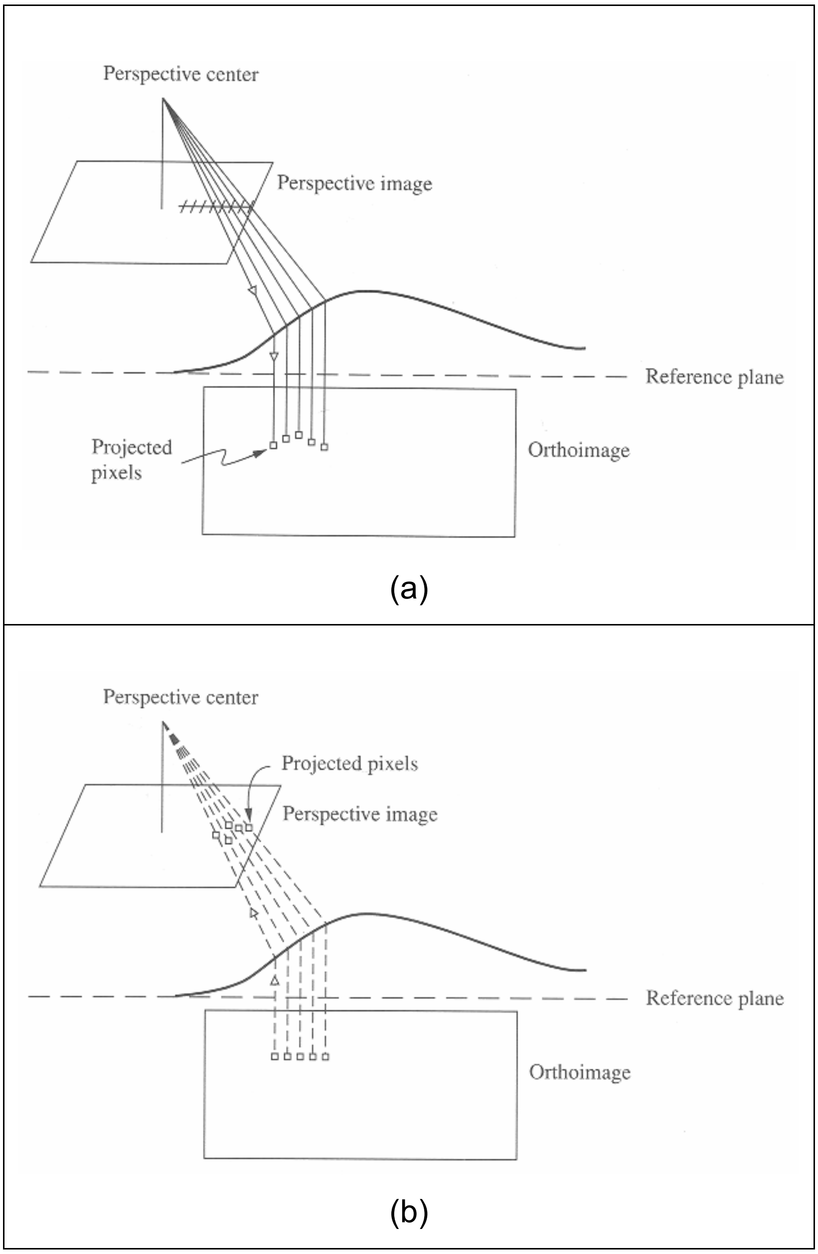

Figure 3.9 Forward and backward projection. (Mikhail et. al., 2001)

CHAPTER 4

STUDY AREA AND DATA SETS

In this chapter, the study area and the data sets used in the study are provided. After describing the study area, the image data of ASTER are explained. Later, the generation method of the reference DEMs from 1:1000 scale vector data is explained. Finally, the GCPs and their collection methods are given.

4.1 The Study Area

The study area (Figure 4.1) is located in central Anatolia. It covers an area of approximately 60 x 60 km and encloses the city of Ankara. There are also several scattered small towns and the lakes Mogan and Eymir are situated in the central part of the study area. The area also contains randomly distributed several small water bodies. The eastern and a part of the northern area are rather mountainous. The forest areas are mostly located in the southern part of the city of Ankara and in the south western part of the mountainous areas. The rest of the study area is characterized by the agricultural fields and open lands. The elevations range from approximately 700 m for the flat areas to 1900 m for the mountainous areas yielding a total relief around 1200 m. The slopes change sharply in mountainous regions approaching up to 70 degrees.

This area was selected due to containing various land-use and land-cover types such as urban, forest, water, mountainous, agriculture and open lands. The other reason is that both in the city of Ankara and in rural

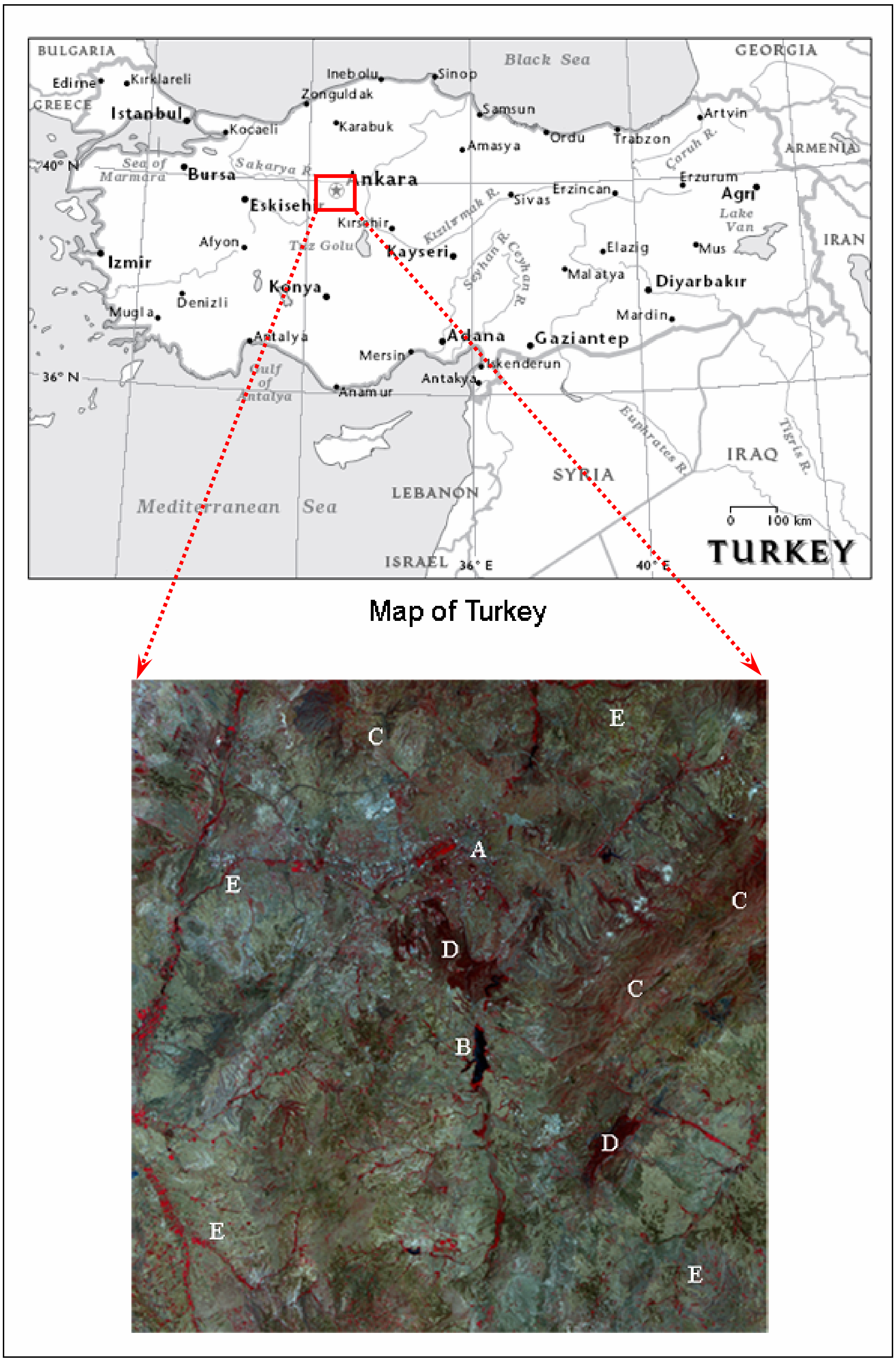

Figure 4.1 ASTER Nadir image of the study area. (A) represents the city center of Ankara, (B) represents Lake Mogan, (C) represents the mountainous sites, (D) represents the forestry areas, and (E) represents the agricultural and open lands.

areas, many roads and paths exist that can be very suitable for the selection and collection of GCPs and check points (CP).

4.2 Data Sets

Three data sets were used in the study: (i) stereo ASTER image data, (ii) vector data, and (iii) orthophotos.

4.2.1 ASTER Image Data

Stereo ASTER images were acquired on July 26, 2002 with a difference of 55 seconds. The images that were taken from the nadir and backward directions compose the stereo nature with an overlapping area of approximately 57.5 x 62 km. Both scenes were completely free from clouds, snow and other effects such as haze and dust. The geographic coordinates of the four corners and the center of the images are given in Table 4.1. Some technical characteristics of the image data are provided in Table 4.2.

Table 4.1 The geographic coordinates of the ASTER images.

Position	Nadir Image		Backward Image	
	Longitude	Latitude	Longitude	Latitude
Upper Left	32.504370	40.145584	32.437595	40.225613
Upper Right	33.234615	40.030784	33.358278	40.155359
Lower Left	32.323155	39.594501	32.202968	39.516573
Lower Right	33.047751	39.480710	33.114271	39.447998
Center	32.865844	39.862825	32.878922	39.862089

Table 4.2 The technical characteristics of the ASTER images.

Property	Nadir Image	Backward Image
Acquisition Date	26.07.2002	26.07.2002
Acquisition Time	08:52:33	08:53:28
Sensor	Near Infrared	Near Infrared
Instrument	VNIR 3N	VNIR 3B
Bits per pixel	16	16
Number of lines	4200	5400
Number of pixels	4100	5000
Processing Level	1A	1A

4.2.2 Vector Data

In this study, 5726 pieces of 1:1000-scale vector data with approximately 20 cm accuracy both in planimetry and height were available to be utilized as reference DEMs. In turn, the reference DEMs will be used to evaluate the generated DEMs. The vector dataset were compiled in 1999 and referred to the European ED 50 datum and Transverse Mercator (Gauss - Krueger) projection. The necessary information regarding the projection system is given in Table 4.3.

Table 4.3 Transverse Mercator projection system details.

True Origin	Longitude	33º 00' 00.0000" E
	Latitude	0º 00' 00.0000" N
False	Easting	500000.000
	Northing	0.000
Scale		1.0000000000

The vector dataset were built using the Microstation SE digital photogrammetric workstation software and composed of more than one hundred layers. Of these layers, those corresponding to contour lines, individual height points, road network, valley creeks and the attributes were utilized for the study. The contour lines were drawn with 50 cm interval. The area covered by the vector data was around 1963 km^2.

4.2.3 Digital Orthophotos

In this study, the 1:5000-scale digital orthophotos were available. The date and the projection system of the orthophotos were same as the vector data. The area covered by the orthophotos was illustrated in Figure 4.2.

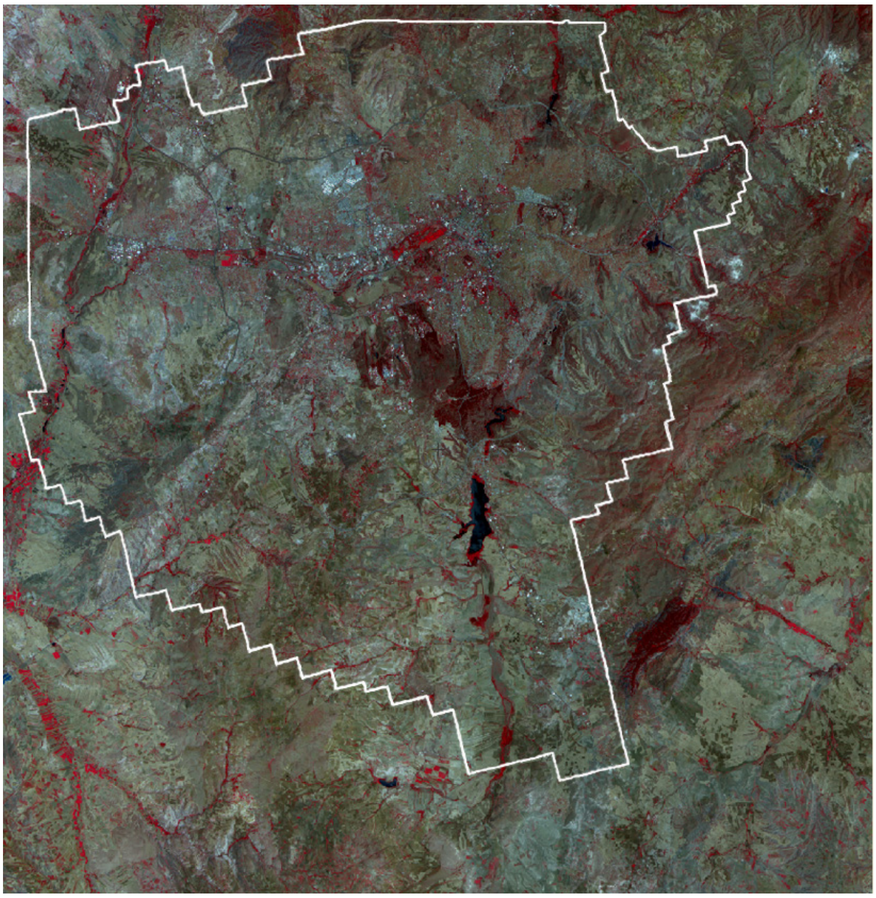

Figure 4.2 The white colored vector polygon shows the coverage of the existing vector data and orthophotos.

4.2.4 The Preparation of the Reference DEM Data from existing 1:1000 Scale Vector Data

Initially, the attribute layer, which caused several technical problems when transferring the vector data to the PCI Geomatica software, was removed automatically from all vector data using Microstation SE software. Next, 5726 separate 1:1000 scale vector files were attempted to be merged to make a single file using Microstation SE. Because of the file size limitation of this software, unfortunately this process was not able to be implemented. Later, 5726 pieces of 1:1000 scale vector data were merged first into smaller subsets. After this first merging process, a total of 114 new vector data segments were generated. The complete names of the files can be found in the Appendix F. Then, all the merged vector data were imported to PCI Geomatica software using the Focus module and a reprojection procedure was performed to them. The output projection used was “WGS 84” ellipsoid and UTM zone-36 row-S. After the reprojection procedure, 114 DEMs with 1 m resolution were created using the “Import & Build DEM” menu of the Orthoengine module. This module uses the “Finite Difference” interpolation method to generate the DEMs. This method performs the interpolation in three steps. In the first step, the vector elevation values are assigned into the corresponding pixels in raster DEM. Next, the elevations for the remaining pixels are interpolated using the Distance Transform algorithm, which estimates the values from those pixels equidistant from the pixels assigned in the first step. In the last step, the Finite Difference algorithm iteratively smooths the raster DEM. During the iterations, the pixels that were assigned in the first step are not changed, while the interpolated pixel values are updated based on the neighbourhood values (Orthoengine user guide, 2003). Two parameters determine the completion of the process, the (i) Number of Iterations and the (ii) Tolerance. The Number of Iterations specifies the maximum number of times the smoothing is applied on raster DEM. The

Tolerance restricts the number of times the smoothing is applied according to how it changes the elevation values of the pixels. For the “Finite Difference” interpolation method, the default values for the Number of Iterations and the Tolerance is 10 and 1, respectively. If the tolerance value of a generated DEM is lower than 1 at the end of 10 iterations, the DEM is accepted. Otherwise, the DEM is considered to contain errors. In this case, the DEM is rejected and the vector data is scrutinized. In the present case, the number of corrected DEMs was 68 and the vector IDs can be found in the Appendix C.

The errors generally caused by the missing elevation or wrongly entered elevation values either in lines, individual points or roads. An example for the missing elevation values is illustrated in Figure 4.3. In this example, the resulting tolerance value for the generated DEM was higher than the acceptable tolerance value. When the generated DEM is visually analyzed, the error can be easily detected even on the overview section (Figure 4.3-b). If the vector data is superimposed on the generated DEM (Figure 4.3-c), the erroneous contour line is apparent. The wrong elevation values that lie along that line were then corrected with the help of the elevation values of the adjacent lines. After the editings, the DEM was generated using the same method and the resulting DEM tolerance value was found to be better than the acceptable tolerance value (Figure 4.3-d).

Figure 4.4 illustrates an error of missing individual point measurements. Similarly, the resulting tolerance value for the generated DEM was higher than the acceptable value. Because the individual points were errant, the true elevations of these points could not be precisely known. Therefore, these points were removed from the data segment. After removing the points, the DEM was regenerated and the resulting tolerance value was found to be better than the acceptable tolerance value.

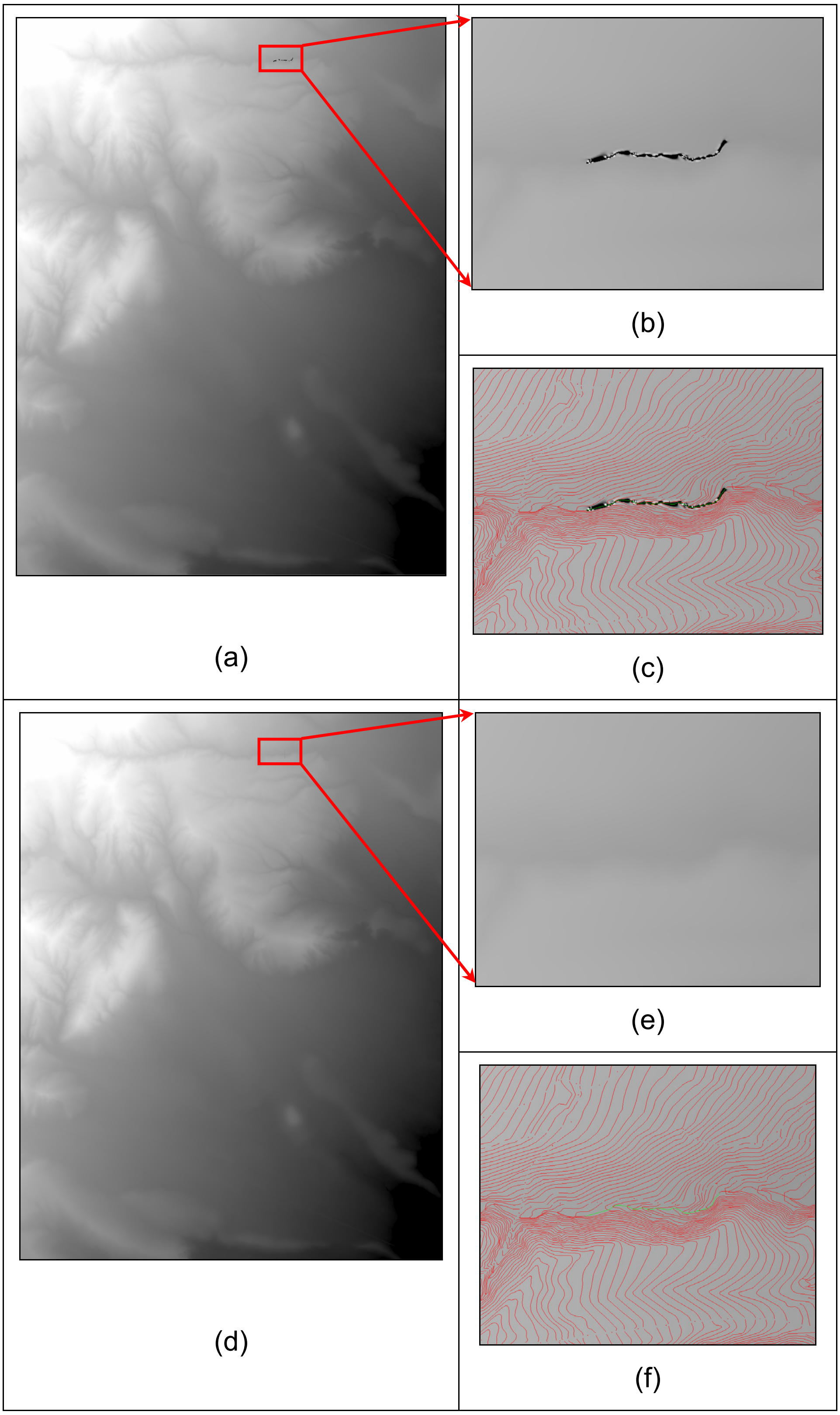

Figure 4.3 An error caused by the missing elevation values.

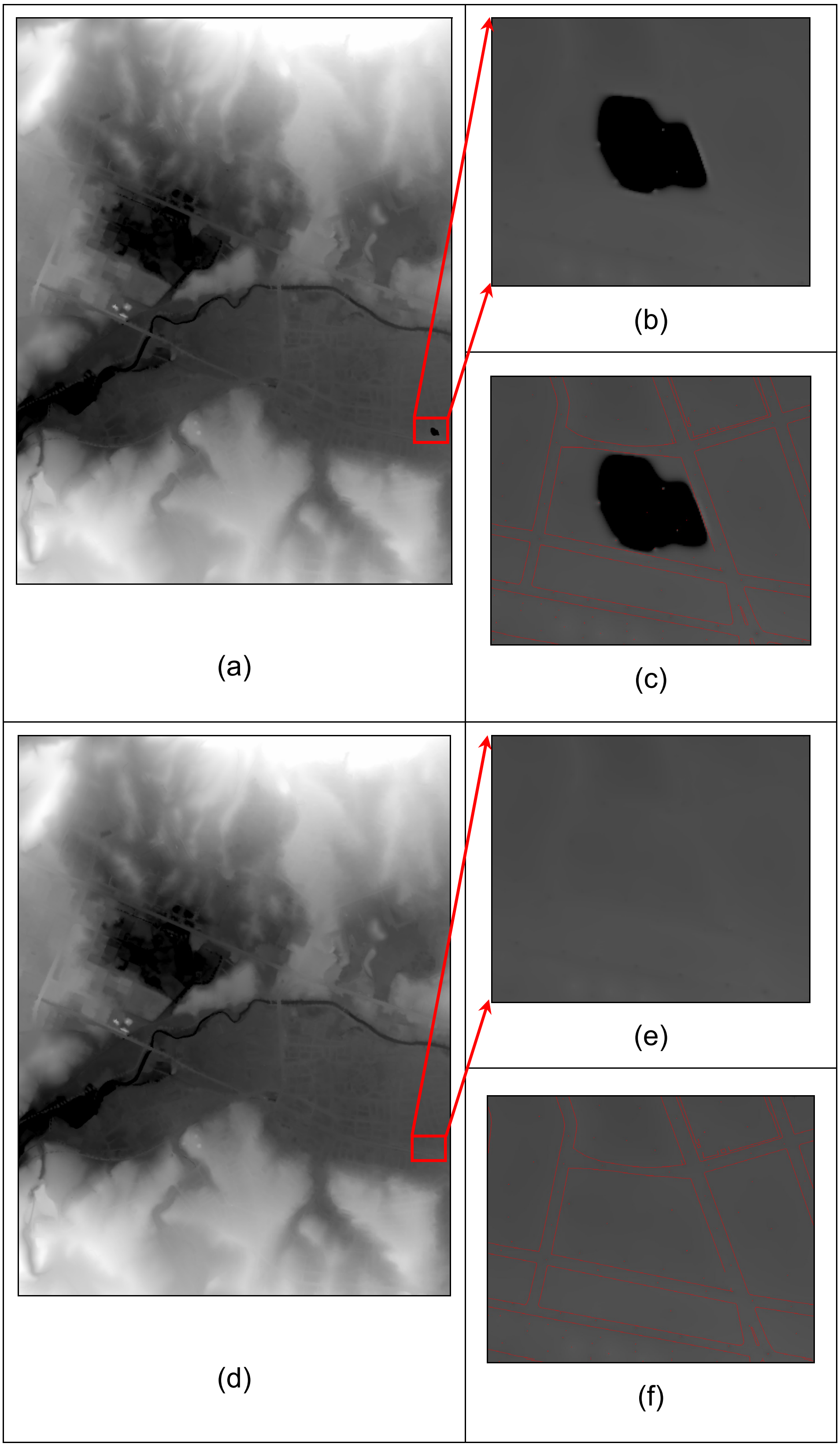

Figure 4.4 An error caused by the missing individual point measurements.

The total number of the corrected vector data parts were 68. Then, two reference DEMs one having 1 m resolution and the other having 30 m resolution were generated using the whole vector dataset. The former was used to obtain the elevations of the GCPs collected with the help of the orthophotos. On the other hand, the latter was used as the reference DEM.

4.3 The Collection of the GCPs

Majority of the study area was covered by 1:5000 scale digital orthophotos, which were used as the main source to collect the GCPs. For the areas that were not covered by the orthophotos, the GCPs were collected through differential GPS measurements.

4.3.1 GCP Collection from 1:5000 Scale Digital Orthophotos

On orthophotos, the ground features presented are in their correct orthographic positions. Therefore, the orthophotos are geometrically equivalent to conventional planimetric maps which compose of line and symbols. Because they are planimetrically correct, the digital orthophotos can be efficiently used as digital maps to select and identify GCPs.

First, the Nadir image with false color composite was displayed using the Orthoengine module and the candidate GCP locations were selected from the image. The candidate GCP locations are the possible GCP locations that can be found on the Nadir image. A total of 158 candidate GCPs were selected throughout the image. Then, the areas covered by the digital orthophotos were visually analyzed and 108 GCPs were found to be falling within the area covered by the orthophotos. During the collection of the GCPs, the digital orthophotos and the ASTER nadir image were also displayed simultaneously on the screen and finally a total of 101 GCPs with the Eastings and the Northings were successfully collected. Seven of the candidate GCPs were not able to be collected because it appears that the points were formed after production of the orthophotos in 1999.

Of the collected 101 GCPs, 4 points were eliminated because their locations were outside the border of the previously generated 1 m resolution DEM. Hence, the elevation values of these points could not be determined. Because the GCPs had to be collected both on the nadir and backward images, 27 GCPs were also removed as their locations were not able to be found on the backward image. Furthermore, 5 points very close to other GCPs and 4 erroneous points were also removed. As a result, a total of 40 GCPs were eliminated and 61 GCPs were kept to be used for the subsequent processes. The coordinates of the 61 GCPs are provided in Appendix D. For three GCPs, the locations on the image and their corresponding locations on the orthophoto are illustrated in Figure 4.5.

4.3.2 GCP Collection through Differential GPS Measurements

The coordinates of the Differential GCPs (DGCPs) were measured in the field using ASHTECH Z-Surveyor receivers. These receivers are double frequency sensor type receivers. After completing the field work, the row differential GPS positioning data were evaluated using ASHTECH Office suite version 2.0. Finally, the DGCPs were obtained based on European ED 50 datum and the Transverse Mercator (Gauss - Krueger) projection. The output coordinate system of the GCPs was reprojected to “WGS 84” ellipsoid and UTM zone-36 row-S projection.

The differential GPS observations were made between 18 October 2004 and 05 November 2004. Of the two GPS receivers, one was placed at a base station whose coordinates are precisely known and the other was moved to each point whose coordinates are to be measured. At each GCP

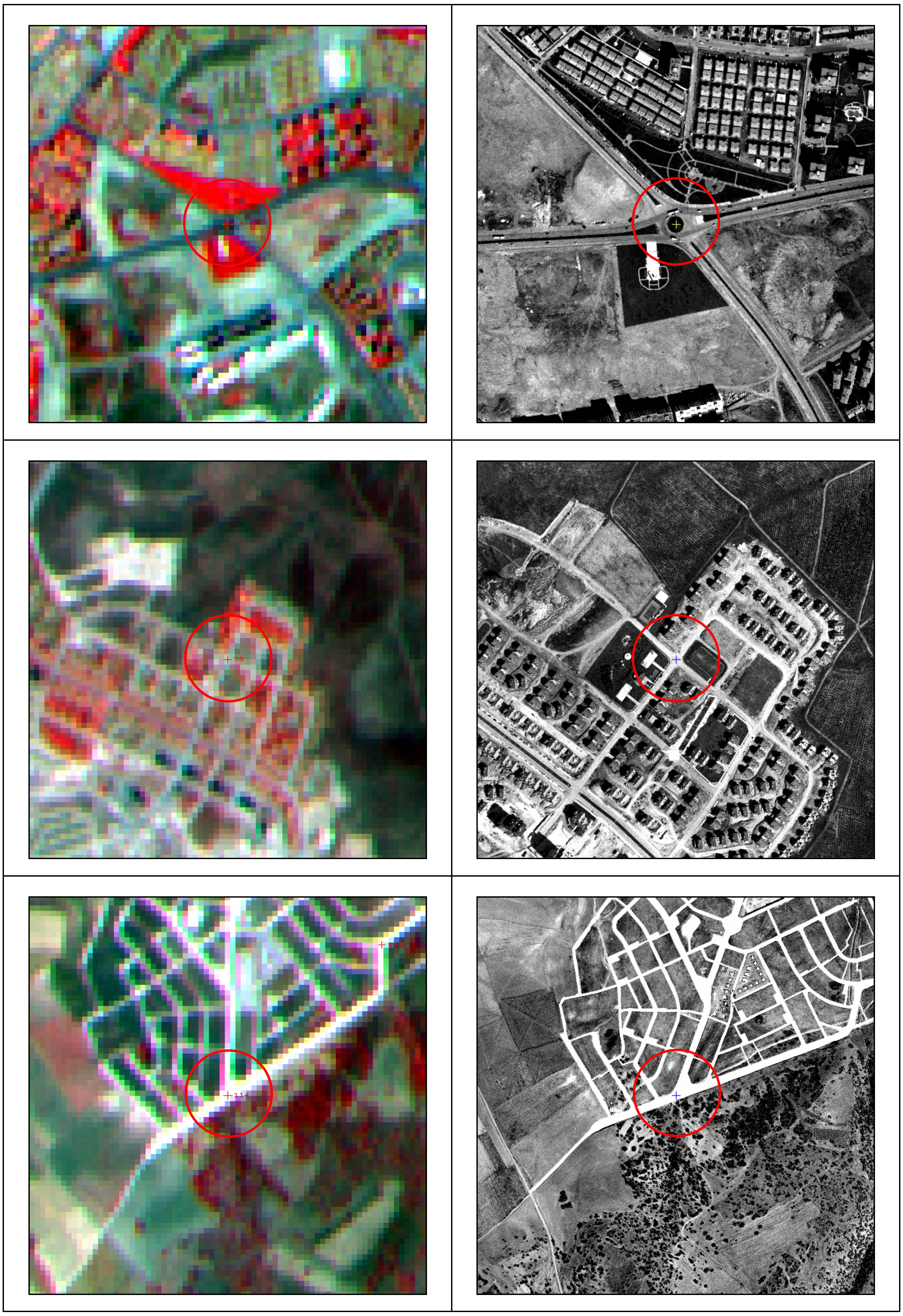

Figure 4.5 Three GCPs on the image and their corresponding locations on the orthophotos.

to be measured, the rover receiver received satellite signals for approximately 10 minutes. Ten minute receiving time was sufficient for determining the coordinates of a point with at least 1 meter accuracy.

Of the collected 158 candidate GCP points, 108 points were within the region covered by the existing reference digital orthophotos. For the remaining 50 points, it was necessary to make measurements on the ground. Due to the medium resolution of the ASTER stereo images, the locations of the candidate GCPs were not quite distinct to be identified. Therefore, for preventing possible confusions about the locations of the points, for each point, the site on the image was printed on A3 size paper and also displayed on the screen of a notebook computer. Of the 50 candidate points, 36 GCPs were identified on the ground and their coordinates were measured using the DGPS method in three dimensional mode. Unfortunately, the locations of the 14 points were not able to be found on the ground and they were discarded.

Of the collected 36 GCPs, 11 out of 20 points were eliminated due to their high residual errors. The remaining 9 points were removed because their corresponding point locations were not able to be found on the backward image. Consequently, 16 GCPs were successfully collected both on the nadir and backward image for the subsequent processes. The coordinates of the 16 GCPs determined through DGPS are provided in Appendix D.

CHAPTER 5

DEM GENERATION FROM STEREO ASTER IMAGERY

In this chapter, the Terra satellite which carries the ASTER sensor is explained. Later, the DEM generation process from stereo ASTER images is given. Finally, the results of the assessment of the generated DEMs are given. The results of DEM accuracy analysis comprise two sections, (i) the results of the least squares bundle adjustment and (ii) the results of DEM accuracy evaluation.

5.1 Earth Observation Satellite Terra

The advanced methods in computing and image processing technologies let the users to use space imagery in a useful manner more than ever. Today, a series of Earth observation satellites monitor our planet and collect huge number of images that could be utilized for many studies. Landsat and Spot series are probably the most considered and famous satellites. On the other hand, the Terra satellite, a part of Earth Observing System (EOS) of NASA, is one of the flagships to take on the role of observing the Earth. The images taken by the Terra satellite give opportunity to researchers to monitor the Earth's continents, atmosphere and oceans only from a single platform.

The Terra satellite was launched in December 1999 and began operations in February 2000. It carries five independent sensors (i) ASTER, (ii) CERES, (iii) MISR, (iv) MODIS and (v) MOPITT. The satellite's orbit is roughly perpendicular to the Earth's spin and operates sun-synchronous

Table 5.1 The orbit characteristics of the Terra satellite.

Parameter	Specification
Orbits / cycle	233
Cycle duration	16 days
Number of orbits per day	14
Altitude	705 km
Inclination	98.3 deg
Orbital Period	98.88 min
Equatorial crossing at local time	10:30 am

orbit with an inclination of 98.3 deg, at an altitude of 705 km. The satellite takes 98.88 minutes to complete one revolution around the Earth and completes about 14 orbits per day. Terra's pattern of orbits repeats itself every 16 days or 233 orbits. The orbit characteristics of the Terra satellite are given in Table 5.1.

5.1.1 Advanced Spaceborne Thermal Emission and Reflection Radiometer (ASTER)

ASTER is a cooperative effort between NASA and Japan's Ministry of Economy Trade (METI), with the collaboration of scientific and industrial organizations in both countries (Abrams et. al., 2003). ASTER is advanced multispectral imager that covers a wide spectral region with 14 bands from the visible to thermal infrared with varying spatial, spectral and radiometric resolutions. The stereo coverage is provided by an additional backward looking near-infrared band.

ASTER is composed of three different subsystems: (i) the Visible and Near-Infrared (VNIR), (ii) the Shortwave Infrared (SWIR) and (iii) the Thermal Infrared (TIR) (Yamaguchi et. al., 1998). The VNIR has three bands with a spatial resolution of 15 m, and an additional backward telescope for stereo coverage. The SWIR has 6 bands with a spatial resolution of 30 m. The TIR has five bands with a spatial resolution of 90 m. Each subsystem operates in a different spectral region with its own telescope(s).

5.1.1.1 The VNIR Instrument

The VNIR subsystem consists of two independent telescope assemblies to minimize image distortion in the backward and nadir looking telescopes. The detectors for each of the bands consist of 5000 element silicon charge-coupled detectors (CCD’s). Only 4000 of the detectors are used at a time. A time lag occurs between the acquisition of the backward image and the nadir image. During this time Earth rotation displaces the image center. The VNIR subsystem automatically extracts the correct 4000 pixels based on orbit position information supplied by the EOS platform (Abrams et. al, 2003). Despite the focal plane of the nadir telescope contains three line arrays, the backward looking telescope focal plane contains a single detector array. Onboard calibration of the two VNIR telescopes is accomplished with either of two independent calibration devices for each telescope.

The stereo image acquisition of ASTER is accomplished by the VNIR subsystem. Two independent nadir and backward looking telescopes work together to obtain along-track stereoscopic images. The images taken from the nadir and backward looking telescopes compose the stereo nature with a B/H ratio of about 0.6 and an intersection angle of 27.6°. Figure 5.1 illustrates the along-track stereo image acquisition system of the ASTER sensors. (Hirano et. al., 2003). Since the two telescopes can be rotated up to 24° to provide extensive across-track pointing capability and five day revisit capability, across-track stereo imaging with a B/H ratio (close to 1) is also possible (Toutin, 2002).

5.1.1.2 The SWIR Instrument

The SWIR subsystem uses a single aspheric refracting telescope. The detector in each of the six bands is a Platinum Silicide-Silicon (PtSi-Si) Schottky barrier linear array cooled to 80 K. The on-orbit design life of the cooler is 50000 hours. Six optical bandpass filters are used to provide spectral separation. A calibration device similar to that used for the VNIR subsystem is used for in-flight calibration (Abrams et. al, 2003).

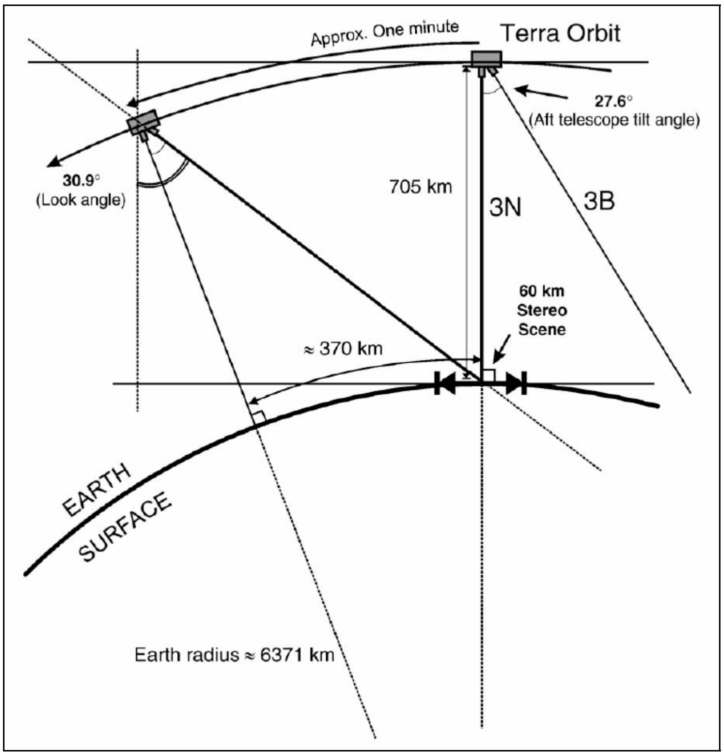

Figure 5.1 ASTER stereo geometry.

5.1.1.3 The TIR Instrument

Unlike the VNIR and SWIR telescopes, the telescope of the TIR subsystem is fixed with pointing and scanning done by a mirror. Each band uses 10 Mercury-Cadmium-Telluride (HgCdTe) detectors in a staggered array with optical band pass filters over each detector element. The ASTER Instrument characteristics and significant ASTER functions and components are summarized in Table 5.2 and Table 5.3, respectively (Abrams et. al, 2003).

Table 5.2 ASTER instrument characteristics.

Subsystem	Band No.	Spectral Range(μm)	Spatial Resolution(m)	Quantization Level(bits)
VNIR	1	0.52-0.60	15	8
	2	0.63-0.69		
	3N	0.78-0.86		
	3B	0.78-0.86		
SWIR	4	1.60-1.70	30	8
	5	2.145-2.185		
	6	2.185-2.225		
	7	2.235-2.285		
	8	2.295-2.365		
	9	2.360-2.430		
TIR	10	8.125-8.475	90	12
	11	8.475-8.825		
	12	8.925-9.275		
	13	10.25-10.95		
	14	10.95-11.65		

Table 5.3 Significant ASTER functions and components.

Parameter	VNIR	SWIR	TIR
Telescope Optics	Pushbroom	Pushbroom	Whiskbroom
Focal Plane(Detector)	D=82.25 mm (Nadir) D=94.28 mm (Back.)	D=190 mm	D=240 mm
Cross Track Pointing	Telescope rotation ±24°	Pointing mirror rotation ±8.55°	Scan mirror rotation ±8.55°

5.1.2 Clouds and the Earth's Radiant Energy System (CERES)

There are two identical CERES instruments aboard Terra that measures the Earth's total radiation budget and provide cloud property estimates that enable scientists to assess the clouds' roles in radiative fluxes from the surface to the top of the atmosphere. Ceres has a coarse spatial resolution which is 21 km. One CERES instrument will operate in a cross-track scan mode and the other is a biaxial scan mode. The cross-track mode will essentially continue the measurements of the Earth Radiation Budget Experiment (ERBE) mission as well as the Tropical Rainfall Measuring Mission (TRMM), while the biaxial scan mode will provide new angular flux information that will improve the derivation of the Earth's radiation balance (Web 1).

5.1.3 Multi-angle Imaging Spectro-Radiometer (MISR)

To fully understand the Earth's climate, and to determine how it may be changing, we need to know the amount of sunlight that is scattered in different directions under natural conditions. MISR is designed to address this need by using cameras pointed at nine different angles. One camera points at nadir the others provide forward and backward viewing angles. As the instrument flies, each region of the Earth’s surface is successively imaged by all nine cameras in each of four wavelengths (blue, green, red and near-infrared). MISR has a spatial resolution of 275 m (Web 2).

5.1.4 Moderate-resolution Imaging Spectro-radiometer (MODIS)

MODIS is viewing the entire Earth’s surface every 1 to 2 days and acquiring data in 36 spectral bands. These data will improve our understanding global dynamics and processes occurring on the land, in the oceans and in the lower atmosphere. MODIS is playing a vital role in the development of validated, global and interactive Earth system models to predict global change accurately (Web 3). The instrument provides high radiometric sensitivity (12 bits) ranging in wavelength from 0.4 μm to 1.4 μm. Two bands are imaged at a resolution of 250 m at nadir, with five bands at 500 m and the remaining 29 bands at 1km. A ±55 degree scanning pattern achieves a 2330 km swath width (Web 4).

5.1.5 Measurements of Pollution in Troposphere (MOPITT)

MOPITT is an instrument designed to enhance our knowledge of the lower atmosphere and to particularly observe how it interacts with the land and ocean biospheres. MOPITT’s spatial resolution 22 km at nadir and it sees the Earth in swaths that are 640 km wide. MOPITT has 8 channels and scans across the satellite flight track ±26.1 deg in 13 seconds (Web 5).

5.2 Digital Elevation Model Generation from ASTER Data

The digital elevation models (DEM) were generated using the Orthoengine module of the PCI Geomatica software. This module uses a rigorous mathematical model (Toutin's model) developed in Canada Centre for Remote Sensing (CCRS) and reflects the physical reality of the complete viewing geometry and integrates all the distortions generated during image acquisition (Toutin and Cheng, 2002). The module has also specific mathematical model for aerial images and capabilities to rectify satellite or aerial images by using polynomial and rational function based models. The distortions handled by the Toutin's model are as follows:

- Distortions due to platform
- Distortions due to the sensor
- Distortions due to the Earth
- Deformations due to the cartographic projection.

Integrating all these distortions in a mathematical model produces a set of correlated unknown parameters which later reduced to a set of independent uncorrelated set (Toutin and Cheng, 2002). Toutin's model is said to be the only satellite mathematical model that can be applied to various VIR and SAR sensors (ASAR, ASTER, EOC, EROS, ERS, IRS, IKONOS, JERS, LANDSAT, MERIS, QUICKBIRD, RADARSAT and SPOT). Based on the quality of the GCPs, the accuracy of the Toutin's model was proven to be within one-third of a pixel for medium resolution VIR images, one to two pixels for high-resolution VIR images, and within one resolution cell for SAR images (Toutin and Cheng, 2002).

5.2.1 Radiometric Correction

The ASTER data was purchased in level 1A data format. The level 1A data format consists of image data, the radiometric coefficients, the geometric coefficients and other auxiliary data without applying the coefficients to the image data to maintain the original data values (ASTER Users guide part II, 2003). Because the original data values are preserved in Level 1A format, PCI Geomatica recommends it to obtain the highest DEM accuracy (Orthoengine user guide, 2003).

First, the projection of the output DEMs was determined as Universal Transverse Mercator (UTM) zone 36 and row S on WGS 84 ellipsoid. Then, the projection information of the GCPs was determined same as the output projection of the DEMs and the output pixel spacing of the DEMs to be generated was determined as 15 m. The output pixel spacing is trivial at this stage because the output pixel spacing information can also be determined at the final stage of the DEM generation. Next, because the radiometric coefficients were not applied on Level 1A data, the radiometric preprocessing was carried out. The algorithm used to preprocess the data was described as (ASTER Users guide part II, 2003):

$$L = A \times V / G + D \qquad \text{(for VNIR and SWIR bands)}$$
$$L = A \times V + C \times V^2 + D \qquad \text{(for TIR bands)}$$

where, L is the radiometrically corrected value, A is the linear coefficient value, V is the raw Digital Number (DN) value, G is the gain value, D is the offset value and C is the non-linear coefficient value. The first formula was used to correct the nadir and backward VNIR ASTER images. Tables 5.4 and 5.5 show the structure of the radiometric coefficients available for nadir and backward images.

Table 5.4 VNIR band (1, 2, 3N).

Detector Number	**Offset**	**Linear coefficient**	**Gain**
1	D[1]	A[1]	G[1]
2	D[2]	A[2]	G[2]
3	D[3]	A[3]	G[3]
4	D[4]	A[4]	G[4]
…	…	…	…
…	…	…	…
…	…	…	…
4098	D[4098]	A[4098]	G[4098]
4099	D[4099]	A[4099]	G[4099]
4100	D[4100]	A[4100]	G[4100]

Table 5.5 VNIR band (3B).

Detector Number	**Offset**	**Linear coefficient**	**Gain**
1	D[1]	A[1]	G[1]
2	D[2]	A[2]	G[2]
3	D[3]	A[3]	G[3]
4	D[4]	A[4]	G[4]
…	…	…	…
…	…	…	…
…	…	…	…
4998	D[4998]	A[4998]	G[4998]
4999	D[4999	A[4999]	G[4999]
5000	D[5000]	A[5000]	G[5000]

The radiometric correction formula was also integrated into the Orthoengine module by PCI Geomatica itself. When the raw images are loaded into the module, the software automatically reads the radiometric coefficients available in the header file and performs the radiometric pre-processing operation automatically. In order to be sure of the correctness of the preprocessing operation, several parts of the image were randomly selected and the manually calculated values were checked with the output values of the software. It was found that the manually collected values were identical to the output values of the software. Figure 5.2 shows for two selected areas of the nadir image before and after the preprocessing operations. The importance of the preprocessing step was demonstrated in a previous study conducted by Toutin (2002) who states that the preprocessing operation improves the overall DEM accuracy by a factor of 10% (Toutin, 2002).

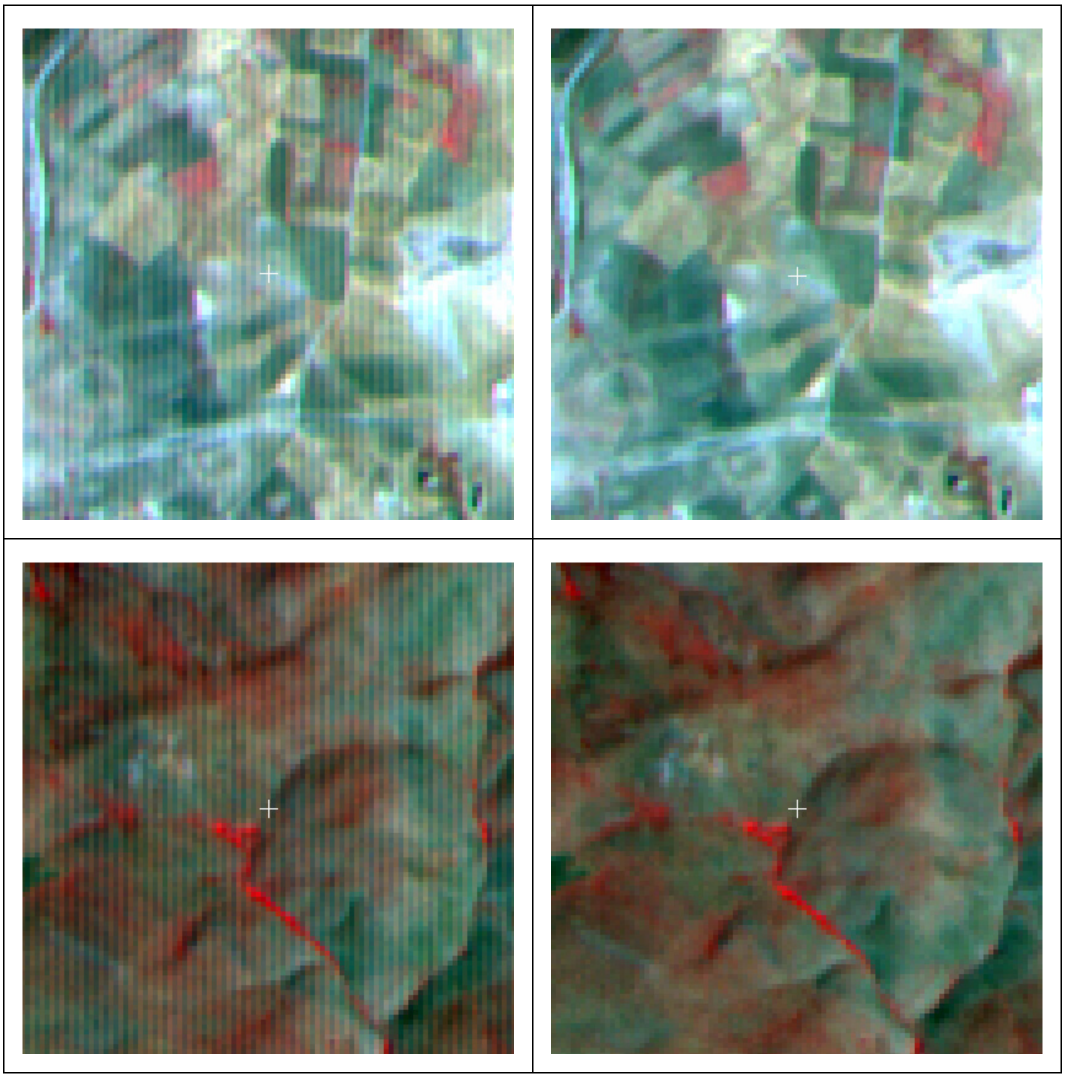

Figure 5.2 Before and after pre-processing operation.

5.2.2 Collection of the Stereo GCPs

After the radiometric correction of the nadir and backward images, both images were displayed on the screen to collect the stereo GCPs by using the GCP collection menu of the Orthoengine module. In this module, various input sources are available for the GCPs. The GCPs can be collected either manually from the images, from another geocoded image, from vectors, from chip databases or from tablets. The menu also allows users to import GCPs that are available in a text file composed in a specific format.

In the present case, the GCPs were collected manually. To collect the GCPs from a stereo image, first, both images were displayed simultaneously on the screen. When two images were displayed, the one in a viewer was labeled “working” and the other was labeled “reference”. The GCP collection window collects and displays the GCPs from the image from the “working” viewer only. Initially, the nadir image was labeled “working” and the backward image was labeled “reference”. Then, the first GCP’s ID is set up and the GCP is collected on the nadir image as precisely as possible. Later, the backward image was labeled “working” and the nadir image was labeled “reference”. When the same ID of the GCP was typed in for the backward image, the georeferencing information of the GCP was automatically taken from the previous entry. The only missing part was the pixel and the line coordinates of the GCP on the backward image. The Orthoengine module can estimate the possible location of the GCP by using an automatic correlation feature available in the GCP collection windows. Therefore, there is no need to search for the corresponding GCP location on the backward image. The automatic correlation guides the user to locate the possible location of the GCP on the backward image. But, the user must verify the estimated positions and adjust them before accepting the GCP on the backward image (Orthoengine user guide, 2003). Afterwards, the GCP location is fixed and the GCP is accepted. This stereo GCP collection process was therefore repeated for the available 77 GCPs. The positions of the GCPs were located on both images as precisely as possible. Then, the overall root mean square error (RMSE) of the stereo model was automatically computed for the nadir and backward images by the software.

Among the available 77 GCPs, first, the evenly distributed 8 were selected as GCPs and the remaining 69 were released as CPs. Therefore, the rectification process was started using 8 GCPs. Then, the the number of GCPs was increased to 16, 24 and 32 respectively to assess the effect of the number of GCPs on DEM accuracy of the ASTER imagery. During the process, 8, 16, 24 and 32 numbers of GCPs were named as set 1, 2, 3, and 4, respectively. The number of CPs used for the sets 2, 3, and 4 were 61, 53, and 45, respectively. Figure 5.3 illustrates four sets of GCPs and CPs.

Later, the bundle adjustment was carried out for all the sets by using the "model calculations" menu. The bundle adjustment is simply referred to the computation of the unknowns of the stereo model. It is a method used to calculate the position and the orientation of the sensor at the time when the image was taken (Orthoengine user guide, 2003). The results of the bundle adjustment for the sets, namely the residuals or the RMS errors of the GCPs and CPs, help determine the results and the quality of the stereo model. The RMSE values of the GCPs and the check points are given in Appendix E.

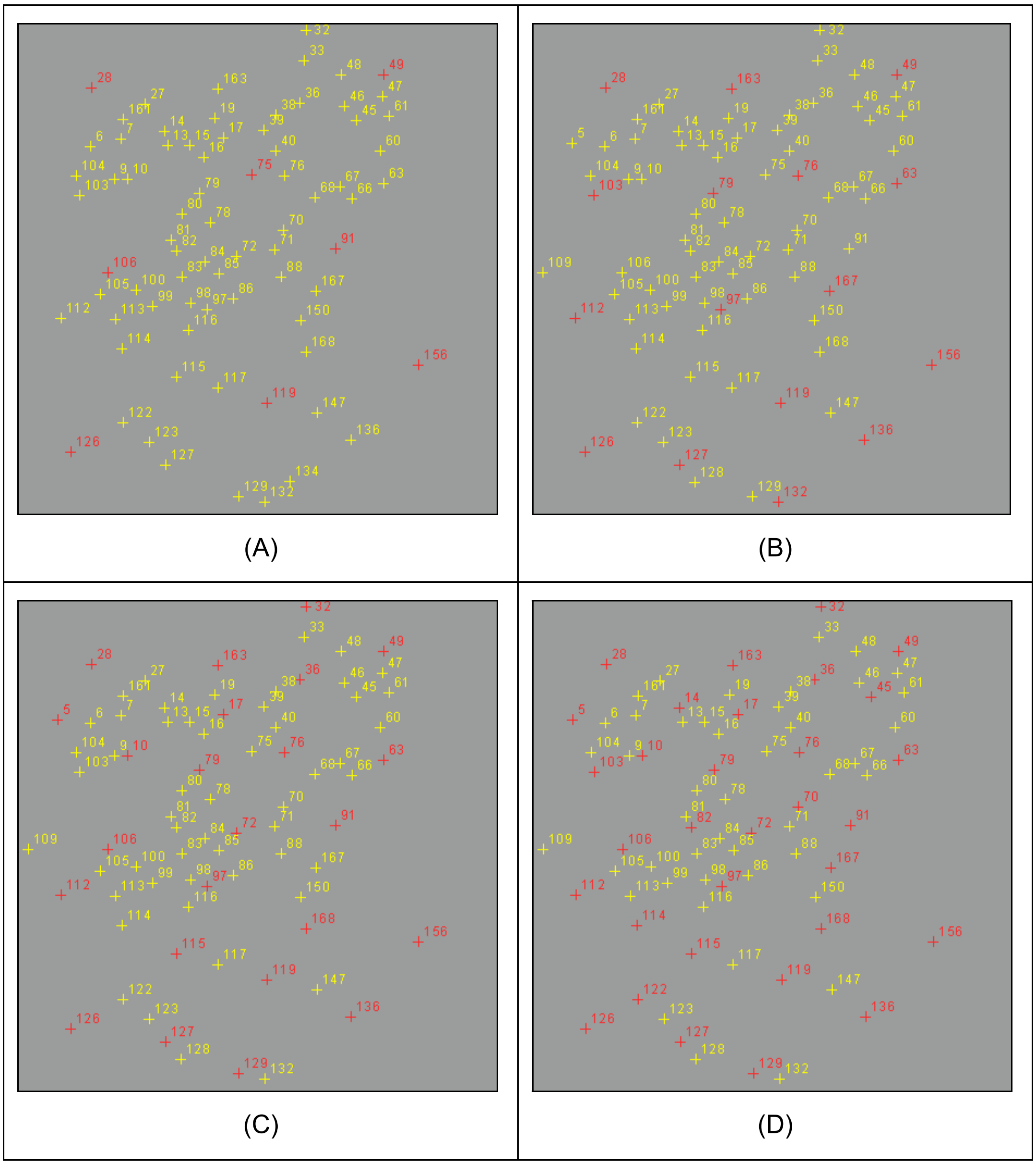

Figure 5.3 Four sets of GCPs and CPs. The red points indicate the location of the GCPs, whereas the yellow points indicate the location of the CPs. The distribution of (A) 8 GCPs, (B) 16 GCPs, (C) 24 GCPs, and (D) 32 GCPs.

5.2.3 DEM Generation

The Orthoengine module can generate DEMs from various input sources such as rasters, vectors, points or stereo images. The DEM generation using the stereo images has an additional initial stage prior to the DEM generation that is the epipolar images must be generated from the input stereo image pairs. The epipolar images are stereo pairs that are reprojected so that the left and right images have a common orientation. Therefore, the matching features between the two images appear only along a common x axis. Because the epipolar images increase the speed of the correlation process and reduce the possibility of incorrect matches (Orthoengine user guide, 2003) they are necessary prior to DEM generation in the Orthoengine module.

To generate the epipolar images, the nadir image was selected as the left image and the backward image was selected as the right image. The "down sample factor", which is the number of pixels and lines used to calculate for one epipolar image, was selected as 1 to retain the original pixel size of the input images. Then, the epipolar images were generated successfully in a minute. Figure 5.4 illustrates the generated left and right epipolar images for GCP set 2.

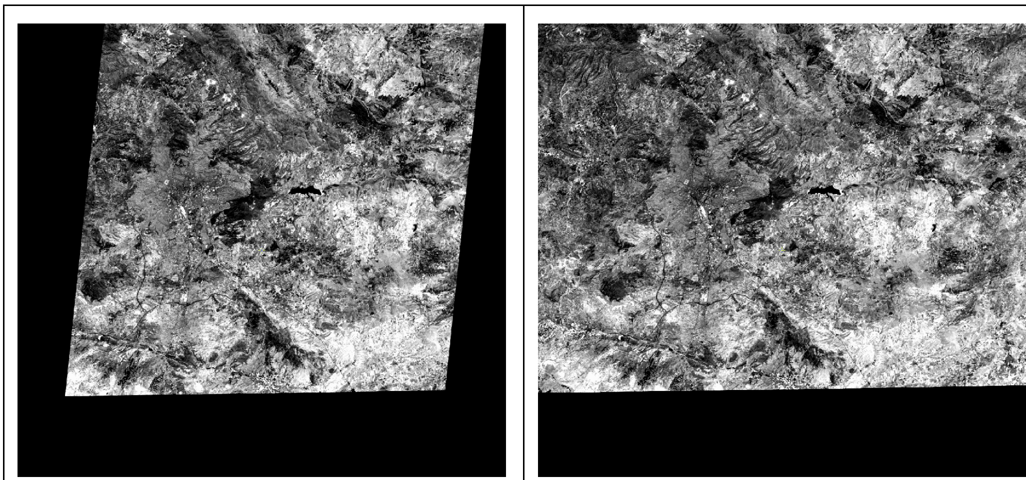

(a) (b)

Figure 5.4 The epipolar images that are generated from the (a) nadir and (b) backward images.

Once the epipolar images were generated, the DEMs were extracted for all GCP sets using the “DEM from Stereo” segment. To do that, the generated epipolar images were selected as input images. The program requires the estimated minimum and maximum elevation values for the terrain within the area covered by the stereo pair. These values are used to estimate the search area for the correlation stage and it is recommended that increasing the range between the estimated minimum and maximum elevations for the terrain reduces the failure areas (Orthoengine user guide, 2003). The estimated minimum and maximum elevations for the area was taken from the Shuttle Radar Topography Mission (SRTM) - 90 m resolution data. This data has been released to the public with free of charge and it was directly downloaded from the World Wide Web (Web 6). The minimum and maximum elevation values that were estimated from the SRTM data for the study area were 700 m and 1900 m, respectively. A 500 m cushion on each side of the elevation range was given in order to reduce the failure areas in the generated

DEMs (Hurtado, 2002). Thus, the minimum and maximum elevation values determined for the study area were 200 m and 2400 m, respectively.

The Orthoengine module performs image matching based on a hierarchical image matching approach. This approach integrates a pyramid of reduced resolution images that are generated from the epipolar images. In the first part of the approach, very coarse versions of the epipolar images were tried to be matched. This allows the matching of certain features which forms the basis for the subsequent correlation attempts. The next correlation attempts were performed on higher resolution versions of the images. Finally, the correlation was performed on full resolution epipolar images, which provides the highest precision for the terrain in the generated DEM (Orthoengine user guide, 2003). The level of the correlation pyramid can be manipulated by using the "DEM Detail" parameter which determines how precisely the terrain is represented in the generated DEM. Three types of DEM details (high, medium and low) can be selected. The "Low detail" means that the correlation process stops at the higher (coarser) level of the image pyramid and the detail levels of the generated DEMs are low. Similarly, the "Medium detail" means that the correlation process stops at the average level of the image pyramid and the detail levels of the generated DEMs are moderate. The "High detail" means that the correlation process continues until the full resolution image matching is finished and the level of the details of the generated DEMs is high. In the present case, all three possible choices were selected and performed separately. It was found that, the best results were obtained using the "Medium detail" solution and this DEM detail was selected for all the sets of GCPs.

The last important factor that affects the DEM accuracy is the "Pixel Sampling Interval". This parameter controls the size of the output pixel in the generated DEMs. The pixel sampling interval can be selected as 1, 2, 4, 8, 16 and 32. The higher the number of the pixel sampling interval, the larger the pixel size of the output DEM is and the faster the DEM is generated. Figure 5.5 illustrates the condition of the pixel sampling interval of 2. Because the ASTER images have a moderate resolution in the present case the pixel sampling interval of 2 was selected (Orthoengine user guide, 2003).

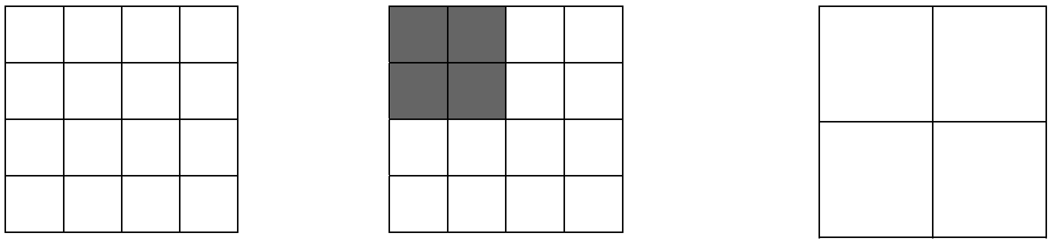

(a) epipolar image (b) pixel sampling of 2 (c) Output DEM

Figure 5.5 The illustration of the pixel sampling intervals

In addition to the above explained parameters, the values for the failure and background were used as “-100” and “-150”, respectively. The channel type for the output DEM was selected as 32 bits for all sets and the “fill holes and filter” box was also selected to enhance the output quality of the DEMs. The “fill holes and filter” parameter interpolates the failed areas and filters the elevation values automatically.

After assigning the values for all parameters required to generate a DEM, the epipolar DEMs were extracted for the above mentioned four sets of GCPs. The matching pixel positions extracted from the two epipolar images were used to calculate the 3D coordinate positions of the pixels by using the computed mathematical model. At this stage, the generated DEMs were not the final DEMs and they are called epipolar DEMs because they are neither georeferenced nor free from errors (Figure 5.6).

The information report of the epipolar DEM generation processes and the elevation RMS errors related to the GCPs and the CPs for all sets are given in Appendix F.

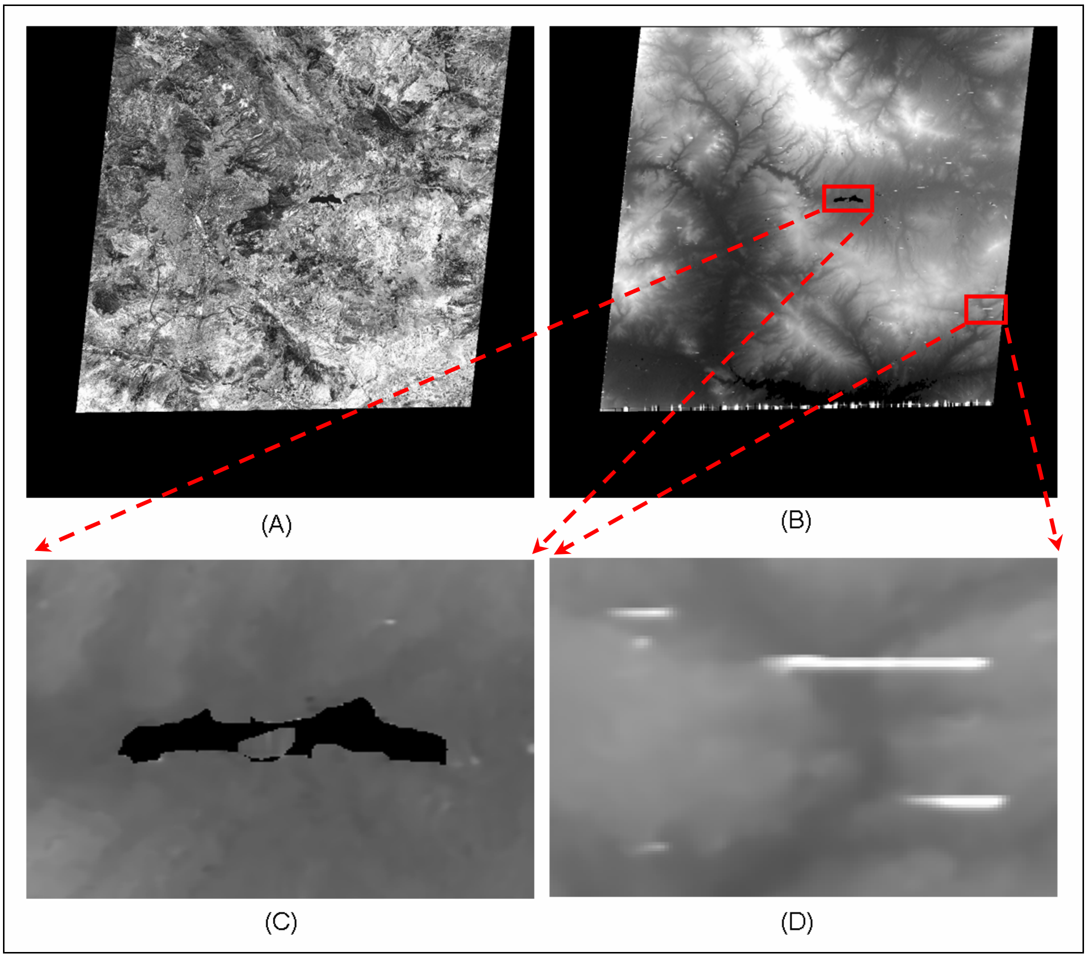

Figure 5.6 (A) The epipolar image of the nadir image of ASTER, (B) the stereo extracted epipolar DEM using GCP set 2, (C) image matching failure over Lake Mogan, and (D) multiple blunders occurred during image matching.

5.2.4 Post-processing and Geocoding the Generated DEM

Next, a post-processing operation was applied on the generated epipolar DEMs in order to remove the errors introduced during DEM generation (Figure 5.6 C-D). The main reason for applying a post-processing operation was to smooth out the failure areas and blunders existing in the epipolar DEMs. The Orthoengine module provides the specialized manually editing features that include the creation of masks and replacing the elevation values under these masks with the user-defined or average values. It also provides powerful filtering and interpolation features and specific tool strategies for common errors encountered during the DEM generation. These tools equalize the pixel values over lakes, compensate for forests and urban areas, neutralize for cloud-covered areas and deals with noise.

As mentioned earlier, the failure and background values were assigned "-100" and "-150" prior to the DEM generation. However, it was observed that several failure areas on the generated epipolar DEMs contained the value of "-150". Initially, a correction procedure was applied to the generated epipolar DEMs to assign all failure areas to "-100" and the background value to "-150". This operation was accomplished at these steps: First, a unique value "-200" was assigned as the new background value. Then, all other "-100" and "-150" values were automatically selected and "-100" was assigned. Finally, the correct background value "-150" were reassigned to the pixels which have "-200" values. After finishing these steps, all failure and background values were assigned "-100" and "-150" correctly.

Later, the failure areas were examined by switching back and forth between the image channel and the epipolar DEM. Several scattered failure areas were observed over Lake Mogan (Figure 5.6-C) and small water bodies. Therefore, the lake correction was performed. The failure area over the Lake Mogan was masked. The masked region was extended on the border by one pixel using the “erode holes” command in order to be sure that all failure values are included within the masked area. Then, for all DEM pixels within the masked area, the elevation value of 973 m, which was taken from the vector data, was assigned as the new elevation value. Later, the blunders were visually located, masked and an elevation of “-100” was assigned to them. The visual inspection and editing step was the most tedious and time consuming step because the blunders were randomly distributed all around the DEM with varying sizes (Figure 5.6-D). Subsequently, all failure areas were masked and their regions were increased by one pixel. The failed values were then replaced with the values calculated from the valid pixels surrounding the failed pixels using the “interpolate” command. This command uses an estimate weighted distance calculated from the neighboring valid pixels of the failed pixels and only applicable for small areas containing less than 200 pixels (Orthoengine user guide, 2003). Finally, the noise removal strategy suggested by the Orthoengine user guide manual was applied on the epipolar DEMs. Two filters were used by the Noise removal algorithm to identify the failed pixel values (Orthoengine user guide, 2003). The first filter calculates the average and the variance of the eight elevation values immediately surrounding each pixel, excluding the failed and background pixels. If the center pixel is more than two standard deviations away from the average, it is replaced with the average value. The second filter counts the number of failed values immediately surrounding the pixel being analyzed. If five or more failed pixels border the center pixel, then the center pixel is set to a failed value.

After detecting the failed pixels by the noise removal algorithm, they were interpolated from the surrounding valid pixels. Finally, a Gaussian smoothing filter, which calculates the weighted sum of all pixels in a three by three kernel and assigns the value to the center pixel in the kernel, was applied to the epipolar DEMs for twice.

After performing the post-processing operation, the epipolar DEMs were purified from the failure areas and blunders. Next the epipolar DEMs were geocoded in a projection system. In order to that the “geocode extracted epipolar DEM” menu was used. Now, the post-processed epipolar DEMs were selected as the input DEMs. The output pixel size remained as 30 m and the DEMs were geocoded to Universal Transverse Mercator (UTM) zone 36 and row S on WGS 84 ellipsoid. Next, the accuracies of the generated DEMs were determined.

5.2.5 Evaluation of the DEMs

In order to assess the accuracies of the generated DEMs, a bitmap which covers the region of the reference DEM, was generated by using the Focus Module. Later, this bitmap was used to mask out the region for which reference data were not available for the generated DEMs. After performing the masking operation, the DEMs were ready for performing various accuracy analyses. The elevation differences between the generated DEMs and the reference DEM can be computed in several ways. The first one is to export both the generated and the reference DEM elevations in a text file and than calculate the differences between the two by using a commercial software such as SPSS or Microsoft EXCEL. But, handling of approximately 2.2 million elevation points would be quite hard for such software. In addition, this method would be time consuming and may not be useful. In the present case the accuracy assessment was carried out using the “IMAGESUB” command of the Focus Module. This command automatically calculates the differences between the two input DEMs and produces a resulting difference DEM. Next, the standard deviation (bias) of the elevation difference values were automatically computed from the difference DEM values within using Focus module. The comparison between the reference DEM and the generated DEMs were performed twice. First, the reference DEM was compared with the DEMs which are not post-processed (not-edited DEM). The second comparison was carried out after the DEMs were post-processed (edited DEM). The comparison of the two different results gave an opportunity to assess the importance of the post-processing operation. The histograms of the differences between the DEMs and the results of the comparison are given in Appendix G.

In order to assess the accuracies of the generated DEMs based on the slopes, the reference digital slope map was produced from the reference DEM. The digital slope map was generated automatically by using the “SLP” command of the Focus Module. This command calculates the slopes using a plane formed by the vector connecting the left and right neighbours and the vector connecting the upper and lower neighbours of a pixel (Orthoengine user guide, 2003). Finally, masks were generated from the digital slope map for every 10 degree interval by using the “THR” command of the Focus Module and these masks were used to evaluate the accuracies of the generated DEMs based on the slopes.

To compute the accuracies based on land cover types, the raw image had to be orthorectified and visually classified. Therefore, the Nadir image was orthorectified using the Orthoengine module and the best GCP configuration of set 2. The nadir image was preferred due to its strong image geometry relative to the backward image. For performing the orthorectification the generated DEM with GCP set 2 was used as the source DEM. Because the pixel size of the generated DEM was 30 m, the output pixel size of the orthophotos was also set to 30 m. The projection information of the output orthorectified images were defined as UTM zone 36 and row S on WGS 84 ellipsoid, which is identical to the projection information of the DEMs generated. Next, the area covered by the reference DEM was visually classified from the orthorectified image into five main land cover types (water, urban, forest, mountainous and others) using the Focus Module. Then for each class, the previously generated bitmaps for each class were used to assess the accuracies of the DEMs based on land cover types.

5.3 The Assessment of the ASTER DEMs

5.3.1 The Results of the Least Squares Bundle Adjustment

As mentioned in the previous part, DEMs were generated using four different sets of GCPs that are 8, 16, 24, and 32. For each set, the remaining points out of 77 GCPs were used as CPs for each set. Table 5.6 summarizes the results of the RMSE for each set of control and check points.

Table 5.6 The Results of the least squares adjustment for the four sets of GCPs.

Results of LSA	GCPs / CPs	RMS Error (m)			
		X	Y	XY	Z
Set 1	8	4.50	5.25	6.90	14.70
	67	10.35	6.30	12.15	6.40
Set 2	16	9.00	6.00	10.80	11.80
	61	10.35	6.30	12.15	5.90
Set 3	24	9.60	6.15	11.40	14.20
	53	9.45	6.60	11.55	8.40
Set 4	32	9.90	5.55	11.40	11.90
	45	9.15	6.75	11.40	7.40

The results given in the Table 5.6 were computed by taking the average of the nadir and backward RMSE values. The individual RMS errors of the nadir and the backward images are given in Appendix H. As can be seen in Table 5.6, for all sets, the GCP RMSE values were found to be less than 1 pixel in both planimetry and elevation. Surprisingly, the best total planimetric accuracy was obtained as ± 6.90 m (0.46 pixels) with 8 GCPs. On the other hand, the RMS error increased to 10.80 m (0.72 pixels) for 16 GCPs and became stable for 24 GCPs and 32 GCPs as 11.40 m (0.76 pixels). If we look at the trends individually for X and Y directions, similar to the total error results, the best accuracy was achieved using set 1 both in X and Y direction. However, one important point is that a systematic increase in X direction can be easily observed for sets 2, 3 and 4 with respect to set 1. The Y direction RMS errors demonstrate small differences between each other with a narrow range of 5.25 m (0.35 pixels) to 6.15 m (0.41 pixels). The 5 m RMSE difference between set 1 and the other sets might have been caused by the less number of GCPs used in the first set. Besides, no logical explanation could be made about the remarkably high planimetric accuracy of the set 1. The total RMS error values for the GCPs and CPs are illustrated in Figure 5.7.

Despite the extreme accuracy achieved for the GCPs with less than half a pixel size using set 1, the results proved that the RMSE of CPs for set 1 are not affected from that high accuracy. Furthermore, all sets demonstrate good coherency and consistency in planimetric accuracy for the CPs. The RMSE values for sets 1 and 2 are the same and equal to 12.15 m (0.81 pixels). The RMSE values for CPs decreased to 11.55 m (0.77 pixels) for set 3 and 11.40 m (0.76 pixels) for set 4. Therefore, the best planimetric accuracy for CPs was provided by the set 4.

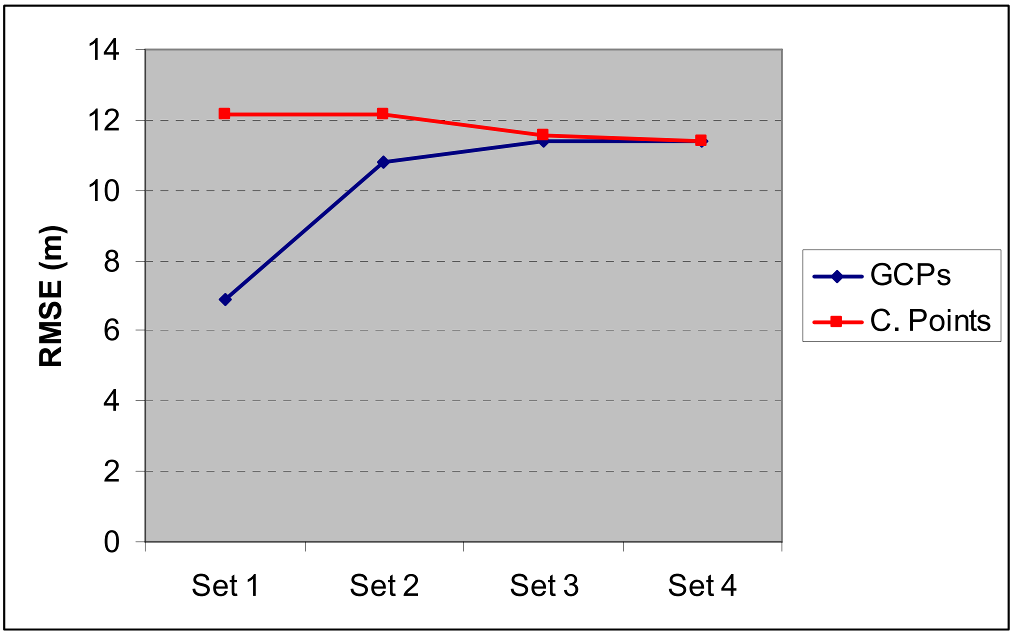

Figure 5.7 The planimetric total RMS error values for the GCPs and CPs for all sets

The assessment of the elevations of the points, for all sets, is also important as the elevation RMS errors may give initial signs of the overall DEM accuracy. The best elevation RMSE for both GCPs and CPs was computed for set 2 as 11.80 m (0.79 pixels) and 5.90 m (0.39 pixels), respectively. An irregular trend of the accuracy was observed for both GCPs and CPs in the elevation accuracy. This irregular trend is illustrated graphically in Figure 5.8. Unfortunately, no logical explanation can be made about this trend for the elevation accuracy of the GCPs.

The GCP elevation accuracy for sets 2 and 4, and sets 1 and 3 show similar results. However, for all sets, the elevation RMS error values for the CPs were relatively better than the elevation RMS error values of the GCPs. The RMS errors were approximately half a pixel size and varied between 5.90 m (0.39 pixels) and 8.90 m (0.59 pixels). One point to note is that, for all sets, the RMSE values for GCPs and CPs were found to be less than one pixel size in both planimetry and elevation.

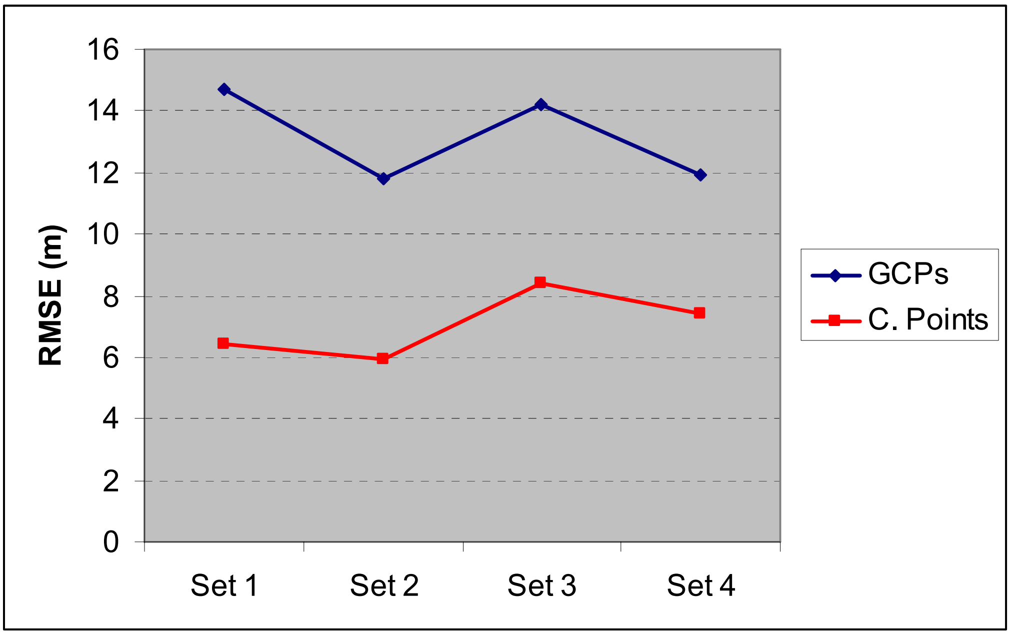

Figure 5.8 The elevation RMS error values for the GCPs and check points for all sets

In addition to the assessment of the RMSE values, the maximum errors of the least squares adjustment were also evaluated. The assessment of the maximum errors give indications of the stability of the model used for the least squares adjustment (Toutin, 2004). For four sets, the results of the maximum errors computed for the GCPs and CPs are given in Table 5.7.

As can be seen in Table 5.7, the maximum errors refer to the GCPs with the highest total error. Similar to the planimetric RMSE results, for GCPs the best maximum planimetric error was computed for set 1. However, this good result was not significant because the maximum error for CPs was around two pixels. It is obvious that, for all sets, the total planimetric errors were highly affected from the errors in X direction as when compared with Y direction; the errors in X direction are remarkably high. It is also clear that all planimetric errors were better than the size of two pixels. For elevation the maximum error values were better for sets 1 and 2 than the

Table 5.7 The maximum errors computed for all sets.

Results of LSA	GCPs / CPs	Maximum Error (m)			
		X	Y	XY	Z
Set 1	8	8.55	-3.60	9.30	32.50
	67	-27.45	-6.75	28.35	17.50
Set 2	16	-25.50	4.35	25.95	31.90
	61	-26.55	4.35	27.00	18.60
Set 3	24	-27.00	0.75	27.00	43.20
	53	-25.20	9.90	27.00	21.50
Set 4	32	-28.80	-1.05	28.95	42.00
	45	-26.55	8.70	28.05	20.80

sets 3 and 4. Unfortunately, the reason for this nearly 10 m elevation difference between the sets cannot be explained.

5.3.2 The Assessment of the DEMs

The results of the initial DEM evaluation were obtained from the CPs. The best accuracy of 5.9 m (0.39 pixels) was computed using set 2. The summary of the results for each set is given in Table 5.6. In fact, the final accuracy obtained from the 61 CPs was excellent and was close to one third of a pixel size of the ASTER imagery. However, because this accuracy was obtained using only 61 points, it might not reflect the overall DEM accuracy.

To assess the accuracies of the DEMs, first, the DEMs generated for all sets were evaluated without applying any post-processing operation except for the corrections applied over water bodies. The results obtained from the statistical evaluations are given in Table 5.8. The accuracy assessment was performed by comparing the reference DEM with each of the stereo extracted DEMs using 2,171,664 points.

Table 5.8 The results of the DEMs generated without post-processing.

Set ID	Before Post-processing (m)		
	Bias	Min. Error	Max. Error
1	17.10	-327.63	1069.85
2	17.76	-375.00	1066.96
3	18.28	-343.51	1041.33
4	18.09	-348.66	1011.26

The accuracies for the generated DEMs were 17.10 m for set 1, 17.76 m for set 2, 18.28 m for set 3 and 18.09 m for set 4. It is clear that, the computed accuracies for approximately 2.2 million points were 2 or 3 times higher than the accuracies computed for the CPs. This confirms that, the computed accuracies using CPs are almost trivial and do not reflect the actual DEM accuracy. It is also important to evaluate the minimum and maximum errors of the generated DEMs. The minimum errors around -350 m and the maximum errors around 1050 m of the generated DEMs demonstrate that the DEMs contain serious local errors. These errors might be occurred from the incorrectly computed matching points during image matching process. Further investigation was carried out to find the total number and the locations of these blunders. In this study, the elevation points which lie outside the region of -3σ and +3σ were defined as blunders. The results of the investigation for each DEM generated are given in Table 5.9.

Table 5.9 The total number of the blunders detected in the generated DEMs

Set ID	Before Post-processing (m)			Total Number	Percentage (‰)
	Bias	Min. Bound	Max. Bound		
1	17.10	-51.3	51.3	13.788	6.35
2	17.76	-53.28	53.28	13.190	6.07
3	18.28	-54.84	54.84	10.788	4.97
4	18.09	-54.27	54.27	11.242	5.18

As can be seen in Table 5.9, for each set, more than 10.000 points fell outside the -3σ and +3σ range. Actually, the percentage of the blunders occurred in the DEMs were less than %1 of all the points. However, these blunders must be located and removed before performing any kind of subsequent process. After the visual investigation of the locations of the blunders, it was observed that the blunders mostly occurred in the mountainous areas. However, it was also observed that even in the flat areas some localized blunders were present. Two of the common blunders are illustrated in Figure 5.9.

Next, the DEMs were post-processed using both the manual and the automatic methods provided by the Orthoengine module of PCI Geomatica. The results obtained from the statistical evaluations are given in Table 5.10.

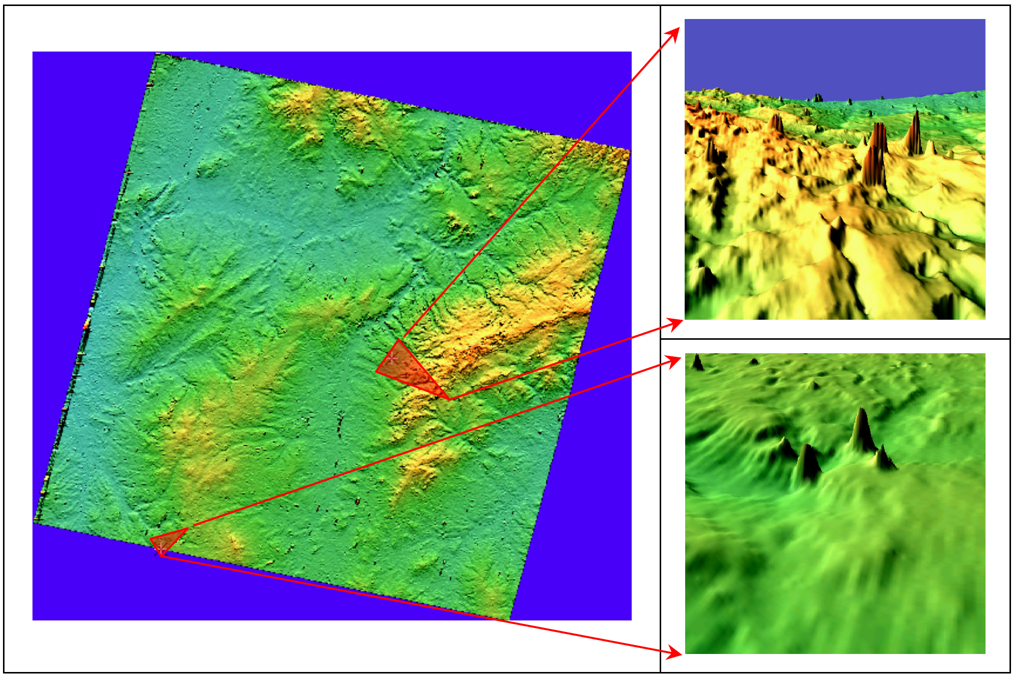

Figure 5.9 The blunders occurred after generating the DEM.

Table 5.10 The results of the DEMs generated after post-processing.

Set ID	After Post-processing(m)		
	Bias	Min. Error	Max. Error
1	11.13	-122.27	166.05
2	10.93	-112.91	158.25
3	12.36	-141.40	156.03
4	12.09	-124.41	160.74

As can be seen in Table 5.10, the accuracies after the post-processing were 11.13 m, 10.93 m, 12.36 m and 12.09 m for set 1, set 2, set 3 and set 4, respectively. Despite the accuracy achieved using CPs did not reflect the overall DEM accuracy; the trend found using CPs may reflect the trend of the final accuracy of the output DEMs. The minimum and maximum errors ensure that considerable number of the erroneous elevation values was removed through post-processing. The resulting scenes after the post-processing stage for the blunders removal are illustrated in Figure 5.10.

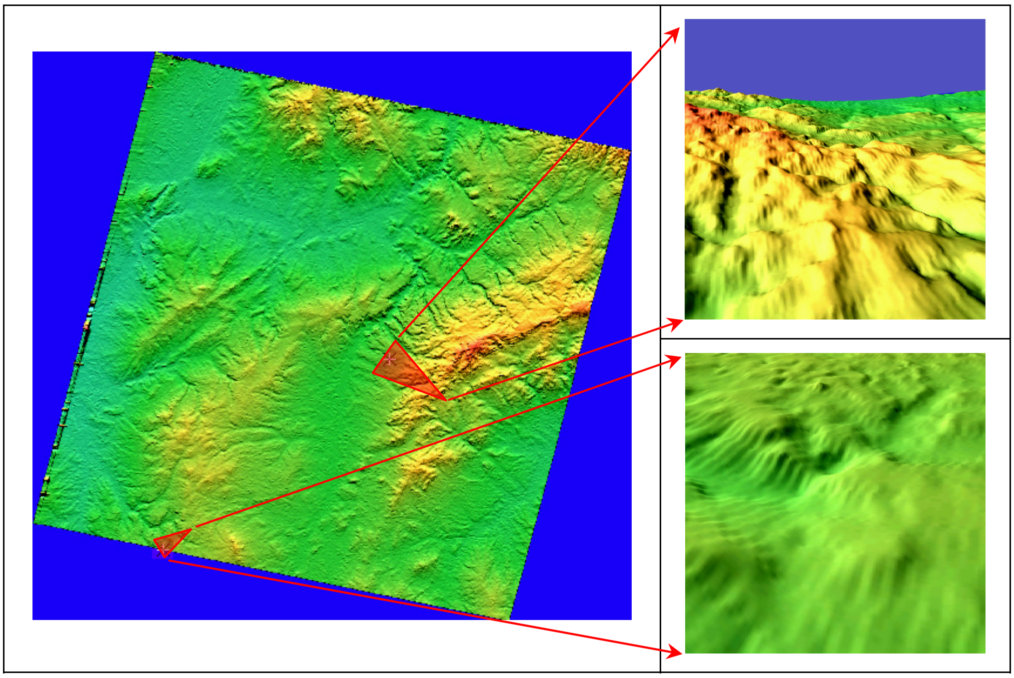

Figure 5.10 The resulting scenes after applying post-processing.

For each set the total increase in the accuracy after post-processing is demonstrated in Table 5.11. After applying the post-processing, about 35% increase was achieved in the accuracy for all sets. The highest increase was observed for set 2 with 6.83 m. The increase in the accuracy after applying the post-processing indicates the importance of the post-processing operation stage.

Table 5.11 The results of the DEMs generated using four GCP sets.

Set ID	**Before Post-processing (m)**	**After Post-processing (m)**	**Decrease the error (%)**
Set 1	17.10	11.13	34.9
Set 2	17.76	10.93	38.5
Set 3	18.28	12.36	32.4
Set 4	18.09	12.09	33.2

The results of the differences in the accuracy of the DEMs before and after post-processing are given in Table 5.12. When the number of elevation points was counted before post-processing, it was observed that only 36.59% of the points fell within the region of -5 m and 5 m. After applying the post-processing, a small amount of increase was achieved and 37% of the points were in the region when compared to the reference DEM. In general, for all cases, (within 5, 10, 15 and 20 m) only 1% increases in the accuracy was achieved. These small amounts of increases prove that the post-processing stage generally removed the blunders in the DEMs. However, it did not have a remarkable affect on the accuracy of the points which were within the acceptable limits.

Table 5.12 Differences between the reference DEM and the DEM generated using set 2

DEM	Number of Points	Percentage (%)			
		Within 5 m	**Within 10 m**	**Within 15 m**	**Within 20 m**
Before Post-processing	2,171,664	36.59	66.20	82.80	90.54
After Post-processing		37.00	67.16	83.91	91.55

Further analysis was performed for the most accurate DEM generated using 16 GCPs. The analysis performed was based on the comparisons of the profiles between the DEM generated and the reference DEM. The profiles are generated in horizontal, vertical and diagonal directions on the generated and the reference DEMs. The profiles used for each direction are given in Figure 5.11.

The results of the profile comparison are given in Figure 5.12. As can be seen in the figure, at lower elevations, transects that were taken from the generated DEM match with those taken from the reference DEM. On the

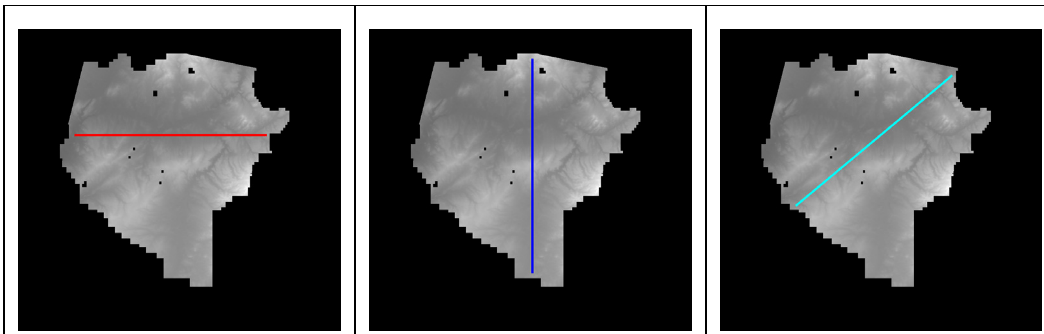

(a) (b) (b)

Figure 5.11 The (a) horizontal, (b) vertical and (c) diagonal transects that were taken for the profile comparison between the generated DEM and the reference DEM.

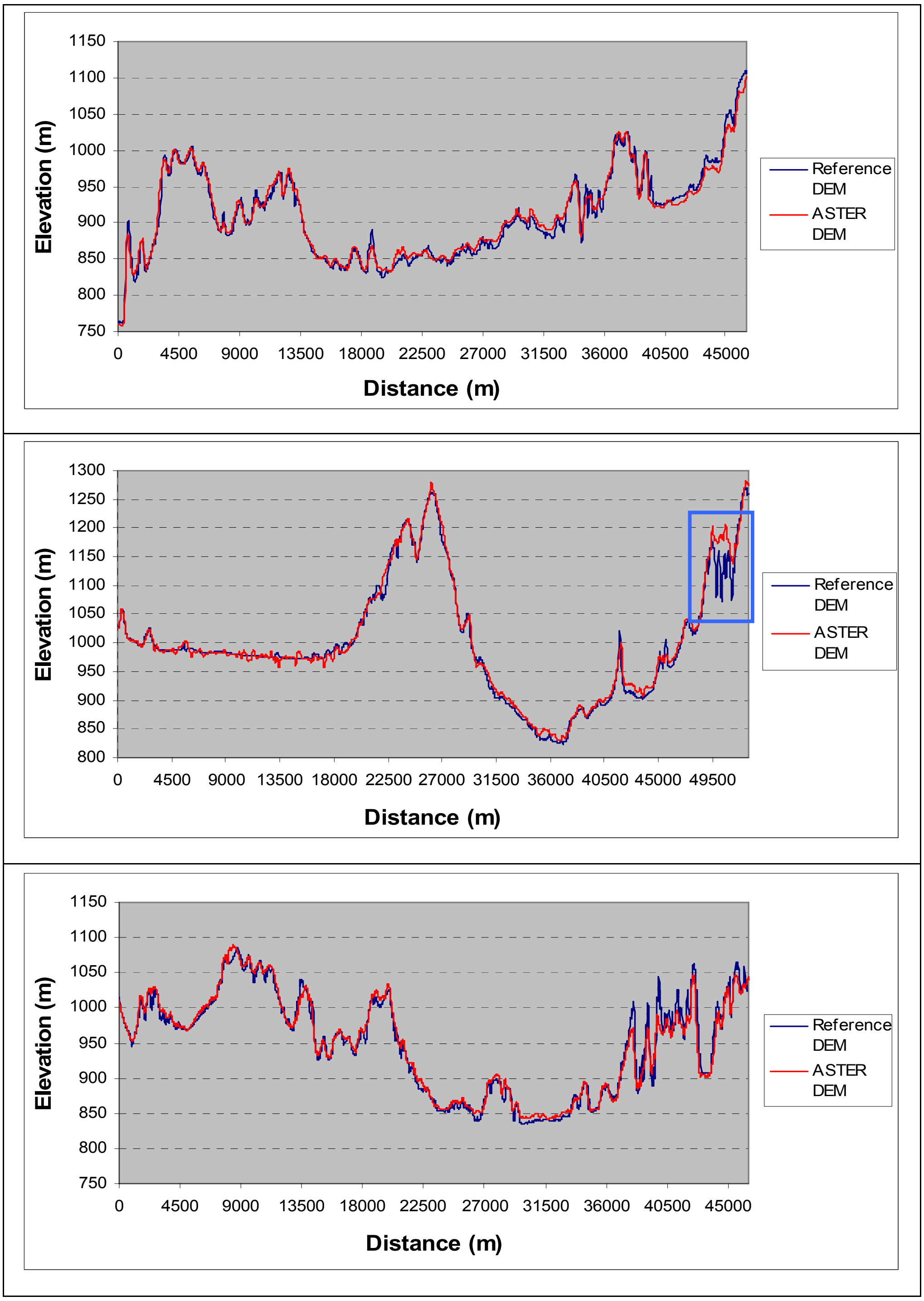

Figure 5.12 The comparisons of the profiles of the generated ASTER DEM and the reference DEM. The first figure represents the horizontal profile, the middle figure represents the vertical profile, and the third figure represents the diagonal profile.

other hand, at higher elevations the deviations from the reference DEM increased. Those results also confirm the usefulness of the post-processing operations because most of the blunders that were found in mountainous areas were removed through post-processing.

The blue rectangle in the middle of Figure 5.12 demonstrates that still blunders exist in the generated DEMs after applying the post-processing operation. Even though the exhausting efforts were spent for the post-processing operation, the middle figure confirms that the blunders were not removed entirely. The similar statement was also made by Hirano et. al. (2003).

As mentioned in the previous chapter, further evaluation of the generated DEMs was carried out based on the slopes. To do that, the slope map of the reference DEM was generated and overlaid with the generated ASTER DEM. Table 5.13 represents the elevation accuracies based on the selected slope intervals.

First of all, it was apparent that most of the DEM pixels within the reference data had slopes less than 10º. Furthermore, less than 1% of the pixels had the slopes higher than 40º. As expected, the best accuracy (8.24 m) was found for the flat areas where the slope ranged between 0º and 10º. Without performing any kind of correlation tests, figure shows that the accuracies are almost linearly correlated with the slopes. The degree of the correlation between the accuracies and the slopes was computed using the Pearson’s correlation test as 0.99. This glaring result makes certain that the computed final accuracies of the points depend on the

Table 5.13 The accuracies of the DEM based on the selected terrain slope intervals.

Slope Interval	Pixels (%)	Bias (m)
0-10	72.309	8.24
11-20	20.694	13.98
21-30	5.339	19.56
31-40	1.574	24.19
41-50	0.078	29.32
51-60	0.005	32.85
61-70	0.001	39.26

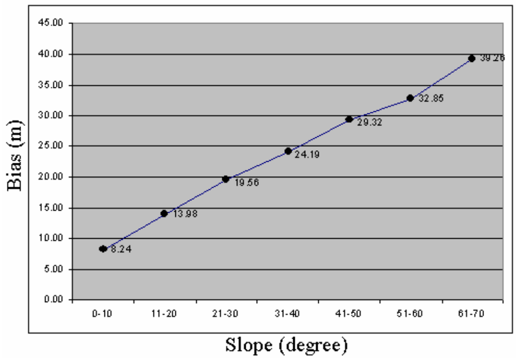

degrees of slope on the terrain. The results of the slope analysis were also coherent with a previous study conducted by Toutin (2002).

The last assessment performed was based on the land cover types. To perform this assessment, the ASTER image within the region of the reference DEM was classified into five main classes namely water, urban, forest, mountainous, and the other classes through visual interpretation (Figure 5.13). Then, for each class, the accuracy assessment was carried out.

The resulting accuracies were found to be 5.01 m, 8.03 m, 12.69 m, 17.14 m, and 10.21 m for water, urban, forest, mountainous, and other areas, respectively. As expected, the class water produced the highest accuracy because the elevations were given manually over water areas during post-processing. The worst results were obtained over the mountainous areas.

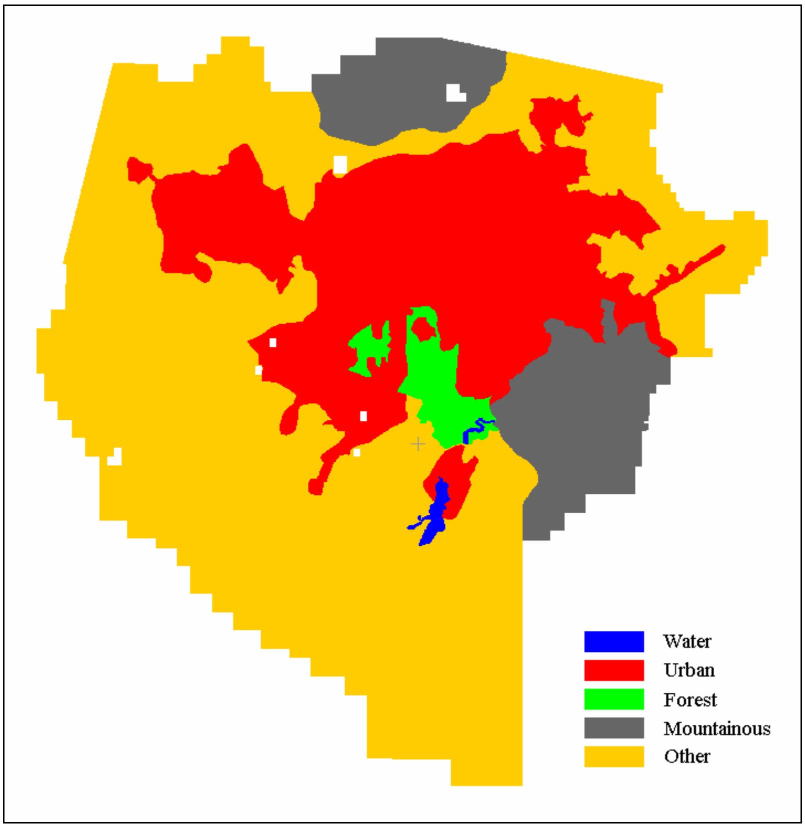

Figure 5.13 The visually classified ASTER imagery.

However, despite the fact that the mountainous areas act as the most problematic class, the accuracy was around one pixel size of the ASTER imagery. The classes urban and forest produced satisfactory results if it is considered that the generated elevation models using the satellite imagery were actually the Digital Surface Models (DSMs). In this respect, the accuracies of 8.03 m and 12.69 m accuracies for the classes urban and forest would be satisfactory to accept the results as pleasing outcomes, respectively. For the class others, the accuracy of 10.21 m preserve the final total accuracy of the generated DEMs. The relationship between the accuracies and five classes is illustrated in Figure 5.14.

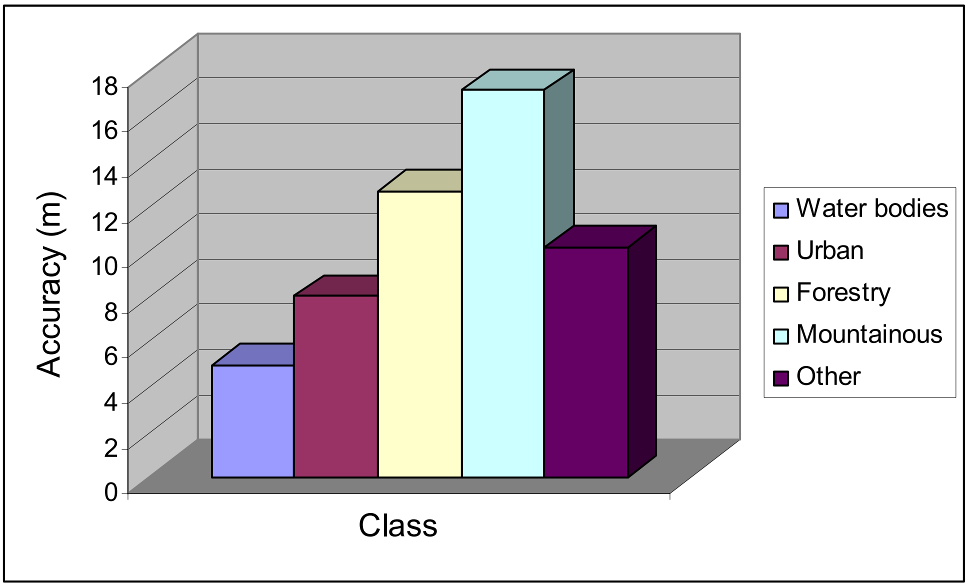

Figure 5.14 The relationship between the accuracies and five classes.

CHAPTER 6

ORTHORECTIFICATION OF ASTER IMAGERY

In this chapter, The processing steps of the orthorectification performed in the study using the MATLAB software are provided first. Then, the results for orthorectification of the ASTER image using twelve different models are provided.

6.1 The Orthorectification of ASTER Data

The orthorectification process of ASTER data includes the following main steps (Gacemer, 2002):

- Locating the GCPs collected through various sources such as orthophotos, GPS etc. on the image,
- Selecting a DEM file which covers the area of the image and contains the elevation values for each pixel on the image,
- Producing the mathematical model and calculating the unknowns of the mathematical model with the aid of the collected GCPs on the image, and
- Calculating the residual errors of the GCPs and CPs based on the calculated mathematical model to assess the quality of the generated orthorectified image.

In the present case, the orthorectification was performed using 12 different mathematical models. These models are:

1. Toutin’s model
2. Orun and Natarajan model
3. First order 2D polynomial model
4. Second order 2D polynomial model
5. Third order 2D polynomial model
6. First order rational function model
7. Second order rational function model
8. Third order rational function model
9. First order polynomial functions with relief
10. Second order polynomial functions with relief
11. Direct Linear Transformation
12. Projective Transformation

The DEM used in the orthorectification process was the most accurate DEM generated from the stereo images. The nadir ASTER image was selected to be orthorectified for all models.

Among the 12 models, the *Toutin’s model* was the only one implemented using the Orthoengine module of PCI Geomatica. This model was developed by Dr. Toutin and licensed to the software through Canada Center for Remote Sensing (CCRS). It is based on the principals of the complete viewing geometry and models all the distortions generated during image acquisition. The projection information of the GCPs and the output orthorectified images were selected as UTM zone 36 and row S on WGS 84 ellipsoid. Of the available 77 points, first, 40 were selected as the GCPs. The remaining 37 points were selected as CPs to be used for assessing the accuracy of the generated orthorectified images. The resampling of the orthorectified image digital numbers was carried out using the nearest neighbor technique. In order to find the effect of the number of GCPs on the accuracy of the orthorectification, the nadir image was rectified using 45, 50, 55, 60, 65, 70, and 77 GCPs.

The mathematical models for remaining 11 models were developed using Matlab 6.5.0 and applied on the nadir image. In Matlab environment, each of the above models was implemented using the macros. In general, a macro first reads the image data to be orthorectified and the related DEM data. Later, the GCP and the check point information were read from a text file. PCI Geomatica software was used to create the GCP and check point data text files. By means of the GCPs, the estimation of the unknown parameters of the model and calculation of the residual errors for each GCP and check point was performed. Next, the output file was created and the orthorectification was performed using the backward algorithm. The residuals for each GCP and check point were written in a new text file and error vector diagrams related to the GCPs and check points were written to new text files. Finally, the output orthorectified image was exported to a desired image file format. The macro also computes the variance-covariance matrix of the unknowns of the models and able to export the matrix to a text file. The general process is illustrated in Figure 6.1.

Obviously, some models may require additional information as input. For example, because *Orun and Natarajan model* is a rigorous model; initially, it requires internal orientation parameters, initial approximations of the exterior orientation parameters and some sensor parameters. Furthermore, unlike the simple geometric models, the model utilizes the collinearity equations, therefore it requires all input coordinates in a Cartesian coordinate system. A transformation to GCP coordinates (UTM) to a Local Cartesian coordinate system was also performed in the macro for *Orun and Natarajan model*. Definitions of the coordinate systems are given in Appendix I.

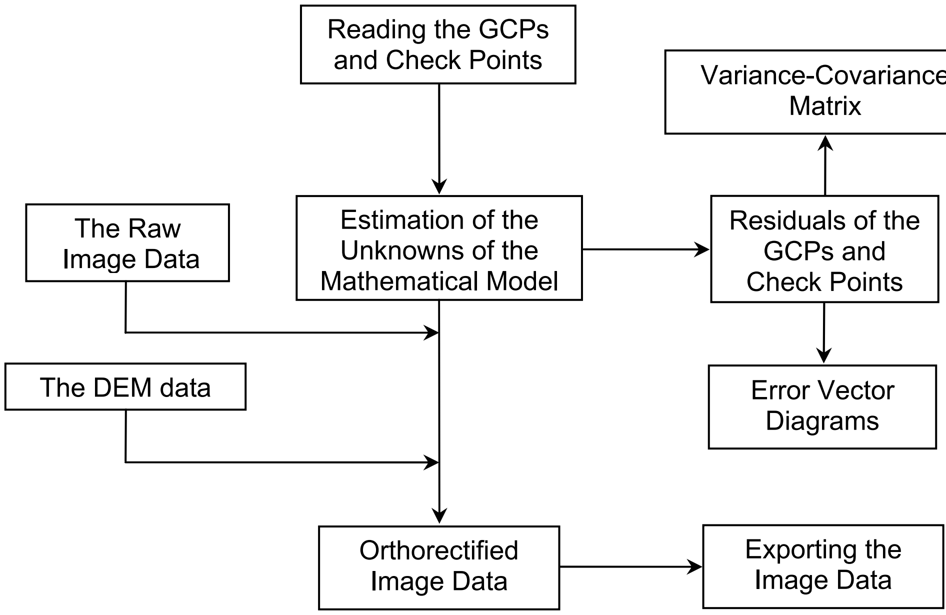

Figure 6.1 The general architecture of a macro written in Matlab.

Similarly, *Second and Third Order Rational Functions* require some additional input parameters such as h value increment. Because the *Second and Third Order Rational Functions* include some correlated parameters, they require regularization to the normal equations in the least squares adjustment solution (Tao and Hu, 2001). The Tikhonov regularization method is used in the macro and this method includes a parameter (h value) which is to be determined for the optimum solution for the second and third order of the model (Neumaier, 1998). Consequently, an increment value for this h parameter must be determined prior to the estimation of the model unknown parameters.

6.2 The Assessment of the Orthorectified ASTER Imagery

The models used for the orthorectification process include (1) *Toutin's model*, (2) *Orun and Natarajan model*, (3-5) *Polynomial Models* (first to third degree), (6-8) *Rational Functions* (first to third degree), (9-10)

Polynomial Functions with Relief (first and second degree), (11) *Direct Linear Transformation (DLT)*, and (12) *Projective Transformation*. Because the *Third Order Rational Functions* requires at least 39 GCPs, for all models, the minimum number of the GCP was set to 40 at the beginning. Later, the GCPs were incremented by five at each step until the number of the GCPs reach to 70. Finally, for all models the image was orthorectified using 77 GCPs. The RMS errors were computed using the following equations:

$$\mathrm{RMSE_X} = \sqrt{\frac{\sum_{i=1}^{N}(X_{comp} - X_{org})^2}{N-1}} \qquad \mathrm{RMSE_Y} = \sqrt{\frac{\sum_{i=1}^{N}(Y_{comp} - Y_{org})^2}{N-1}}$$

$$\mathrm{RMSE_{Total}} = \sqrt{\mathrm{RMSE_X^2} + \mathrm{RMSE_Y^2}}$$

where;

Xcomp, Ycomp = the computed coordinates,

Xorg, Yorg = the original coordinates of the GCPs,

N = the number of the GCPs

6.2.1 The Results of the Toutin's Model

The *Toutin's model* reflects the physical reality of the complete viewing geometry and integrates all the distortions generated during image acquisition. Therefore, the most accurate results are expected from this model. The results of the least squares bundle adjustment of the GCPs are given in Table 6.1.

Table 6.1 The results of the least squares adjustment of the GCPs for the *Toutin's model*.

Model	GCPs	GCPs		
		Residual X	**Residual Y**	**Overall**
Toutin's	40	0.75	0.31	**0.81**
	45	0.73	0.32	**0.80**
	50	0.72	0.34	**0.80**
	55	0.73	0.36	**0.81**
	60	0.72	0.35	**0.80**
	65	0.72	0.34	**0.80**
	70	0.70	0.34	**0.78**
	77	0.67	0.34	**0.75**

When using 40 GCPs, the *Toutin's model* produced 11.25 m (0.75 pixels) residual error in X, 4.65 m (0.31 pixels) residual error in Y and 12.15 m (0.81 pixels) overall accuracy. It is also clear that up to 70 GCPs, no improvement was observed in terms of the overall GCP accuracy. When 70 and 77 GCPs were used, a little increase was observed but neither of them reached the accuracy better than 11.25 m (0.75 pixels). Error vectors of the 77 GCPs for the *Toutin's model* are given in Appendix J. The remaining points out of 77 GCPs were used as CPs. The results for the CPs are given in Table 6.2.

Table 6.2 The results of the least squares adjustment of the CPs for the *Toutin's model*.

Model	C. Points	Check Points		
		Residual X	**Residual Y**	**Overall**
Toutin's	37	0.63	0.43	**0.76**
	32	0.61	0.42	**0.74**
	27	0.60	0.37	**0.70**
	22	0.52	0.33	**0.62**
	17	0.51	0.36	**0.62**
	12	0.38	0.39	**0.54**
	7	0.32	0.37	**0.49**

The accuracies of the CPs were observed at a range between 11.40 m (0.76 pixels) and 7.35 m (0.49 pixels). It is clear that the lower the number of CPs, the better the accuracy. It was surprising that when using 7 CPs the accuracy was around half a pixel and the corresponding accuracy for 70 GCPs was not better than 11.7 m (0.78 pixels). Thus, the accuracy that can be obtained using the *Toutin's model* was around 11.25 m (0.75 pixels) for the whole image. Figure 6.2 illustrates the accuracies of the GCPs and CPs in terms of the number of points.

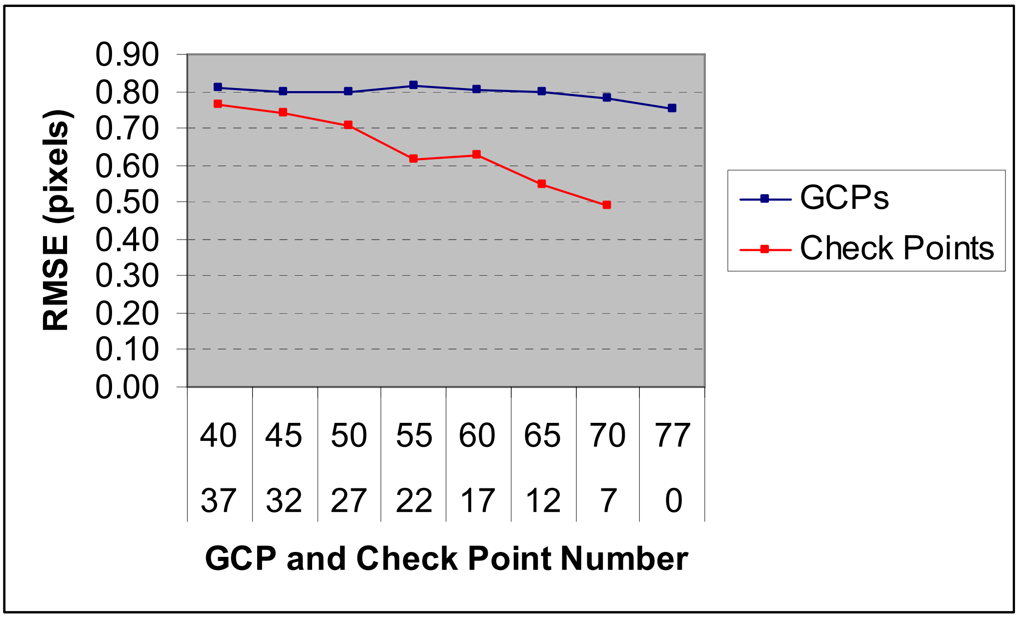

Figure 6.2 The accuracies of the GCPs and CPs for the *Toutin's model*.

6.2.2 The Results of the Orun and Natarajan Model

The second rigorous model tested was the *Orun and Natarajan model*. In this model, the phi and kappa elements were approximated as constants and the remaining parameters were estimated up to second order equations of time. Therefore, it was possible to solve the unknowns in a single least squares adjustment procedure. The model was tested using a

Local Cartesian coordinate system and the initial values of the exterior orientation parameters were taken from the ephemeris data of the ASTER image. For this model, results of the least squares bundle adjustment of the GCPs are given in Table 6.3.

Table 6.3 The results of the least squares adjustment of the GCPs for the *Orun and Natarajan model*.

Model	GCPs	GCPs		
		Residual X	**Residual Y**	**Overall**
ON's	40	0.73	0.34	**0.81**
	45	0.71	0.34	**0.79**
	50	0.70	0.36	**0.79**
	55	0.72	0.37	**0.81**
	60	0.71	0.36	**0.79**
	65	0.70	0.35	**0.79**
	70	0.69	0.36	**0.77**
	77	0.66	0.35	**0.75**

As can be seen in Table 6.3, when 40 GCPs were used the *Orun and Natarajan model* produced 12.15 m (0.81 pixels) accuracy. Similar to the results of the *Toutin's model*, up to 70 GCPs, no improvement was observed on the overall accuracy of the GCPs. When all points were used as GCPs, the overall accuracy reach to 11.25 m (0.75 pixels) which is identical to results of the *Toutin's model* at 77 GCPs. It is also evident that the error trend of the GCPs was similar to the trend in *Toutin's model*. Despite the fact that the *Toutin's model* integrates more corrections than the *Orun and Natarajan model* such as the lens distortion, internal orientation, atmospheric refraction etc., the results obtained using the *Orun and Natarajan model* was nearly identical to the results of the *Toutin's model*. Error vectors of the 77 GCPs for the model *Orun and Natarajan* are given in Appendix J.

The results of the CPs obtained using the *Orun and Natarajan model* are given in Table 6.4. The results obtained from the CPs indicates a consistency in itself and shows a trend of decrease starting from 11.25 m (0.75 pixels) with 37 GCPs to 8.25 m (0.55 pixels) with 7 GCPs.

Table 6.4 The Results of the least squares adjustment of the CPs for the *Orun and Natarajan model*.

Model	C. Points	Check Points		
		Residual X	Residual Y	Overall
ON's	37	0.64	0.40	**0.75**
	32	0.65	0.39	**0.76**
	27	0.63	0.37	**0.73**
	22	0.53	0.34	**0.63**
	17	0.51	0.36	**0.63**
	12	0.39	0.38	**0.55**
	7	0.37	0.38	**0.53**

It is clear that the orthorectification accuracy of the *Orun and Natarajan model* did not produce accuracy better than 11.25 m (0.75 pixels). Figure 6.3 illustrates the accuracies for the GCPs and CPs in terms of the number of points.

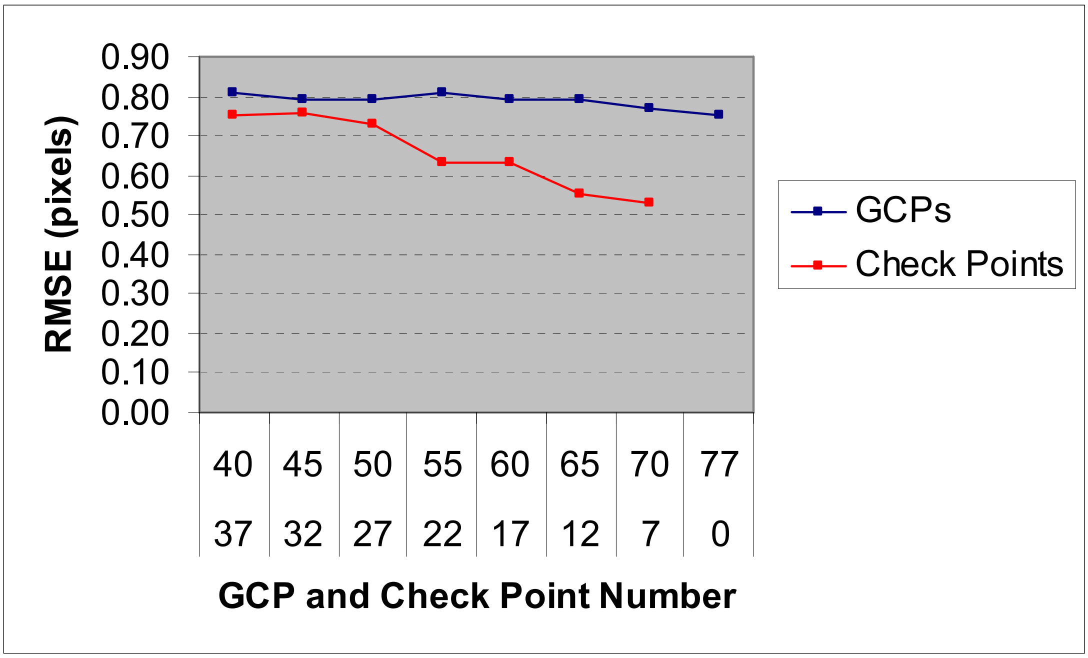

Figure 6.3 The accuracies of the GCPs and CPs accuracies for the *Orun and Natarajan model*.

6.2.3 The Results of the 2D Polynomial Functions

As mentioned in the previous chapter, *First, Second and Third Order 2D Polynomial Functions* were tested. When testing the *Third Order 2D Polynomial Function* it was found that matrix B in the least squares adjustment was ill-conditioned and therefore, matrix B^TB in normal equations became singular. To find the cause of the singularity, the variance-covariance matrix of the *Second Order 2D Polynomial Function* was generated. The variance-covariance matrix of the *Second Order 2D Polynomial Function* is given in Table 6.5. It is obvious that, in the *Second Order 2D Polynomial Function* the parameters a_0 and a_4 and the parameters b_0 and b_4 were highly correlated. It was found that, this high correlation was the cause of the problem encountered when solving the *Third Order 2D Polynomial Function*.

Table 6.5 The Variance - Covariance matrix of the unknowns for the *Second Order Polynomial model*

Parameters	**a_0**	**a_1**	**a_2**	**a_3**	**a_4**	**a_5**	**b_0**	**b_1**	**b_2**	**b_3**	**b_4**	**b_5**	
a_0	1	-0.079	-0.998	0.163	0.993	0.036	0	0	0	0	0	0	**1**
a_1	-0.079	1	0.023	0.239	0.035	-0.975	0	0	0	0	0	0	**X**
a_2	-0.998	0.023	1	-0.177	-0.998	0.018	0	0	0	0	0	0	**Y**
a_3	0.163	0.239	-0.177	1	0.203	-0.446	0	0	0	0	0	0	**X^2**
a_4	0.993	0.035	-0.998	0.203	1	-0.078	0	0	0	0	0	0	**Y^2**
a_5	0.036	-0.975	0.018	-0.446	-0.078	1	0	0	0	0	0	0	**X*Y**
b_0	0	0	0	0	0	0	1	-0.079	-0.998	0.163	0.993	0.036	**1**
b_1	0	0	0	0	0	0	-0.079	1	0.023	0.239	0.035	-0.975	**X**
b_2	0	0	0	0	0	0	-0.998	0.023	1	-0.177	-0.998	0.018	**Y**
b_3	0	0	0	0	0	0	0.163	0.239	-0.177	1	0.203	-0.446	**X^2**
b_4	0	0	0	0	0	0	0.993	0.035	-0.998	0.203	1	-0.078	**Y^2**
b_5	0	0	0	0	0	0	0.036	-0.975	0.018	-0.446	-0.078	1	**X*Y**
	1	**X**	**Y**	**X^2**	**Y^2**	**X*Y**	**1**	**X**	**Y**	**X^2**	**Y^2**	**X*Y**	**Coefficients**

In order to solve the problem, the term Y^2 of the *Third Order 2D Polynomial Function* was eliminated. Later, the *Third Order 2D Polynomial Function* was solved. The accuracies of the GCPs for the *First, Second and Third Order 2D Polynomial Functions* are given in Table 6.6. As expected, the worst accuracy was achieved using the *2D Affine Function* with the RMSE values higher than 2 pixels for all GCP combinations. On the other hand, the best accuracies were obtained for the *Second and Third Order 2D Polynomial Functions* as 17.25 m (1.15 pixels) and 14.85 m (0.99 pixels), respectively when 77 GCPs were used. These results ensure that the higher the order of the function, the better the fit to the GCPs. Error vectors of the 77 GCPs for the 2D Polynomial Models are given in Appendix J.

Table 6.6 The accuracies of the GCPs for the *First, Second, and Third Order 2D Polynomial Functions*.

GCPs	2D Polynomial Model		
	1st Order	2nd Order	3rd Order
40	2.75	1.23	0.99
45	2.73	1.24	1.03
50	2.65	1.21	1.04
55	2.63	1.20	1.04
60	2.56	1.20	1.04
65	2.53	1.20	1.04
70	2.48	1.17	1.01
77	2.41	1.15	0.99

However, to make a clear decision about the best 2D function in terms of the accuracy, the accuracies obtained for the CPs must also be evaluated. The accuracies obtained for the CPs are given in Table 6.7.

Table 6.7 The accuracies of the CPs for the *First, Second, and Third Order 2D Polynomial Functions*.

CPs	**2D Polynomial Model**		
	1st Order	**2nd Order**	**3rd Order**
37	2.17	1.14	1.11
32	2.03	1.06	0.97
27	2.02	1.08	0.96
22	1.87	1.06	0.90
17	1.91	1.02	0.85
12	1.74	0.92	0.74
7	1.74	1.00	0.81

As can be seen in Table 6.7, the results for the CPs were similar to the results obtained using the GCPs. The RMSE value for the first order was around two pixels while for the second order it was around one pixel. On the other hand, it was observed that the third order provided an accuracy less than one pixel except for using the 37 CPs. Based on the results obtained from GCPs and CPs, it is obvious that the most accurate 2D polynomial function for this site was the *Third Order 2D Polynomial model* with an accuracy of 0.99 when all points were used. The error trend for the GCPs and CPs versus the number of GCPs and CPs is given in Figure 6.4 and Figure 6.5, respectively.

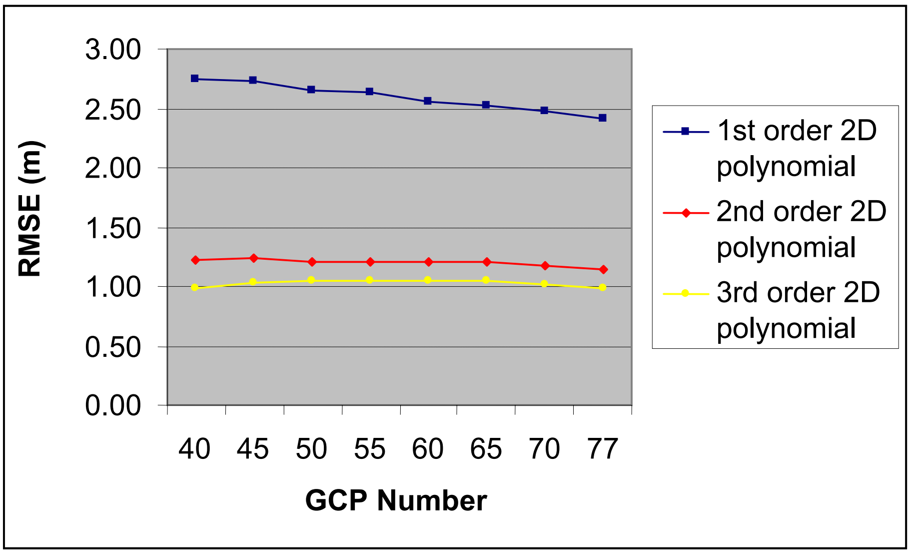

Figure 6.4 The accuracies of the GCPs for the 2D polynomial functions.

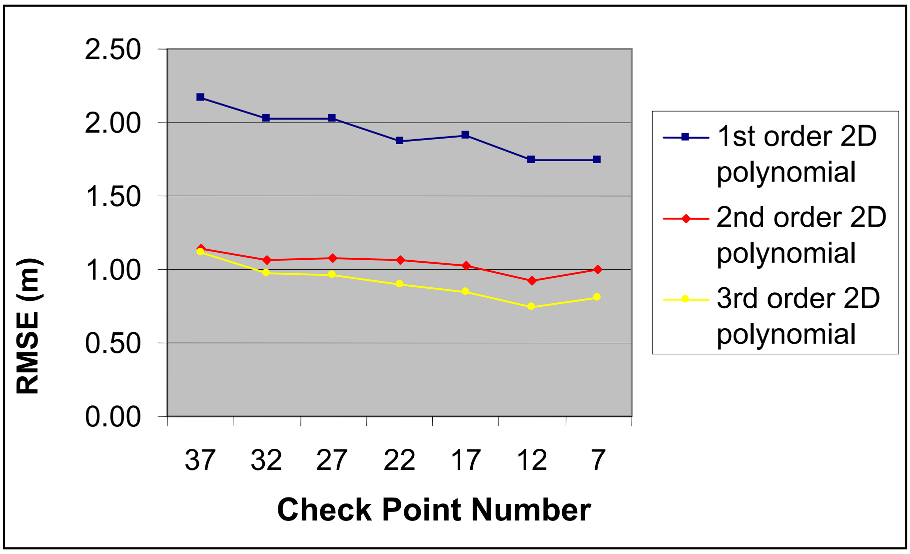

Figure 6.5 The accuracies of the CPs for the 2D polynomial functions.

6.2.4 The Results of the Rational Functions

Similar problem which appeared for the *Third Order 2D Polynomial Function* was also encountered when trying to solve the *Second and Third Order Rational Functions*. However, the estimation of the rational function coefficients (RFCs) using the least squares adjustment for the *Second and Third Order Rational Functions* was quite challenging. There were many more unknown parameters than any of the polynomial functions of the *Second and Third Order Rational Functions*. Therefore, the increase in the number of the unknown parameters directly increased the possibility of the correlation between the parameters as well. Accordingly, the correlated parameters were not able to be solved using a direct least squares adjustment solution.

One method to solve the *Third Order 2D Polynomial Function* was to remove one of the correlated terms in the least squares adjustment. However, because the number of the correlated parameters were quite high for the *Second and Third Order Rational Functions* the removal of the parameters would not be logical. The second method uses successive iterations to solve the correlated parameters. Initially, one of the correlated parameters was fixed and the other parameters were estimated using the least squares adjustment. Later, the solved parameters were fixed and the other correlated parameters were estimated. This iteration continued until the corrections of the parameters were negligible. The third method performs regularization to the normal equations in the least squares adjustment. After the regularization process, the matrix B^TB in normal equations became invertible. Since this method was generally used in the previous studies (Tao and Hu, 2001; Tao and Hu, 2001; Hu and Tao, 2002), it was used therefore to solve the problem of the correlated terms in this study.

The regularization method is called Tikhonov regularization because it was first derived by Tikhonov in 1963. For a well-conditioned approximation problem and equally weighted observations, the general least squares solution described in Appendix B can be used:

$$\boldsymbol{\delta} = (\mathbf{B}^T\mathbf{B})^{-1}\mathbf{B}^T\mathbf{C}$$

where, **δ** is the estimated parameters matrix, **B** is the design matrix and **C** is the observation matrix. When B becomes ill-conditioned, the matrix of the B^TB turns out to be singular. So, the least squares solution for this situation is impossible or increasingly useless. For this kind of situations, an improvement must be done to B^TB by modifying it. The simplest way to achieve this is by adding a small multiplication of the identity matrix to the B^TB matrix. Because B^TB is usually symmetric and positive semi-definite, the matrix $B^TB + h^2\mathrm{I}$ has its eigenvalues in $[h^2, h^2 + \|B^TB\|]$ and, hence, a condition number ≤ $(h^2 + \|B^2\|)\ /\ h^2$ that becomes smaller as h increases (Neumaier, 1998). With this replacement, the general least squares adjustment solution turns into regularized Tikhonov form as:

$$\boldsymbol{\delta} = (\mathbf{B}^\mathbf{T}\mathbf{B} + \mathbf{h}^\mathbf{2}\mathbf{I})^{-1}\mathbf{B}^T\mathbf{C}$$

where, **δ** is the estimated parameters matrix, **B** is the design matrix, **C** is the observation matrix, **I** is the identity matrix, and **h** is the regularization parameter. Naturally, the only parameter that differ the regularized solution from the original least squares solution is the regularization parameter. Therefore, the determination of the regularization parameter h is quite important and directly affects the results of the adjustment. Typically, the solutions are computed for a large number of different values, and an h value which minimizes the CP residuals is selected. The results of an experiment are shown in Figure 6.6, in which the *Second Order Rational*

Functions are used. This experiment was generated using 40 GCPs and 37 CPs. As can be seen in the figure, the accuracies for the CPs were less than one pixel at a broad range of h values. Based on the tests, it was found that a reasonable good convergence could be reached in two iterations. When the h value is between 0.0007 and 0.05, the errors of the CPs were also not sensitive to the particular h value as long as h was within that range (Figure 6.6). Because the global minimum error of the CPs (0.72 pixels) for the *Second Order Rational Functions* was reached for the h value of 0.0012, this result was used therefore for the subsequent error analysis of the *Second Order Rational Functions*.

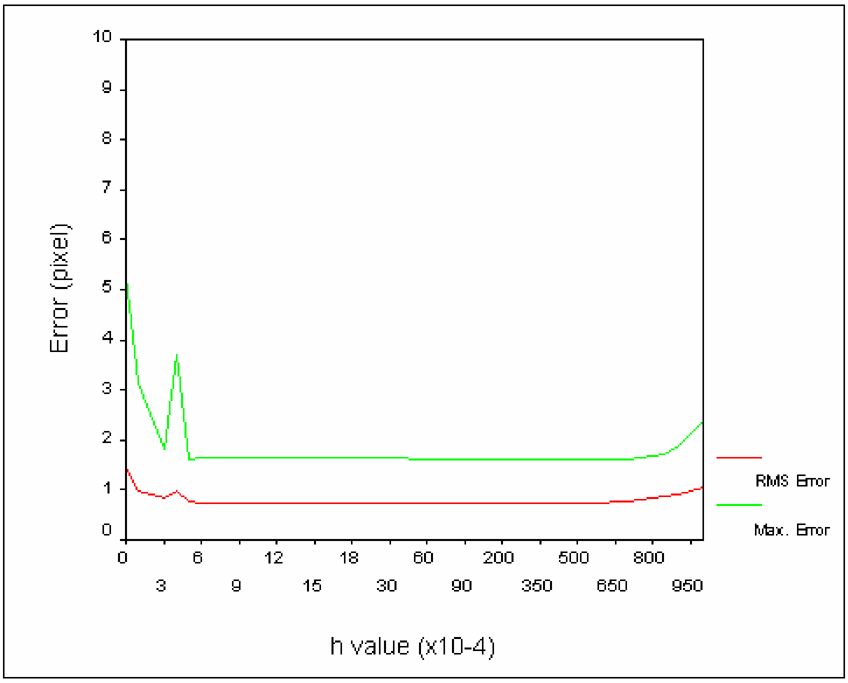

Figure 6.6 Error versus h at CPs for the *Second Order Rational Functions*.

A similar procedure was implemented for the *Third Order Rational Functions* as well. Figure 6.7 illustrates the results obtained from the implementation of the different h values for the *Third Order Rational Functions*.

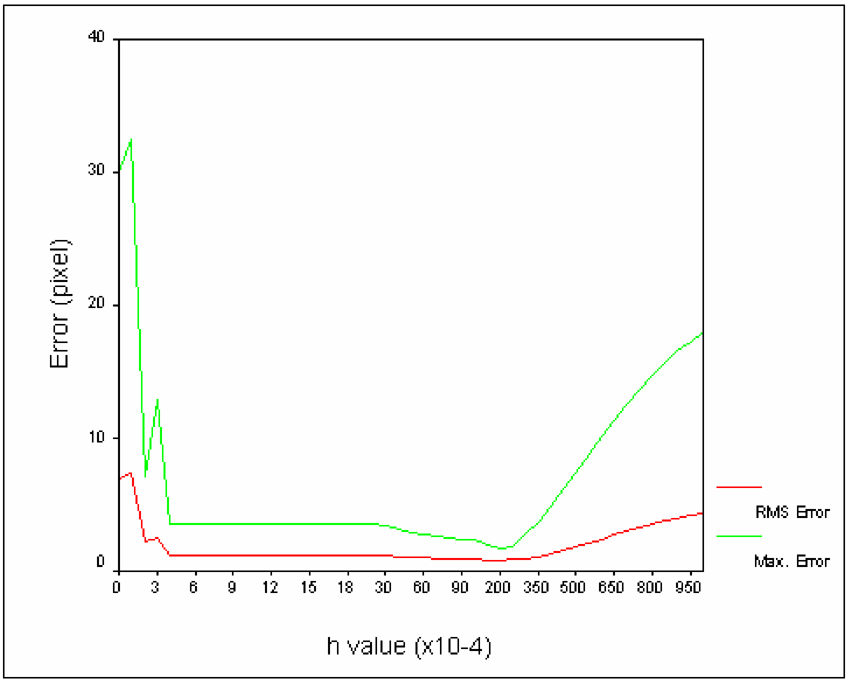

Figure 6.7 Error versus h at CPs for the *Third Order Rational Functions*.

As can be seen in Figure 6.7, the trends of the RMSE on CPs and the trend of the maximum error are different from the trends of the *Second Order Rational Functions*. Based on the experiment, it was found that a reasonable good convergence could be reached in two iterations. This time, it was found that the errors of the CPs were sensitive to the particular h values (Figure 6.7). Because the global minimum error of the CPs (0.83 pixels) using the *Third Order Rational Functions* reached to the h value of 0.0194 this result was therefore used for the subsequent error analysis of the *Third Order Rational Functions*.

The RMSE values computed for the GCPs using the *First, Second, and Third Order Rational Functions* are given in Table 6.8. The results indicate that the *First Order Rational Functions* produce accuracy around 10.5 m (0.7 pixels). If the *Second Order Rational Functions* are used the accuracy improves approximately to 7.5 m (0.5 pixels). The best accuracy for the

GCPs was obtained as 6 m (0.4 pixels) using the *Third Order Rational Functions*. For the *First Order Rational Functions*, the best accuracy was achieved using 77 GCPs. Conversely, for the *Second and Third Order Rational Functions*, the best accuracy was achieved using 40 GCPs. The trends of the GCPs for the rational functions are given in Figure 6.8. Error vectors of the 77 GCPs for the Rational Functions are given in Appendix J.

Table 6.8 The overall accuracies of the GCPs for the *First, Second and Third Order Rational Functions*.

GCPs	**Rational Functions**		
	1st Order	**2nd Order**	**3rd Order**
40	0.77	0.42	0.26
45	0.75	0.47	0.29
50	0.76	0.50	0.33
55	0.78	0.53	0.38
60	0.77	0.52	0.38
65	0.77	0.51	0.38
70	0.75	0.51	0.39
77	0.73	0.51	0.40

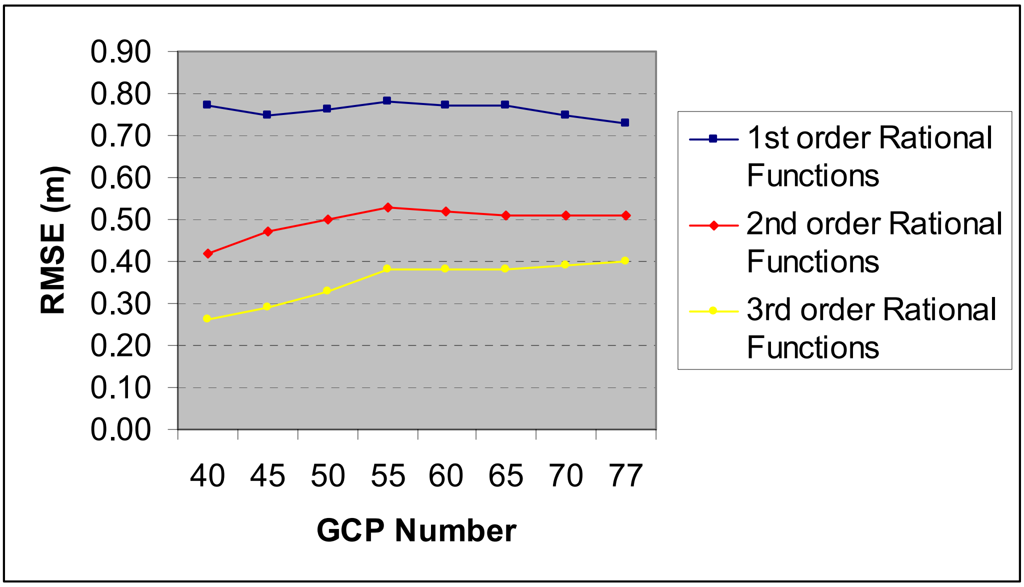

Figure 6.8 The accuracies of the GCPs for the Rational Functions.

The reason for the trends of the *Second and Third Order Rational Functions* was the implementation of the regularization parameter in the least squares adjustment. Because the h value used for all GCP combinations was computed using 40 GCPs, the GCP accuracy was decreased a little with the increase in the number of GCPs. Based on the results, it is clear that the best GCP accuracy was achieved for the *Third Order Rational Functions*. However, in order to make a clear statement, the accuracies were also evaluated for the CPs. The results computed for the CPs with the use of *First, Second and Third Order Rational Functions* are given in Table 6.9.

Table 6.9 The overall accuracies of the CPs for the *First, Second, and Third Order Rational Functions*.

C. Points	**Rational Functions**		
	1st Order	**2nd Order**	**3rd Order**
37	0.75	0.73	0.84
32	0.77	0.65	0.80
27	0.73	0.60	0.85
22	0.64	0.54	0.61
17	0.64	0.55	0.59
12	0.55	0.59	0.63
7	0.56	0.63	0.72

As can be seen in Table 6.9, the trends for the CPs for the *First, Second and Third Order Rational Functions* resemble the trends of the GCPs. The affect of the regularization parameter is observed for the CP RMSE values of the *Second and Third Order Rational Functions*. Although the *Third Order Rational Functions* fits the GCPs very well, the CP accuracies of the *Third Order Rational Functions* were found to be the worst when compared to the accuracies of the *First and Second Order Rational Functions*. On the other hand, the best accuracy was achieved using the

Second Order Rational Functions. Although a good decreasing trend was found for the *First Order Rational Functions*, the GCP accuracies were not good enough when compared with the *Second and Third Order Rational Functions*. The error trends of the CPs are given in Figure 6.9.

As a conclusion, the determination of the regularization parameter was found to be a crucial factor to solve the higher order rational functions. The affect of the regularization parameter was observed both in the GCP and CP RMSE values. Finally, the *Second Order Rational Functions* was found to be the optimum rational function model for the orthorectification of the ASTER imagery.

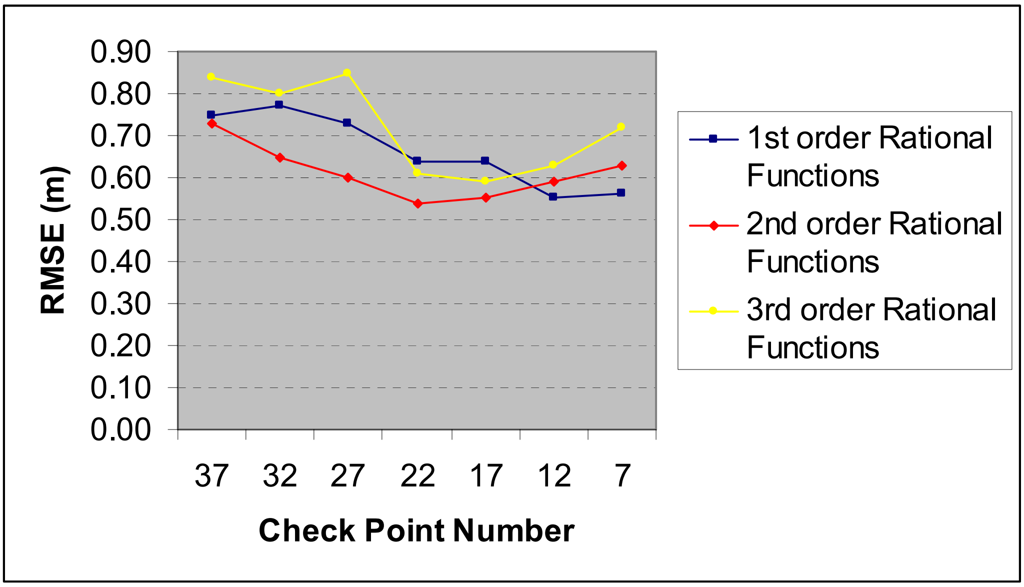

Figure 6.9 The CP accuracies for the Rational Functions.

6.2.5 The Results of the 3D Polynomial Functions

In this study, only the special forms of the 3D polynomial functions were tested. First, the ASTER image was orthorectified by using the model developed by Pala and Pons (1995). Then, the second order of the previous model was developed and executed. The results of the *First and Second Order 3D Polynomial models* with relief are given in Table 6.10.

The results obtained for the GCPs using the first order were around 28.5 m (1.9 pixels) and these results were certainly not satisfying. Although the first order model was stated to be good for orthorectifying SPOT imagery (Pala and Pons, 1995), the model does not produce good results for the ASTER imagery. However, the developed second order model produced very good results that were around 9 m (0.6 pixels). It is clear that the results of the *Second Order 3D Polynomial model with Relief* were three times better than the results of the *First Order 3D Polynomial model with Relief*. Figure 6.10 also demonstrates this big difference of the GCP accuracies between the two models. Error vectors of the 77 GCPs for the models first and second order 3D polynomial models with relief are given in Appendix J.

For the first order, the RMSE value of 26.4 m (1.76 pixels) for CPs decreased below 1 pixel (0.94 pixels) when 70 GCPs were used. On the other hand, the accuracies of the *Second Order 3D Polynomial model with Relief* were observed at a range between 11.70 m (0.78 pixels) and 8.25 m (0.55 pixels). These results demonstrate the consistency of the developed *Second Order 3D Polynomial model with Relief*. The trends of the CP RMSE values of the *First and Second Order 3D Polynomial model with Relief* are given in Figure 6.11.

Table 6.10 The overall results of the GCPs for the *First and Second Order 3D Polynomial Functions with Relief*.

3D Special Functions					
GCPs	**1st Order**	**2nd Order**	**C. Points**	**1st Order**	**2nd Order**
40	**1.92**	**0.61**	37	**1.76**	**0.78**
45	**1.97**	**0.61**	32	**1.62**	**0.76**
50	**1.88**	**0.64**	27	**1.74**	**0.69**
55	**1.90**	**0.67**	22	**1.64**	**0.60**
60	**1.84**	**0.66**	17	**1.79**	**0.59**
65	**1.92**	**0.66**	12	**1.06**	**0.55**
70	**1.88**	**0.65**	7	**0.94**	**0.58**
77	**1.81**	**0.64**	0	**-**	**-**

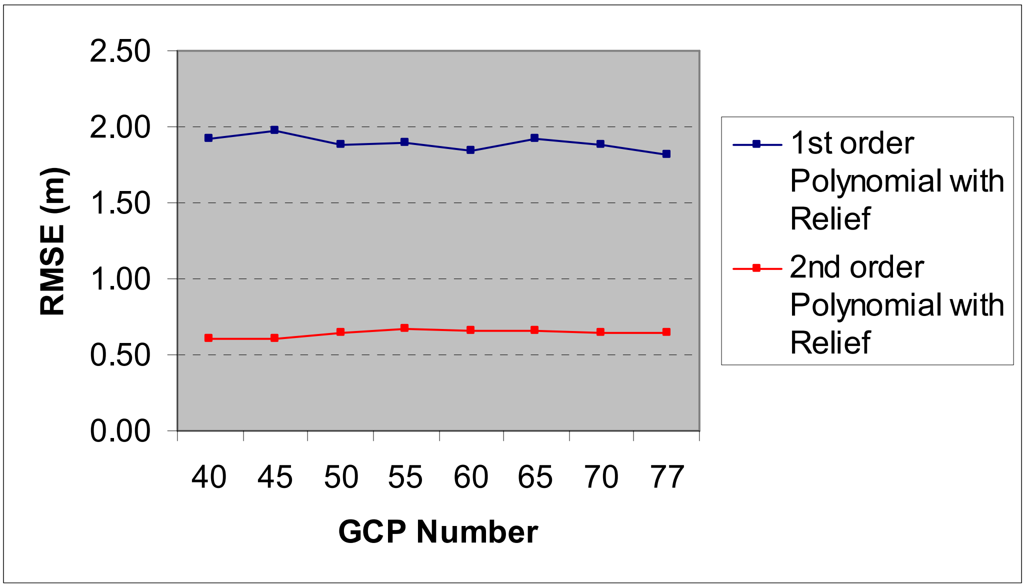

Figure 6.10 The GCP accuracies for the *First and Second Order 3D Polynomial Functions with Relief*.

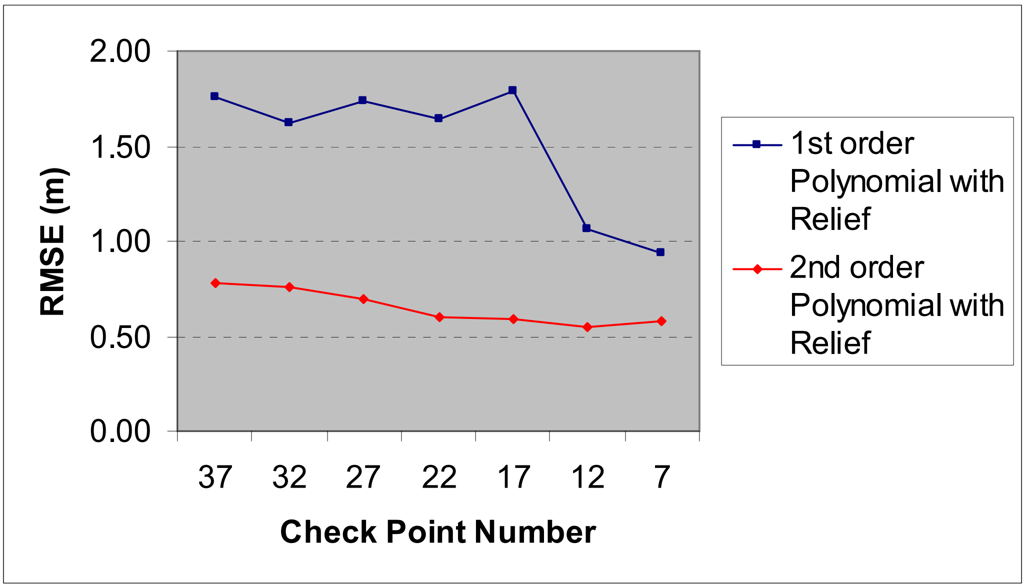

Figure 6.11 The CP accuracies for the *First and Second Order 3D Polynomial Functions with Relief*.

6.2.6 The Results of the Direct Linear Transformation

The results of the GCPs for the *DLT model* are given in Table 6.11. It was found that, the accuracy of the *DLT model* was not better than one pixel both in X and Y direction for all GCP combinations. Therefore, for all GCP combinations, the overall GCP accuracy was worse than 24 m (1.6 pixels). One important point to note is that for performing the orthorectification process a Local Cartesian Coordinate system was used. Error vectors of the 77 GCPs for the *DLT model* are given in Appendix J.

Table 6.11 The Results of the least squares adjustment of the GCPs for the *DLT function*.

Model	GCPs	GCPs		
		Residual X	**Residual Y**	**Overall**
DLT	40	1.42	1.05	**1.76**
	45	1.40	1.08	**1.77**
	50	1.39	1.04	**1.74**
	55	1.38	1.05	**1.74**
	60	1.34	1.01	**1.68**
	65	1.35	1.03	**1.70**
	70	1.32	1.03	**1.67**
	77	1.28	1.00	**1.62**

The accuracies of the CPs computed using the *DLT model* is given in Table 6.12. As can be seen in Table 6.12, the accuracies of all CPs were better than the accuracies of the GCPs. The worst and the best errors were 24.15 m (1.61 pixels) and 16.2 m (1.08 pixels), respectively. The trends in the accuracies of the GCPs and CPs with respect to the number of GCPs and CPs are given in Figure 6.12.

Table 6.12 The results of the least squares adjustment of the CPs for the *DLT model*.

Model	C. Points	Check Points		
		Residual X	**Residual Y**	**Overall**
DLT	37	1.29	0.97	**1.61**
	32	1.18	0.97	**1.52**
	27	1.33	0.68	**1.49**
	22	1.18	0.73	**1.39**
	17	1.30	0.76	**1.51**
	12	0.90	0.86	**1.24**
	7	0.79	0.73	**1.08**

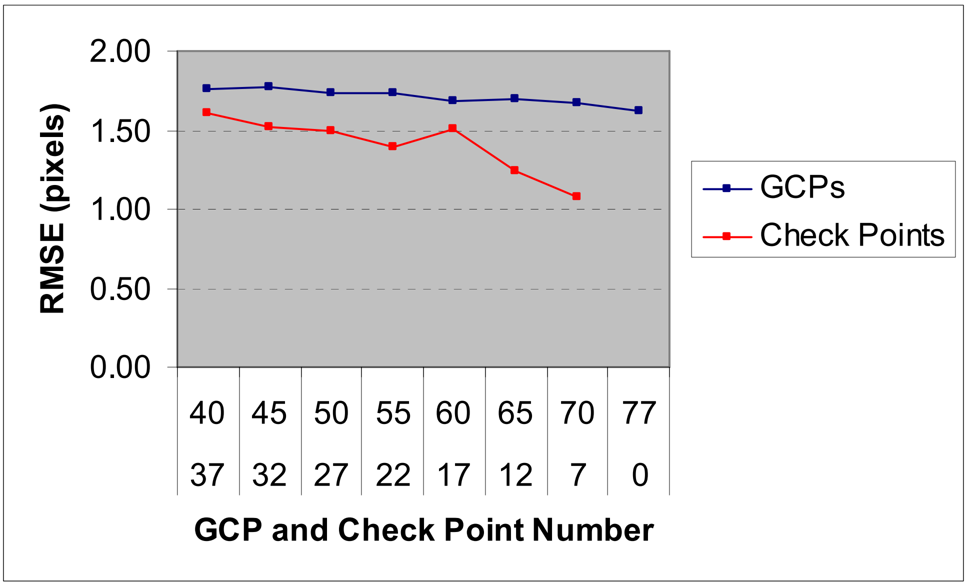

Figure 6.12 The overall accuracies of the GCPs and CPs for the *DLT model*.

6.2.7 The Results of the Projective Transformation

The results of the assessments of the GCPs for *Projective Transformation model* are given in Table 6.13. Because the modified projective transformation function was used for the orthorectification, the residuals in Y direction are almost identical to the results of the first order polynomial model. Similar to the *Orun and Natarajan* and the *DLT models*, a Local Cartesian Coordinate System was used in the orthorectification process of the *Projective Transformation model*. It is believed that, the difference in the coordinate systems used in the adjustment procedure is the reason for the small differences between the residuals in Y direction.

Table 6.13 The assessment results of the least squares adjustment of the GCPs for the *Projective Transformation model*.

Model	**GCPs**	**GCPs**		
		Residual X	**Residual Y**	**Overall**
Projective Transformation	40	1.21	0.30	**1.25**
	45	1.21	0.30	**1.25**
	50	1.17	0.34	**1.22**
	55	1.16	0.36	**1.21**
	60	1.15	0.35	**1.20**
	65	1.16	0.34	**1.20**
	70	1.13	0.34	**1.18**
	77	1.10	0.34	**1.16**

The assessment results of the GCPs indicate that the overall accuracy for all GCP combinations was not better than 17.4 m (1.16 pixels). It is also obvious that, the residuals in X direction increased the overall residual of the GCPs. Error vectors of the 77 GCPs for the *Projective Transformation* are given in Appendix J.

The accuracies of the CPs are given in Table 6.14. Similar to the results of the *DLT model*, the accuracies of all the CPs were better than the accuracies of the GCPs. However, the results were slightly better than the *DLT model*. The trends for the accuracies of the GCPs and CPs with respect to the number of GCPs and CPs are illustrated in Figure 6.13.

Table 6.14 The results of the least squares adjustment of the CPs for the *DLT model*.

Model	**C. Points**	**Check Points**		
		Residual X	**Residual Y**	**Overall**
Projective Transformation	37	1.05	0.41	**1.13**
	32	0.98	0.41	**1.06**
	27	1.02	0.37	**1.09**
	22	1.02	0.32	**1.07**
	17	0.97	0.35	**1.03**
	12	0.84	0.39	**0.93**
	7	0.93	0.38	**1.00**

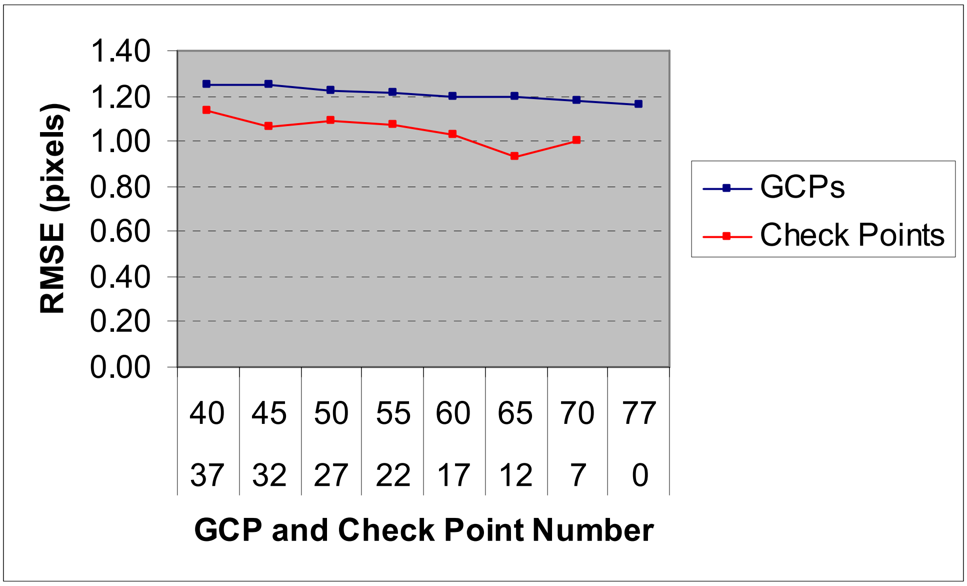

Figure 6.13 The overall accuracies of the GCPs and CPs for the *Projective Transformation model*.

6.2.8 The Comparative Evaluation of the Results of the Orthorectification Process

The assessments of the results of the orthorectification using 12 models are given in Table 6.15. Of these models, the *First Order Polynomial Function* was the only model which provided RMSE over two pixels for both GCPs and CPs. Therefore, it can be stated that the results of the *First Order Polynomial Function* were the worst among 12 models and should definitely not be used. The accuracies of the *First Order Polynomial Function with Relief* and the *DLT models* were higher than 1.5 pixels. Although, for these models the accuracies of the CPs were better than the accuracies of the GCPs, it can be stated that these models have limited orthorectification capabilities and therefore, they should not be used either.

The *Second Order Polynomial* and the *Projective Transformation models* produced almost the same results for the GCPs and CPs with a little higher than one pixel size of the ASTER imagery. For these models, the accuracies of the CPs were around one pixel. For the *Third Order Polynomial model*, the accuracy of the GCPs was one pixel. For this model, the accuracies of the CPs reveal that there is not much distortion away from the GCPs with respect to other two models. Consequently, the models *Second Order Polynomial*, *Projective Transformation*, and the *Third Order Polynomial* can be used for the orthorectification of the ASTER imagery when sub pixel accuracy is not required and if the other high accurate models are not available.

The accuracies of the two rigorous models, the *Orun and Natarajan* and the *Toutin's models* were found to be identical to each other. The trends for the GCPs and CPs were almost indistinguishable for these two models. The best accuracy from these models was computed to be 0.75 pixels. Similarly, the model *First Order Rational Functions* produced similar accuracies when compared to the rigorous models. The trend for the GCPs and CPs were similar to the rigorous models as well. Consequently, the results of the orthorectification using the *Orun and Natarajan*, *Toutin's models* and the *First Order Rational Functions* were good in terms of the accuracy both for the GCPs and CPs.

The models *Second and Third Order Rational Functions* provided the results approximately half a pixel size when the assessments are carried out based on the GCPs. Furthermore, the model *Third Order Rational Functions* provided results as accurate as a quarter of a pixel size. However, it was observed that the accuracies of the CPs were affected conversely in the model *Third Order Rational Functions*. Although the model *Third Order Rational Functions* fits the GCPs very well, it distorted the CPs a little more when compared with the model *Second Order*

Table 6.15 The summary of the RMSE of the Orthorectification of ASTER Imagery using twelve models

Model	GCPs	Check P.	GCPs			Check Points		
			Residual X	**Residual Y**	**Overall**	**Residual X**	**Residual Y**	**Overall**
Orun and Natarajan Model	40	37	0.73	0.34	**0.81**	0.64	0.40	**0.75**
	45	32	0.71	0.34	**0.79**	0.65	0.39	**0.76**
	50	27	0.70	0.36	**0.79**	0.63	0.37	**0.73**
	55	22	0.72	0.37	**0.81**	0.53	0.34	**0.63**
	60	17	0.71	0.36	**0.79**	0.51	0.36	**0.63**
	65	12	0.70	0.35	**0.79**	0.39	0.38	**0.55**
	70	7	0.69	0.36	**0.77**	0.37	0.38	**0.53**
	77	0	0.66	0.35	**0.75**	-	-	**-**
Toutin's Model	40	37	0.75	0.31	**0.81**	0.63	0.43	**0.76**
	45	32	0.73	0.32	**0.80**	0.61	0.42	**0.74**
	50	27	0.72	0.34	**0.80**	0.60	0.37	**0.70**
	55	22	0.73	0.36	**0.81**	0.52	0.33	**0.62**
	60	17	0.72	0.35	**0.80**	0.51	0.36	**0.62**
	65	12	0.72	0.34	**0.80**	0.38	0.39	**0.54**
	70	7	0.70	0.34	**0.78**	0.32	0.37	**0.49**
	77	0	0.67	0.34	**0.75**	-	-	**-**
1st order Polynomial Functions	40	37	2.74	0.30	**2.75**	2.13	0.41	**2.17**
	45	32	2.71	0.31	**2.73**	1.99	0.41	**2.03**
	50	27	2.63	0.34	**2.65**	1.99	0.36	**2.02**
	55	22	2.61	0.36	**2.63**	1.84	0.32	**1.87**
	60	17	2.53	0.35	**2.56**	1.88	0.35	**1.91**
	65	12	2.50	0.34	**2.53**	1.70	0.39	**1.74**
	70	7	2.46	0.35	**2.48**	1.70	0.37	**1.74**
	77	0	2.39	0.35	**2.41**	-	-	**-**

Table 6.15 Continued

Model	GCPs	Check P.	GCPs			Check Points		
			Residual X	Residual Y	Overall	Residual X	Residual Y	Overall
2nd order Polynomial Functions	40	37	1.20	0.30	**1.23**	1.06	0.41	**1.14**
	45	32	1.20	0.30	**1.24**	0.97	0.43	**1.06**
	50	27	1.17	0.33	**1.21**	1.01	0.38	**1.08**
	55	22	1.15	0.35	**1.20**	1.01	0.32	**1.06**
	60	17	1.15	0.34	**1.20**	0.96	0.35	**1.02**
	65	12	1.15	0.34	**1.20**	0.84	0.38	**0.92**
	70	7	1.12	0.34	**1.17**	0.92	0.38	**1.00**
	77	0	1.10	0.34	**1.15**	-	-	**-**
3rd order Polynomial Functions	40	37	0.94	0.29	**0.99**	1.02	0.42	**1.11**
	45	32	0.99	0.29	**1.03**	0.86	0.45	**0.97**
	50	27	0.98	0.33	**1.04**	0.87	0.40	**0.96**
	55	22	0.98	0.35	**1.04**	0.84	0.32	**0.90**
	60	17	0.98	0.34	**1.04**	0.78	0.35	**0.85**
	65	12	0.98	0.34	**1.04**	0.63	0.39	**0.74**
	70	7	0.96	0.34	**1.01**	0.72	0.38	**0.81**
	77	0	0.93	0.34	**0.99**	-	-	**-**
Direct Linear Transformation	40	37	1.42	1.05	**1.76**	1.29	0.97	**1.61**
	45	32	1.40	1.08	**1.77**	1.18	0.97	**1.52**
	50	27	1.39	1.04	**1.74**	1.33	0.68	**1.49**
	55	22	1.38	1.05	**1.74**	1.18	0.73	**1.39**
	60	17	1.34	1.01	**1.68**	1.30	0.76	**1.51**
	65	12	1.35	1.03	**1.70**	0.90	0.86	**1.24**
	70	7	1.32	1.03	**1.67**	0.79	0.73	**1.08**
	77	0	1.28	1.00	**1.62**	-	-	**-**

Table 6.15 Continued

Model	GCPs	Check P.	GCPs			Check Points		
			Residual X	Residual Y	Overall	Residual X	Residual Y	Overall
1st order Rational Functions	40	37	0.72	0.28	**0.77**	0.63	0.42	**0.75**
	45	32	0.69	0.28	**0.75**	0.65	0.43	**0.77**
	50	27	0.69	0.32	**0.76**	0.62	0.37	**0.73**
	55	22	0.70	0.34	**0.78**	0.55	0.32	**0.64**
	60	17	0.69	0.33	**0.77**	0.54	0.35	**0.64**
	65	12	0.69	0.33	**0.77**	0.40	0.38	**0.55**
	70	7	0.67	0.33	**0.75**	0.41	0.39	**0.56**
	77	0	0.65	0.33	**0.73**	-	-	**-**
2nd order Rational Functions	40	37	0.33	0.26	**0.42**	0.56	0.46	**0.73**
	45	32	0.38	0.27	**0.47**	0.48	0.45	**0.65**
	50	27	0.39	0.31	**0.50**	0.45	0.40	**0.60**
	55	22	0.42	0.33	**0.53**	0.41	0.35	**0.54**
	60	17	0.41	0.32	**0.52**	0.38	0.39	**0.55**
	65	12	0.40	0.32	**0.51**	0.41	0.43	**0.59**
	70	7	0.40	0.32	**0.51**	0.47	0.41	**0.63**
	77	0	0.40	0.33	**0.51**	-	-	**-**
3rd order Rational Functions	40	37	0.20	0.17	**0.26**	0.52	0.65	**0.84**
	45	32	0.21	0.20	**0.29**	0.46	0.65	**0.80**
	50	27	0.22	0.25	**0.33**	0.52	0.67	**0.85**
	55	22	0.25	0.29	**0.38**	0.43	0.42	**0.61**
	60	17	0.26	0.28	**0.38**	0.41	0.42	**0.59**
	65	12	0.26	0.28	**0.38**	0.41	0.48	**0.63**
	70	7	0.26	0.28	**0.39**	0.48	0.53	**0.72**
	77	0	0.28	0.29	**0.40**	-	-	**-**

Table 6.15 Continued

Model	GCPs	Check P.	GCPs			Check Points		
			Residual X	Residual Y	Overall	Residual X	Residual Y	Overall
1st order Polynomial with Relief	40	37	1.90	0.28	**1.92**	1.71	0.42	**1.76**
	45	32	1.95	0.28	**1.97**	1.56	0.43	**1.62**
	50	27	1.86	0.32	**1.88**	1.70	0.38	**1.74**
	55	22	1.87	0.34	**1.90**	1.61	0.33	**1.64**
	60	17	1.81	0.33	**1.84**	1.75	0.35	**1.79**
	65	12	1.89	0.33	**1.92**	0.99	0.38	**1.06**
	70	7	1.85	0.33	**1.88**	0.85	0.39	**0.94**
	77	0	1.78	0.33	**1.81**	-	-	**-**
2nd order Polynomial with Relief	40	37	0.55	0.27	**0.61**	0.65	0.43	**0.78**
	45	32	0.55	0.27	**0.61**	0.62	0.44	**0.76**
	50	27	0.56	0.31	**0.64**	0.57	0.39	**0.69**
	55	22	0.58	0.33	**0.67**	0.50	0.34	**0.60**
	60	17	0.58	0.32	**0.66**	0.46	0.36	**0.59**
	65	12	0.58	0.32	**0.66**	0.38	0.39	**0.55**
	70	7	0.56	0.32	**0.65**	0.44	0.38	**0.58**
	77	0	0.55	0.32	**0.64**	-	-	**-**
Projective Transformation	40	37	1.21	0.30	**1.25**	1.05	0.41	**1.13**
	45	32	1.21	0.30	**1.25**	0.98	0.41	**1.06**
	50	27	1.17	0.34	**1.22**	1.02	0.37	**1.09**
	55	22	1.16	0.36	**1.21**	1.02	0.32	**1.07**
	60	17	1.15	0.35	**1.20**	0.97	0.35	**1.03**
	65	12	1.16	0.34	**1.20**	0.84	0.39	**0.93**
	70	7	1.13	0.34	**1.18**	0.93	0.38	**1.00**
	77	0	1.10	0.34	**1.16**	-	-	**-**

Rational Functions. Therefore, the model *Second Order Rational Functions* is said to be better than the model *Third Order Rational Functions*. The model *Second Order Polynomial with Relief* produced results closer to the models *Second and Third Order Rational Functions*. The accuracies of the CPs for the model second order polynomial with relief were better than the model *Third Order Rational Functions* and almost equal to the accuracies of the model *Second Order Rational Functions*.

Based on the results, it can be stated that the model *Second Order Rational Functions* appears to be the best model to orthorectify the ASTER imagery. However, the model *Second Order Rational Functions* suffers from the correlated parameters within the model. Because of the correlations between some of the parameters within this model, the implementation of the *Second Order Rational Functions* can only be performed by modifying the least squares adjustment solution. Therefore, although the accuracy of the model *Second Order Polynomial with Relief* was a little bit worse than the accuracy of the model *Second Order Rational Functions*, it can be stated that the model *Second Order Polynomial with Relief* appears to be superior to the model *Second Order Rational Functions* in terms of simplicity and consistency. Furthermore, the minimum number of GCPs required for the model *Second Order Polynomial with Relief* was significantly lower than the model *Second Order Rational Functions*. Therefore, the developed model *Second Order Polynomial with Relief* can be efficiently used for the orthorectification of the ASTER imagery. The comparative evaluations of the GCPs and CPs for the twelve models are also illustrated in Figures 6.14 and 6.15, respectively.

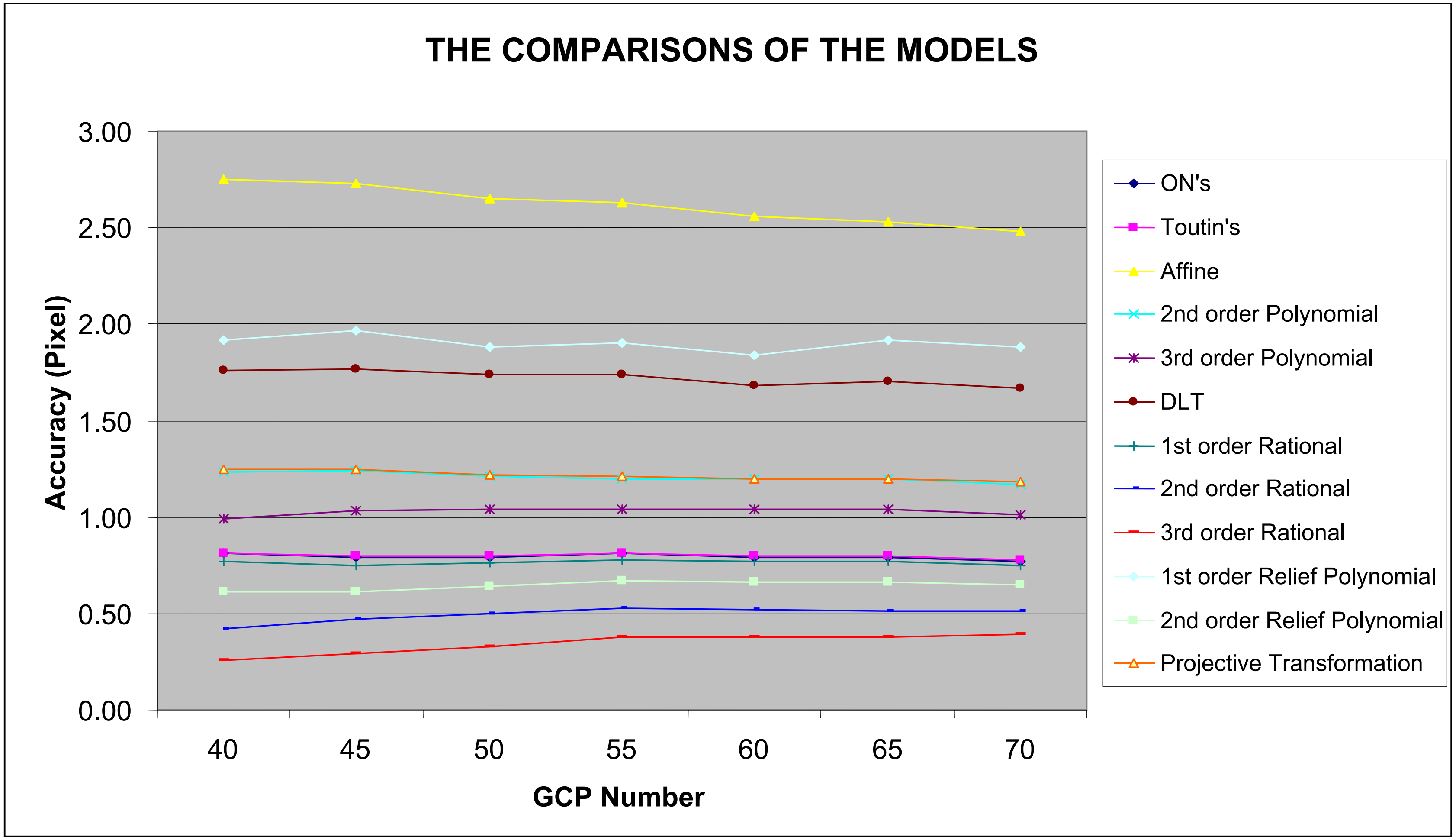

Figure 6.14 The comparisons of the models in terms of the accuracies of GCPs

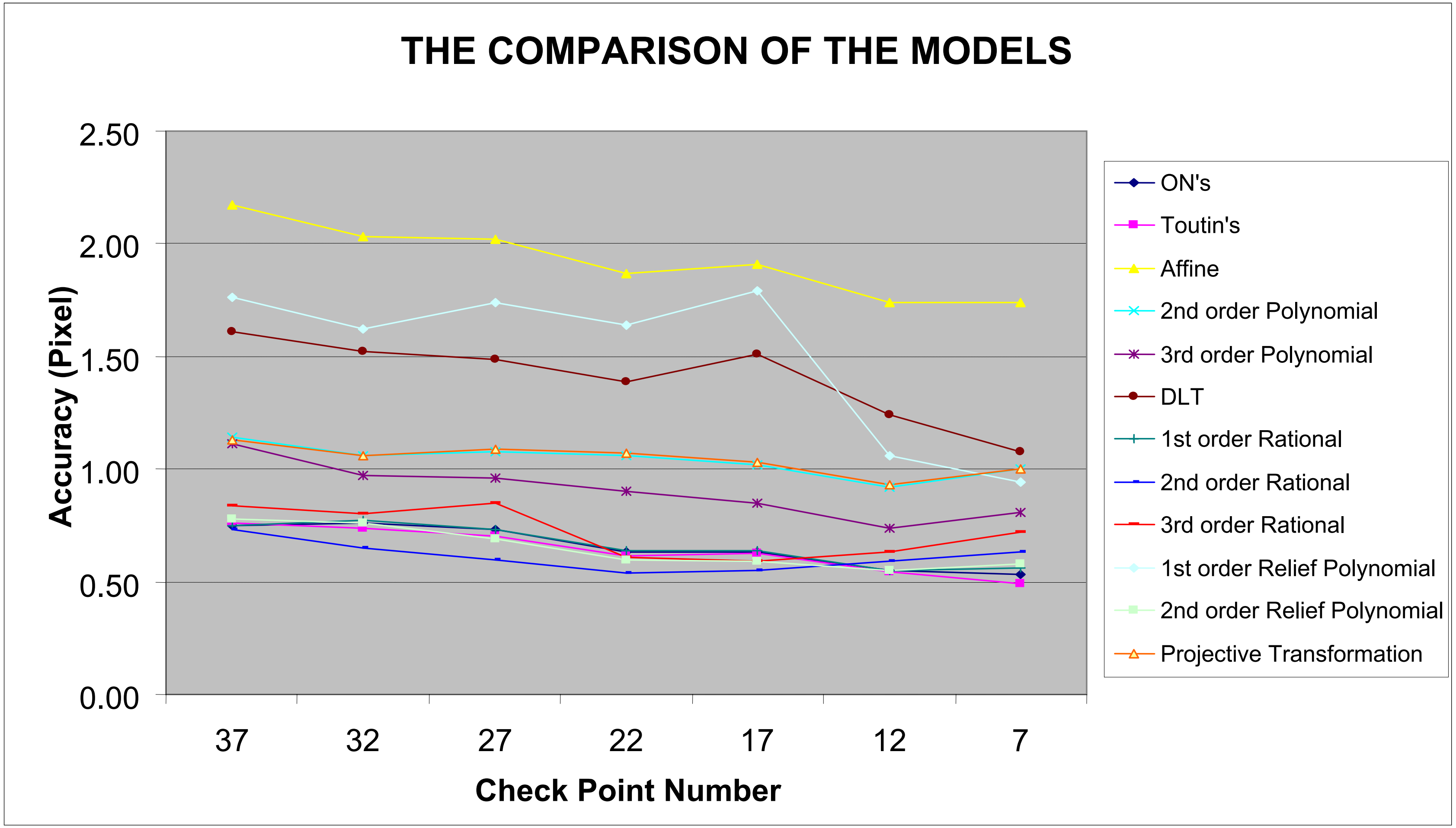

Figure 6.15 The comparisons of the models in terms of the accuracies of the CPs

CHAPTER 7

CONCLUSIONS AND RECOMMENDATIONS

In this chapter, the conclusions derived from this study are described and the recommendations concerning further studies are given.

7.1 Conclusions

The conclusions derived from the assessment of the ASTER DEMs are as follows:

- The high average matching success achieved for ASTER DEMs (around 97%) ensures the quality of ASTER along-track stereo image acquisition system.

- The CP and overall accuracy analysis revealed that the best DEM accuracy was achieved using evenly distributed 16 GCPs. However, the computed overall accuracies for the DEMs were two or three times higher than the accuracies computed for the CPs. This confirms that the accuracies of CPs are almost trivial and do not reflect the actual DEM accuracies.

- Most of the blunders occurred during the correlation procedure was observed over lakes and mountainous areas. However, it was also observed that even in the flat areas some localized blunders were present.

- It was found that the automated filtering techniques were not enough to remove the blunders in the generated DEMs. Therefore, manual post-processing is required to remove those blunders. It can be concluded that the post processing and blunder removal of the generated DEMs were crucial operations that affect the overall DEM accuracy up to 38%.

- The slope analysis indicated that there was a strong positive correlation (0.99) between the DEM accuracy and the slopes.

- The assessments performed based on the land cover types revealed that the best accuracy was found for the class water (5.01 m). Furthermore, the classes urban and forest produced satisfactory results. On the other hand, the worst results were obtained for the mountainous areas (17.14 m).

- According to the results obtained, an elevation accuracy of 11 m can be achieved using the ASTER stereo imagery with a reasonable number of GCPs. Therefore ASTER stereo imagery can provide the medium scale DEMs through its powerful along-track stereo image acquisition system.

The conclusions derived from the assessment of the orthorectified ASTER imagery are as follows:

- Of the used twelve different models, the model first order 2D polynomial has provided the worst results. Therefore, this model should definitely not be used for the orthorectification of ASTER imagery.

- The accuracies of the models first order polynomial with relief and DLT was also found problematic. Hence, it can be concluded that these models have limited orthorectification capabilities and should not be used either.

- The models second order 2D polynomial and projective transformation produced accuracies a little higher than one pixel size of ASTER imagery. For the third order 2D polynomial, the model accuracy was one pixel. Consequently, these models can be used when sub pixel accuracy is not required and if other high accurate models are not available.

- The two rigorous models, the Orun and Natarajan and the Toutin's were found identical to each other. Meanwhile, the model first order rational function produce similar accuracy results to the rigorous models. So, these models can definitely be used for the orthorectification of the ASTER imagery.

- The models second and third order rational functions provided accuracy results around half a pixel size. The model third order rational function distorted the CPs a little more when compared with the model second order rational functions. The developed model second order polynomial with relief produced similar results approaching to these models.

- When solving the model third order 2D polynomial, second and third order rational functions, over-parameterization was recognized. This over-parameterization was more serious in models second and third order rational functions. Therefore, solving the models second and third order rational functions require additional steps when compared to the other mathematical models.

- The determination of the regularization parameter when solving the models second and third order rational functions is found to be quite important. Furthermore, the results reveal that these models are highly affected from the regularization parameter used.

- According to the results obtained, the model second order rational function appears to be the best model to orthorectify ASTER imagery. However, the over-parameterization in the model decreases the model consistency. The accuracy of the model second order polynomial with relief was a little bit worse than the accuracy of the model second order rational functions. However, it can be stated that the developed model appears to be superior to the model second order rational function in terms of simplicity and consistency. Therefore, the developed model second order polynomial with relief can be efficiently used for the orthorectification of the ASTER imagery.

- The results also revealed that the generated DEMs from stereo ASTER images can be efficiently used for the orthorectification of ASTER images.

7.2 Recommendations

The followings are recommended for further studies:

- It is recommended that a similar study should be carried out using different satellite images which have similar resolutions. The results obtained using different satellite images can be compared.

- Different test sites can be used to evaluate the accuracies of the DEMs and orthoimages generated from ASTER images. Therefore, the accuracies that can be achieved from ASTER images can become definite.

- The second and third order DLT and third order polynomial with relief models can be developed and implemented. Thus, the results of these models can be assessed and compared with the other models.

- An automated GCP selection algorithm can be developed and used for selecting the GCPs for both DEM generation and orthorectification. Therefore, the requirement for the manual GCP selection can be significantly reduced or eliminated.

REFERENCES

1. Abrams, M., Hook, S., and Ramachandran, B., (2003), ASTER User Handbook Version 2.

2. ASTER Users Guide Part II, ver. 4, (2003).

3. Bannari, A., Morin, D., Benie, G. B., and Bonn, F. J., (1995), A Theoritical review of different mathematical models of geometric corrections applied to remote sensing images, Remote Sensing Reviews, Vol. 13, pp. 27-47.

4. Chen, L. C., and Lee, L. H., (1993), Rigorous Generation of Digital Orthophotos from SPOT Images, Photogrammetric Engineering and Remote Sensing, Vol. 59, No. 5, pp. 655-661.

5. Cuartero, A., Felicisimo, A. M., and Ariza, F. J., (2004), Accuracy of DEM Generation from Terra-ASTER Stereo Data, Commission IV, WG VI/4, ISPRS Congress.

6. Di, K., Ma, R., and Li, R. X., (2003), Rational Functions and Potential for Rigorous Sensor Model Recovery, Photogrammetric Engineering and Remote Sensing, Vol. 69, No. 1, pp. 33-41.

7. Eckert, S., Kellenberger, T., and Itten, K., (2005), Accuracy Assessment of Automatically Derived Digital Elevation Models from ASTER data in Mountanious Terrain, International Journal of Remote Sensing, Vol. 26, No. 9, pp. 1943-1957.

8. El-Manadili, Y., and Novak, K., (1996), Precision Rectification of SPOT Imagery using the Direct Linear Transformation Model, Photogrammetric Engineering and Remote Sensing, Vol. 62, No. 1, pp. 67-72.

9. Fonseca, L. M. G., and Manjunath, B. S., (1996), Registration Techniques for Multisensor Remotely Sensed Imagery, Photogrammetric Engineering and Remote Sensing, Vol. 62, No. 9, pp. 1049-1056.

10. Fraser C. S., and Hanley, H. B., (2003), Bias Compensation in Rational Functions for IKONOS Satellite Imagery, Photogrammetric Engineering and Remote Sensing, Vol. 69, No. 1, pp. 53-57.

11. Fritsch, D., and Stallmann, D., (2000), Rigorous Photogrammetric Processing of High Resolution Satellite Imagery, Vol. XXXIII, ISPRS Congress.

12. Gacemer, O., (2002), Geometric Correction Accuracy of IRS 1C/D Pan Imagery using Map versus GPS Control Points, M.Sci. Thesis, Middle East Technical University.

13. Goncalves, J. A., and Oliviera, A. M., (2004), Accuracy Analysis of DEMs Derived from ASTER Imagery, Commission III, WG III/2, ISPRS Congress.

14. Gugan, D. J., (1987), Practical Aspects of Topographic Mapping from SPOT Imagery, Photogrammetric Record, 12(69), pp. 349-355.

15. Gugan D. J., and Dowman, I. J., (1988), Topographic Mapping from SPOT Imagery, Photogrammetric Engineering and Remote Sensing, Vol. 54, No. 10, pp. 1409-1414.

16. Hirano, A., Welch, R., and Lang, H., (2003), Mapping from ASTER Stereo Image Data: DEM Validation and Accuracy Assessment, ISPRS Journal of Photogrammetry and Remote Sensing, Vol. 57, pp. 356-370.

17. Hu, Y., and Tao, V., (2002), Updating Solutions of the Rational Function Model using Additional Control Information, Photogrammetric Engineering and Remote Sensing, Vol. 68, No. 7, pp. 715-723.

18. Kim, T., Shin, D., and Lee, Y.R., (2001), Development of a Robust Algorithm for Transformation of a 3D Object Point onto a 2D Image Point for Linear Pushbroom Imagery, Photogrammetric Engineering and Remote Sensing, Vol. 67, No. 4, pp. 449-452.

19. Konecny, G., (1979), Methods and Possibilities for Digital Differential Rectification, Photogrammetric Engineering and Remote Sensing, Vol. 45, No. 6, pp. 727-734.

20. Kratky, V., (1989), Rigorous Photogrammetric Processing of SPOT Images at CCM Canada, ISPRS Journal of Photogrammetry and Remote Sensing, Vol. 44, pp. 53-71.

21. Kraus, K., (1993), Photogrammetry Volume 1.

22. Krupnik, A., (2003), Accuracy Prediction for Ortho-image Generation, Photogrammetric Record, 18(101), pp. 41-58.

23. Lang, H., and Welch, R., “Algorithm Theoretical Basis Document for ASTER Digital Elevation Models”.

24. Leberl, F., Maurice, K., Thomas, J. K., and Millot, M., (1994), Automated Radar Image Matching Experiment, ISPRS Journal of Photogrammetry and Remote Sensing, Vol. 49, pp. 19-33.

25. Li, R., Zhou, G., Schmidt, N. J., Fowler, C., and Tuell, G., (2002), Photogrammetric Processing of High-Resolution Airborne and Satellite Linear Array Stereo Images for Mapping Applciations, International Journal of Remote Sensing, Vol. 23, No. 20, pp. 4451-4473.

26. Lillesand, T. M., Kiefer, R. W., and Chipman, J. W., (2004), Remote Sensing and Image Interpretation.

27. Manual of Photogrammetry Fourth Edition, (1980), American Society for Photogrammetry and Remote Sensing.

28. Manual of Photogrammetry Fifth Edition, (2004), American Society for Photogrammetry and Remote Sensing.

29. Matlab 6.5.0 manual, (2002), Learning Matlab, Getting Started – Introduction to Matlab.

30. Mikhail, E. M., Bethel, J. S., and McGlone, J. C., (2001), Introduction to Modern Photogrammetry.

31. Neumaier, A., (1998), Solving Ill-Conditioned and Singular Linear Systems: A Tutorial on Regularization, SIAM Review, Vol. 40, No. 3, pp. 636-666.

32. Novak, K., (1992), Rectification of Digital Imagery, Photogrammetric Engineering and Remote Sensing, Vol. 58, No. 3, pp. 339-344.

33. Okamoto, A., Ono, T., Akamatsu, S., Fraser, C., Hattori, S., and Hasegawa, H., (1999), Geometric Characteristics of Alternative Triangulation Models for Satellite Imagery, In Proceedings of ASPRS Annual Conference (CD-ROM), Oregon.

34. Orun, A. B., and Natarajan, K., (1994), A Modified Bundle Adjustment Software for SPOT Imagery and Photography: Tradeoff, Photogrammetric Engineering and Remote Sensing, Vol. 60, No. 12, pp. 1431-1437.

35. Pala, V., and Pons, X., (1995), Incorporation of Relief in Polynomial-Based Geometric Corrections, Photogrammetric Engineering and Remote Sensing, Vol. 61, No. 7, pp. 935-944.

36. PCI Geomatics, OrthoEngine User Guide, (2003).

37. Priebbenow, R., and Clerici, E., (1988), Cartographic Applications of SPOT Imagery, Colleque International SPOT-1: Utilisation des images, bilan, resultats, Paris, France, pp. 1189-1194.

38. Radhadevi, P. V., Ramachandran, R., and Mohan, A. S. R. K. V. M., (1998), Restitution of IRS-1C PAN Data using an Orbit Attitude Model and Minimum Control, ISPRS Journal of Photogrammetry and Remote Sensing, Vol. 53, pp. 262-271.

39. Rodriguez, V., Gigord, P., Gaujac, A. C., and Munier, P., (1988), Evaluation of the Stereoscopic Accuracy of the SPOT Satellite, Photogrammetric Engineering and Remote Sensing, Vol. 54, No. 2, pp. 217-221.

40. Salamonowicz, P. H., (1986), Satellite Orientation and Position for Geometric Correction of Scanner Imagery, Photogrammetric Engineering and Remote Sensing, Vol. 52, No. 4, pp. 491-499.

41. Shi, W., and Shaker, A., (2003), Analysis of Terrain Elevation Effects on Ikonos Imagery Rectification Accuracy by using Non-Rigorous Models, Photogrammetric Engineering and Remote Sensing, Vol. 69, No. 12, pp. 1359-1366.

42. Tao, C. V., and Hu, Y., (2001), Use of the Rational Function Model for Image Rectification, Canadian Journal of Remote Sensing, pp. 593-602.

43. Tao, C. V., and Hu, Y., (2001), A Comprehensive Study of the Rational Function Model for Photogrammetric Processing, Photogrammetric Engineering and Remote Sensing, Vol. 67, No. 12, pp. 1347-1357.

44. Tao, C. V., and Hu, Y., (2002), 3D Reconstruction Methods Based on the Rational Function Model, Photogrammetric Engineering and Remote Sensing, Vol. 68, No. 7, pp. 705-714.

45. Toutin, T., (1995), Generating DEM from Stereo Images with a Photogrammetric Approach: Examples with VIR and SAR Data, EARSEL Journal “Advances in Remote Sensing”, Vol. 4, No. 2, pp. 110-117.

46. Toutin, T., (1999), Map Making with Remote Sensing Data, Proceedings of the NATO Advanced Research Workshop on Remote Sensing for Environmental Data in Albania: A Strategy for Integrated Management, pp. 65-87.

47. Toutin, T., (2001), Review Article: Elevation Modelling from Satellite Visible and Infrared (VIR) Data, International Journal of Remote Sensing, Vol. 22, No. 6, pp. 1097-1125.

48. Toutin, T., and Cheng, P., (2001), DEM Generation with ASTER Stereo Data, Earth Observation Magazine, Vol. 10, No. 6, pp. 10-13.

49. Toutin, T., and Cheng, P., (2002), Comparison of Automated Digital Elevation Model Extraction Results using Along-track ASTER and Across-track SPOT images, SPIE Journal, Optical Engineering, Vol. 41, No. 9, pp. 2102-2106.

50. Toutin, T., (2002), Three Dimensional Topographic Mapping with ASTER Stereo Data in Rugged Topography, IEEE Transactions on Geoscience and Remote Sensing, Vol. 40, No. 10, pp. 2241-2247.

51. Toutin, T., (2004), Comparison of Stereo-Extracted DTM from Different High-Resolution Sensors: SPOT-5, EROS-A, IKONOS-II, and Quickbird, IEEE Transactions on Geoscience and Remote Sensing, Vol. 42, No. 10, pp. 2121-2129.

52. Toutin, T., (2004), Review Article: Geometric Processing of Remote Sensing Images: Models, Algorithms and Methods, International Journal of Remote Sensing, Vol. 25, No. 10, pp. 1893-1924.

53. Web 1, NASA Terra Spacecraft CERES Instrument Information. Retreived 15 July 2005, from the World Wide Web: http://terra.nasa.gov/About/CERES/index.php

54. Web 2, NASA Terra Spacecraft MISR Instrument Information. Retreived 15 July 2005, from the World Wide Web: http://terra.nasa.gov/About/MISR/index.php

55. Web 3, NASA Terra Spacecraft MODIS Instrument Information. Retreived 15 July 2005, from the World Wide Web: http://terra.nasa.gov/About/MODIS/index.php

56. Web 4, NASA Terra Spacecraft MODIS Design Concept. Retreived 15 July 2005, from the World Wide Web: http://modis.gsfc.nasa.gov/about/design.php

57. Web 5, NASA Terra Spacecraft MOPITT Instrument Information. Retreived 15 July 2005, from the World Wide Web: http://terra.nasa.gov/About/MOPIT/index.php

58. Web 6, NASA SRTM data download server. Retreived 15 July 2005, from the World Wide Web: ftp://e0mss21u.ecs.nasa.gov/srtm/

59. Web 7, National Geographic Society, (2003), Xpeditions Atlas. Retreived 16 July 2005, from the World Wide Web: http://www.nationalgeographic.com/xpeditions/atlas/index.html?Parent=mideast&Rootmap=turkey&Mode=d

60. Web 8, OGC (OpenGIS Consortium), 1999. The OpenGIS Abstract Specification - Topic 7: The Earth Imagery Case, Retreived 16 July 2005, from the World Wide Web: http://portal.opengeospatial.org/files/index.php?artifact_id=892

61. Welch, R., Jordan, T., Lang, H., and Murakami, H., (1998), ASTER as a Source for Topographic Data in the Late 1990's, IEEE Transactions on Geoscience and Remote Sensing, Vol. 36, No. 4, pp. 1282-1289.

62. Westin, T., (1990), Precision Rectification of SPOT Imagery, Photogrammetric Engineering and Remote Sensing, Vol. 56, No. 2, pp. 247-253.

63. Wolf, P. R., and Dewitt, B. A., (2000), Elements of Photogrammetry with Applications in GIS 3rd Edition.

64. Yamaguchi, Y., Kahle, A. B., Tsu, H., Kawakami, T., and Pniel, M., (1998), Overview of Advanced Spaceborne Thermal Emission and Reflection Radiometer (ASTER), IEEE Transactions on Geoscience and Remote Sensing, Vol. 36, No. 4, pp. 1062-1071.

65. Zoej, M. J. V., and Petrie, G., (1998), Mathematical Modelling and Accuracy Testing of SPOT Level 1B Stereopairs, Photogrammetric Record, 16(91), pp. 67-82.

APPENDIX A

The definitions and the derivation of the collinearity equations are explained in (Mikhail et. al., 2001):

The three orientation parameters may be considered as three sequential rotations, ω, Φ, and κ. These orientation parameters will be implicitly expressed in the nine elements of a 3x3 rotation matrix M. This matrix is orthogonal and will have the sense of being applied to the object space coordinates to produce coordinates parallel to the image space system. Considering only the rotation and neglecting other parameters, such as scale,

$$\begin{bmatrix} x \\ y \\ z \end{bmatrix} = M \begin{bmatrix} X \\ Y \\ Z \end{bmatrix}$$

where, x, y, and z are the image space coordinates and X, Y, and Z are the object space coordinates. Since M is orthogonal, its inverse is equal to its transpose, and the order of the previous equation can be reversed:

$$\begin{bmatrix} x \\ y \\ z \end{bmatrix} = M^T \begin{bmatrix} X \\ Y \\ Z \end{bmatrix}$$

In the previous equation, the origins of the two coordinate systems are assumed to coincide. In fact the origins do not coincide, and shift terms are introduced to place a local origin of object space coordinates at the perspective center. The differences in magnitude between the image space vector and the corresponding object space vector necessitates the introduction of a scale factor, k, in to the equation.

$$\begin{bmatrix} x \\ y \\ z \end{bmatrix} = kM \begin{bmatrix} X - X_L \\ Y - Y_L \\ Z - Z_L \end{bmatrix}$$

The image space coordinates for a frame camera system will have a z coordinate fixed at the negative of the principal distance, or focal length. In addition, there may be small offsets x_0 and y_0 from a fiducial-based origin to a perspective center origin. These are reflected in the revised image space coordinates:

$$\begin{bmatrix} x - x_0 \\ y - y_0 \\ -f \end{bmatrix} = kM \begin{bmatrix} X - X_L \\ Y - Y_L \\ Z - Z_L \end{bmatrix}$$

The matrix M can be expressed in terms of its elements:

$$\begin{bmatrix} x - x_0 \\ y - y_0 \\ -f \end{bmatrix} = k \begin{bmatrix} m_{11} & m_{12} & m_{13} \\ m_{21} & m_{22} & m_{23} \\ m_{31} & m_{23} & m_{33} \end{bmatrix} \begin{bmatrix} X - X_L \\ Y - Y_L \\ Z - Z_L \end{bmatrix}$$

Multiplying the matrix and vector on the right hand side of the equation, we obtain three scalar equations instead of a matrix equation:

$$x - x_0 = k\left[m_{11}\left(X - X_L\right) + m_{12}\left(Y - Y_L\right) + m_{13}\left(Z - Z_L\right)\right]$$
$$y - y_0 = k\left[m_{21}\left(X - X_L\right) + m_{22}\left(Y - Y_L\right) + m_{23}\left(Z - Z_L\right)\right]$$
$$- f = k\left[m_{31}\left(X - X_L\right) + m_{32}\left(Y - Y_L\right) + m_{33}\left(Z - Z_L\right)\right]$$

The scalar factor is something of nuisance parameter and can be eliminated by dividing the first two equations by the third to obtain the classical form of the collinearity equations:

$$x - x_0 = -f \frac{m_{11}\left(X - X_L\right) + m_{12}\left(Y - Y_L\right) + m_{13}\left(Z - Z_L\right)}{m_{31}\left(X - X_L\right) + m_{32}\left(Y - Y_L\right) + m_{33}\left(Z - Z_L\right)}$$

$$y - y_0 = -f \frac{m_{21}\left(X - X_L\right) + m_{22}\left(Y - Y_L\right) + m_{23}\left(Z - Z_L\right)}{m_{31}\left(X - X_L\right) + m_{32}\left(Y - Y_L\right) + m_{33}\left(Z - Z_L\right)}$$

APPENDIX B

The definitions and the derivation of the least squares solutions are explained in (Manual of Photogrammetry, 1980):

B.1 Development of Normal Equations of the Least Squares Adjustment

Let Y be a random variable the expected value of which may be expressed as a linear function of n variables $X_1, X_2, X_3, \ldots$ and X_n; i.e.

$$E(Y) = a_1X_1 + a_2X_2 + a_3X_3 + \ldots + a_nX_n \qquad (1.1)$$

where the X_i's are the independent variables and Y is the dependent variable. Linear equations of this form are often encountered in geodetic surveying and photogrammetry. The problem generally concerns the determination of the most probable values for the set of coefficients a_1, a_2, a_3 and a_n. To do so, observations can be made on Y at various values of the parameters ($X_1, X_2, X_3 \ldots$ and X_n). For example, suppose that by setting $X_1 = x_{11}, X_2 = x_{12}, X_3 = x_{13} \ldots X_n = x_{1n}$, we observe that $Y = y_1$. This set of observations represents one experiment and gives rise to one observation equation as follows:

$$\upsilon_1 + y_1 = x_{11}\, a_1 + x_{12}\, a_2 + x_{13}\, a_3 + \ldots + x_{1n}\, a_n$$

where υ_1 is the residual in the observation y_1. By transferring y_1 to the right-hand side, this equation may also be written as

$$u_1 = x_{11} a_1 + x_{12} a_2 + x_{13} a_3 + . . . + x_{1n} a_n - y_1. \tag{1.2}$$

In general, the experiment is repeated *m* times to obtain *m* independent measurements of *Y* for *m* different combinations of the values of X_i's. Since each experiment gives rise to one observation equation as in (1.2), the mathematical model will consist of *m* observation equations as follows:

$$\begin{aligned}
u_1 &= x_{11} a_1 + x_{12} a_2 + x_{13} a_3 + ... + x_{1n} a_n - y_1 \\
u_2 &= x_{21} a_1 + x_{22} a_2 + x_{23} a_3 + ... + x_{2n} a_n - y_2 \\
u_3 &= x_{31} a_1 + x_{32} a_2 + x_{33} a_3 + ... + x_{3n} a_n - y_3 \\
&. \\
&. \\
&. \\
u_m &= x_{m1} a_1 + x_{m2} a_2 + x_{m3} a_3 + ... + x_{mn} a_n - y_m
\end{aligned} \tag{1.3}$$

If m=n, no least-squares adjustment is possible or necessary since there are as many equations as unknowns. In such a case, it is necessary to assume that no error is present in the measurements (y_i's) by setting u_1 = 0 for i = 1 to m. Equations (1.3) are then reduced to n equations involving n unknowns, and a unique solution can be obtained.

If $m > n$, the least squares method may be used to find the most probable values of the residuals and the coefficients; that is, $u_1, u_2, u_3 . . . u_m, a_1, a_2, a_3 . . .$ and a_n. However, the measurements (y_i's) should satisfy the two fundamental assumptions of least squares:

- The residual (u_i) has a normal distribution with a mean of zero and a variance σ_i, for i = 1 to m.
- The observations $y_1, y_2, y_3 . . .$ and y_m are mutually independent.

The υ_i's are random errors, each having its own normal distribution described by the following function:

$$f(\upsilon_i) = \frac{1}{\sqrt{2\pi}\sigma_i} e^{-\frac{1}{2}\left(\frac{\upsilon_i}{\sigma_i}\right)^2}$$

Moreover, since these observations are mutually independent, their joint distribution function is the product of their individual distribution function; i.e.

$$f(\upsilon_1, \upsilon_2 ..., \upsilon_n) = \frac{1}{\sqrt{2\pi}\sigma_1} e^{-\frac{1}{2}\left(\frac{\upsilon_1}{\sigma_1}\right)^2} \cdot \frac{1}{\sqrt{2\pi}\sigma_2} e^{-\frac{1}{2}\left(\frac{\upsilon_2}{\sigma_2}\right)^2} \cdots \frac{1}{\sqrt{2\pi}\sigma_n} e^{-\frac{1}{2}\left(\frac{\upsilon_n}{\sigma_n}\right)^2}$$

$$= \left(\frac{1}{\sqrt{2\pi}}\right)^n \left(\frac{1}{\sigma_1} \cdot \frac{1}{\sigma_2} \cdots \frac{1}{\sigma_n}\right) e^{-\frac{1}{2}\sum_{i=1}^{n}\left(\frac{\upsilon_i}{\sigma_i}\right)^2}$$

The most probable set of errors ($\upsilon_1, \upsilon_2, \upsilon_3 \ldots \upsilon_n$) will be that which maximize the above probability function. However, to maximize the probability, we must minimize the term

$$\sum_{i=1}^{n}\left(\frac{\upsilon_i}{\sigma_i}\right)^2.$$

That is, the most probable value of μ based on a given set of observations is that value of μ which makes

$$\sum_{i=1}^{n} \frac{\upsilon_i^2}{\sigma_i^2} = \text{minimum} \qquad (1.4)$$

Since such a solution of μ minimizes the sum of the squares of the residuals υ_i's, it is called a least squares solution. According to the derivation presented, the most probable set of υ_i's is that which minimize the term (1.4) with respect to the unknown parameters a_1, a_2, a_3 . . . and a_n. That is, the following conditions must be satisfied by the most probable values of a_1, a_2, a_3 . . . a_n :

$$\text{letting } \mathrm{Q} = \sum_{\mathrm{i}=1}^{\mathrm{m}} p_i \upsilon_i^{\,2} \text{ where } p_i = \left(\frac{1}{\sigma_i}\right)^2 ;$$

$$\begin{aligned} \frac{\partial \mathrm{Q}}{\partial \mathrm{a}_1} &= 0 \\ \frac{\partial \mathrm{Q}}{\partial \mathrm{a}_2} &= 0 \\ \frac{\partial \mathrm{Q}}{\partial \mathrm{a}_3} &= 0 \\ &\;\,. \\ &\;\,. \\ &\;\,. \\ \frac{\partial \mathrm{Q}}{\partial \mathrm{a}_n} &= 0 \end{aligned} \tag{1.5}$$

From equation (1.2)

$$
\begin{aligned}
p_1\upsilon_1^{\ 2} = {} & p_1x_{11}^{\ 2}a_1^{\ 2} + p_1x_{12}^{\ 2}a_2^{\ 2} + p_1x_{13}^{\ 2}a_3^{\ 2} + \ldots + p_1x_{1n}^{\ 2}a_n^{\ 2} + p_1y_1^{\ 2} + \ldots \\
& \ldots + 2p_1x_{11}a_1\left[x_{12}a_2 + x_{13}a_3 + x_{14}a_4 + \ldots + x_{1n}a_n - y_1\right] + \ldots \\
& \ldots + 2p_1x_{12}a_2\left[x_{13}a_3 + x_{14}a_4 + x_{15}a_5 + \ldots + x_{1n}a_n - y_1\right] + \ldots \\
& . \\
& . \\
& . \\
& \ldots - 2p_1x_{1n}y_1a_n.
\end{aligned}
$$

Thus,

$$
\begin{aligned}
\mathrm{Q} = \sum_{i=1}^{m} p_i\upsilon_i^{\ 2} = {} & \left(\sum_{i=1}^{m} p_ix_{i1}^{\ 2}\right)a_1^{\ 2} + \left(\sum_{i=1}^{m} p_ix_{i2}^{\ 2}\right)a_2^{\ 2} + \ldots + \left(\sum_{i=1}^{m} p_ix_{in}^{\ 2}\right)a_n^{\ 2} + \sum_{i=1}^{m} p_iy_i^{\ 2} + \ldots \\
& \ldots + 2a_1\sum_{\mathrm{i}=1}^{\mathrm{m}} p_ix_{i1}\left[a_2x_{i2} + a_3x_{i3} + a_4x_{i4} + \ldots + a_nx_{in} - y_i\right] + \ldots \\
& \ldots + 2a_2\sum_{\mathrm{i}=1}^{\mathrm{m}} p_ix_{i2}\left[a_3x_{i3} + a_4x_{i4} + a_5x_{i5} + \ldots + a_nx_{in} - y_i\right] + \ldots \\
& \ldots + \left(2\sum_{i=1}^{m} p_ix_{in}y_i\right)a_n.
\end{aligned}
\tag{1.6}
$$

Then, from the conditions stated in equations (1.5),

$$
\begin{aligned}
& \frac{\partial \mathrm{Q}}{\partial \mathrm{a}_1} = \left(\sum p_ix_{i1}^{\ 2}\right)a_1 + \left(\sum p_ix_{i1}x_{i2}\right)a_2 + ... + \left(\sum p_ix_{i1}x_{in}\right)a_n - \sum p_ix_{i1}y_i = 0 \\
& \frac{\partial \mathrm{Q}}{\partial \mathrm{a}_2} = \left(\sum p_ix_{i1}x_{i2}\right)a_1 + \left(\sum p_ix_{i2}^{\ 2}\right)a_2 + ... + \left(\sum p_ix_{i2}x_{in}\right)a_n - \sum p_ix_{i2}y_i = 0 \\
& . \\
& . \\
& . \\
& \frac{\partial \mathrm{Q}}{\partial \mathrm{a}_1} = \left(\sum p_ix_{i1}x_{in}\right)a_1 + \left(\sum p_ix_{i2}x_{in}\right)a_2 + \ldots + \left(\sum p_ix_{in}^{\ 2}\right)a_n - \sum p_ix_{in}y_i = 0
\end{aligned}
\tag{1.7}
$$

These are the so-called normal equations. They include as many equations as unknowns. Thus, this set of equations gives a unique solution to the unknown parameters, a_i's. This unique solution is also the most probable solution based on the given set of observations on Y. Having solved for the a_i's in equations (1.7), the most probable residuals can then be computed by substituting the values of the a_i's into equations (1.3).

The normal equations (1.7) may be expressed in matrix notation as follows:

$$\begin{bmatrix} \sum p_i x_{i1}^2 & \sum p_i x_{i1} x_{i2} & \sum p_i x_{i1} x_{i3} & . & . & . & \sum p_i x_{i1} x_{in} \\ \sum p_i x_{i2} x_{i1} & \sum p_i x_{i2}^2 & \sum p_i x_{i2} x_{i3} & . & . & . & \sum p_i x_{i2} x_{in} \\ \sum p_i x_{i3} x_{i1} & \sum p_i x_{i3} x_{i2} & \sum p_i x_{i3}^2 & . & . & . & \sum p_i x_{i3} x_{in} \\ . & . & . & & & & . \\ . & . & . & & & & . \\ \sum p_i x_{in} x_{i1} & \sum p_i x_{in} x_{i2} & \sum p_i x_{in} x_{i3} & . & . & . & \sum p_i x_{in}^2 \end{bmatrix} \begin{bmatrix} a_1 \\ a_2 \\ a_3 \\ . \\ . \\ a_n \end{bmatrix} = \begin{bmatrix} \sum p_i x_{i1} y_i \\ \sum p_i x_{i2} y_i \\ \sum p_i x_{i3} y_i \\ . \\ . \\ \sum p_i x_{in} y_i \end{bmatrix} \quad (1.8)$$

B.2 Matrix Formulation

The development of the normal equations as described in the previous section can be performed more conveniently using matrix notation. The set of observation equations in (1.3) may be written in matrix notation as follows:

$$\mathbf{V} = \mathbf{B}\boldsymbol{\delta} - \mathbf{C} \; ; \qquad (2.1)$$

where

$$\mathbf{B}_{(\mathbf{m},\mathbf{n})} = \begin{bmatrix} x_{11} & x_{12} & x_{13} & . & . & . & x_{1n} \\ x_{21} & x_{22} & x_{23} & . & . & . & x_{2n} \\ . & . & . & & & & . \\ . & . & . & & & & . \\ . & . & . & & & & . \\ x_{m1} & x_{m2} & x_{m3} & . & . & . & x_{mn} \end{bmatrix} \quad \boldsymbol{\delta}_{(\mathbf{n},\mathbf{1})} = \begin{bmatrix} a_1 \\ a_2 \\ a_3 \\ . \\ . \\ a_n \end{bmatrix} \text{ and } \mathbf{C}_{(\mathbf{m},\mathbf{1})} = \begin{bmatrix} y_1 \\ y_2 \\ y_3 \\ . \\ . \\ y_m \end{bmatrix}$$

According to the principle of least squares, the most probable solution for the **δ**-matrix is that which minimizes

$$\mathrm{Q} = \sum_{i=1}^{n} \left(\frac{\upsilon_i}{\sigma_i} \right)^2 .$$

It can be shown that

$$\mathrm{Q} = \sum_{i=1}^{n} \left(\frac{\upsilon_i}{\sigma_i} \right)^2 = \mathbf{V}^{\mathbf{T}}\mathbf{W}\mathbf{V}, \tag{2.2}$$

where **W** is the weight matrix and is defined as follows:

$$\mathbf{W} = \sigma_0^{\ 2} \begin{bmatrix} \sigma y_1^{\ 2} & & & & & & \\ & \sigma y_2^{\ 2} & & & & & \\ & & \sigma y_3^{\ 2} & & & & \\ & & & . & & & \\ & & & & . & & \\ & & & & & . & \\ & & & & & & \sigma y_m^{\ 2} \end{bmatrix}^{-1} \tag{2.3}$$

Substituting equation (2.1) into (2.2) yields

$$\mathbf{Q} = (\mathbf{B\delta} - \mathbf{C})^{\mathrm{T}}\,\mathbf{W}(\mathbf{B\delta} - \mathbf{C});$$

$$\mathbf{Q} = (\boldsymbol{\delta}^{\mathrm{T}}\mathbf{B}^{T} - \mathbf{C}^{\mathrm{T}})(\mathbf{WB\delta} - \mathbf{WC}).$$

Therefore,

$$\mathbf{Q} = \boldsymbol{\delta}^{\mathrm{T}}\mathbf{B}^{\mathrm{T}}\mathbf{WB\delta} - \boldsymbol{\delta}^{\mathrm{T}}\mathbf{B}^{\mathrm{T}}\mathbf{WC} - \mathbf{C}^{\mathrm{T}}\mathbf{WB\delta} + \mathbf{C}^{\mathrm{T}}\mathbf{WC} \qquad (2.4)$$

Since the problem is to find the **δ**-matrix which minimizes **Q**, the following condition must be satisfied by the solution:

$$\frac{\partial \mathrm{Q}}{\partial \delta} = 0$$

From equation (2.4),

$$\frac{\partial \mathrm{Q}}{\partial \delta} = 2\mathbf{B}^{\mathrm{T}}\mathbf{WB\delta} - \mathbf{B}^{T}\mathbf{WC} - (\mathbf{C}^{T}\mathbf{WB})^{T}$$

Hence,

$$2\mathbf{B}^{T}\mathbf{WB\delta} - 2\mathbf{B}^{T}\mathbf{WC} = 0\,;$$

or

$$(\mathbf{B}^{T}\mathbf{WB})\boldsymbol{\delta} = \mathbf{B}^{T}\mathbf{WC} \qquad (2.5)$$

which is the normal equation for the model stated by equation (2.1). It can be easily seen that equations (2.5) and (1.8) are equivalent.

APPENDIX C

Table C.1 The generated 114 vector segments during the merging process

H0D06	I0A01	I9A17	I9B22
H0D11	I0A02	I9A18	I9B23
H0D16	I0A06	I9A19	I9B24
H8C19	I0A07	I9A20	I9B25
H8C20	I0A11	I9A21	I9C01
H8C24	I8B03	I9A22	I9C02
H8C25	I8B04	I9A23	I9C03
H9C10	I8B05	I9A24	I9C06
H9C14	I8B10	I9A25	I9C07
H9C15	I8B14	I9B01	I9C08
H9C16	I8B15	I9B02	I9C11
H9C17	I8B19	I9B03	I9C12
H9C18	I8B20	I9B04	I9C13
H9C19	I8B25	I9B05	I9C17
H9C20	I9A01	I9B06	I9C18
H9C21	I9A02	I9B07	I9D01
H9C22	I9A03	I9B08	I9D02
H9C23	I9A04	I9B09	I9D03
H9C24	I9A05	I9B10	I9D04
H9C25	I9A06	I9B11	I9D05
H9D16	I9A07	I9B12	I9D08
H9D17	I9A08	I9B13	I9D09
H9D18	I9A09	I9B14	I9D10
H9D19	I9A10	I9B15	I9D15
H9D20	I9A11	I9B16	
H9D21	I9A12	I9B17	
H9D22	I9A13	I9B18	
H9D23	I9A14	I9B19	
H9D24	I9A15	I9B20	
H9D25	I9A16	I9B21	

Table C.2 The corrected 68 vector segments during the reference DEM generation

H8C25	I9A22
H9C14	I9A25
H9C15	I9B01
H9C17	I9B04
H9C18	I9B05
H9C19	I9B06
H9C22	I9B07
H9C23	I9B08
H9C24	I9B09
H9C25	I9B10
H9D17	I9B11
H9D18	I9B12
H9D22	I9B13
H9D23	I9B14
H9D25	I9B15
I0A01	I9B16
I0A06	I9B17
I0A11	I9B18
I8B03	I9B19
I8B10	I9B20
I9A01	I9B21
I9A02	I9B22
I9A03	I9B23
I9A04	I9C01
I9A05	I9C02
I9A07	I9C03
I9A08	I9C08
I9A09	I9C11
I9A10	I9C12
I9A11	I9C13
I9A13	I9C17
I9A14	I9C18
I9A19	I9D03
I9A20	I9D05

APPENDIX D

Table D.1 The coordinates of the GCPs collected from the reference orthophotos.

Point ID	Eastings	Northings	Heights
5	458900.655	4430233.917	804.87
6	462987.925	4428973.537	800.779
7	467171.370	4429174.052	834.464
9	465058.625	4424224.938	818.112
10	466755.500	4423974.500	812.242
13	473012.750	4427098.375	841.112
14	473037.750	4428955.250	871.619
15	475842.313	4426419.625	830.39
16	477217.000	4424668.500	864.252
17	480436.266	4426583.438	874.623
19	479931.766	4429203.500	893.357
27	471357.325	4432766.058	959.893
28	464990.623	4436256.142	819.575
32	494648.109	4437697.000	933.627
33	493338.359	4434015.750	1073.023
36	491475.016	4428764.500	873.36
38	487979.016	4427994.375	923.29
39	485934.266	4426408.938	882.01
40	486841.078	4423452.375	852.297
45	498221.703	4425201.000	1127.905
46	497105.818	4427228.595	1072.385
60	500431.734	4420720.250	1014.407
63	499665.297	4416532.250	1142.957
66	495054.828	4415515.656	1067.191
67	494011.797	4417297.125	1063.813
68	490336.172	4416678.813	1083.783
70	485051.922	4413346.875	1235.655
71	483307.933	4411145.552	1192.046
72	478177.859	4411426.375	1202.65
75	482862.016	4421134.938	855.472

Table D.1 Continued

Point ID	Eastings	Northings	Heights
76	487142.859	4420202.844	886.057
78	475967.703	4416280.125	1004.543
79	475598.078	4420271.688	831.277
80	472598.953	4418101.500	883.161
81	470366.297	4415201.219	959.892
82	470738.953	4413590.250	941.615
83	470589.234	4410214.500	1029.6
84	474035.113	4411599.223	1057.327
85	475475.359	4409679.875	1165.569
86	476430.266	4406232.125	1089.426
88	483357.797	4407558.500	973.595
91	491290.328	4409750.125	1247.951
97	472657.328	4405504.969	1211.8
98	470785.766	4406820.500	1204.017
99	465786.266	4407332.500	1021.535
100	464278.547	4409841.250	1035.239
103	460031.125	4423079.000	857.466
104	460218.625	4425758.375	825.171
105	459377.109	4410301.375	1113.671
106	461120.040	4412777.216	1202.715
114	460480.734	4402834.250	995.572
115	466621.484	4397880.000	1218.708
116	469583.016	4403429.375	1227.122
119	477414.859	4392193.125	1054.555
136	487173.266	4385408.938	1097.064
147	483607.578	4389748.813	1044.815
150	484531.328	4401668.625	1029.419
161	468144.270	4431521.565	903.927
163	481266.859	4432720.000	967.911
167	487420.203	4404886.125	1085.994
168	484187.641	4397552.500	1014.383

Table D.2 The coordinates of the GCPs measured on the ground using the differential GPS technique.

Point ID	Eastings	Northings	Heights
47	502405.118	4427493.626	1210.33
48	497634.174	4431201.860	1136.69
49	503295.927	4430138.372	1194.92
61	502706.444	4424861.660	1095.00
109	450943.568	4414889.222	751.59
112	453675.891	4408300.373	928.95
113	460599.072	4406692.824	948.62
117	471491.957	4395401.587	1101.38
122	458208.854	4393683.147	1132.60
123	460903.401	4390509.870	1197.60
126	450536.101	4391347.792	851.60
127	462339.333	4387179.475	1216.60
128	463733.406	4384589.610	1243.60
129	470674.569	4381362.180	1159.05
132	473858.508	4379897.723	1080.40
156	498421.347	4392933.048	1086.85

APPENDIX E

Table E.1 The RMSE values of the results of the bundle adjustment of ASTER nadir image using the GCP set 1.

Point ID	Total Residual	Residual X	Residual Y	Type
28	0.17	-0.12	0.12	GCP
49	0.38	-0.09	0.37	GCP
75	0.62	0.57	-0.24	GCP
91	0.55	-0.55	0.04	GCP
106	0.09	0.00	-0.09	GCP
119	0.09	0.08	-0.02	GCP
126	0.44	-0.25	0.36	GCP
156	0.58	0.53	0.24	GCP
6	1.03	-0.34	-0.97	Check
7	0.43	-0.16	-0.40	Check
9	0.50	-0.49	0.07	Check
10	0.46	0.40	0.22	Check
13	0.61	0.48	-0.38	Check
14	1.36	1.36	0.15	Check
15	0.90	0.77	0.47	Check
16	0.92	0.92	-0.10	Check
17	0.70	0.69	0.07	Check
19	0.32	0.31	-0.08	Check
27	0.23	0.23	-0.04	Check
32	0.47	0.07	-0.47	Check
33	0.38	0.02	-0.38	Check
36	0.22	0.05	-0.22	Check
38	0.34	-0.20	-0.27	Check
39	0.36	0.02	0.36	Check
40	0.16	-0.05	0.15	Check
45	0.61	-0.61	0.08	Check

Table E.1 Continued

Point ID	Total Residual	Residual X	Residual Y	Type
47	0.62	-0.19	-0.59	Check
48	0.27	0.14	0.23	Check
60	0.53	0.10	0.52	Check
61	1.11	0.71	-0.86	Check
63	0.84	-0.72	-0.43	Check
66	0.90	-0.29	0.86	Check
67	0.51	-0.50	-0.12	Check
68	0.54	-0.20	0.50	Check
70	0.21	-0.21	-0.04	Check
71	0.53	-0.53	-0.02	Check
72	0.20	0.09	0.19	Check
76	0.37	-0.28	0.24	Check
78	1.27	1.26	0.18	Check
79	0.79	0.70	0.36	Check
80	1.01	0.96	0.32	Check
81	0.25	0.09	-0.23	Check
82	0.85	0.84	0.09	Check
83	0.72	0.72	0.05	Check
84	1.00	0.89	0.45	Check
85	0.49	0.49	0.10	Check
86	0.52	0.45	0.26	Check
88	0.96	-0.86	0.44	Check
97	0.22	0.21	0.07	Check
98	0.40	0.38	0.14	Check
99	0.63	0.25	0.58	Check
100	0.65	0.61	0.22	Check
103	0.92	-0.77	0.50	Check
104	1.07	-1.05	-0.20	Check
105	0.37	-0.06	0.37	Check
112	1.89	-1.83	-0.45	Check
113	0.92	-0.91	-0.16	Check
114	0.61	-0.23	0.57	Check
115	1.14	1.01	-0.53	Check
116	1.46	1.41	0.39	Check
117	0.40	0.33	0.23	Check
122	0.96	0.96	0.03	Check

Table E.1 Continued

Point ID	Total Residual	Residual X	Residual Y	Type
123	1.19	1.19	0.06	Check
127	1.54	1.54	0.00	Check
129	0.63	-0.63	-0.03	Check
132	0.91	-0.57	0.70	Check
134	1.79	-1.17	1.36	Check
136	1.37	1.18	0.70	Check
147	1.32	-1.24	0.45	Check
150	0.72	-0.59	0.41	Check
161	0.59	0.45	0.37	Check
163	0.25	0.19	0.16	Check
167	0.68	-0.62	0.29	Check
168	0.79	-0.69	-0.40	Check

Residual Units: Image Pixels

Residual Information for ASTER Nadir Image:

GCPs:	8	X RMS:	0.38	Y RMS: 0.24
C. Points:	67	X RMS:	0.72	Y RMS: 0.41

Table E.2 The RMSE values of the results of the bundle adjustment of ASTER backward image using the GCP set 1.

Point ID	Total Residual	Residual X	Residual Y	Type
28	0.43	0.03	-0.43	GCP
49	0.32	0.09	0.30	GCP
75	0.13	0.12	0.06	GCP
91	0.22	-0.22	-0.03	GCP
106	0.06	0.06	-0.01	GCP
119	0.19	0.08	0.18	GCP
126	0.55	-0.46	0.30	GCP
156	1.04	0.26	-1.00	GCP
6	0.88	-0.58	-0.66	Check
7	0.89	0.11	-0.88	Check
9	0.86	-0.82	-0.25	Check
10	0.38	0.14	0.36	Check
13	0.41	-0.12	-0.39	Check
14	1.47	1.47	-0.06	Check
15	0.89	0.34	0.82	Check
16	0.60	0.52	0.29	Check
17	0.74	0.69	0.25	Check
19	0.66	0.55	0.36	Check
27	0.57	0.52	-0.24	Check
32	0.40	0.39	0.08	Check
33	0.27	0.26	0.09	Check
36	0.45	-0.07	-0.45	Check
38	0.71	-0.22	0.67	Check
39	0.20	0.03	0.20	Check
40	0.34	-0.32	0.11	Check
45	0.46	-0.46	-0.03	Check
46	0.68	0.48	0.48	Check
47	0.86	-0.83	0.22	Check
48	0.62	0.62	0.05	Check
60	0.30	-0.20	-0.22	Check
61	0.39	0.29	-0.26	Check
63	0.42	-0.42	-0.03	Check

Table E.2 Continued

Point ID	Total Residual	Residual X	Residual Y	Type
67	0.31	-0.16	0.27	Check
68	0.91	-0.69	0.60	Check
70	0.36	-0.36	-0.03	Check
71	0.87	-0.84	0.24	Check
72	0.26	-0.16	0.21	Check
76	0.70	-0.58	0.40	Check
78	0.90	0.68	0.59	Check
79	0.90	0.80	0.40	Check
80	0.50	0.43	0.27	Check
81	0.29	0.20	0.21	Check
82	0.68	0.67	0.09	Check
83	0.42	0.40	0.15	Check
84	0.96	0.72	0.64	Check
85	0.61	0.45	0.41	Check
86	0.29	0.29	0.03	Check
88	0.79	-0.35	0.71	Check
97	0.49	0.48	0.07	Check
98	0.53	0.42	0.33	Check
99	0.80	-0.24	0.77	Check
100	0.23	0.17	0.15	Check
103	0.80	-0.79	0.10	Check
104	0.85	-0.74	-0.42	Check
105	0.59	-0.26	0.53	Check
112	1.18	-1.16	-0.23	Check
113	0.14	-0.14	0.02	Check
114	0.41	0.01	0.41	Check
115	1.29	1.14	0.60	Check
116	1.25	1.15	0.47	Check
117	0.96	0.62	0.74	Check
122	0.79	0.76	0.22	Check
123	1.11	0.88	0.67	Check
127	1.79	1.67	0.64	Check
129	0.47	0.32	-0.35	Check
132	0.16	0.10	0.13	Check
134	1.36	-1.05	0.86	Check
136	1.00	0.95	0.32	Check

Table E.2 Continued

Point ID	Total Residual	Residual X	Residual Y	Type
147	1.26	-1.26	0.04	Check
150	1.07	-1.02	-0.34	Check
161	0.81	0.75	-0.29	Check
163	0.71	0.57	0.43	Check
167	0.50	-0.39	-0.32	Check
168	0.81	-0.80	-0.15	Check

Residual Units: Image Pixels

Residual Information for ASTER Nadir Image:

GCPs: 8 X RMS: 0.23 Y RMS: 0.45

C. Points: 67 X RMS: 0.66 Y RMS: 0.44

Table E.3 The RMSE values of the results of the bundle adjustment of ASTER nadir image using the GCP set 2.

Point ID	Total Residual	Residual X	Residual Y	Type
28	0.25	-0.11	-0.23	GCP
49	0.79	0.29	0.74	GCP
63	0.41	-0.19	-0.36	GCP
76	0.09	-0.06	0.07	GCP
79	0.91	0.91	0.09	GCP
97	0.14	0.12	0.07	GCP
103	0.25	-0.14	0.20	GCP
112	1.08	-0.87	-0.64	GCP
119	0.47	-0.34	-0.33	GCP
126	0.46	0.44	0.15	GCP
127	1.04	1.04	-0.03	GCP
132	1.73	-1.70	0.29	GCP
136	0.54	0.50	0.21	GCP
156	0.70	0.67	-0.22	GCP
163	0.13	-0.06	0.11	GCP
167	0.57	-0.56	0.12	GCP

5	1.46	-1.46	0.00	Check
6	1.33	0.05	-1.33	Check
7	0.70	0.03	-0.70	Check
9	0.25	-0.08	-0.24	Check
10	0.77	0.76	-0.10	Check
13	0.85	0.57	-0.62	Check
14	1.38	1.37	-0.07	Check
15	0.88	0.85	0.23	Check
16	1.05	1.01	-0.31	Check
17	0.73	0.72	-0.10	Check
19	0.33	0.25	-0.22	Check
27	0.20	0.07	-0.19	Check
32	0.37	-0.10	-0.35	Check
33	0.23	-0.13	-0.19	Check
38	0.36	-0.17	-0.32	Check
39	0.26	0.10	0.24	Check

Table E.3 Continued

Point ID	Total Residual	Residual X	Residual Y	Type
40	0.14	0.14	-0.03	Check
45	0.39	-0.29	0.26	Check
46	0.56	0.52	0.22	Check
47	0.34	0.21	-0.26	Check
48	0.55	0.22	0.50	Check
60	0.90	0.71	0.54	Check
61	1.47	1.30	-0.68	Check
66	0.83	0.09	0.82	Check
67	0.22	-0.18	-0.14	Check
68	0.49	-0.02	0.49	Check
70	0.25	-0.25	0.04	Check
71	0.57	-0.57	0.00	Check
72	0.22	0.02	0.22	Check
75	0.87	0.74	-0.45	Check
78	1.36	1.36	0.06	Check
80	1.19	1.19	0.08	Check
81	0.52	0.32	-0.41	Check
82	1.09	1.08	-0.11	Check
83	0.88	0.87	-0.08	Check
84	1.03	0.97	0.35	Check
85	0.46	0.45	0.08	Check
86	0.45	0.43	0.15	Check
88	0.77	-0.75	0.21	Check
91	0.47	-0.46	0.09	Check
98	0.37	0.34	0.15	Check
99	0.67	0.51	0.44	Check
100	0.95	0.94	0.11	Check
104	0.71	-0.47	-0.53	Check
105	0.55	0.43	0.34	Check
106	0.36	0.36	-0.04	Check
109	1.80	-1.77	0.29	Check
113	0.52	-0.39	-0.35	Check
114	0.45	0.17	0.42	Check
115	1.00	0.85	-0.53	Check
116	1.38	1.32	0.41	Check
117	0.08	0.06	0.05	Check

Table E.3 Continued

Point ID	Total Residual	Residual X	Residual Y	Type
122	1.05	1.05	0.00	Check
123	0.94	0.94	0.05	Check
128	1.09	1.02	0.39	Check
129	1.71	-1.68	-0.30	Check
147	1.72	-1.72	0.03	Check
150	0.63	-0.62	0.15	Check
161	0.50	0.48	0.14	Check
168	1.10	-0.82	-0.73	Check

Residual Units: Image Pixels

Residual Information for ASTER Nadir Image:

GCPs: 16 X RMS: 0.69 Y RMS: 0.32

C. Points: 61 X RMS: 0.78 Y RMS: 0.37

Table E.4 The RMSE values of the results of the bundle adjustment of ASTER backward image using the GCP set 2.

Point ID	Total Residual	Residual X	Residual Y	Type
28	0.72	-0.01	-0.72	GCP
49	0.37	0.12	0.36	GCP
63	0.10	-0.02	-0.10	GCP
76	0.50	-0.46	0.20	GCP
79	0.93	0.92	0.17	GCP
97	0.17	0.15	0.08	GCP
103	0.26	-0.23	-0.12	GCP
112	0.49	-0.35	-0.34	GCP
119	0.38	-0.38	0.02	GCP
126	0.21	0.01	0.21	GCP
127	1.11	0.87	0.69	GCP
132	1.07	-1.07	-0.05	GCP
136	0.44	0.43	0.06	GCP
156	1.47	0.66	-1.31	GCP
163	0.31	0.07	0.30	GCP
167	0.60	-0.39	-0.46	GCP
5	1.48	-1.21	-0.86	Check
6	0.97	-0.23	-0.94	Check
7	1.15	0.22	-1.13	Check
9	0.69	-0.48	-0.49	Check
10	0.44	0.42	0.11	Check
13	0.63	-0.15	-0.62	Check
14	1.37	1.35	-0.26	Check
15	0.67	0.30	0.60	Check
16	0.48	0.47	0.09	Check
17	0.57	0.57	0.06	Check
19	0.36	0.31	0.18	Check
27	0.44	0.18	-0.41	Check
32	0.11	-0.11	-0.02	Check
33	0.26	-0.25	0.06	Check
36	0.63	-0.11	-0.62	Check
38	0.65	-0.39	0.52	Check

Table E.4 Continued

Point ID	Total Residual	Residual X	Residual Y	Type
40	0.27	-0.26	-0.09	Check
45	0.41	-0.41	-0.06	Check
46	0.64	0.46	0.44	Check
47	0.79	-0.75	0.27	Check
48	0.36	0.35	0.07	Check
60	0.46	0.30	-0.35	Check
61	0.73	0.66	-0.31	Check
66	1.22	-0.47	1.12	Check
67	0.17	0.02	0.16	Check
68	0.84	-0.66	0.51	Check
70	0.63	-0.63	-0.03	Check
71	1.09	-1.07	0.21	Check
72	0.51	-0.46	0.21	Check
75	0.23	0.18	-0.14	Check
78	0.77	0.61	0.47	Check
80	0.55	0.54	0.08	Check
81	0.29	0.28	0.08	Check
82	0.77	0.77	-0.06	Check
83	0.38	0.38	0.05	Check
84	0.83	0.62	0.55	Check
85	0.44	0.20	0.39	Check
86	0.12	0.11	-0.06	Check
88	0.60	-0.29	0.53	Check
91	0.28	-0.28	-0.05	Check
98	0.37	0.14	0.34	Check
99	0.70	-0.16	0.68	Check
100	0.32	0.31	0.08	Check
104	0.70	-0.19	-0.68	Check
105	0.52	0.00	0.52	Check
106	0.14	0.14	0.02	Check
109	1.44	-1.36	0.47	Check
113	0.24	0.23	-0.09	Check
114	0.40	0.22	0.33	Check
115	0.96	0.72	0.63	Check
116	0.95	0.81	0.50	Check
117	0.69	0.19	0.66	Check

Table E.4 Continued

Point ID	Total Residual	Residual X	Residual Y	Type
122	0.61	0.56	0.25	Check
123	0.80	0.34	0.72	Check
128	1.17	0.83	0.83	Check
129	0.97	-0.87	-0.43	Check
147	1.67	-1.66	-0.19	Check
150	1.18	-1.06	-0.52	Check
161	0.82	0.65	-0.50	Check
168	0.98	-0.91	-0.36	Check

Residual Units: Image Pixels

Residual Information for ASTER Nadir Image:

GCPs: 16 X RMS: 0.52 Y RMS: 0.48

C. Points: 61 X RMS: 0.60 Y RMS: 0.46

Table E.5 The RMSE values of the results of the bundle adjustment of ASTER nadir image using the GCP set 3.

Point ID	Total Residual	Residual X	Residual Y	Type
5	1.08	-1.08	0.01	GCP
10	0.80	0.80	-0.01	GCP
17	0.58	0.58	0.01	GCP
28	0.33	0.21	-0.25	GCP
32	0.36	-0.24	-0.27	GCP
36	0.17	0.09	-0.14	GCP
49	0.90	0.18	0.88	GCP
63	0.23	-0.17	-0.16	GCP
72	0.49	-0.32	0.37	GCP
76	0.30	-0.18	0.24	GCP
79	0.82	0.79	0.23	GCP
91	0.67	-0.61	0.29	GCP
97	0.34	-0.23	0.25	GCP
106	0.15	0.14	0.06	GCP
112	0.95	-0.83	-0.47	GCP
115	0.60	0.51	-0.31	GCP
119	0.43	-0.42	-0.04	GCP
126	0.61	0.39	0.47	GCP
127	0.77	0.72	0.27	GCP
129	1.80	-1.80	0.05	GCP
136	0.98	0.81	0.55	GCP
156	1.26	1.25	0.11	GCP
163	0.27	-0.22	0.16	GCP
168	0.93	-0.81	-0.45	GCP
6	1.32	0.28	-1.29	Check
7	0.67	0.13	-0.66	Check
9	0.16	0.00	-0.16	Check
13	0.76	0.53	-0.55	Check
14	1.33	1.33	-0.01	Check
15	0.84	0.77	0.33	Check
16	0.91	0.88	-0.20	Check
19	0.18	0.11	-0.14	Check

Table E.5 Continued

Point ID	Total Residual	Residual X	Residual Y	Type
33	0.37	-0.35	-0.10	Check
38	0.38	-0.33	-0.20	Check
39	0.37	-0.04	0.37	Check
40	0.13	0.02	0.13	Check
45	0.59	-0.42	0.42	Check
46	0.53	0.38	0.37	Check
47	0.15	0.11	-0.11	Check
48	0.62	0.03	0.62	Check
60	1.07	0.76	0.75	Check
61	1.39	1.30	-0.49	Check
66	1.03	0.05	1.03	Check
67	0.27	-0.26	0.05	Check
68	0.69	-0.18	0.67	Check
70	0.58	-0.55	0.20	Check
71	0.86	-0.85	0.17	Check
75	0.67	0.60	-0.30	Check
78	1.15	1.13	0.20	Check
80	1.08	1.05	0.22	Check
81	0.30	0.14	-0.26	Check
82	0.90	0.90	0.05	Check
83	0.64	0.63	0.08	Check
84	0.87	0.71	0.51	Check
85	0.28	0.13	0.24	Check
86	0.39	0.17	0.35	Check
88	0.97	-0.87	0.44	Check
98	0.32	0.00	0.32	Check
99	0.68	0.29	0.62	Check
100	0.79	0.74	0.26	Check
103	0.27	0.02	0.27	Check
104	0.54	-0.23	-0.48	Check
105	0.54	0.27	0.47	Check
109	1.49	-1.43	0.43	Check
113	0.54	-0.51	-0.16	Check
114	0.63	0.00	0.63	Check
116	1.13	0.96	0.60	Check
117	0.36	-0.18	0.32	Check

Table E.5 Continued

Point ID	Total Residual	Residual X	Residual Y	Type
122	0.82	0.78	0.26	Check
123	0.70	0.62	0.32	Check
128	1.00	0.72	0.69	Check
132	1.80	-1.68	0.66	Check
147	1.64	-1.61	0.35	Check
150	0.79	-0.68	0.41	Check
161	0.58	0.56	0.16	Check
167	0.73	-0.64	0.36	Check

Residual Units: Image Pixels

Residual Information for ASTER Nadir Image:

GCPs: 24 X RMS: 0.71 Y RMS: 0.33

C. Points: 53 X RMS: 0.69 Y RMS: 0.45

Table E.6 The RMSE values of the results of the bundle adjustment of ASTER backward image using the GCP set 3.

Point ID	Total Residual	Residual X	Residual Y	Type
5	1.12	-0.86	-0.72	GCP
10	0.65	0.58	0.28	GCP
17	0.64	0.61	0.22	GCP
28	0.66	0.23	-0.62	GCP
32	0.31	-0.22	0.23	GCP
36	0.37	-0.05	-0.36	GCP
49	0.40	0.12	0.39	GCP
63	0.24	0.21	-0.13	GCP
72	0.55	-0.55	-0.03	GCP
76	0.52	-0.35	0.38	GCP
79	1.06	1.00	0.36	GCP
91	0.35	-0.20	-0.30	GCP
97	0.18	0.00	-0.18	GCP
106	0.22	0.06	-0.22	GCP
112	0.36	-0.27	-0.23	GCP
115	0.60	0.47	0.37	GCP
119	0.44	-0.43	-0.11	GCP
126	0.53	-0.20	0.49	GCP
127	0.64	0.45	0.45	GCP
129	1.38	-1.19	-0.69	GCP
136	0.66	0.63	-0.19	GCP
156	1.92	1.23	-1.47	GCP
163	0.36	0.02	0.36	GCP
168	0.89	-0.78	-0.42	GCP
6	0.78	0.02	-0.78	Check
7	1.07	0.38	-1.00	Check
9	0.45	-0.30	-0.33	Check
13	0.46	-0.06	-0.46	Check
14	1.43	1.42	-0.15	Check
15	0.87	0.38	0.78	Check
16	0.59	0.53	0.25	Check
19	0.45	0.32	0.32	Check

Table E.6 Continued

Point ID	Total Residual	Residual X	Residual Y	Type
33	0.39	-0.37	0.12	Check
38	0.78	-0.37	0.69	Check
39	0.21	-0.01	0.21	Check
40	0.21	-0.16	0.13	Check
45	0.35	-0.35	-0.04	Check
46	0.72	0.49	0.52	Check
47	0.75	-0.71	0.26	Check
48	0.30	0.28	0.10	Check
60	0.57	0.54	-0.20	Check
61	0.85	0.83	-0.20	Check
66	1.17	-0.29	1.13	Check
67	0.25	0.17	0.18	Check
68	0.75	-0.58	0.48	Check
70	0.73	-0.68	-0.27	Check
71	1.10	-1.10	0.00	Check
75	0.27	0.27	0.05	Check
78	0.77	0.61	0.46	Check
80	0.64	0.61	0.20	Check
81	0.32	0.30	0.11	Check
82	0.79	0.79	0.00	Check
83	0.34	0.34	0.01	Check
84	0.75	0.58	0.48	Check
85	0.22	0.11	0.19	Check
86	0.18	0.06	-0.17	Check
88	0.59	-0.19	0.55	Check
98	0.10	-0.01	0.10	Check
99	0.69	-0.22	0.65	Check
100	0.28	0.27	0.03	Check
103	0.01	0.00	0.00	Check
104	0.55	0.07	-0.54	Check
105	0.39	-0.05	0.39	Check
109	1.28	-1.02	0.76	Check
113	0.21	0.21	-0.03	Check
114	0.38	0.13	0.36	Check
116	0.66	0.62	0.23	Check
117	0.52	0.04	0.52	Check

Table E.6 Continued

Point ID	Total Residual	Residual X	Residual Y	Type
122	0.29	0.26	0.14	Check
123	0.52	-0.04	0.52	Check
128	0.66	0.37	0.55	Check
132	1.31	-1.28	-0.24	Check
147	1.59	-1.55	-0.34	Check
150	1.11	-0.94	-0.57	Check
161	0.89	0.77	-0.45	Check
167	0.62	-0.26	-0.56	Check

Residual Units: Image Pixels

Residual Information for ASTER Nadir Image:

GCPs: 24 X RMS: 0.58 Y RMS: 0.49

C. Points: 53 X RMS: 0.57 Y RMS: 0.44

Table E.7 The RMSE values of the results of the bundle adjustment of ASTER nadir image using the GCP set 4.

Point ID	Total Residual	Residual X	Residual Y	Type
5	1.29	-1.29	0.00	GCP
10	0.66	0.66	-0.05	GCP
14	1.17	1.17	-0.03	GCP
17	0.50	0.50	-0.02	GCP
28	0.24	-0.07	-0.23	GCP
32	0.41	-0.27	-0.30	GCP
36	0.21	0.12	-0.17	GCP
45	0.46	-0.28	0.37	GCP
49	0.89	0.36	0.81	GCP
63	0.20	0.07	-0.18	GCP
70	0.55	-0.53	0.14	GCP
72	0.47	-0.36	0.30	GCP
76	0.25	-0.13	0.21	GCP
79	0.75	0.73	0.19	GCP
82	0.83	0.83	-0.03	GCP
91	0.55	-0.49	0.25	GCP
97	0.33	-0.30	0.15	GCP
103	0.25	-0.13	0.21	GCP
106	0.08	0.00	-0.08	GCP
112	1.11	-0.91	-0.65	GCP
114	0.47	-0.08	0.46	GCP
115	0.62	0.41	-0.46	GCP
119	0.44	-0.43	-0.10	GCP
122	0.67	0.67	0.04	GCP
126	0.39	0.34	0.19	GCP
127	0.59	0.59	0.07	GCP
129	1.93	-1.92	-0.07	GCP
136	1.06	0.89	0.58	GCP
156	1.55	1.54	0.18	GCP
163	0.40	-0.37	0.15	GCP
167	0.63	-0.53	0.33	GCP
168	0.87	-0.73	-0.47	GCP

Table E.7 Continued

Point ID	Total Residual	Residual X	Residual Y	Type
7	0.68	-0.06	-0.68	Check
9	0.26	-0.15	-0.21	Check
13	0.69	0.39	-0.57	Check
15	0.73	0.66	0.30	Check
16	0.82	0.79	-0.23	Check
19	0.16	0.00	-0.16	Check
27	0.25	-0.17	-0.19	Check
33	0.41	-0.39	-0.14	Check
38	0.41	-0.34	-0.23	Check
39	0.35	-0.06	0.34	Check
40	0.11	0.04	0.11	Check
46	0.59	0.49	0.32	Check
47	0.34	0.29	-0.17	Check
48	0.57	0.09	0.56	Check
60	1.24	1.01	0.72	Check
61	1.64	1.54	-0.54	Check
66	1.03	0.22	1.00	Check
67	0.12	-0.12	0.02	Check
68	0.64	-0.09	0.63	Check
71	0.84	-0.83	0.12	Check
75	0.68	0.60	-0.33	Check
78	1.08	1.07	0.15	Check
80	0.99	0.98	0.17	Check
81	0.34	0.06	-0.34	Check
83	0.56	0.56	-0.01	Check
84	0.78	0.65	0.43	Check
85	0.18	0.07	0.16	Check
86	0.31	0.15	0.27	Check
88	0.90	-0.81	0.40	Check
98	0.23	-0.09	0.21	Check
99	0.54	0.21	0.50	Check
100	0.66	0.65	0.14	Check
104	0.67	-0.40	-0.53	Check
105	0.36	0.15	0.32	Check
109	1.52	-1.49	0.29	Check
113	0.67	-0.59	-0.30	Check

Table E.7 Continued

Point ID	Total Residual	Residual X	Residual Y	Type
116	1.00	0.87	0.47	Check
117	0.31	-0.24	0.21	Check
123	0.51	0.50	0.12	Check
128	0.76	0.57	0.50	Check
132	1.87	-1.77	0.58	Check
147	1.59	-1.55	0.34	Check
150	0.71	-0.60	0.38	Check
161	0.36	0.33	0.15	Check

Residual Units: Image Pixels

Residual Information for ASTER Nadir Image:

GCPs: 32 X RMS: 0.72 Y RMS: 0.31

C. Points: 45 X RMS: 0.68 Y RMS: 0.44

Table E.8 The RMSE values of the results of the bundle adjustment of ASTER backward image using the GCP set 4.

Point ID	Total Residual	Residual X	Residual Y	Type
5	1.34	-1.09	-0.78	GCP
10	0.49	0.44	0.22	GCP
14	1.29	1.28	-0.17	GCP
17	0.57	0.54	0.20	GCP
28	0.64	-0.03	-0.64	GCP
32	0.33	-0.24	0.22	GCP
36	0.39	-0.03	-0.39	GCP
45	0.25	-0.25	0.02	GCP
49	0.52	0.24	0.46	GCP
63	0.38	0.38	-0.06	GCP
70	0.68	-0.65	-0.18	GCP
72	0.58	-0.58	0.05	GCP
76	0.48	-0.32	0.36	GCP
79	0.99	0.94	0.31	GCP
82	0.72	0.72	-0.03	GCP
91	0.21	-0.10	-0.19	GCP
97	0.13	-0.05	-0.12	GCP
103	0.19	-0.18	-0.06	GCP
106	0.19	-0.08	-0.18	GCP
112	0.52	-0.40	-0.33	GCP
114	0.30	0.04	0.30	GCP
115	0.57	0.40	0.41	GCP
119	0.43	-0.42	-0.10	GCP
122	0.18	0.15	0.10	GCP
126	0.44	-0.31	0.31	GCP
127	0.57	0.35	0.45	GCP
129	1.42	-1.26	-0.67	GCP
136	0.72	0.71	-0.12	GCP
156	2.01	1.44	-1.40	GCP
163	0.39	-0.10	0.38	GCP
167	0.54	-0.17	-0.51	GCP
168	0.82	-0.71	-0.41	GCP

Table E.8 Continued

Point ID	Total Residual	Residual X	Residual Y	Type
7	1.05	0.20	-1.03	Check
9	0.60	-0.46	-0.39	Check
13	0.53	-0.18	-0.50	Check
15	0.79	0.28	0.74	Check
16	0.50	0.45	0.22	Check
19	0.38	0.23	0.31	Check
27	0.39	0.02	-0.39	Check
33	0.43	-0.39	0.17	Check
38	0.78	-0.38	0.68	Check
39	0.19	-0.03	0.19	Check
40	0.18	-0.15	0.10	Check
46	0.80	0.57	0.56	Check
47	0.67	-0.58	0.34	Check
48	0.37	0.33	0.16	Check
60	0.73	0.70	-0.18	Check
61	1.00	0.99	-0.16	Check
66	1.19	-0.16	1.18	Check
67	0.35	0.27	0.22	Check
68	0.73	-0.51	0.53	Check
71	1.09	-1.08	0.08	Check
75	0.26	0.26	0.01	Check
78	0.73	0.56	0.47	Check
80	0.55	0.53	0.16	Check
81	0.24	0.22	0.09	Check
83	0.28	0.28	0.00	Check
84	0.73	0.53	0.49	Check
85	0.26	0.07	0.25	Check
86	0.15	0.05	-0.15	Check
88	0.57	-0.14	0.55	Check
98	0.17	-0.08	0.15	Check
99	0.70	-0.31	0.63	Check
100	0.17	0.17	0.01	Check
104	0.61	-0.12	-0.60	Check
105	0.43	-0.18	0.39	Check
109	1.33	-1.18	0.61	Check
113	0.14	0.11	-0.09	Check

Table E.8 Continued

Point ID	Total Residual	Residual X	Residual Y	Type
116	0.63	0.56	0.29	Check
117	0.53	0.00	0.53	Check
123	0.53	-0.14	0.51	Check
128	0.62	0.27	0.56	Check
132	1.35	-1.33	-0.23	Check
147	1.53	-1.50	-0.31	Check
150	1.04	-0.88	-0.55	Check
161	0.73	0.57	-0.45	Check

Residual Units: Image Pixels

Residual Information for ASTER Nadir Image:

GCPs: 32 X RMS: 0.61 Y RMS: 0.42

C. Points: 45 X RMS: 0.54 Y RMS: 0.47

APPENDIX F

Table F.1 The information report for the generated epipolar DEM and the elevation RMS errors related to the GCPs and Check Points for set 1.

Program started at 16:36:30
Program stopped at 17:04:18
DEM Extraction summary
CellSpacing: Every 2 Pixel
DEMElevationMin: 200.000000
DEMElevationMax: 2400.000000
DEMBackGroundValue: -150
DEMFailureValue: -100
DEMEditing: Yes
DEMCorrelationSuccessPercent: 0.984549

RMS Error Report on Epipolar DEM File :

GCP ID	DEM Pixel	DEM Line	GCP Elevation	Calculated Elevation	Difference Elevation
28	563.10	1773.00	819.60	812.10	-7.50
49	638.50	495.90	1194.90	1179.60	-15.30
75	1008.40	1069.60	855.50	858.90	3.50
91	1361.10	703.30	1248.00	1239.80	-8.10
106	1362.20	1685.00	1202.70	1212.30	9.60
119	1995.40	990.10	1054.60	1052.30	-2.20
126	2115.60	1829.80	851.60	837.40	-14.20
156	1900.10	340.20	1086.80	1054.40	-32.50

Number of GCPs : 8
RMS Error : 14.70
Average Error : -8.30
Maximum Error : 32.50

Table F.1 Continued

C. Point ID	DEM Pixel	DEM Line	C. Point Elevation	Calculated Elevation	Difference Elevation
6	814.20	1771.90	800.80	803.20	2.40
7	792.90	1639.70	834.50	835.30	0.80
9	965.50	1663.10	818.10	821.10	3.00
10	968.00	1607.10	812.20	812.90	0.60
13	842.30	1434.90	841.10	844.50	3.40
14	779.80	1450.70	871.60	878.00	6.40
15	855.00	1338.90	830.40	838.60	8.20
16	909.20	1279.70	864.30	871.90	7.60
17	834.10	1193.70	874.60	882.50	7.90
19	748.20	1232.20	893.40	901.30	8.00
27	658.10	1537.10	959.90	960.50	0.60
32	414.60	835.60	933.60	935.30	1.70
33	542.20	845.30	1073.00	1077.50	4.50
36	724.10	861.20	873.40	875.40	2.10
38	761.70	965.30	923.30	930.30	7.00
39	821.30	1017.00	882.00	884.60	2.60
40	917.30	963.00	852.30	854.30	2.00
45	820.80	615.50	1127.90	1127.00	-0.90
46	756.60	668.60	1072.40	1074.10	1.70
47	730.40	502.00	1210.30	1204.80	-5.60
48	621.70	684.80	1136.70	1145.60	9.00
60	963.10	509.30	1014.40	999.50	-14.90
61	817.60	471.80	1095.00	1089.10	-5.90
63	1106.40	497.40	1143.00	1129.20	-13.70
66	1155.10	634.70	1067.20	1059.70	-7.50
67	1099.40	682.50	1063.80	1068.30	4.50
68	1132.10	793.30	1083.80	1074.60	-9.20
70	1261.70	930.90	1235.70	1232.60	-3.00
71	1341.20	967.20	1192.00	1191.80	-0.30
72	1349.00	1131.90	1202.70	1204.70	2.10
76	1025.00	925.40	886.10	892.90	6.90
78	1194.00	1245.80	1004.50	1010.20	5.60
79	1061.60	1292.90	831.30	831.90	0.60
80	1144.50	1369.10	883.20	879.10	-4.10
81	1249.50	1413.70	959.90	960.30	0.40
82	1301.90	1388.20	941.60	935.60	-6.00

Table F.1 Continued

C. Point ID	DEM Pixel	DEM Line	C. Point Elevation	Calculated Elevation	Difference Elevation
83	1415.40	1362.80	1029.60	1032.80	3.20
84	1357.10	1265.70	1057.30	1057.90	0.60
85	1416.70	1202.60	1165.60	1166.80	1.20
86	1528.70	1142.80	1089.40	1084.20	-5.20
88	1460.90	935.80	973.60	973.20	-0.40
97	1566.00	1254.90	1211.80	1213.40	1.60
98	1528.30	1325.70	1204.00	1205.90	1.90
99	1528.00	1489.40	1021.50	1026.00	4.50
100	1449.40	1559.50	1035.20	1040.60	5.40
103	1021.00	1813.20	857.50	862.30	4.80
104	931.00	1831.30	825.20	824.00	-1.20
105	1450.80	1718.70	1113.70	1116.50	2.90
112	1538.00	1882.00	929.00	926.50	-2.40
113	1567.70	1647.90	948.60	953.20	4.60
114	1696.80	1617.40	995.60	997.70	2.10
115	1842.00	1378.90	1218.70	1224.20	5.50
116	1645.70	1334.40	1227.10	1235.10	8.00
117	1908.00	1204.00	1101.40	1100.60	-0.70
122	2011.10	1607.70	1132.60	1133.80	1.20
123	2107.90	1494.30	1197.60	1202.30	4.70
127	2214.50	1419.60	1216.60	1217.90	1.30
129	2380.80	1106.10	1159.10	1152.20	-6.80
132	2418.60	994.30	1080.40	1064.20	-16.20
134	2337.70	886.80	1012.90	996.00	-17.00
136	2189.20	627.20	1097.10	1079.60	-17.50
147	2056.10	774.60	1044.80	1036.00	-8.80
150	1654.10	848.20	1029.40	1023.50	-5.90
161	710.60	1629.40	903.90	897.80	-6.10
163	625.90	1219.70	967.90	975.40	7.50
167	1536.70	784.60	1086.00	1079.10	-6.90
168	1793.40	823.80	1014.40	1013.70	-0.70

Number of CPs : 67
RMS Error : 6.40
Average Error : -0.10
Maximum Error : 17.50

Table F.2 The information report for the generated epipolar DEM and the elevation RMS errors related to the GCPs and Check Points for set 2.

Program started at 18:14:07
Program stopped at 18:40:51
DEM Extraction summary
CellSpacing: Every 2 Pixel
DEMElevationMin: 200.000000
DEMElevationMax: 2400.000000
DEMBackGroundValue: -150
DEMFailureValue: -100
DEMEditing: Yes
DEMCorrelationSuccessPercent: 0.984836

RMS Error Report on Epipolar DEM File :

GCP ID	DEM Pixel	DEM Line	GCP Elevation	Calculated Elevation	Difference Elevation
28	564.10	1734.30	819.60	814.10	-5.50
49	639.30	482.30	1194.90	1172.70	-22.20
63	1107.30	483.80	1143.00	1127.80	-15.10
76	1026.00	904.40	886.10	890.70	4.70
79	1062.60	1265.70	831.30	831.20	-0.10
97	1567.00	1229.90	1211.80	1216.90	5.10
103	1021.90	1776.80	857.50	862.80	5.30
112	1538.90	1847.50	929.00	925.40	-3.60
119	1996.50	969.40	1054.60	1056.50	2.00
126	2116.60	1798.90	851.60	840.30	-11.30
127	2215.60	1393.90	1216.60	1222.90	6.30
132	2419.80	973.50	1080.40	1074.00	-6.40
136	2190.30	610.80	1097.10	1087.30	-9.80
156	1901.10	328.00	1086.80	1054.90	-31.90
163	626.90	1192.20	967.90	974.30	6.40
167	1537.80	766.50	1086.00	1080.00	-6.00

Number of GCPs : 16
RMS Error : 11.8
Average Error : -5.1
Maximum Error : 31.9

Table F.2 Continued

C. Point ID	DEM Pixel	DEM Line	C. Point Elevation	Calculated Elevation	Difference Elevation
5	786.50	1873.80	804.90	806.80	1.90
6	815.20	1735.00	800.80	804.10	3.40
7	793.90	1605.00	834.50	837.00	2.50
9	966.50	1629.00	818.10	824.10	6.00
10	969.00	1574.00	812.20	813.60	1.30
13	843.30	1404.30	841.10	844.50	3.30
14	780.80	1419.50	871.60	878.30	6.70
15	856.00	1310.10	830.40	837.90	7.50
16	910.20	1252.20	864.30	871.90	7.70
17	835.10	1167.50	874.60	883.00	8.40
19	749.20	1205.00	893.40	900.90	7.50
27	659.10	1503.60	959.90	961.90	2.00
32	415.50	815.00	933.60	930.50	-3.10
33	543.10	824.80	1073.00	1076.60	3.60
36	725.00	840.80	873.40	873.80	0.50
38	762.60	943.00	923.30	929.50	6.20
39	822.20	994.00	882.00	883.10	1.10
40	918.20	941.20	852.30	853.20	0.90
45	821.70	599.80	1127.90	1123.80	-4.10
46	757.50	651.90	1072.40	1069.20	-3.20
47	731.30	488.30	1210.30	1198.20	-12.20
48	622.60	667.50	1136.70	1138.00	1.40
60	964.00	495.60	1014.40	995.80	-18.60
61	818.50	458.70	1095.00	1082.60	-12.40
66	1156.00	618.80	1067.20	1057.10	-10.10
67	1100.40	665.80	1063.80	1064.00	0.10
68	1133.10	774.80	1083.80	1073.60	-10.20
70	1262.70	910.30	1235.70	1232.10	-3.50
71	1342.20	946.10	1192.00	1191.70	-0.30
72	1350.00	1108.30	1202.70	1205.00	2.30
75	1009.40	1046.10	855.50	856.30	0.80
78	1195.00	1219.80	1004.50	1010.70	6.20
80	1145.50	1340.90	883.20	883.80	0.60
81	1250.50	1385.20	959.90	961.20	1.30
82	1302.90	1360.30	941.60	935.60	-6.10
83	1416.40	1335.70	1029.60	1033.40	3.80

Table F.2 Continued

C. Point ID	DEM Pixel	DEM Line	C. Point Elevation	Calculated Elevation	Difference Elevation
84	1358.10	1240.00	1057.30	1059.30	1.90
85	1417.70	1178.00	1165.60	1167.40	1.80
86	1529.80	1119.40	1089.40	1093.10	3.60
88	1461.90	915.40	973.60	973.90	0.30
91	1362.10	686.40	1248.00	1237.10	-10.80
98	1529.30	1299.60	1204.00	1206.60	2.60
99	1529.00	1460.70	1021.50	1027.80	6.20
100	1450.40	1529.50	1035.20	1041.70	6.40
104	932.00	1794.00	825.20	824.20	-1.00
105	1451.80	1686.30	1113.70	1117.90	4.30
106	1363.20	1652.70	1202.70	1212.10	9.40
109	1327.50	1990.90	751.60	748.40	-3.20
113	1568.70	1617.10	948.60	954.60	6.00
114	1697.80	1587.60	995.60	998.70	3.20
115	1843.10	1352.90	1218.70	1226.30	7.60
116	1646.70	1308.40	1227.10	1236.50	9.30
117	1909.10	1180.30	1101.40	1106.40	5.00
122	2012.10	1579.10	1132.60	1135.10	2.50
123	2109.00	1467.40	1197.60	1206.30	8.70
128	2297.20	1328.00	1243.60	1246.90	3.30
129	2382.00	1084.20	1159.10	1158.30	-0.70
147	2057.30	756.60	1044.80	1042.90	-1.90
150	1655.10	829.20	1029.40	1026.00	-3.40
161	711.50	1594.50	903.90	898.40	-5.50
168	1794.50	805.20	1014.40	1013.90	-0.50

Number of CPs	:	61
RMS Error	:	5.9
Average Error	:	1
Maximum Error	:	18.6

Table F.3 The information report for the generated epipolar DEM and the elevation RMS errors related to the GCPs and Check Points for set 3.

Program started at 19:54:10
Program stopped at 20:25:47
DEM Extraction summary
CellSpacing: Every 2 Pixel
DEMElevationMin: 200.000000
DEMElevationMax: 2400.000000
DEMBackGroundValue: -150
DEMFailureValue: -100
DEMEditing: Yes
DEMCorrelationSuccessPercent: 0.985085

RMS Error Report on Epipolar DEM File :

GCP ID	DEM Pixel	DEM Line	GCP Elevation	Calculated Elevation	Difference Elevation
5	786.60	1873.40	804.90	809.00	4.10
10	969.00	1573.60	812.20	817.70	5.40
17	835.20	1167.10	874.60	881.40	6.80
28	564.20	1734.10	819.60	816.50	-3.00
32	415.70	814.90	933.60	936.30	2.60
36	725.20	840.50	873.40	874.70	1.40
49	639.50	482.20	1194.90	1169.90	-25.00
63	1107.40	483.40	1143.00	1120.10	-22.90
72	1350.10	1107.70	1202.70	1194.30	-8.40
76	1026.00	904.00	886.10	893.60	7.50
79	1062.70	1265.20	831.30	833.90	2.70
91	1362.10	685.90	1248.00	1226.90	-21.00
97	1567.00	1229.20	1211.80	1207.00	-4.80
106	1363.20	1652.00	1202.70	1202.90	0.20
112	1539.00	1846.80	929.00	923.10	-5.80
115	1843.10	1352.10	1218.70	1217.00	-1.70
119	1996.40	968.70	1054.60	1046.90	-7.70
126	2116.70	1798.10	851.60	843.00	-8.60
127	2215.50	1393.10	1216.60	1210.50	-6.10
129	2381.90	1083.50	1159.10	1146.00	-13.10
136	2190.20	610.30	1097.10	1072.20	-24.80
156	1901.00	327.40	1086.80	1043.60	-43.20

Table F.3 Continued

GCP ID	DEM Pixel	DEM Line	GCP Elevation	Calculated Elevation	Difference Elevation
163	627.00	1192.00	967.90	973.10	5.20
168	1794.40	804.60	1014.40	1004.40	-10.00

Number of GCPs : 24
RMS Error : 14.20
Average Error : -7.10
Maximum Error : 43.20

C. Point ID	DEM Pixel	DEM Line	C. Point Elevation	Calculated Elevation	Difference Elevation
6	815.30	1734.60	800.80	804.90	4.10
7	793.90	1604.70	834.50	837.90	3.50
9	966.60	1628.50	818.10	824.60	6.50
13	843.40	1403.90	841.10	845.20	4.10
14	780.90	1419.20	871.60	879.00	7.40
15	856.00	1309.70	830.40	843.10	12.70
16	910.30	1251.80	864.30	871.60	7.30
19	749.30	1204.70	893.40	901.30	7.90
27	659.20	1503.40	959.90	960.50	0.60
33	543.30	824.70	1073.00	1073.10	0.10
38	762.70	942.70	923.30	927.90	4.70
39	822.30	993.60	882.00	886.50	4.50
40	918.30	940.80	852.30	854.60	2.30
45	821.80	599.50	1127.90	1119.60	-8.30
46	757.60	651.60	1072.40	1067.70	-4.70
47	731.40	488.10	1210.30	1193.10	-17.20
48	622.80	667.40	1136.70	1136.70	0.00
60	964.10	495.20	1014.40	992.90	-21.50
61	818.60	458.50	1095.00	1082.80	-12.20
66	1156.10	618.40	1067.20	1052.40	-14.80
67	1100.50	665.40	1063.80	1061.20	-2.60
68	1133.10	774.30	1083.80	1070.20	-13.60
70	1262.70	909.80	1235.70	1222.40	-13.30

Table F.3 Continued

C. Point ID	DEM Pixel	DEM Line	C. Point Elevation	Calculated Elevation	Difference Elevation
71	1342.30	945.50	1192.00	1181.70	-10.40
75	1009.50	1045.70	855.50	861.80	6.30
78	1195.10	1219.30	1004.50	1005.00	0.50
80	1145.50	1340.40	883.20	881.50	-1.70
81	1250.50	1384.60	959.90	958.80	-1.10
82	1302.90	1359.70	941.60	935.20	-6.40
83	1416.50	1335.10	1029.60	1023.90	-5.70
84	1358.20	1239.30	1057.30	1052.70	-4.60
85	1417.70	1177.40	1165.60	1157.80	-7.80
86	1529.80	1118.80	1089.40	1079.70	-9.70
88	1461.90	914.80	973.60	966.80	-6.70
98	1529.30	1298.90	1204.00	1196.50	-7.50
99	1529.10	1460.10	1021.50	1019.80	-1.70
100	1450.40	1528.90	1035.20	1037.70	2.40
103	1022.00	1776.30	857.50	863.20	5.70
104	932.10	1793.50	825.20	825.70	0.60
105	1451.80	1685.60	1113.70	1107.90	-5.80
109	1327.50	1990.20	751.60	752.30	0.80
113	1568.70	1616.40	948.60	951.70	3.10
114	1697.80	1586.80	995.60	994.80	-0.80
116	1646.70	1307.70	1227.10	1224.40	-2.70
117	1909.00	1179.70	1101.40	1097.60	-3.70
122	2012.10	1578.30	1132.60	1128.20	-4.40
123	2109.00	1466.60	1197.60	1194.90	-2.70
128	2297.20	1327.40	1243.60	1232.50	-11.10
132	2419.70	973.00	1080.40	1060.30	-20.10
147	2057.20	756.00	1044.80	1030.50	-14.30
150	1655.10	828.60	1029.40	1018.50	-10.90
161	711.60	1594.10	903.90	897.30	-6.60
167	1537.70	765.90	1086.00	1073.50	-12.50

Number of CPs : 53
RMS Error : 8.40
Average Error : -3.40
Maximum Error : 21.50

Table F.4 The information report for the generated epipolar DEM and the elevation RMS errors related to the GCPs and Check Points for set 4.

Program started at 11:36:55
Program stopped at 12:03:47
DEM Extraction summary
CellSpacing: Every 2 Pixel
DEMElevationMin: 200.000000
DEMElevationMax: 2400.000000
DEMBackGroundValue: -150
DEMFailureValue: -100
DEMEditing: Yes
DEMCorrelationSuccessPercent: 0.984836

GCP ID	DEM Pixel	DEM Line	GCP Elevation	Calculated Elevation	Difference Elevation
5	786.60	1872.30	804.90	808.20	1342.81
10	969.00	1572.30	812.20	817.20	1273.42
14	780.80	1418.30	871.60	879.50	1339.38
17	835.20	1166.20	874.60	882.40	1286.14
28	564.10	1733.60	819.60	816.40	1342.03
32	415.70	814.90	933.60	936.80	1324.85
36	725.10	839.90	873.40	875.60	1218.25
45	821.70	598.70	1127.90	1122.60	1481.6
49	639.40	481.80	1194.90	1172.30	1548.11
63	1107.30	482.10	1143.00	1124.20	1431.35
70	1262.70	908.00	1235.70	1226.50	1626.38
72	1350.00	1105.80	1202.70	1198.80	1617.75
76	1026.00	902.70	886.10	893.30	1205.23
79	1062.70	1263.80	831.30	833.70	1197.5
82	1302.90	1357.80	941.60	936.10	1328.15
91	1362.10	684.10	1248.00	1228.60	1571.09
97	1567.00	1226.90	1211.80	1210.00	1623.78
103	1022.00	1774.80	857.50	865.10	1332.39
106	1363.20	1649.90	1202.70	1208.50	1719.41
112	1539.00	1844.30	929.00	925.10	1374.74
114	1697.80	1584.10	995.60	997.70	1397.4
115	1843.00	1349.20	1218.70	1221.00	1625.69
119	1996.40	965.60	1054.60	1048.50	1311.98
122	2012.10	1575.10	1132.60	1131.40	1536.43

Table F.4 Continued

GCP ID	DEM Pixel	DEM Line	GCP Elevation	Calculated Elevation	Difference Elevation
126	2116.70	1794.50	851.60	846.10	1199.51
127	2215.50	1389.50	1216.60	1214.90	1585.77
129	2381.90	1079.70	1159.10	1149.50	1425.3
136	2190.10	606.90	1097.10	1073.40	1255.24
156	1900.90	324.70	1086.80	1044.90	1191.77
163	627.00	1191.40	967.90	974.90	1374.25
167	1537.70	763.70	1086.00	1074.30	1334.61
168	1794.40	801.90	1014.40	1005.40	1225.26

Number of GCPs : 32
RMS Error : 11.90
Average Error : -4.40
Maximum Error : 42.00

C. Point ID	DEM Pixel	DEM Line	C. Point Elevation	Calculated Elevation	Difference Elevation
6	815.30	1733.50	800.80	805.10	4.30
7	793.90	1603.70	834.50	837.90	3.40
9	966.60	1627.20	818.10	823.30	5.20
13	843.40	1402.90	841.10	846.60	5.50
15	856.00	1308.70	830.40	842.60	12.20
16	910.20	1250.70	864.30	873.40	9.10
19	749.30	1203.90	893.40	900.30	7.00
27	659.20	1502.70	959.90	963.20	3.30
33	543.20	824.40	1073.00	1074.80	1.80
38	762.70	942.00	923.30	926.10	2.80
39	822.30	992.70	882.00	887.50	5.50
40	918.30	939.70	852.30	854.90	2.60
46	757.50	650.90	1072.40	1069.10	-3.30
47	731.40	487.50	1210.30	1197.90	-12.50
48	622.70	666.90	1136.70	1141.20	4.50
60	964.10	494.20	1014.40	993.60	-20.80
61	818.60	457.70	1095.00	1082.80	-12.20
66	1156.10	617.00	1067.20	1054.10	-13.10

Table F.4 Continued

C. Point ID	DEM Pixel	DEM Line	C. Point Elevation	Calculated Elevation	Difference Elevation
67	1100.40	664.00	1063.80	1062.10	-1.70
68	1133.10	772.90	1083.80	1072.90	-10.80
71	1342.20	943.60	1192.00	1185.20	-6.80
75	1009.50	1044.40	855.50	860.80	5.40
78	1195.00	1217.60	1004.50	1009.30	4.70
80	1145.50	1338.80	883.20	882.40	-0.80
81	1250.50	1382.80	959.90	960.40	0.50
83	1416.40	1332.90	1029.60	1029.90	0.30
84	1358.10	1237.40	1057.30	1055.30	-2.00
85	1417.70	1175.30	1165.60	1162.30	-3.30
86	1529.70	1116.50	1089.40	1080.50	-9.00
88	1461.90	912.70	973.60	968.10	-5.50
98	1529.30	1296.60	1204.00	1199.40	-4.60
99	1529.10	1457.70	1021.50	1025.30	3.70
100	1450.40	1526.60	1035.20	1039.00	3.70
104	932.10	1792.20	825.20	826.40	1.20
105	1451.80	1683.30	1113.70	1116.00	2.30
109	1327.50	1988.10	751.60	752.90	1.30
113	1568.70	1613.90	948.60	953.60	5.00
116	1646.70	1305.20	1227.10	1229.00	1.90
117	1909.00	1176.70	1101.40	1099.90	-1.50
123	2109.00	1463.20	1197.60	1199.80	2.20
128	2297.20	1323.60	1243.60	1237.40	-6.20
132	2419.70	969.10	1080.40	1064.90	-15.50
147	2057.10	752.80	1044.80	1029.40	-15.40
150	1655.10	826.20	1029.40	1019.40	-10.00
161	711.60	1593.30	903.90	899.90	-4.10

Number of CPs : 45
RMS Error : 7.40
Average Error : -1.30
Maximum Error : 20.80

APPENDIX G

Table G.1 The results of the elevation differences for the non-edited DEM using the GCP set 1.

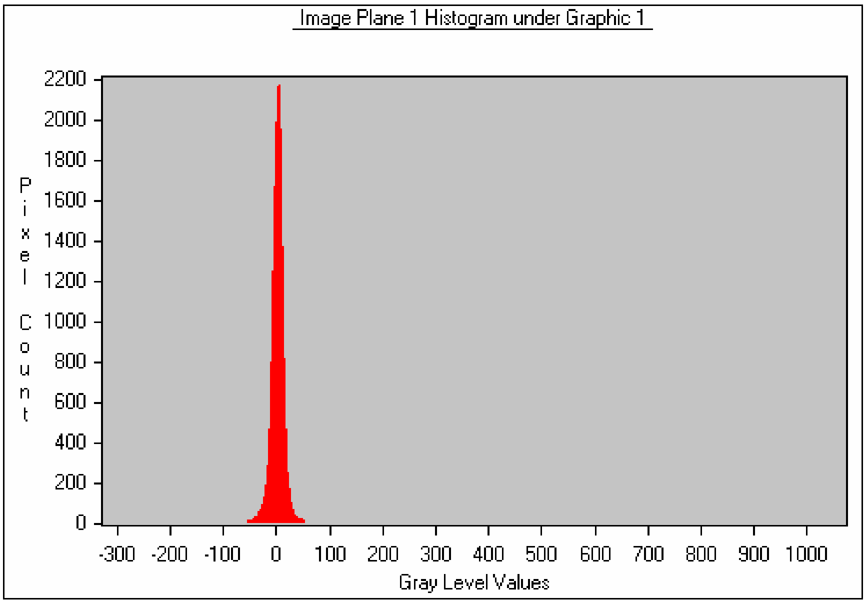

Number of pixels	Mean Value	Median Value	Standart Deviation (m)	Minimum Value (m)	Maximum Value (m)
2.171.664	1.110	1.014	17.104	-327.630	1069.854

Table G.2 The results of the elevation differences for the non-edited DEM using the GCP set 2.

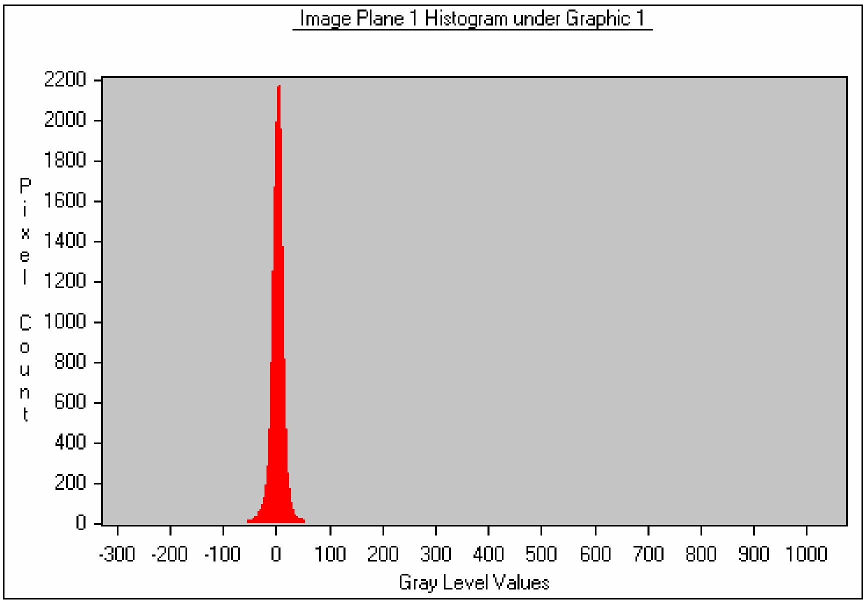

Number of pixels	Mean Value	Median Value	Standart Deviation (m)	Minimum Value (m)	Maximum Value (m)
2.171.664	1.366	1.485	17.762	-375.001	1066.960

Table G.3 The results of the elevation differences for the non-edited DEM using the GCP set 3.

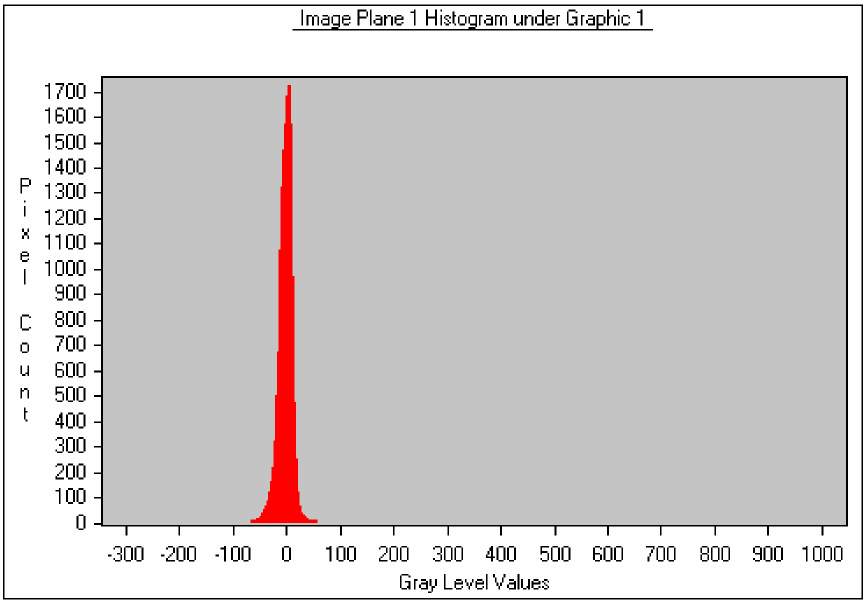

Number of pixels	Mean Value	Median Value	Standart Deviation (m)	Minimum Value (m)	Maximum Value (m)
2.171.664	-3.006	-2.372	18.281	-343.509	1041.326

Table G.4 The results of the elevation differences for the non-edited DEM using the GCP set 4.

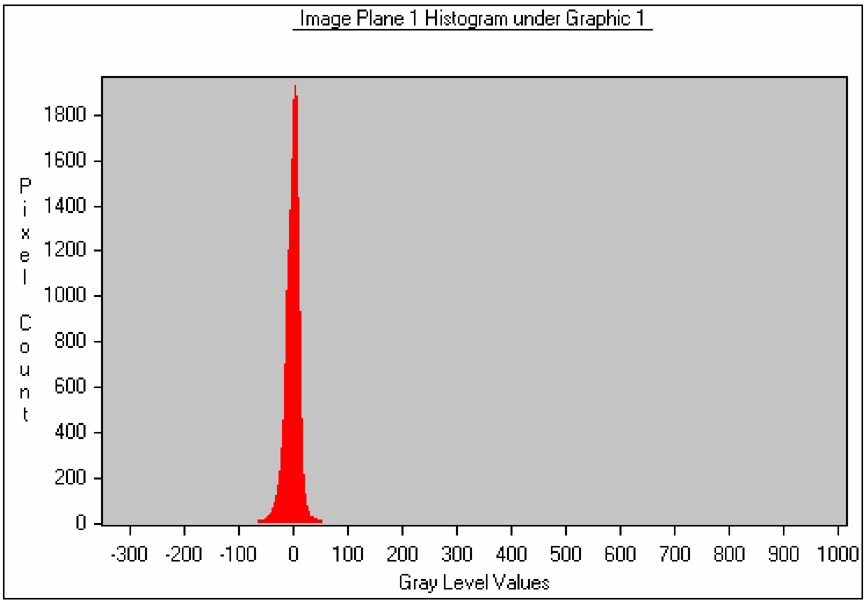

Number of pixels	Mean Value	Median Value	Standart Deviation (m)	Minimum Value (m)	Maximum Value (m)
2.171.664	-1.359	-0.466	18.097	-348.663	1011.255

Table G.5 The results of the elevation differences for the edited DEM using the GCP set 1.

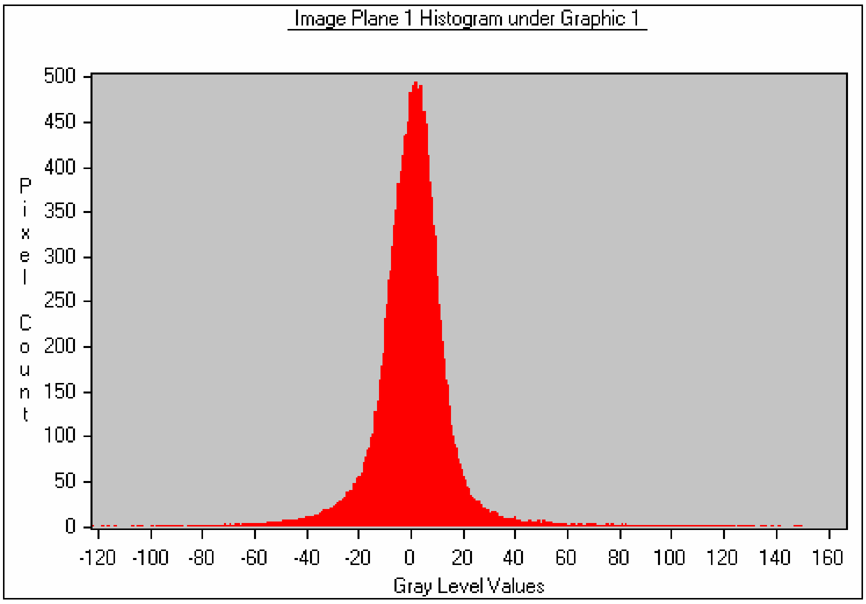

Number of pixels	Mean Value	Median Value	Standart Deviation (m)	Minimum Value (m)	Maximum Value (m)
2.171.664	0.466	0.924	11.125	-122.271	166.045

Table G.6 The results of the elevation differences for the edited DEM using the GCP set 2.

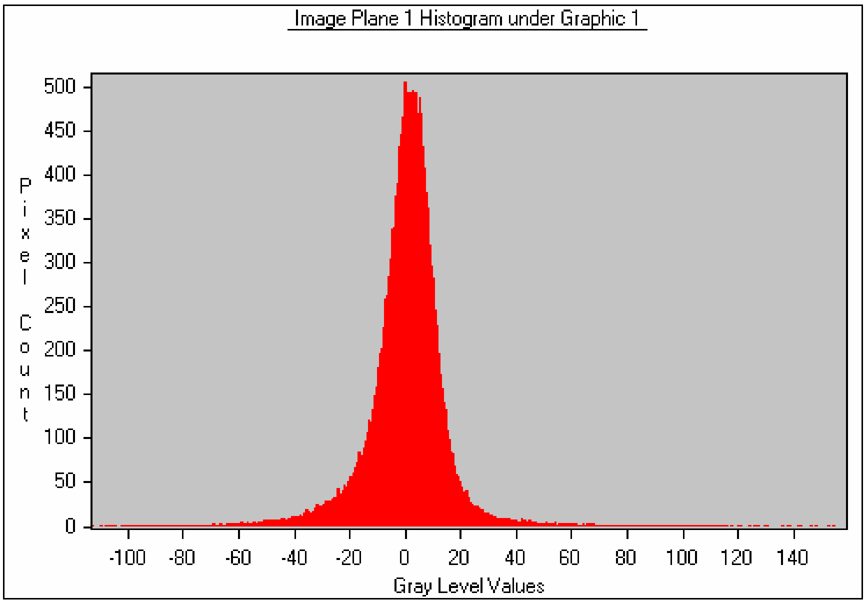

Number of pixels	Mean Value	Median Value	Standart Deviation (m)	Minimum Value (m)	Maximum Value (m)
2.171.664	0.637	1.418	10.929	-112.907	158.253

Table G.7 The results of the elevation differences for the edited DEM using the GCP set 3.

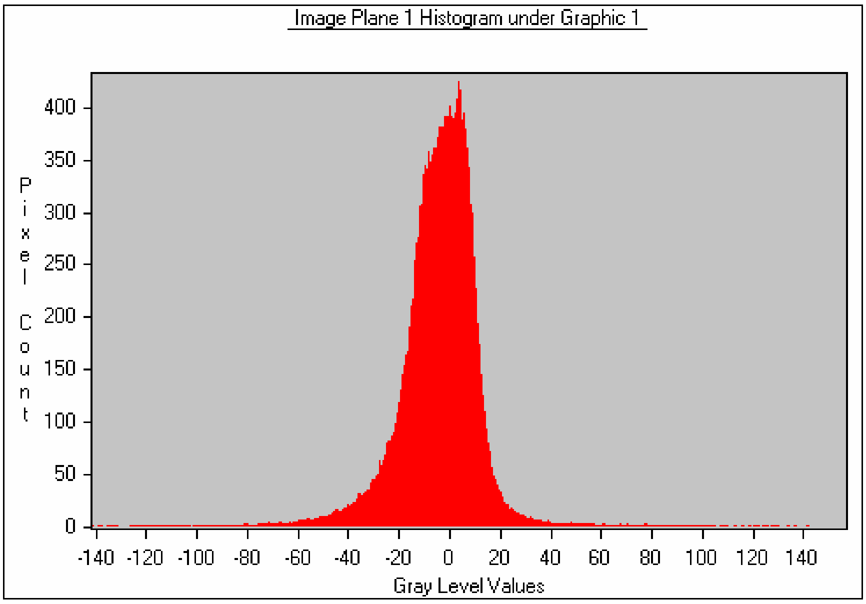

Number of pixels	Mean Value	Median Value	Standart Deviation (m)	Minimum Value (m)	Maximum Value (m)
2.171.664	-3.708	-2.552	12.364	-141.401	156.031

Table G.8 The results of the elevation differences for the edited DEM using the GCP set 4.

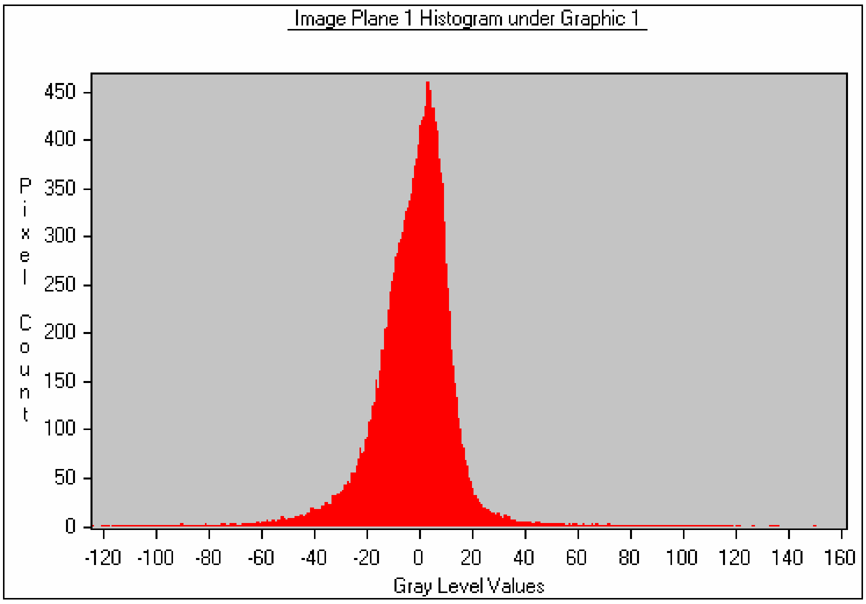

Number of pixels	Mean Value	Median Value	Standart Deviation (m)	Minimum Value (m)	Maximum Value (m)
2.171.664	-2.066	-0.610	12.087	-124.413	160.744

Table G.9 The results of the elevation differences for the non-edited DEM (Count).

Satellite	GCP Number	Total Elevation Points	Number of Elevation Points				
			Within 5m	Within 10m	Within 15m	Within 20m	Within 50m
ASTER	8	2,171,664	895,630	1,548,457	1,866,329	2,004,691	2,151,038
	16		936,934	1,574,614	1,877,211	2,008,282	2,150,369
	24		743,881	1,381,247	1,757,020	1,939,388	2,147,439
	32		794,622	1,437,635	1,798,061	1,966,237	2,149,476

Table G.10 The results of the elevation differences for the non-edited DEM (Percentage).

Satellite	GCP Number	Total Elevation Points	Percentage of Elevation Points				
			Within 5m	Within 10m	Within 15m	Within 20m	Within 50m
ASTER	8	2,171,664	41.24	71.30	85.94	92.31	99.05
	16		43.14	72.51	86.44	92.48	99.02
	24		34.25	63.60	80.91	89.30	98.88
	32		36.59	66.20	82.80	90.54	98.98

Table G.11 The results of the elevation differences for the edited DEM (Count).

Satellite	GCP Number	Total Elevation Points	Number of Elevation Points				
			Within 5m	Within 10m	Within 15m	Within 20m	Within 50m
ASTER	8	2,171,664	917,495	1,582,501	1,896,177	2,029,556	2,164,728
	16		959,668	1,606,898	1,907,095	2,033,429	2,165,102
	24		751,966	1,401,972	1,781,645	1,961,651	2,161,075
	32		803,619	1,458,526	1,822,315	1,988,143	2,162,868

Table G.12 The results of the elevation differences for the edited DEM (Percentage).

Satellite	GCP Number	Total Elevation Points	Percentage of Elevation Points				
			Within 5m	Within 10m	Within 15m	Within 20m	Within 50m
ASTER	8	2,171,664	42.25	72.87	87.31	93.46	99.68
	16		44.19	73.99	87.82	93.63	99.70
	24		34.63	64.56	82.04	90.33	99.51
	32		37.00	67.16	83.91	91.55	99.59

APPENDIX H

Table H.1 The residuals for 8 GCPs and 67 CPs for the nadir and backward ASTER images.

Residual Information in pixels

ASTER Nadir image	**RMS Error**			**Maximum Error**		
	X	**Y**	**Overall**	**X**	**Y**	**Overall**
8 GCPs	0.38	0.24	0.45	0.57	-0.24	0.62
67 CPs	0.72	0.41	0.83	-1.83	-0.45	1.89

ASTER Backward image	**RMS Error**			**Maximum Error**		
	X	**Y**	**Overall**	**X**	**Y**	**Overall**
8 GCPs	0.23	0.45	0.50	0.26	-1.00	1.04
67 CPs	0.66	0.44	0.79	1.67	0.64	1.79

Both images	**RMS Error**			**Maximum Error**		
	X	**Y**	**Overall**	**X**	**Y**	**Overall**
16 GCPs	0.30	0.35	0.46	0.26	-1.00	1.04
134 CPs	0.69	0.42	0.81	-1.83	-0.45	1.89

Table H.1 Continued

Residual Information in meters

ASTER Nadir image	RMS Error			Maximum Error		
	X	Y	Overall	X	Y	Overall
8 GCPs	5.70	3.60	6.75	8.55	-3.60	9.30
67 CPs	10.80	6.15	12.45	-27.45	-6.75	28.35

ASTER Backward image	RMS Error			Maximum Error		
	X	Y	Overall	X	Y	Overall
8 GCPs	3.45	6.75	7.50	3.90	-15.00	15.60
67 CPs	9.90	6.60	11.85	25.05	9.60	26.85

Both images	RMS Error			Maximum Error		
	X	Y	Overall	X	Y	Overall
16 GCPs	4.50	5.25	6.90	3.90	-15.00	15.60
134 CPs	10.35	6.30	12.15	-27.45	-6.75	28.35

Table H.2 The residuals for 16 GCPs and 61 CPs for the nadir and backward ASTER images.

Residual Information in pixels

ASTER Nadir image	RMS Error			Maximum Error		
	X	Y	Overall	X	Y	Overall
16 GCPs	0.69	0.32	0.76	-1.70	0.29	1.73
61 CPs	0.78	0.37	0.86	-1.77	0.29	1.80

ASTER Backward image	RMS Error			Maximum Error		
	X	Y	Overall	X	Y	Overall
16 GCPs	0.52	0.48	0.71	0.66	-1.31	1.47
61 CPs	0.60	0.46	0.76	-1.66	-0.19	1.67

Both images	RMS Error			Maximum Error		
	X	Y	Overall	X	Y	Overall
32 GCPs	0.60	0.40	0.72	-1.70	0.29	1.73
122 CPs	0.69	0.42	0.81	-1.77	0.29	1.80

Table H.2 Continued

Residual Information in meters

ASTER Nadir image	RMS Error			Maximum Error		
	X	Y	Overall	X	Y	Overall
16 GCPs	10.35	4.80	11.40	-25.50	4.35	25.95
61 CPs	11.70	5.55	12.90	-26.55	4.35	27.00

ASTER Backward image	RMS Error			Maximum Error		
	X	Y	Overall	X	Y	Overall
16 GCPs	7.80	7.20	10.65	9.90	-19.65	22.05
61 CPs	9.00	6.90	11.40	-24.90	-2.85	25.05

Both images	RMS Error			Maximum Error		
	X	Y	Overall	X	Y	Overall
32 GCPs	9.00	6.00	10.80	-25.50	4.35	25.95
122 CPs	10.35	6.30	12.15	-26.55	4.35	27.00

Table H.3 The residuals for 24 GCPs and 53 CPs for the nadir and backward ASTER images.

Residual Information in pixels

ASTER Nadir image	RMS Error			Maximum Error		
	X	Y	Overall	X	Y	Overall
24 GCPs	0.71	0.33	0.78	-1.80	0.05	1.80
53 CPs	0.69	0.45	0.82	-1.68	0.66	1.80

ASTER Backward image	RMS Error			Maximum Error		
	X	Y	Overall	X	Y	Overall
24 GCPs	0.58	0.49	0.76	1.23	-1.47	1.92
53 CPs	0.57	0.44	0.72	-1.55	-0.34	1.59

Both images	RMS Error			Maximum Error		
	X	Y	Overall	X	Y	Overall
48 GCPs	0.64	0.41	0.76	1.23	-1.47	1.92
106 CPs	0.63	0.44	0.77	-1.68	0.66	1.80

Table H.3 Continued

Residual Information in meters

ASTER Nadir image	RMS Error			Maximum Error		
	X	Y	Overall	X	Y	Overall
24 GCPs	10.65	4.95	11.70	-27.00	0.75	27.00
53 CPs	10.35	6.75	12.30	-25.20	9.90	27.00

ASTER Backward image	RMS Error			Maximum Error		
	X	Y	Overall	X	Y	Overall
24 GCPs	8.70	7.35	11.40	18.45	-22.05	28.80
53 CPs	8.55	6.60	10.80	-23.25	-5.10	23.85

Both images	RMS Error			Maximum Error		
	X	Y	Overall	X	Y	Overall
48 GCPs	9.60	6.15	11.40	18.45	-22.05	28.80
106 CPs	9.45	6.60	11.55	-25.20	9.90	27.00

Table H.4 The residuals for 32 GCPs and 45 CPs for the nadir and backward ASTER images.

Residual Information in pixels

ASTER Nadir image	RMS Error			Maximum Error		
	X	Y	Overall	X	Y	Overall
32 GCPs	0.72	0.31	0.78	-1.92	-0.07	1.93
45 CPs	0.68	0.44	0.81	-1.77	0.58	1.87

ASTER Backward image	RMS Error			Maximum Error		
	X	Y	Overall	X	Y	Overall
32 GCPs	0.61	0.42	0.74	1.44	-1.40	2.01
45 CPs	0.54	0.47	0.72	-1.50	-0.31	1.53

Both images	RMS Error			Maximum Error		
	X	Y	Overall	X	Y	Overall
64 GCPs	0.66	0.37	0.76	1.44	-1.40	2.01
90 CPs	0.61	0.45	0.76	-1.77	0.58	1.87

Table H.4 Continued

Residual Information in meters

ASTER Nadir image	RMS Error			Maximum Error		
	X	Y	Overall	X	Y	Overall
32 GCPs	10.80	4.65	11.70	-28.80	-1.05	28.95
45 CPs	10.20	6.60	12.15	-26.55	8.70	28.05

ASTER Backward image	RMS Error			Maximum Error		
	X	Y	Overall	X	Y	Overall
32 GCPs	9.15	6.30	11.10	21.60	-21.00	30.15
45 CPs	8.10	7.05	10.80	-22.50	-4.65	22.95

Both images	RMS Error			Maximum Error		
	X	Y	Overall	X	Y	Overall
64 GCPs	9.90	5.55	11.40	21.60	-21.00	30.15
90 CPs	9.15	6.75	11.40	-26.55	8.70	28.05

APPENDIX I

The definitions of the reference systems are explained in (Wolf, 2000):

I.1 Geodetic Coordinate System

Geodetic coordinates for specifying point locations relative to the Earth's surface are latitude Φ, longitude λ, and height h. These coordinates all depend upon a reference ellipsoid for their basis. Latitude and longitude are horizontal components, while the vertical component is height. These three coordinates are illustrated in Figure I.1. This figure shows a point P with a line passing through it, perpendicular to the ellipsoid and extending to the polar axis. This line is called the *normal*. The longitude (λ) of a point is given by the angle in the plane of the equator from the *prime meridian* (usually the meridian through Greenwich, England) to the *local meridian* (meridian passing through the normal line). Values of long
itude range from -180º to +180º with those west of the prime meridian being negative and those to the east being positive. The latitude (Φ) of a point is the angle from the equatorial plane to the normal line. Values of latitude range from -90º to +90º with those north of the equator being positive and those to the south being negative. As also illustrated, height (h) is the distance from the surface of the ellipsoid to the point P, in the same direction as the normal. This value specifies the elevation of a point above the ellipsoid, also known as the *ellipsoid height*.

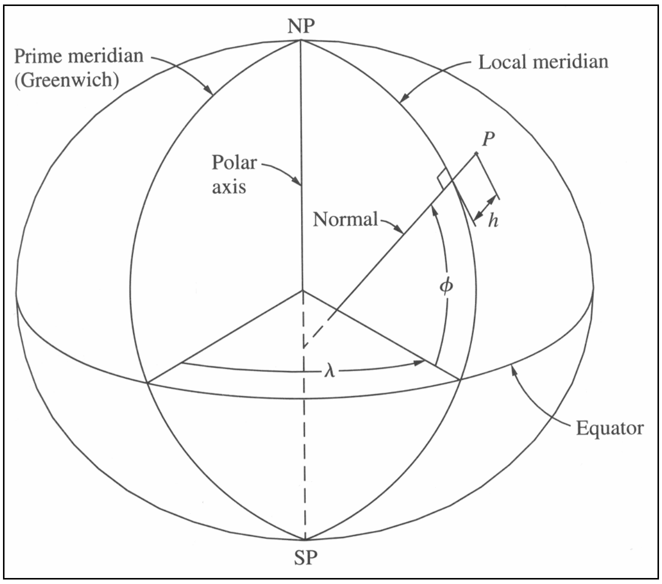

Figure I.1 The geodetic coordinate system

I.2 Geocentric Coordinate System

While geodetic coordinates Φ λ h provide an Earth-based definition for a point's three-dimensional position, they are related to a curved surface (reference ellipsoid). These coordinates are therefore nonorthogonal and as such are unsuitable for analytical photogrammetry, which assumes a rectangular or cartesian coordinate system. The geocentric coordinate system, on the other hand, is a three dimensional X Y Z cartesian system which provides an Earth-centered definition of position, independent of any reference surface. This system has its X Y plane in the plane of the equator with the Z axis extending through the north pole. The X axis is oriented such that its positive end passes through the prime meridian. Figure I.2 illustrates the geocentric coordinate system and its relationship to geodetic coordinates.

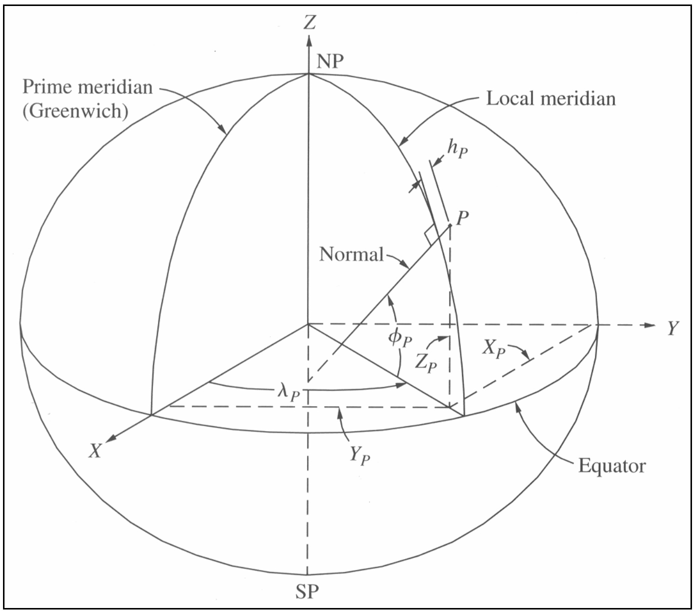

Figure I.2 The geocentric coordinate system

I.3 Local Cartesian Coordinate System

A local cartesian coordinate system is a three dimensional cartesian X Y Z reference system which has its origin placed at a specific point within the projected area. At this local origin, the Z axis extends straight up from the ellipsoid in the same direction as the normal at the origin. The positive X and Y axes are tangent to the ellipsoid and point to the east and north, respectively. Figure I.3 shows the local cartesian coordinate system and its relationship to geocentric and geodetic coordinates. In this figure, the position of the local origin is specified in terms of geodetic coordinates Φ_0, λ_0, and h_0 with the last equal to zero. As shown in Figure I.3, the local origin has geocentric coordinates X_0, Y_0, and Z_0, and point P in the project area has local cartesian coordinates X_{lp}, Y_{lp}, and Z_{lp}.

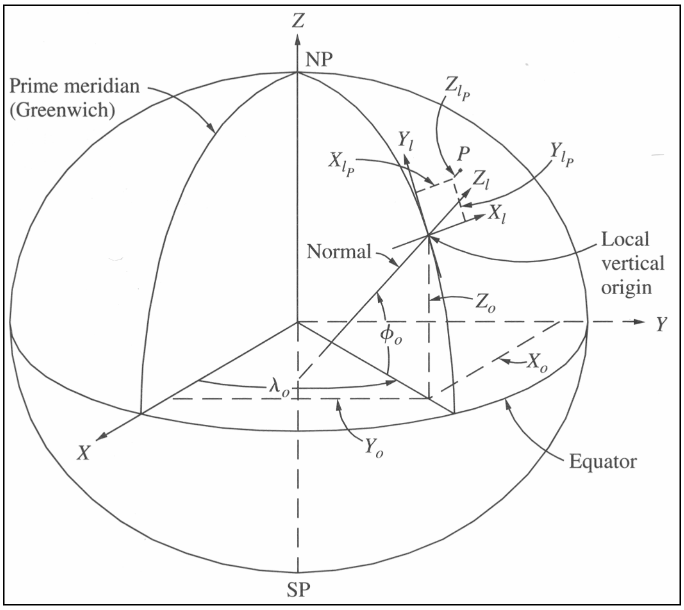

Figure I.3 The local cartesian coordinate system

I.4 UTM Coordinate System

One of the fundemantal products produced through photogrammetry is a map. A map in general, consists of points, lines, arcs, symbols, or images which are placed on a flat, two-dimensional surface such as a sheet of paper or computer display. It is, in a manner of speaking, a scaled representation of what a human would see while walking from point to point in the mapped area. As such, it is preferrable the map present the view-point from directly overhead througout the area. In mapping the Earth's surface, it is impossible to achieve this overhead viewpoint on a two-dimensional medium without distortion because of the Earth's curved shape. Map projections were created to accomplish this viewpoint with a carefully defined and understood amount of distortion.

One of the common map projection system is the *Universal Transverse Mercator* (UTM) system. This system was established to provide worldwide coverage by defining 60 zones, each having a 6º longitude range. UTM zone 1 extends from 180º west longitude to 174º west longitude, with a central meridian of 177º west. Zone numbers increase to the east,at an equal spacing of 6º longitude. For example zone 17 extends from 84º west to 78º west and has a central meridian of 81º longitude. The value of the scale factor along the central meridian k_0 is equal to 0.9996 for every zone, resulting in a maximum scale distortion of 1 part in 2500. Each zone has its origin (Φ_0, λ_0) at the intersection of the equator with the central meridian. The false easting for each zone is 500,000 m; for latitudes north of the equator, the false northing is 0 m, and for latitudes south of the equator, the false northing is 10,000,000 m.

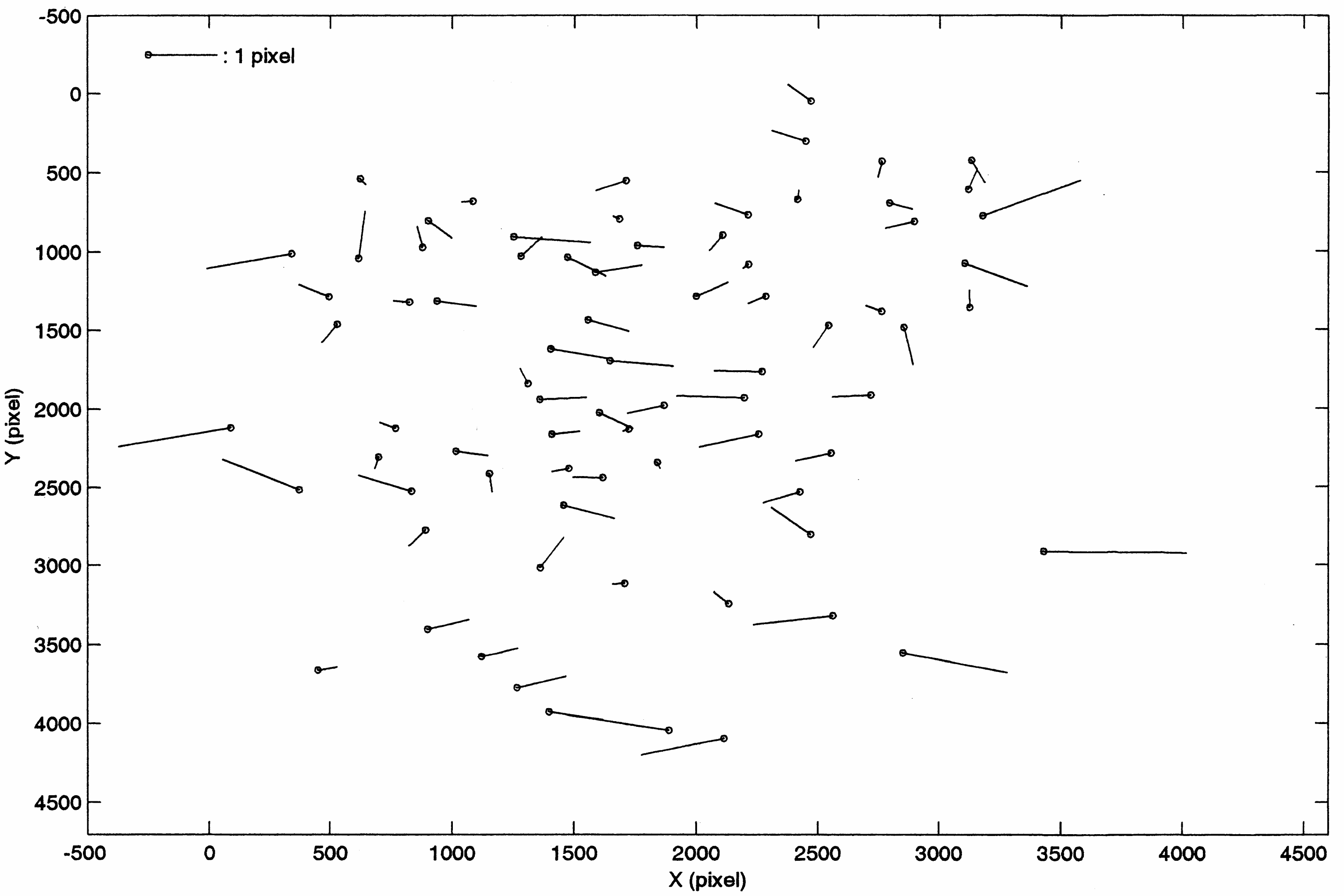

Figure J.1 Error vectors of the 77 GCPs for the Toutin's Model

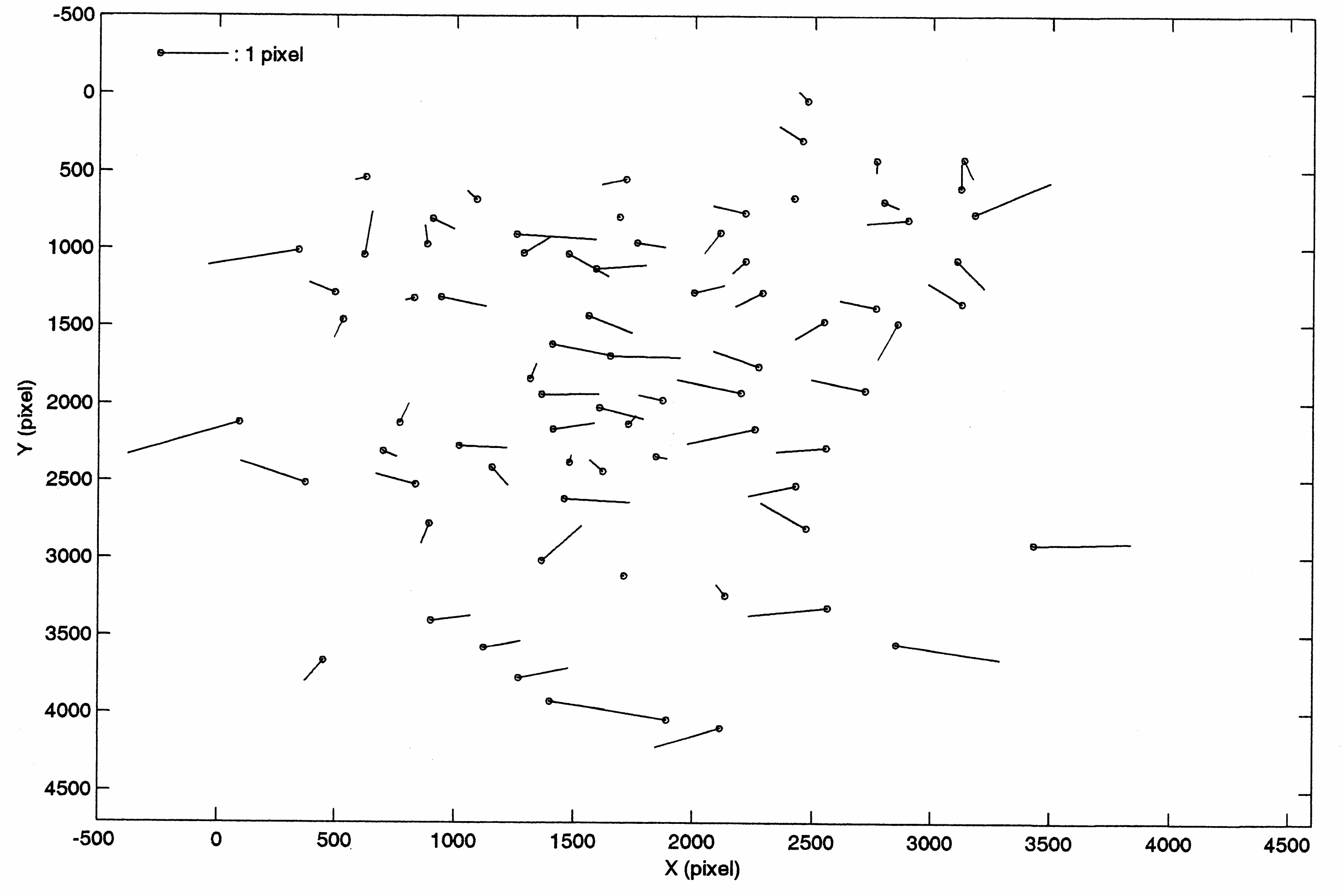

Figure J.2 Error vectors of the 77 GCPs for the model Orun and Natarajan

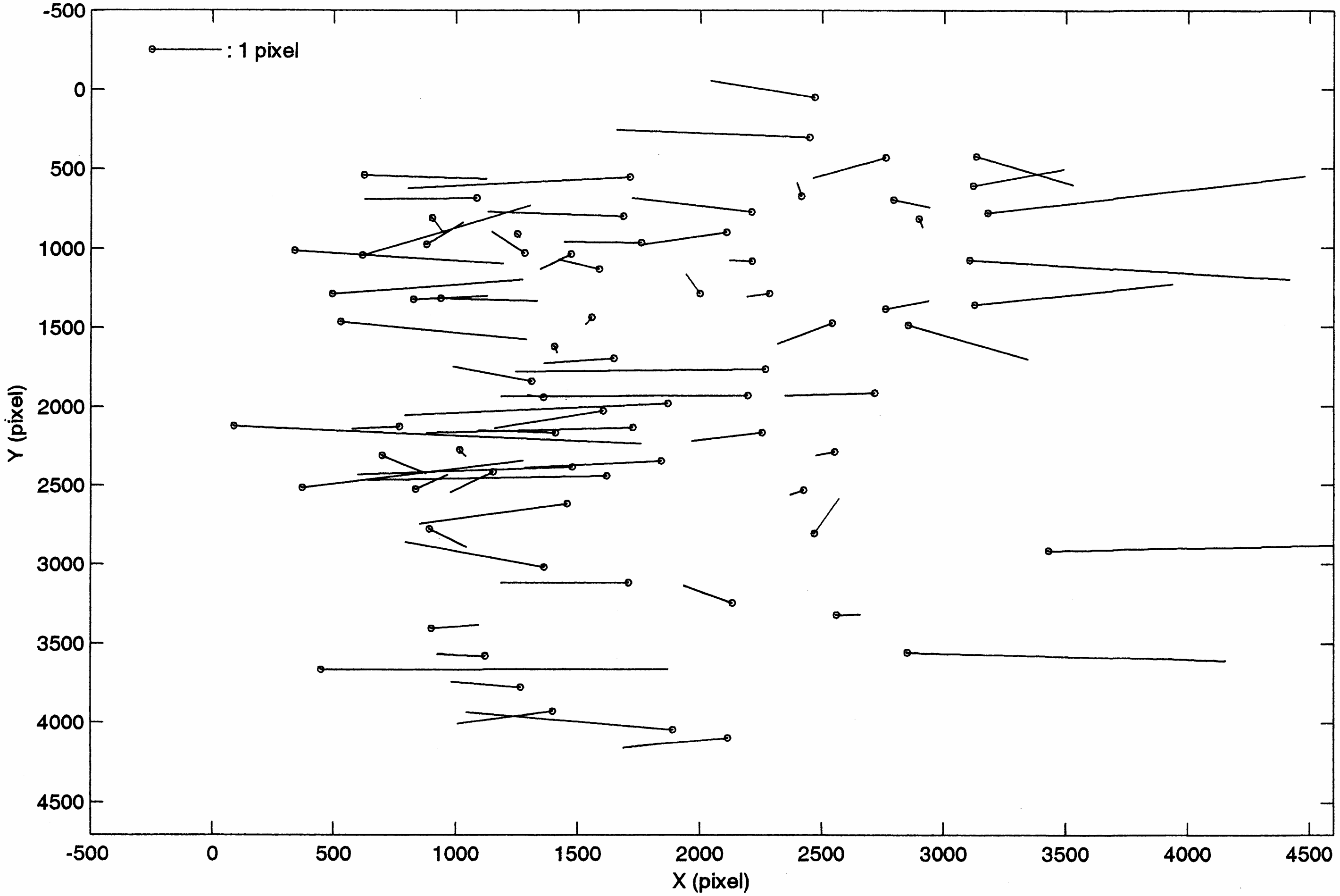

Figure J.3 Error vectors of the 77 GCPs for the Model First Order 2D Polynomial

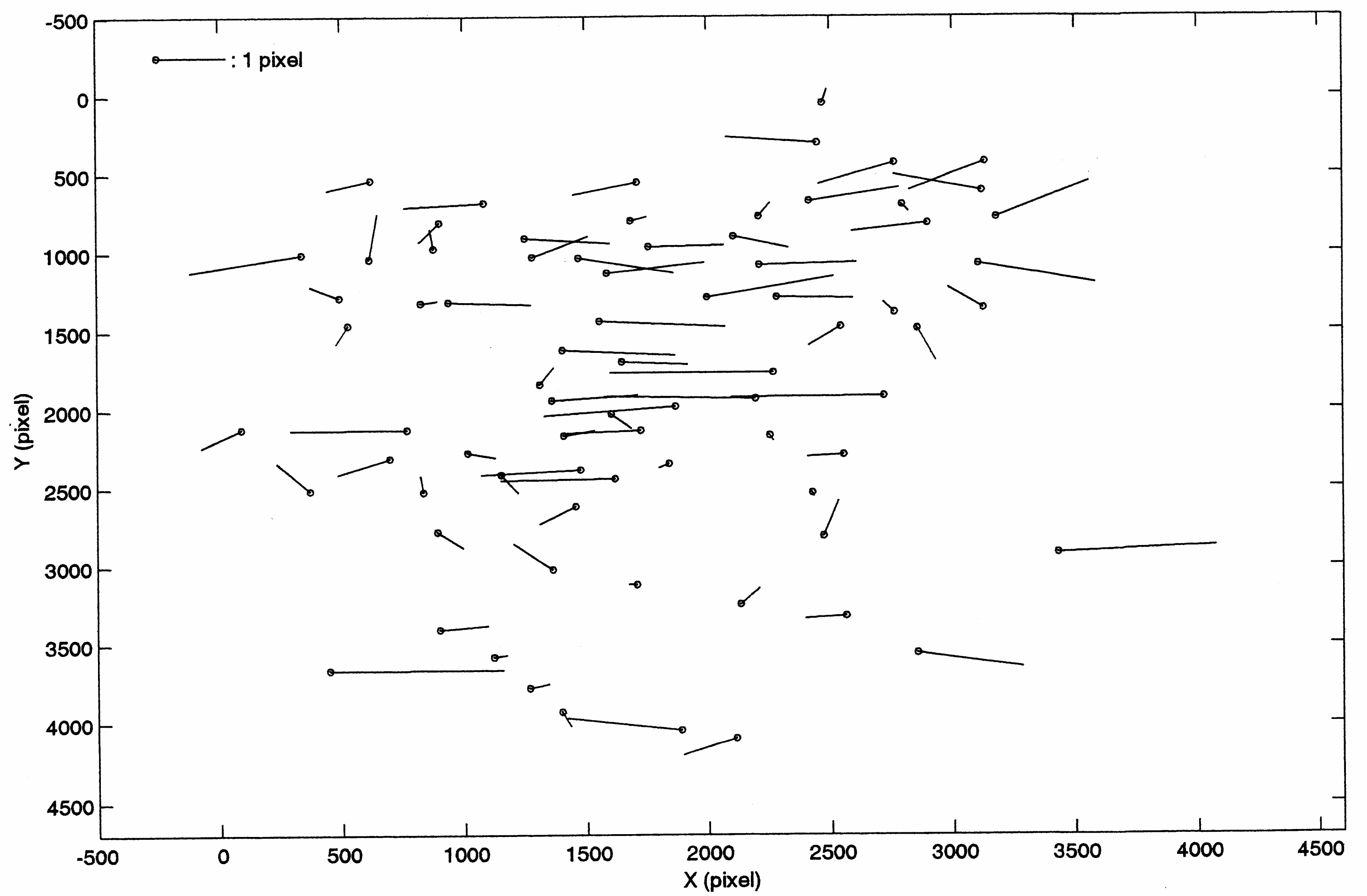

Figure J.4 Error vectors of the 77 GCPs for the Model Second Order 2D Polynomial

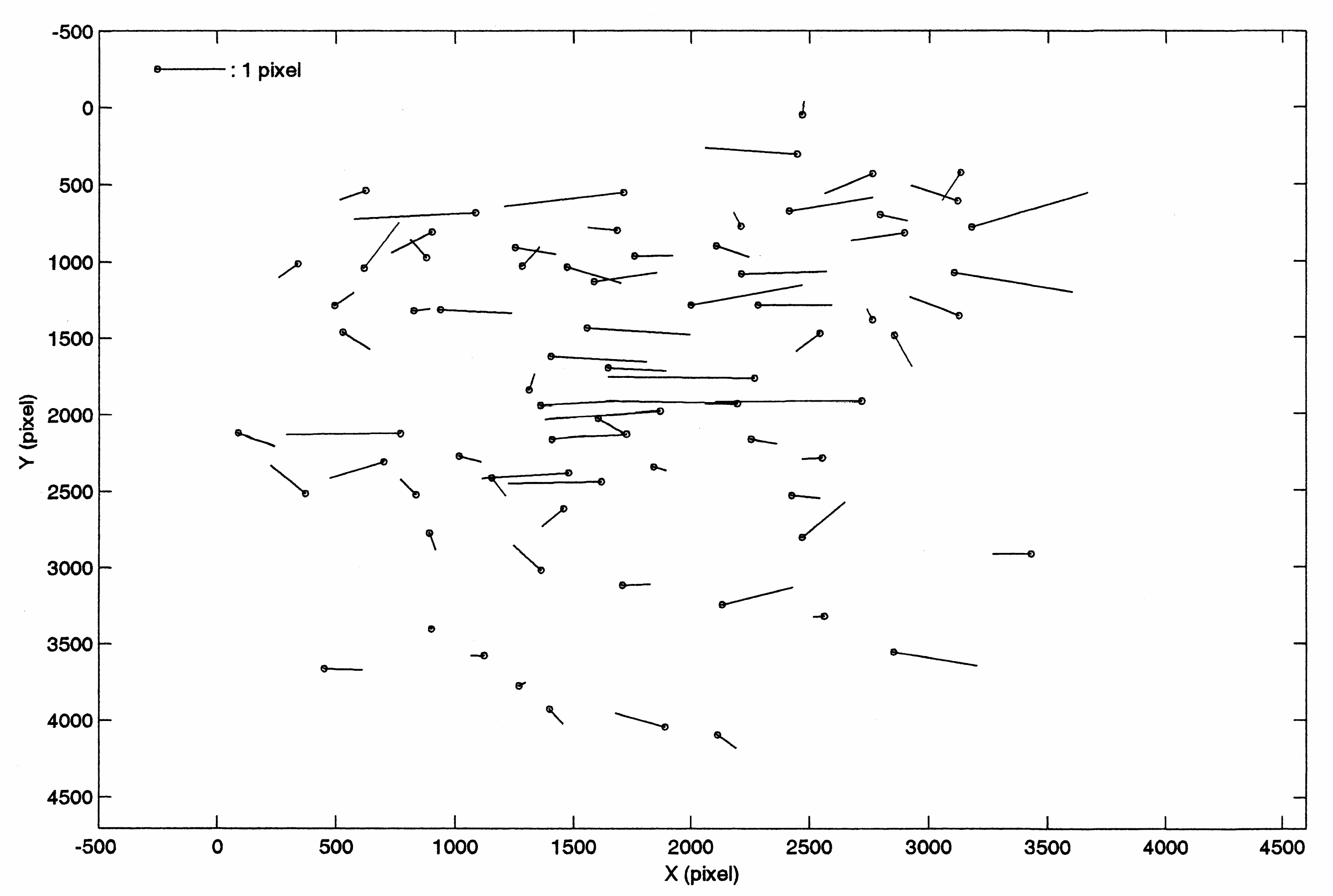

Figure J.5 Error vectors of the 77 GCPs for the Model Third Order 2D Polynomial

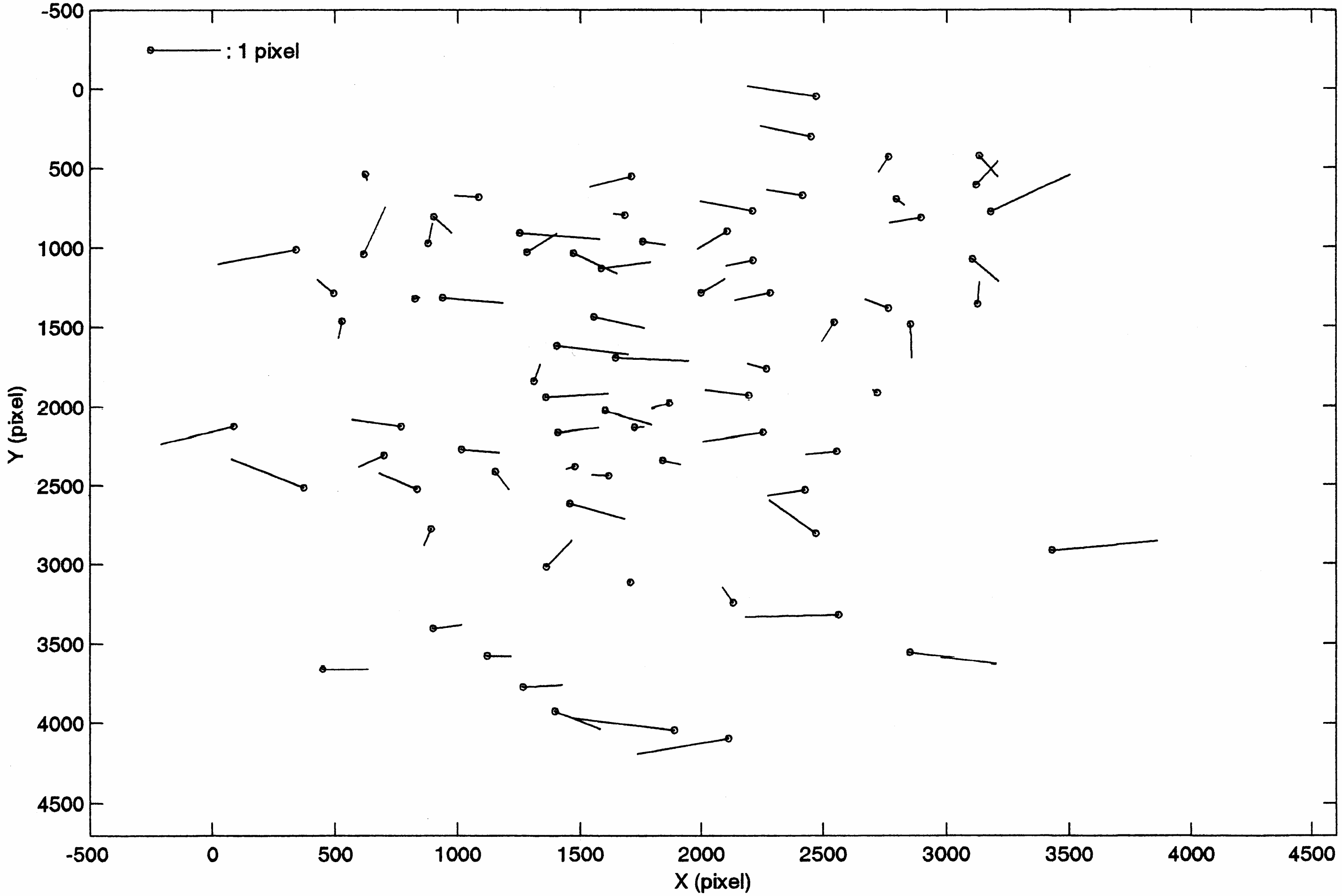

Figure J.6 Error vectors of the 77 GCPs for the Model First Order Rational Function

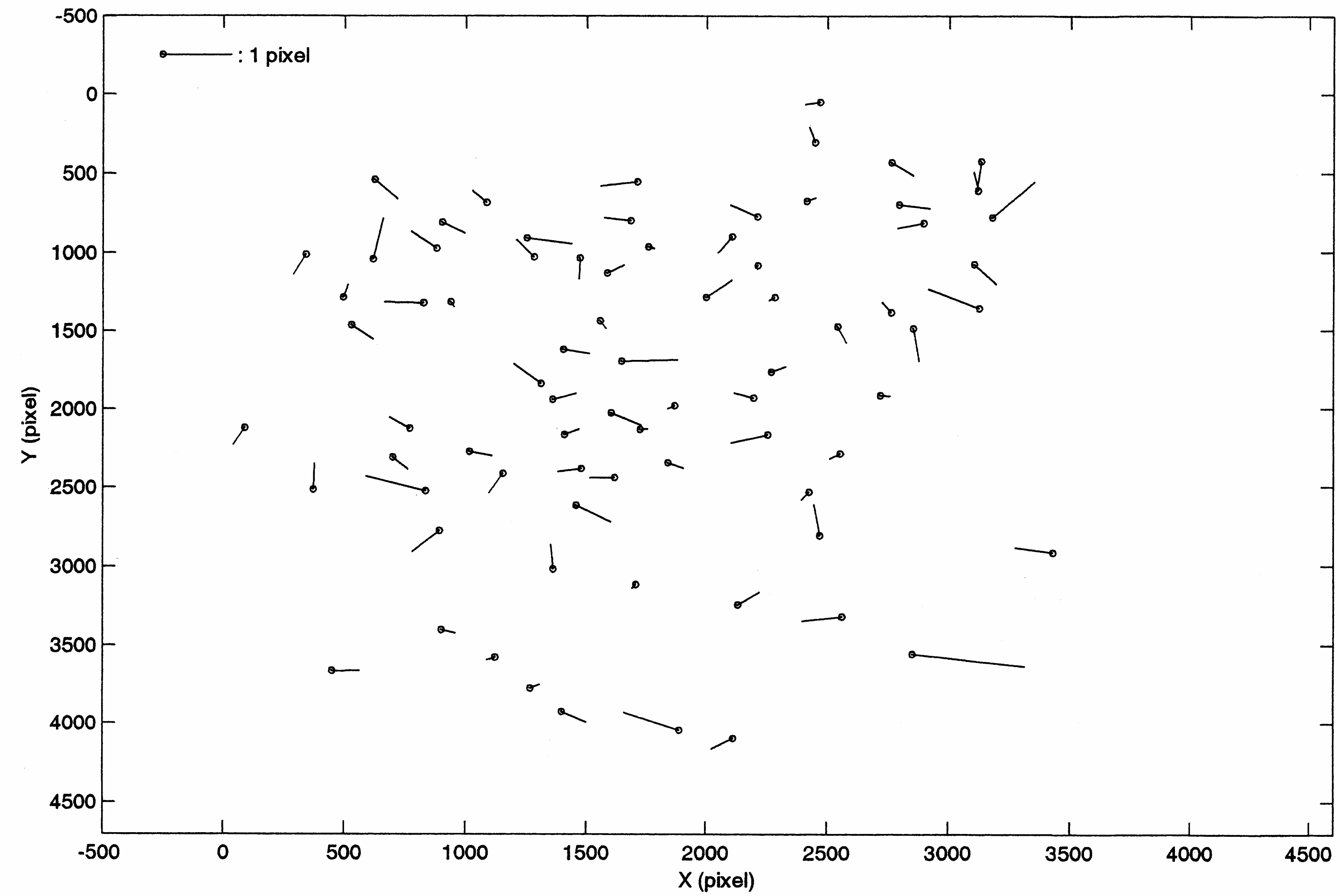

Figure J.7 Error vectors of the 77 GCPs for the Model Second Order Rational Function

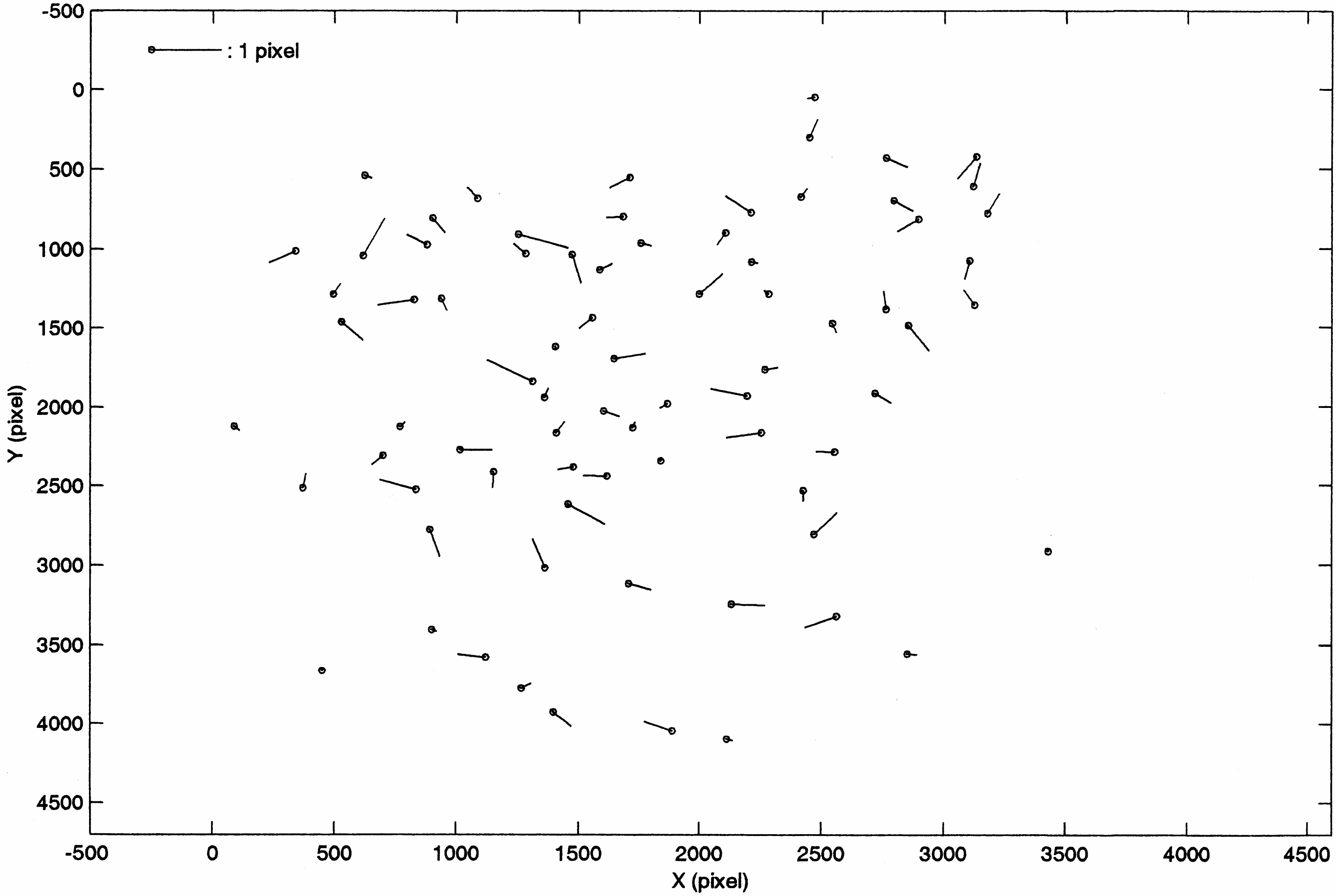

Figure J.8 Error vectors of the 77 GCPs for the Model Third Order Rational Function

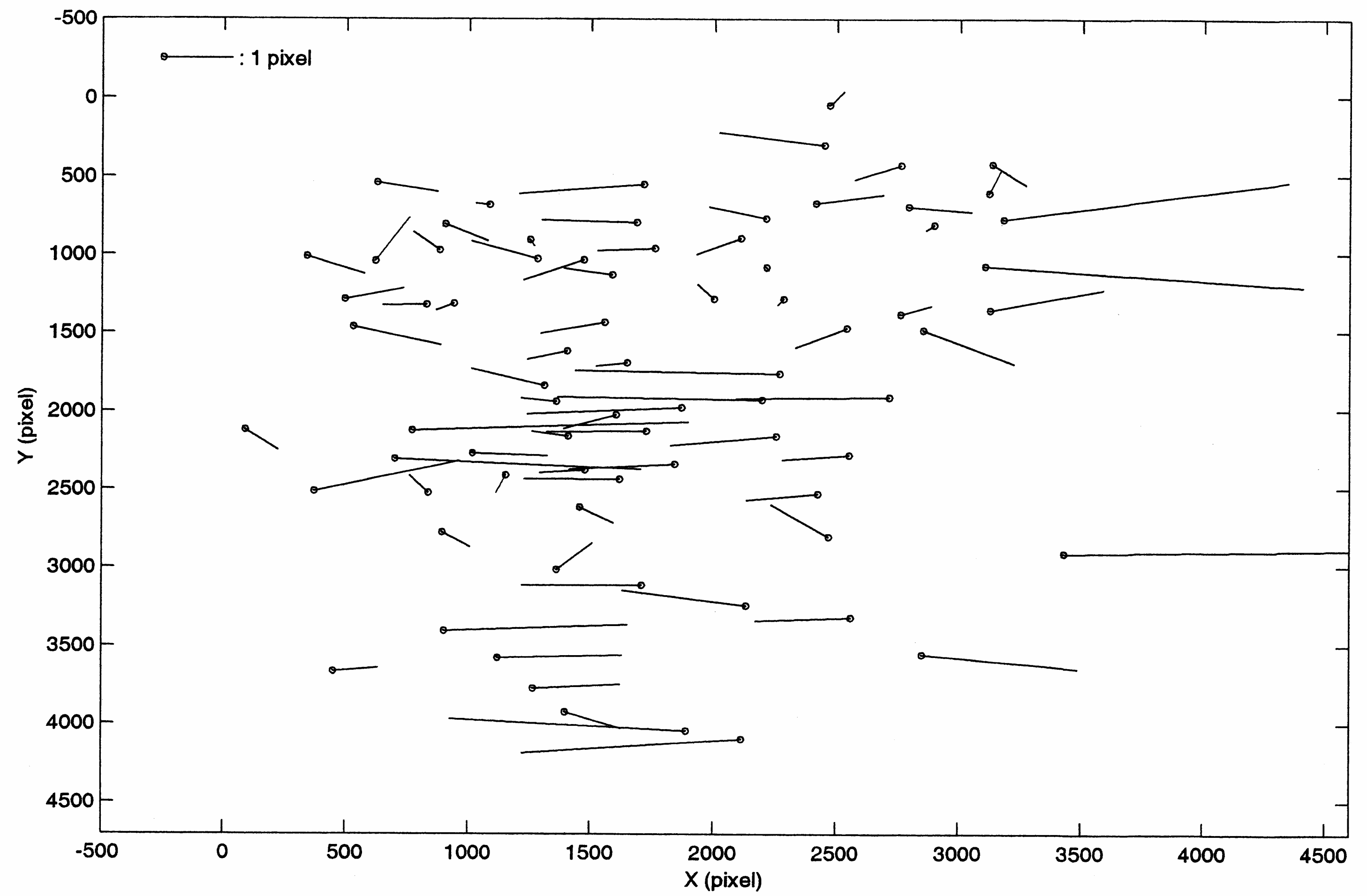

Figure J.9 Error vectors of the 77 GCPs for the Model First Order Polynomial with Relief

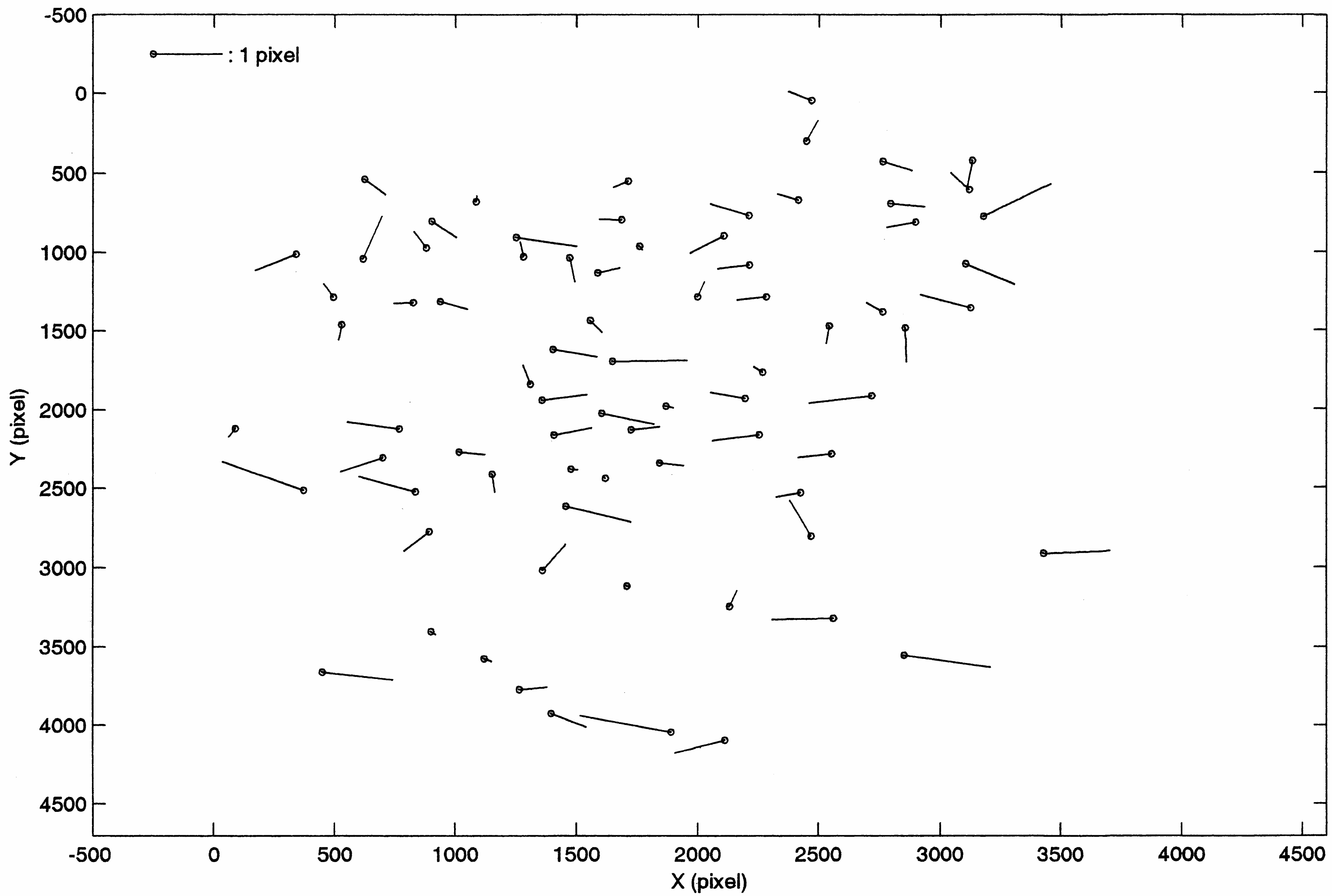

Figure J.10 Error vectors of the 77 GCPs for the Model Second Order Polynomial with Relief

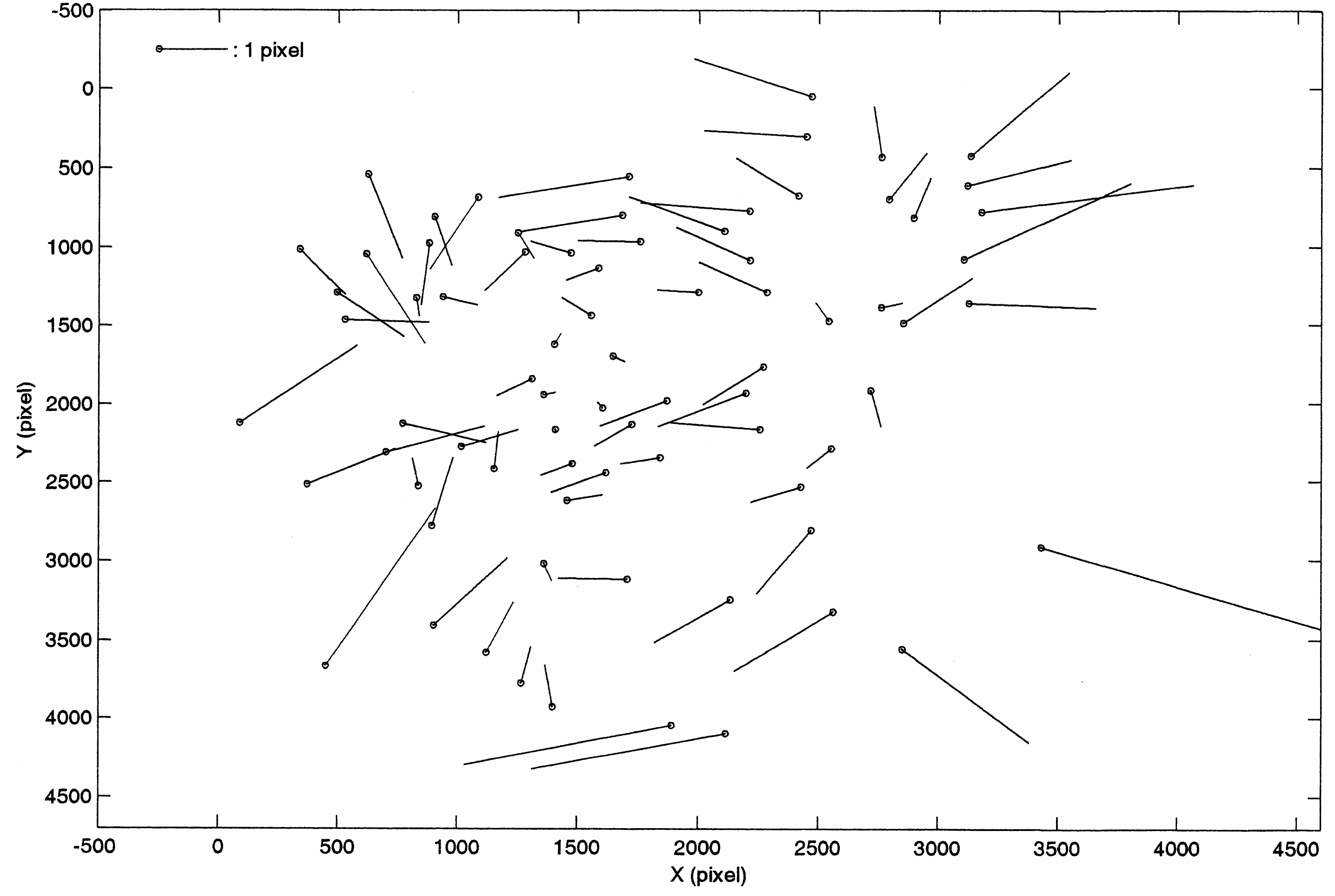

Figure J.11 Error vectors of the 77 GCPs for the Model DLT

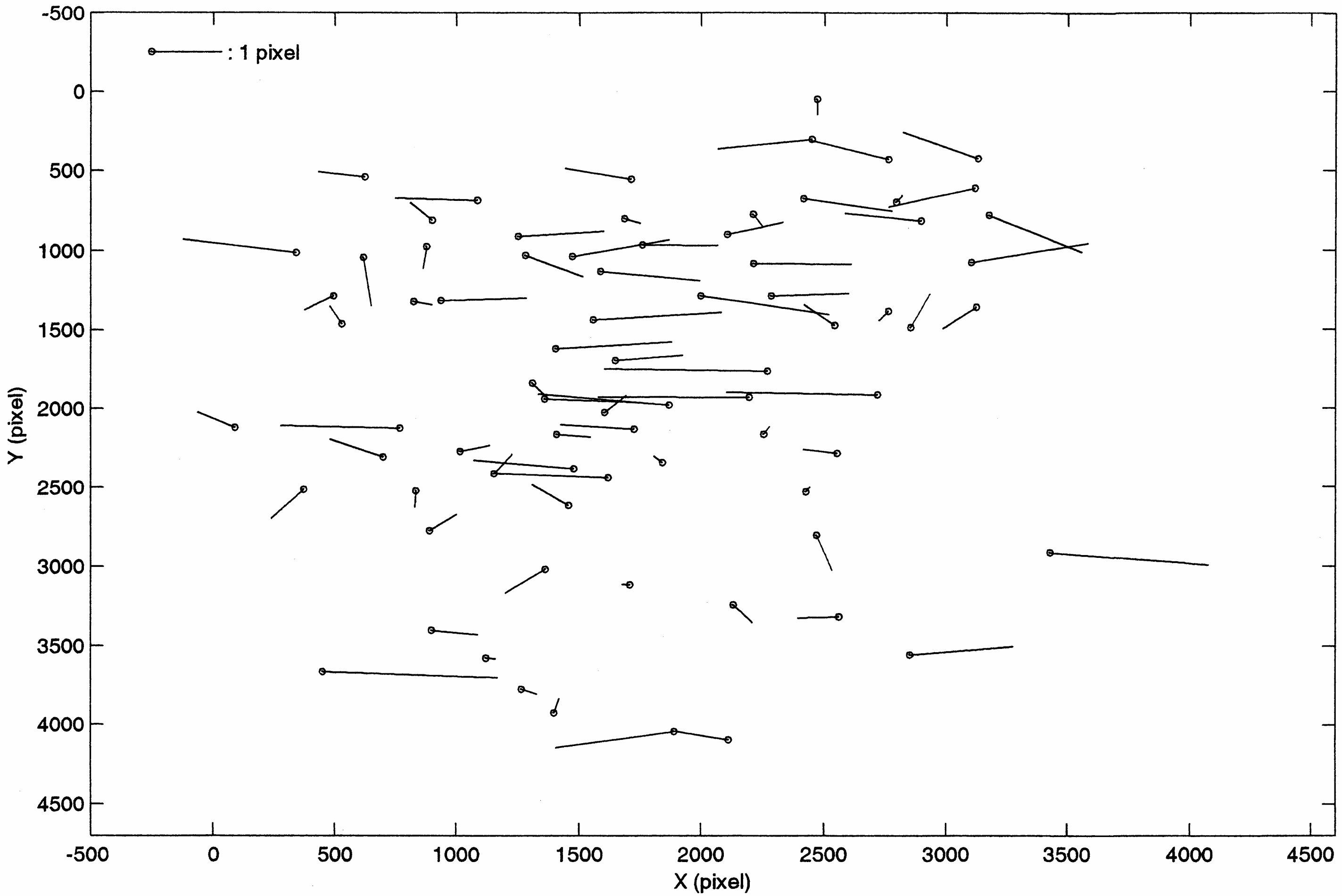

Figure J.12 Error vectors of the 77 GCPs for the Projective Transformation